MICHIGAN STATE UNIVERSITY LIBRARIES
3 1293 01028 1826

This is to certify that the

dissertation entitled

VISCOUS FINGERING FLOWS IN
REACTIVE RESIN SYSTEMS

presented by

Nancy S. Losure

has been accepted towards fulfillment
of the requirements for

Ph.D. degree in Chemical Engineering

Charles A. Petty
Major professor

Date June 28, 1994

MSU is an Affirmative Action/Equal Opportunity Institution

0-12771

LIBRARY
Michigan State
University

PLACE IN RETURN BOX to remove this checkout from your record.
TO AVOID FINES return on or before date due.

DATE DUE	DATE DUE	DATE DUE

MSU is An Affirmative Action/Equal Opportunity Institution

c:\circ\datedue.pm3-p.1

VISCOUS FINGERING FLOWS IN REACTIVE RESIN SYSTEMS

By

Nancy S. Losure

A DISSERTATION

Submitted to
Michigan State University
in partial fulfillment of the requirements
for the degree of

DOCTOR OF PHILOSOPHY

Department of Chemical Engineering

1994

ABSTRACT

VISCOUS FINGERING FLOWS IN REACTIVE RESIN SYSTEMS

By

Nancy Stoneking Losure

Viscous fingering is a flow instability which occurs in fluid flows in which the local viscosity increases in the flow direction. Resin transfer molding (RTM) is a method of manufacturing fiber-reinforced plastic parts wherein a reactive liquid resin is injected into a closed mold that contains the fiber reinforcement (preform). RTM flows exhibit viscosity profiles which increase in the direction of the resin flow when the injection takes place on the same time scale as the gel time of the resin.

Fingering flow in RTM was studied using a Diglycidyl ether of Bisphenol A / Triethylene tetramine (DGEBA/TETA) epoxy resin system. A fingering flow criterion was delineated, based on the resin viscosity (which is a function of reaction extent) and velocity. The results are presented in the form of a moldability diagram, which shows that the operating envelope of the system is cut in half if the viscous fingering flow phenomenon is to be avoided.

The consequences of fingering flow on RTM parts were studied by producing plaques with a variety of finger structures, in neat resin plaques as well as two kinds of glass preforms. It was found that some structures caused no detectable loss of flex modulus, but fingers with multiple, sharp-edged tips caused loss of flex modulus as great as 15%. Other plaques were produced which showed that a simple interface between two batches of DGEBA/TETA epoxy resin is not detrimental to the short beam shear strength of the plaque.

As a part of this work, coefficients for the x and y direction permeabilities, and the longitudinal and transverse dispersion coefficients were determined for a flat plaque mold with a gap width of 0.3 cm, continuous swirl glass mat ($V_f = 0.20$), and woven glass ($V_f = 0.45$) fabric. Also, the reaction kinetics for the DGEBA/TETA epoxy resin system were determined, using Differential Scanning Calorimetry.

THIS WORK IS DEDICATED TO

Mary Elizabeth Harper Thomas
January 14, 1906 to November 12, 1993

ACKNOWLEDGMENTS

Thanks are due to Dr.Charles Petty and Dr. Krishnamurthy Jayaraman, both of the Chemical Engineering Department at Michigan State University. And remember, it is better not to inquire too closely into how sausage and dissertations are made.

Others on my advisory committee must be thanked for favors too numerous to mention. Thank you all: Dr. Lawrence Drzal, CMSC/ MSU; Dr. Roger Morgan, AMEES/MSU; Dr. Brian Thompson, MSM Dept., MSU; and Dr. Sue Selke, Packaging Dept., MSU.

To Mike Rich and Brian Rook of CMSC/MSU and Ed English, Doug Larive, and Brenda Oliver of AMEES/MSU, I wish to pose this rhetorical question: Where would we be without competent, resourceful, cheerful support staff? I only hope that in my next position I find some as good as you.

The Dow Chemical Company supplied Derakane and DGEBA resins, as well as technical advice, and the Hexcel Corporation provided glass mat for preforms. This kind of generous assistance is more widespread and vital than is usually acknowledged. I am very grateful for it.

The present work, and work not presented here are the result of financial support from a variety of agencies. I would like to thank the State of Michigan's Research Excellence Fund, the Dow Fellowship Foundation, the Department of Chemical Engineering at Michigan State University, and most importantly, the Amoco Foundation Fellowship for Future Educators. I shall try to be worthy of your investment. I am also grateful for laboratory facilities of AMEES/MSU in Midland.

And finally, I must thank my husband, Ronald J. Losure. Not every one could deal with a demented PhD candidate when deadlines are looming and the computer is kaput. You have my admiration and thanks.

TABLE OF CONTENTS

LIST OF TABLES xi

LIST OF FIGURES xviii

NOMENCLATURE xxvi

CHAPTER 1: INTRODUCTION 1

OBJECTIVES 2

BACKGROUND 3

FINGERING FLOWS 3

CONSEQUENCES OF FINGERING FLOWS IN REACTIVE RESIN SYSTEMS 22

INTRODUCTION TO RESIN TRANSFER MOLDING 26

THE MOLDABILITY DIAGRAM 27

THE STRUCTURE OF THE PREFORM 34

PHYSICAL PROPERTIES OF COMPOSITE MATERIALS 34

SUMMARY 43

CHAPTER 2: CHARACTERIZATION OF THE RESIN SYSTEMS 44

INTRODUCTION 44

VISCOSITY OF DGEBA/TETA EPOXY 45

MEASUREMENTS 45

DISCUSSION 47

VISCOSITY OF DERAKANE 411 RESIN 51

REACTION KINETICS OF DGEBA/TETA RESIN 54

DISCUSSION 59

VISCOSITY OF DGEBA/TETA EPOXY AS A FUNCTION OF α 64

THE GEL POINT OF DGEBA/TETA EPOXY 64

THE EXOTHERMIC TEMPERATURE OF EPOXY AND DERAKANE RESINS 67

DISCUSSION 70

DETERMINATION OF A SUITABLE CURE CYCLE FOR DGEBA/TETA 73

MEASUREMENT OF VOLUME CHANGE DURING REACTION FOR DGEBA/TETA AND DERAKANE RESINS 74

RESULTS 80

CHAPTER 3: CHARACTERIZATION OF THE POROUS MEDIA 85

INTRODUCTION 85

DESCRIPTION OF POROUS MEDIA 86

DETERMINATION OF THE FIBER VOLUME FRACTION 88

DETERMINATION OF THE PREFORM PERMEABILITY 89

MEASUREMENT PROCEDURE 95

DATA COLLECTION AND SAMPLE CALCULATIONS 98

RESULTS AND DISCUSSION 98

DETERMINATION OF THE DISPERSION COEFFICIENTS 102

PLAQUE PRODUCTION 110

COLORIMETRY 110

DATA COLLECTION AND SAMPLE CALCULATIONS 111

LONGITUDINAL DISPERSION 111

TRANSVERSE DISPERSION 113

RESULTS AND DISCUSSION 116

CHAPTER 4: INVESTIGATION OF THE EFFECT OF A DISTRIBUTION OF RESIN AGE IN RTM PLAQUES 121

BACKGROUND 121

DESCRIPTION OF FINGERING FLOWS DUE TO AGE DISTRIBUTION IN RTM 122

EXPERIMENT PROCEDURES 125

PLAQUE PRODUCTION 125

PLAQUE SAMPLING AND TESTING 130

RESULTS 134

VISCOUS FINGERING FLOW PATTERNS 134

DISCUSSION 135

NEAT RESIN PLAQUES 135

PLAQUES WITH RANDOM MAT PREFORM 141

PLAQUES WITH WOVEN GLASS PREFORM 144

CONCLUSIONS 145

CHAPTER 5: INVESTIGATION OF THE STRENGTH OF THE INTERFACE FORMED BETWEEN RESINS OF DIFFERENT HISTORIES 147

INTRODUCTION 147

THEORY 147

DISCUSSION OF STRESSES ARISING DUE TO SHRINKAGE 149

INTRODUCTION TO SHORT BEAM SHEAR TEST 161

DESCRIPTION OF PLAQUE PRODUCTION 168

DESCRIPTION OF PLAQUE TESTING 170

PLAQUE TESTING RESULTS 171

CONCLUSIONS 178

CHAPTER 6: ESTABLISHMENT OF FINGERING FLOW CRITERION FOR RTM180
INTRODUCTION 180
THEORY 181
EXPERIMENT APPARATUS AND PROCEDURE 191
PROCEDURE 195
EXPERIMENT RESULTS 196
DISCUSSION 207
CONCLUSION 215
CHAPTER 7: THE MOLDABILITY DIAGRAM FOR FINGERING FLOW 216
INTRODUCTION 216
DISCUSSION OF MOLDABILITY DIAGRAM BOUNDARIES 216
CONCLUSION 222
CHAPTER 8: CONCLUSIONS AND RECOMMENDATIONS 226
CONCLUSIONS 226
RECOMMENDATIONS 230
APPENDIX A: MATERIAL AND APPARATUS 233
EPOXY RESIN SYSTEM: 233
EPOXIDATION REACTION: 234
DERAKANE® RESIN SYSTEM: 235
OTHER CHEMICALS 236
GLASS MATS 236
APPARATUS 237
APPENDIX B: DERIVATIONS 238
METHOD OF CALCULATING PERMEABILITY COEFFICIENTS 238

DERIVATION OF THE LONGITUDINAL DISPERSION COEFFICIENT 245

REGRESSION METHOD USED TO CALCULATE DISPERSION COEFFICIENTS 249

APPENDIX C: DATA AND CALCULATIONS 254

REFERENCES 389

LIST OF TABLES

Table Page

Table 1.1: Typical physical properties of fibers and resins. (After Hull, 1981)..... 42

Table 2.1: Kinetics Parameters from DSC temperature Scans..... 62

Table 2.2: Exothermic temperatures for Epoxy and Derakane resins..... 69

Table 2.3: Residual cure of DGEBA/TETA resin..... 74

Table 2.4: Summary of results of DGEBA/TETA epoxy resin characterization..... 82-83

Table 2.5: Results of Derakane 411 resin characterization..... 84

Table 3.1: Typical preform volume fractions..... 88

Table 3.2: Data from permeability run 5.7.E. $\Delta P = 0.3$ psig, Do = 0.95 cm, preform: swirl mat, Vf = 0.18..... 100

Table 3.3: Summary of permeability experiment data..... 100

Table 3.4: Permeability of preforms..... 102

Table 3.5: The longitudinal dispersion coefficients..... 118

Table 3.6: The transverse dispersion coefficients..... 118

Table 3.7: Dispersion coefficient results..... 119

Table 4.1: Plaque production variables..... 130

Table 4.2: Summary of physical properties by type of fingering feature..... 140

Table 5.1: Numerical results of short beam shear testing..... 172

Table 5.2: Summary of visual inspection of specimen fracture surfaces..... 177

Table 6.1: Ranges of dimensionless quantities for fingering flow experiments..... 186

Table 6.2: Typical parameters for RTM processes..... 190

Table 6.3: Injection speeds and volumetric flow rates used in the fingering flow experiments. 194

Table 6.4: Experimental parameters. 197

Table 7.1: Values for moldability diagram. 222

Table 7.2: Values of viscosity model coefficients for three reactive resin systems. 223

Table C.1: Viscosity by time data for DGEBA/TETA epoxy resin system. Data were taken on Brookfield viscometer. Isothermal at 323 °K. 255

Table C.2: Data from Rheometrics viscometer. Includes G' and G" data as well as viscosity data. Lowest reliable torque reading is 2.0 g·cm. 256-257

Table C.3: Time by viscosity data for Derakane® 411 resin. Data taken on Brookfield viscometer, isothermal at 22 °C. 257

Table C.4: DSC data for DGEBA/TETA epoxy system. Scan rate is 1 °C/min. ... 258-259

Table C.5: DSC data for DGEBA/TETA epoxy system. Scan rate is 2 °C/min. ... 261-262

Table C.6: DSC data for DGEBA/TETA epoxy system. Scan rate is 5°C/min. 264-265

Table C.7: DSC data for DGEBA/TETA epoxy system. Scan rate is 10°C/min. .. 267-268

Table C.8: DSC data for DGEBA/TETA epoxy system. Scan rate is 20°C/min. .. 270-271

Table C.9: DSC data for DGEBA/TETA epoxy system. Scan rate is 30°C/min. .. 273-275

Table C.10: DSC data for DGEBA/TETA epoxy system. Scan rate is 40°C/min. 277-279

Table C.11: DSC data for DGEBA/TETA epoxy system. Scan rate is 50°C/min. 281-283

Table C.12: Exotherm data for DGEBA/TETA epoxy resin and Derakane® 411 resin. 285-286

Table C.13: Data from residual cure runs on DGEBA/TETA epoxy resin. 287

Table C.14: Shrinkage data for DGEBA/TETA epoxy resin. 290-291

Table C.15: Shrinkage data for Derakane® 411 resin. 291-292

Table C.16: Summary of calculatione for permeability rune. Viscosity = 290 mPa·sec, Ro = 0.952 cm. 293

Table C.17: Results of permeability calculations. 293

Table C.18: Data from permeability runs. 294-295

Table C.19: Longitudinal dispersion coefficient summary. 302

Table C.20: Location of resin/air interface by time for longitudinal dispersion runs. 302

Table C.21: Absorbance versus location for longitudinal dispersion run, 5.14.AB, no preform. Origin at (x,y) = (8.9,-2.5). 304-305

Table C.22: Absorbance versus location for longitudinal dispersion run, 5.20.AA., random swirl mat preform. Origin at (x,y) = (11.0,-2.5) 306-308

Table C.23: Absorbance versus location for longitudinal dispersion run, 5.20.AB., random swirl mat preform. origin at (x,y) = (11.0,-2.5) 308-310

Table C.24: Absorbance versus location for longitudinal dispersion run, 5.21.AA., woven fabric preform. Origin at (x,y) = (10.0,-2.5) 312-313

Table C.25: Absorbance versus location for longitudinal dispersion run, 5.21.AB, woven fabric preform. Origin at (x,y) = (10.0,-2.5) 314-315

Table C.26: Location of resin/air interface by time for transverse dispersion runs. 316

Table C.27: Absorbance by location data for transverse dispersion, 5.25.A. 317-319

Table C.28: Absorbance by location data for transverse dispersion, 5.26A. 319-322

Table C.29: Absorbance by location data for transverse dispersion, 5.27.A. 322-325

Table C.30: Fingered structures of sample bars. 333-335

Table C.31: Physical properties testing for Derakane plaques with fingered structures. Plaque 9.11.A; Woven fabric preform. All spans 80 mm. 335

Table C.32: Physical properties testing for Derakane plaques with fingered structures. Plaque 9.15.A; woven fabric preform. All spans 80 mm. 336

Table C.33: Physical properties testing for Derakane plaques with fingered structures. Plaque 9.16.A; swirl mat preform. All spans 80 mm. 337

Table C.34: Physical properties testing for Derakane plaques with fingered structures. Plaque 9.17.A; swirl mat preform. All spans 80 mm. 338

Table C.35: Physical properties testing for Derakane plaques with fingered structures. Plaque 9.18.A; no preform. All spans 80 mm. 339

Table C.36: Physical properties testing for Derakane plaques with fingered structures. Plaque 9.21.A; no preform. All spans 80 mm. 339

Table C.37: Physical properties testing for Derakane plaques with fingered structures. Plaque 9.22.A; no preform. All spans 80 mm. 339

Table C.38: Physical properties testing for Derakane plaques with fingered structures. Plaque 10.06.A; swirl mat preform, no age difference. All spans 80 mm. 341

Table C.39: Physical properties testing for Derakane plaques with fingered structures. Plaque 10.07.B no preform, no age difference between batches. All spans 80 mm. 341

Table C.40: Physical properties testing for Derakane plaques with fingered structures. Plaque 10.12.A swirl mat preform, very long injection. All spans 80 mm. 342

Table C.41: Short beam shear testing of two-ply bars. Epoxy resin, Δt = 0 min, Batch 1 tested in tension. 343

Table C.42: Short beam shear testing of two-ply bars. Epoxy resin, Δt = 15 min, Batch 1 tested in tension. 344

Table C.43: Short beam shear testing of two-ply bars. Epoxy resin, Δt = 45 min, Batch 1 tested in tension. 345

Table C.44: Short beam shear testing of two-ply bars. Epoxy resin, Δt = 60 min, Batch 1 tested in tension. 346

Table C.45: Short beam shear testing of two-ply bars. Epoxy resin, Δt = 75 min, Batch 1 tested in tension. 347

Table C.46: Short beam shear testing of two-ply bars. Epoxy resin, Δt = 90 min, Batch 1 tested in tension. 347

Table C.47: Short beam shear testing of two-ply bars. Epoxy resin, Δt = 120 min, Batch 1 tested in tension. 348

Table C.48: Short beam shear testing of two-ply bars. Epoxy resin, Δt = 75 min, and interface treated with Teflon spray. Batch 1 tested in tension. 348

Table C.49: Short beam shear testing of two-ply bars. Epoxy resin, Δt = 0 min, Batch 2 tested in tension. 349

Table C.50: Short beam shear testing of two-ply bars. Epoxy resin, Δt = 15 min, Batch 2 tested in tension. 350

Table C.51: Short beam shear testing of two-ply bars. Epoxy resin, Δt = 45 min, Batch 2 tested in tension. 351

Table C.52: Short beam shear testing of two-ply bars. Epoxy resin, Δt = 60 min, Batch 2 tested in tension. 351

Table C.53: Short beam shear testing of two-ply bars. Epoxy resin, Δt = 75 min, Batch 2 tested in tension. 352

Table C.54: Short beam shear testing of two-ply bars. Epoxy resin, Δt = 90 min, Batch 2 tested in tension. 352

Table C.55: Short beam shear testing of two-ply bars. Epoxy resin, Δt = 120 min, Batch 2 tested in tension. 353

Table C.56: Short beam shear testing of two-ply bars. Epoxy resin, Δt = 75 min, and interface treated with Teflon spray. Batch 2 tested in tension. 353

Table C.57: Summary of failure modes for two-ply bars in short beam shear. See Figure C.38. 354

Table C.58: Summary of fingering flow run conditions. 356

Table C.59: Data and calculations for fingering flow run # 8.20.A. V = 862.8. 357-358

Table C.60: Data and calculations for fingering flow run # 8.20.B. V = 493.0. 359-360

Table C.61: Data and calculations for fingering flow run # 8.24.B. V = 403.4. 361-363

Table C.62: Data and calculations for fingering flow run # 9.9.A V = 1120.5. 364

Table C.63: Data and calculations for fingering flow run # 9.9.B. V = 1120.5. 365

Table C.64: Data and calculations for fingering flow run # 9.17.A V = 168.1. 366-367

Table C.65: Data and calculations for fingering flow run # 9.20.A. V = 1658. 367

Table C.66: Data and calculations for fingering flow runs which had no fingers. Calculations are for the interface. 368

LIST OF FIGURES

Figure Page

Figure 1.1: Fingering flow: clear fluid being displaced from random fiber mat by dyed fluid. Viscosity ratio = 1.3:1 4

Figure 1.2: Flow between two flat plates. 6

Figure 1.3 Pressure profile in viscous fingering flow 9

Figure 1.4: Dimensionless growth rate of fingers of various wavenumber (reciprocal width), after Tan and Homsy, (1985). 16

Figure 1.5: Most dangerous wavenumber as a function of viscosity ratio. 18

Figure 1.6 Viscosity profiles in a flow cell, various types of fluids. 20

Figure 1.7: Relative operating areas of Reaction Injection Molding (RIM), Structural-RIM, and Resin Transfer Molding. 28

Figure 1.8: Moldability diagram for RTM, after Macosko, (1989, pg. 128). 29

Figure 1.9: Structure of a woven preform. 35

Figure 1.10: Tensile deformation of a rectangular prism. 37

Figure 1.11: Bending deformation of a rectangular prism. 39

Figure 1.12: Two kinds of fiber-reinforced composite bars. 41

Figure 2.1: Viscometer configurations, Brookfield (couette) and Rheometrics (parallel plate). 46

Figure 2.2: Viscosity data of the DGEBA/TETA resin system. 48

Figure 2.3: Viscosity model for DGEBA/TETA resin system: polynomial 50

Figure 2.4: Viscosity model for DGEBA/TETA resin: power law. 52

Figure 2.5: Viscosity profile for Derakane resin system. 53

Figure 2.6: Differential Scanning Calorimetry scan of DGEBA/TETA resin system. Scan rate = 10° K/min. 58

Figure 2.7: Kinetics data and model for DGEBA/TETA resin system. 60

Figure 2.8: Conversion (α) versus time for DGEBA/TETA resin system. 62

Figure 2.9: Viscosity as a function of extent of reaction for DGEBA/TETA resin system. 65

Figure 2.10: Complex shear modulus for DGEBA/TETA resin system. 68

Figure 2.11: Exotherm of DGEBA/TETA resin system. 71

Figure 2.12: Exotherm of Derakane® resin system. 72

Figure 2.13: DSC scan of DGEBA/TETA sample cured for 2 hours at 50° C for 2 hours. 75

Figure 2.14: Dilatometer, an apparatus for measuring volume of reacting resin. 77

Figure 2.15: Volume profile of DGEBA/TETA resin system during cure. 78

Figure 2.16: Volume profile of Derakane® resin system during cure. 79

Fiugre 3.1: Schematic of glass mats for preform. 87

Figure 3.2: Permeability measurement, coordinates and definitions. 91

Figure 3.3: Data from permeability run 5.7.E, graphed as radius in x direction versus radius in y direction. 93

Figure 3.4: Data from permeability run 5.7.E, graphed as F(Rxe) versus time. 94

Figure 3.5: Schematic of flow cell for permeability measurements. 96

Figure 3.6: Apparatus for constant pressure injection. 97

Figure 3.7: Photograph from permeability run 5.7.E; polybutene flowing through random glass preform. 99

Figure 3.8: Schematic of diffusion across an interface between two fluids. 104

Figure 3.9: Resin injection scheme for determining longitudinal dispersion coefficient. 106

Figure 3.10: Resin injection scheme for determining transverse dispersion coefficient. 107

Figure 3.11: Flow front velocities in plaques for longitudinal dispersion measurements. 112

Figure 3.12: Typical concentration data on similarity plot for longitudinal dispersion plaque. No preform. 114

Figure 3.13: Flow front velocities in plaques for transverse dispersion measurements. .. 115

Figure 3.14: Typical concentration data on similarity plot for transverse dispersion plaque. Woven mat preform. 117

Figure 4.1: Viscosity profiles in RTM which may be accomplished by the manipulation of the injection protocol. 124

Figure 4.2: The viscosity of Derakane resin as a function of time, at 20°C. 127

Figure 4.3: The RTM mold used to produce plaques with resins of different ages. 128

Figure 4.4: Typical finished plaques showing Batch 1 as light and Batch 2 as dark. 132

Figure 4.5: Position of the test bars in the 3-point bend test fixture. 133

Figure 4.6: Results of the 3-point bend testing, neat resin plaques. 136

Figure 4.7: Results of the 3-point bend testing, random swirl glass preform, Vf = 0.21. 137

Figure 4.8: Results of the 3-point bend testing, woven glass preform, Vf = 0.45. 138

Figure 4.9: Multi-tip finger structure from Plaque 9.16.A. Note feathery edges to fingers. 143

Figure 4.10: Multi-tip structure from Plaque 9.17.A. Note sharp edges to fingers. 143

Figure 5.1: Schematic of a two-ply plaque. 150

Figure 5.2: Schematic of a two-ply bar where shrinkage of top ply causes curvature ... 152

Figure 5.3: Schematic of a two-ply bar where shrinkage causes a change in thickness.. 154

Figure 5.4: Internal stresses in a two-ply plaque enclosed in a mold on all sides. 156

Figure 5.5: Schematic of volumetric shrinkage in a system with a curved interface. 158

Figure 5.6: Sample bar and test coordinates for short beam shear test. 162

Figure 5.7: Tensile and Shear stresses within bar under 3-point bending. 166

Figure 5.8: Typical fracture surfaces of two-ply bar specimens. 167

Figure 5.9: The horizontal plaque mold. 169

Figure 5.10: Maximum tensile stress in 2-ply specimen bars, tested with Batch 1 in tension. 173

Figure 5.11: Maximum tensile stress in 2-ply specimen bars, tested with Batch 2 in tension. 174

Figure 5.12: Comparison between the two test orientations. 175

Figure 6.1: Schematic of flow between two flat plates. 182

Figure 6.2: Illustration of resin ages in mold. 187

Figure 6.3: Viscosity profiles in the mold, calculated for resin temperature of 50° C, and several times. 189

Figure 6.4: Schematic of the mold used in fingering flow experiments. 192

Figure 6.5: Apparatus for continuous in-line mixing and injection of resin. 193

Figure 6.6: A typical series of photographs of a fingering flow experiment. Run 8.20.A, no preform, resin and mold temperatures 50° C. 198-204

Figure 6.7: Definition of finger dimensions. 206

Figure 6.8: Finger tip locations in run 8.20.A. 208

Figure 6.9: Mobility ratio, $\mathcal{M}$ versus dimensionless velocity, $\mathcal{V}$, based on age of resin at interface. 209

Figure 6.10: Mobility ratio, $\mathcal{M}$, versus dimensionless velocity, $\mathcal{V}$, based on age of oldest resin in the mold. 210

Figure 6.11: Finger growth rate versus dimensionless velocity. 211

Figure 6.12: Finger width versus dimensionless velocity. 212

Figure 7.1: Moldability diagram for DGEBA/TETA resin system and injection molding apparatus of Figure 6.4 and 6.5. 217

Figure 7.2: Moldability diagram of DGEBA/TETA system, with fingering criterion of $\mathcal{M}$ = 20 added. 220

Figure 7.3: Moldability diagram of DGEBA/TETA system, with both branches of fingering criterion added. 221

Figure 7.4: Mobility ratio, $\mathcal{M}$, as a function of α for several resin systems. 224

Figure 8.5: The moldability diagram for DGEBA/TETA epoxy resin in RTM, with the fingering criterion superimposed. 228

Figure B.1: Flow between two flat plates with coordinates for calculating permeability of preforms from data. 239

Figure B.2: Comparison of elliptical and circular flow fronts. 242

Figure B.3: Example plots of data from permeability experiments 246

Figure B.4: Coordinates and definitions for derivation of longitudinal dispersion coefficient. 247

Figure B.5 Coordinates and definitions for derivation of transverse dispersion coefficient 251

Figure C.1: Graph of DSC data, DGEBA/TETA epoxy resin. Scan rate is 1 °C/min. ... 260

Figure C.2: Graph of DSC data, DGEBA/TETA epoxy resin. Scan rate is 2 °C/min ..263

Figure C.3: Graph of DSC data, DGEBA/TETA epoxy resin. Scan rate is 5°C/min. 266

Figure C.4: Graph of DSC data, DGEBA/TETA epoxy resin. Scan rate is 10°C/min... 269

Figure C.5: Graph of DSC data, DGEBA/TETA epoxy resin. Scan rate is 20°C/min... 272

Figure C.6: Graph of DSC data, DGEBA/TETA epoxy resin. Scan rate is 30°C/min... 276

Figure C.7: Graph of DSC data, DGEBA/TETA epoxy resin. Scan rate is 40°C/min... 280

Figure C.8: Graph of DSC data, DGEBA/TETA epoxy resin. Scan rate is 50°C/min... 284

Figure C.9: Sample Residual cure run, of DGEBA/TETA epoxy resin on DSC. Resin was cured at 50 °C for two hours, then at room temp. for 2 days before DSC run. 288

Figure C.10: Sample Residual cure run, of DGEBA/TETA epoxy resin on DSC. Resin was cured at room temp. for 2 days before DSC run. 289

Figure C.11: Graph of Dx by Dy for permeability run 5.7.B. 296

Figure C.12: Graph of F(Rxe) versus time for permeability run 5.7.B. 296

Figure C.13: Graph of Dx by Dy for permeability run 5.7.C. 297

Figure C.14: Graph of F(Rxe) versus time for permeability run 5.7.C. 297

Figure C.15: Graph of Dx by Dy for permeability run 5.7.D. 298

Figure C.16: Graph of F(Rxe) versus time for permeability run 5.7.D. 298

Figure C.17: Graph of Dx by Dy for permeability run 5.7.E. 299

Figure C.18: Graph of F(Rxe) versus time for permeability run 5.7.E. 299

Figure C.19: Graph of Dx by Dy for permeability run 5.7.F. 300

Figure C.20: Graph of F(Rxe) versus time for permeability run 5.7.F. 300

Figure C.21: Graph of Dx by Dy for permeability run 5.7.G. 301

Figure C.22: Graph of F(Rxe) versus time for permeability run 5.7.G. 301

Figure C.23: Location of resin/air interface by time for longitudinal dispersion runs..... 303

Figure C.24: Similarity plot of longitudinal dispersion data and model for 5.14.AB: no preform. 303

Figure C.25: Similarity plot of longitudinal dispersion data and model for 5.20.AA and 5.20.AB: swirl mat preform. 311

Figure C.26: Similarity plot of longitudinal dispersion data and model for 5.21.AA, and 5.21.AB, woven fabric preform. 311

Figure C.23: Position of flow front by time for transverse dispersion runs. 326

Figure C.24: Similarity plot of transverse dispersion data and model for 5.25.A, no preform. 326

Figure C.25: Similarity plot of transverse dispersion data and model for 5.26.A, swirl mat preform. 327

Figure C.26: Similarity plot of transverse dispersion data and model for 5.27.A, woven fabric preform. 327

Figure C.27: Cut-up diagram of Plaque 9.11.A. Derakane resin; woven fabric preform.328

Figure C.28: Cut-up diagram of Plaque 9.15.A. Derakane resin; woven fabric preform.328

Figure C.29: Cut-up diagram of Plaque 9.16.A. Derakane resin; swirl mat preform. ... 329

Figure C.30: Cut-up diagram of Plaque 9.17.A. Derakane resin; swirl mat preform. ... 329

Figure C.31: Cut-up diagram of Plaque 9.18.A. Derakane resin; no preform. 330

Figure C.32: Cut-up diagram of Plaque 9.21.A. Derakane resin; no preform. 330

Figure C.33: Cut-up diagram of Plaque 9.22.A. Derakane resin; no preform. 331

Figure C.34: Cut-up diagram of Plaque 10.6.A Derakane resin; swirl mat preform, no age difference between batches. 331

Figure C.35: Cut-up diagram of Plaque 10.07.B. Derakane resin; no preform. No age difference between batches..... 332

Figure C.36: Cut-up diagram of Plaque 10.12.A Derakane resin; swirl mat preform, very long injection. 332

Figure C.37: Explanation of terms used in Table C.57..... 355

Figure C.38: Photographs for fingering flow run 8.19.A. Photos 1 and 2..... 369-370

Figure C.39: Photographs for fingering flow run 8.19.B. Photos 1 and 2..... 371-372

Figure C.40: Photographs for fingering flow run 8.20.B. Photos 1 and 2..... 373-375

Figure C.41: Photographs for fingering flow run 8.24.A. Photos 1 and 2..... 376-377

Figure C.42: Photographs for fingering flow run 8.24.B. Photos 1 and 2..... 378-379

Figure C.43: Photographs for fingering flow run 9.9.A. Photos 1 and 2..... 380-381

Figure C.44: Photographs for fingering flow run 9.9.B. Photos 1 and 2..... 382-383

Figure C.45: Photographs for fingering flow run 9.17.A. Photos 1 and 2..... 384-385

Figure C.47: Photographs for fingering flow run 9.20.A. Photos 1 and 2..... 386-387

Figure C.48: Photograph for fingering flow run 9.21.A. Photo 1. 388

Figure C.49: Photograph for fingering flow run 9.22.A. Photo 1 388

NOMENCLATURE

A,B,C,D,E: empirical fitting constants for viscosity functions [dimensionless]
b: width of a flow cell or a bar of solid material [length]
C: relative concentration of a solute [dimensionless]
Ca: capillary number [dimensionless]
C_E: coefficient of thermal expansion [length/length/°C]
C_p: heat capacity [energy/mass/°K]
C_1, C_2: empirical fitting constants for viscosity functions [dimensionless]
d: deflection of a solid bar of material under load [length]
d_p: particle size [length]
D_L: longitudinal dispersion coefficient [length^2/time]
D_o: molecular diffusion coefficient [length^2/time]
D_x, D_y: diameters of fluid flow fronts Chapter 3 [length]
D_T: transverse dispersion coefficient [length^2/time]
$\mathcal{D}$: effective dispersion coefficient [length^2/time]
E_a: activation energy of the polymerization reaction [energy/mass]
E_b: bending modulus [force]
E_t: tensile modulus [force]
e : ratio of transverse to longitudinal dispersion coefficients [dimensionless]
$\mathcal{F}$: formation factor for porous media [dimensionless]
F: load on a bar of solid material [force]
g: acceleration due to gravity [length/time^2]
G*: complex shear modulus of a fluid [force/area]
G' : storage modulus of a viscoelastic fluid [force/area]
G" : loss modulus of a viscoelastic fluid [force/area]
h: thickness of a flow cell or a bar of solid material [length]
H: heat flow in calorimeter [energy/mass]
H_o: heat of reaction [energy/mass]
I: moment of inertia [length^4]
k: wavenumber, in Chapter 1 [dimensionless]
k : reaction time constant, Chapter 2 [min^{-1}]
k_o: pre-exponential factor of reaction time constant [min^{-1}]
K_e: permeability equivalent [length^2]
K_{xx}, K_{yy}: components of the permeability tensor [length^2]
L: length of a finger, Chapter 6 [length]
L: length of a bar of solid material, Chapters 4 and 5 [length]
L_L, L_T: constants used in calculation of longitudinal and transverse dispersion coefficients [length]
m: exponent for reaction rate equation [dimensionless]

m_1, m_2: slopes of graphs used to determine permeability
$\mathcal{M}$: mobility ratio [dimensionless]
n: exponent for reaction rate equation [dimensionless]
P: pressure [force/area]
Pe: Peclet number [dimensionless]
Q: volume flow rate [volume/time]
r: radius of curvature or radius of fiber [length]
R: natural log of viscosity ratio [dimensionless]
Re: Reynolds number [dimensionless]
R_f: radius of the flow front, Chapter 3 [length]
R_g : gas constant [energy/moles/°K]
R_0 : radius of the mold inlet, Chapter3 [length]
R^2: fitting coefficient [dimensionless]
$\mathcal{R}$: reaction rate [moles A consumed/volume/time]
S_V: volume shrinkage [volume/volume]
S_L: linear shrinkage [length/length]
t: time [time]
T: temperature [temperature]
U: interstitial velocity [length/time]
v: velocity [length/time]
V : volume [volume]
V_f: volume fraction of fibers [dimensionless]
V_r : volume fraction of resin [dimensionless]
$\mathcal{V}$: dimensionless velocity [dimensionless]
x,y,z: spatial coordinates [length]
x_I, y_I: the coordinates of an interface [length]
X_e: x coordinate in an equivalent system [length]
α: extent of reaction [dimensionless]
α_g: extent of reaction when resin gels [dimensionless]
β: temperature scan rate in differential scanning calorimetry [°K/min]
γ: surface tension , Chapter 1 [force/length]
γ: shear strain Chapter 2 [time $^{-1}$]
ΔT_{AD}: adiabatic temperature rise in reacting resin [° C]
ΔT_{exo}: exothermic temperature rise in reacting resin [° C]
ε: porosity of a porous medium, the volume fraction of space inside the structure of the medium [dimensionless]
ε_x: strain in a solid material in the x coordinate [dimensionless]
η^*: complex viscosity [force·time/area]
κ: permeability of a porous medium [length ^{2}]
λ: growth rate of fingers, Chapter 6 [dimensionless]
μ: viscosity [force·time/area]
ν: Poisson's ratio [dimensionless]
ρ: density [mass/volume]

σ: packing consistency, in Chapter 1 [dimensionless]
σ: growth rate of fingers in Chapter 1 [dimensionless]
σ: tensile (+) or compressive (-) stress in Chapters 4 and 5 [force/area]
σ^*: tensile strength [force/area]
τ: shear stress, Chapter 2 and 3 [force/area]
υ: stoichiometric ratio [dimensionless]
ω: oscillation rate of complex viscosity test [cycles/time]

CHAPTER 1

INTRODUCTION

The production of composite parts through liquid molding techniques such as resin transfer molding (RTM) and structural reaction injection molding (S-RIM) requires that liquid plastic resin be made to flow through a fibrous porous medium, the preform, which is contained in a closed mold. In order to minimize the molding cycle time, the resin will be injected on a time scale such that the gel point will be reached shortly after injection is complete. When the injection time is an appreciable fraction of the gel time, the oldest resin in the mold may be significantly more viscous than the newest resin (Gonzales-Romero, 1990).

Viscosity gradients of this kind are known to cause flow instabilities called viscous fingering. Viscous fingering occurs in the recovery of crude oil by injection of a displacing fluid into oil-bearing rock, and in flushing process liquor from packed beds and filters, using a solvent. (Perkins, 1965; Hill, 1952).

It is proposed that viscous fingering may also occur in RTM, due to viscosity gradients generated in the flowing resin by the formation of large molecules during the reaction. The features of RTM which distinguish it from flows in which viscous fingering has previously been studied are the reactive nature of the fluid, and the fibrous nature of the porous medium. Because the viscosity of the fluid is increasing with time due to the polymerization reaction, viscous fingers are expected to arise readily in RTM flows, if the damping mechanisms such as dispersive mixing are not too great. The fibrous nature of the porous media is expected to influence the amount of dispersive mixing, and the size and shape of fingers. If fingering flow does occur, then there will be a more or less

complex interface where the finger and the fluid through which it is penetrating come in contact. The resin at the interface may or may not achieve the same mechanical properties as the remainder of the resin. If the interface is weaker than the bulk resin, then fingering flow will be detrimental to the performance of the RTM part in which it occurs.

OBJECTIVES

The objective of the present work is to investigate the phenomenon of viscous fingering flow as it occurs in RTM, to determine what molding conditions are necessary and sufficient to produce fingering flows, and to give engineering utility to the fingering flow criterion by presenting it on a moldability diagram. In addition the mechanical properties of RTM plaques will be studied to determine whether fingering flows in RTM are detrimental to the properties of finished parts.

Chapter 1 of the present work describes the prior art in fingering flows. Further sections of the chapter include discussions of the RTM process, with emphasis on the moldability diagram, and a discussion which draws on the thermoplastic weld-line literature to describe the nature of the interface which may be produced in fingering flow.

In experimental work, fingering flows were studied in two commercial resin systems, Derakane 411 vinyl ester resin from Dow chemical, and DGEBA/TETA epoxy resin. Two preforms, a random swirl mat from Vetrotex, and a woven glass fabric from Hexcel Corp. were studied along with neat resin (no preform) flows. Characterization of the physical and chemical properties of the two resins is described in Chapter 2, and characterization of the preforms is described in Chapter 3. Knowledge of the characteristics of the resins and preforms is then used in the remainder of the work, where needed.

In Chapter 4, experiments are described wherein RTM plaques using Derakane resin were made containing interfaces due to viscous fingering flows, in order to analyze the effect that such interfaces would have on the physical properties the plaques. It was

found that some features of fingered interfaces seemed to be associated with a loss of flexural modulus. However, the difficulty of reliably sampling similar features from which statistically significant results could be drawn led to the manufacture of plaques with interfaces of large area and known history.

A DGEBA/TETA epoxy resin system was used to produce plaques with large areas of interface, which could be reliably sampled for tests of physical properties. Chapter 5 describes the manufacture and testing of these plaques, and shows that the type of interface represented by this kind of plaque has little to no effect on the short beam shear strength of the finished RTM part.

The same DGEBA/TETA epoxy resin was used with an RTM mold and injection unit to do the flow-visualization studies reported in Chapter 6. Conditions under which viscous fingering flows would and would not form were outlined in Chapter 6, then synthesized as a fingering flow criterion and applied to the moldability diagram in Chapter 7.

Chapter 8 contains the significant conclusions and recommendations of the present work, with regard to the existence of fingering flows in RTM, and their effect on the physical properties of finished RTM parts.

BACKGROUND

FINGERING FLOWS

Fingering flows are produced when a fluid is displacing a more viscous fluid, either in an open channel, or in a porous medium. Figure 1.1 shows an example of fingering flow where a clear fluid is being displaced by a dyed fluid radially, from the center outward. The viscosity ratio, μ_{clear}/μ_{dyed} is 1.3:1. Both fluids are solutions of water in glycerine, so they are completely miscible. The interface between the two fluids is very jagged, with pointed projections arising from a basic oval shape in generally radial directions. These projections are identified as viscous fingers. They are not merely due to



Figure 1.1: Fingering flow: clear fluid being displaced from random fiber mat by dyed fluid. Viscosity ratio = 1.3:1.

the flow of the fluid through the porous medium. An earlier photograph in the same series shows the clear fluid making a smooth oval flow front as it displaces air from the porous medium with no evidence of channeling due to anisotropic permeability. Since air is much less viscous than the clear fluid, the interface between the air and fluid phases is stable; no fingers are propagated. Except that these fluids are not reacting, the flow cell geometry, porous medium, flow rate and viscosity ratio are similar to those found in RTM. This kind of miscible displacement has been examined by Tan and Homsy (1985), and a stability criterion has been formulated. One of the goals of the present work is to discover a stability criterion for an RTM system. To that end, the existing literature provides insight into the form that such a criterion should take. The discussion below relates some of the points of development of the studies of viscous fingering flows. These studies are then extended to form the basis for the investigation of viscous fingering flow in reactive resin systems.

Figure 1.2 shows a flow cell with fluid 1 being displaced by fluid 2. The flow is in the x direction, while the y direction is taken through the thickness (h) of the cell, and the z direction is parallel to the width (b) of the cell. The cell dimensions are generally taken as length >> width >> thickness. This assumption allows the flow in an empty cell, known by the name 'Hele-Shaw cell' to be modeled by equations identical to Darcy's law for flow through a porous medium. The viscosity ratio, $\mu_1/\mu_2 > 1$ is assumed throughout this discussion. All symbols from the sources cited below have been translated to the symbols used in Figure 1.2, which also appear in the Glossary.

Saffman and Taylor (1958) are generally credited with the first publication of an analysis of fingering flow with immiscible fluids, although the phenomenon had been of concern to those working in the fields of secondary crude oil recovery and regeneration of catalyst beds for some time. For example, Hill, in 1952 published an investigation into

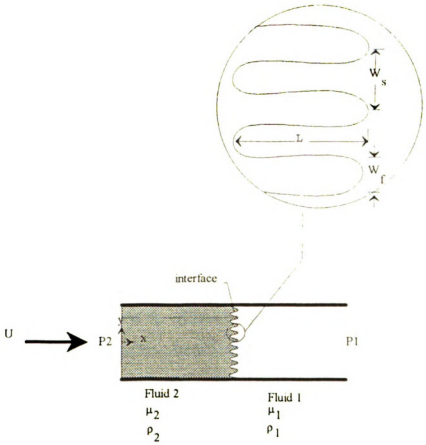


FIG102.DRW

Figure 1.2: Flow between two flat plates.

the phenomenon of "channeling" of wash water through sugar solutions in packed beds of charcoal particles. Hill's derivation of a stability criterion and the accompanying photographs make it clear that Hill was investigating the same phenomenon as Saffman, though calling it channeling.

Viscous fingers are the result of an instability in the interface between two fluids flowing through a cell such as that depicted in Figure 1.2. If the interface were stable, it would remain flat or parabolic throughout the flow period, because small disturbances to the interface shape that would arise by chance would not tend to grow, but would tend to be rejoined to the main interface. However, when the viscosity of the downstream fluid is greater than the viscosity of the upstream fluid, the pressure gradient is as depicted in Figure 1.3. The outlet pressure is fixed, and the flow cell is initially charged with the higher viscosity fluid, which is allowed to escape at the end of the flow cell. As the low viscosity fluid (μ_1) displaces the higher viscosity fluid (μ_2) at a constant velocity (U), the inlet pressure required to drive the flow decreases, because a greater proportion of the flow cell is being occupied by the low viscosity fluid. In the portions of the cell occupied by fluids 1 and 2, respectively, the local pressure gradients remain constant, because these are governed by the viscosity of the fluid, through Darcy's law:

$$-\frac{dP}{dx} = \frac{\mu}{\kappa} U \qquad (1.1)$$

Where the pressure drop due to the flow in the x direction is related to the fluid viscosity, μ, the permeability of the porous medium, κ, and the velocity of the flow, U. A "packet" of fluid 2 which gets slightly ahead of the interface experiences a surrounding pressure gradient which is greater than what it would see if it were behind the interface. This packet of fluid would then increase its (local) velocity (U) by an amount proportional to the increase in the pressure gradient surrounding it. As this packet of fluid 2 advances into the region occupied by fluid 1 (downstream of the interface), it elongates into a viscous

finger. This explanation is due to Saffman and Taylor (1952). More rigorously, Saffman used Eq. (1.1) to treat the interaction of density and viscosity differences and show that the ability of small disturbances to the interface to grow into fingers depends on both the density difference and viscosity difference such that a stability criterion can be stated as:

$$\frac{s}{k}\left(\frac{\mu_1}{\kappa_1}+\frac{\mu_2}{\kappa_2}\right)=\left(\frac{\mu_1}{\kappa_1}-\frac{\mu_2}{\kappa_2}\right)U-(\rho_1-\rho_2)g \tag{1.2}$$

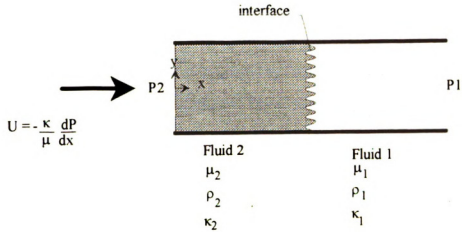
where κ_1 and κ_2 are the permeability of the porous medium in regions occupied by fluids 1 and 2 respectively. s is the growth rate of the fingers, k is the wavelength of fingers (reciprocal finger width), and U is the fluid velocity. If the permeability of the porous medium is constant, i.e., if $\kappa_1 = \kappa_2$, and density effects can be ignored, then the growth rate can be calculated as:

$$s=\frac{\mu_1-\mu_2}{\mu_1+\mu_2}U_o k \tag{1.3}$$

which leads to the stability criterion:

$$\begin{aligned}\mu_1 > \mu_2 \quad &\Rightarrow s>0 \Rightarrow \text{unstable}\\ \mu_1 < \mu_2 \quad &\Rightarrow s<0 \Rightarrow \text{stable}\end{aligned} \tag{1.4}$$

When the growth rate of fingers, s, is less than zero, any disturbances to the interface do not grow into fingers. When s is greater than zero, disturbances will tend to grow, and fingers will be observable. It should be noted that a small but positive value for s may lead to fingers which grow so slowly as not to be visible in the time scale of the experiment. Saffman and Taylor show that in an immiscible flow system, the growth rate of fingers, s, depends on the magnitude of the viscosity contrast, the size of the fingers, and on the flow velocity. The surface tension at the interface between the two fluids does not enter into the criterion, although experimentally, Saffman and Taylor observe that at low flow rates,



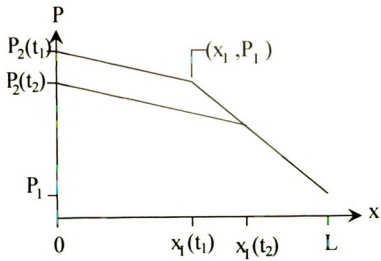


Figure 1.3 Pressure profile in viscous fingering flow.

fingers tend to be single, with a tip shape determined by the value of γ, and a finger width that is characteristically half the cell width. At faster flows, fingers are more numerous and narrower, but still with tip shapes dictated by the interfacial tension.

The stability criterion of Saffman and Taylor shows that in an immiscible displacement, where the viscosity contrast is definite and does not vary with time, fingers will form *whenever* the viscosity ratio is unfavorable, if there is no density difference. When density differences do play a role, the fingering can be exacerbated or damped depending on the direction of flow and the magnitude of the density difference. In miscible flows, however, another damping mechanism exists. As discussed below, dispersive mixing of the two fluids at their interface would tend to make the viscosity profile gradual rather than sharp over the course of the displacement in time and distance, and so some authors have derived stability criteria which allow for flows with unfavorable viscosity gradients that do not develop fingers. It is expected that RTM systems will be more similar to miscible displacement than immiscible displacement because the reactive resin is, after all, miscible with itself, and because the fluid viscosity is a function of the location of the fluid in the mold, gradually increasing in the direction of the flow. Therefore, the following discussion will focus on the stability of miscible systems, so that parallels can be drawn for use in analyzing RTM flows.

Slobod and Thomas (1963) studied fingering of miscible oils in a granular porous medium using isotope-tagged tracer fluid and X-ray photography to show the evolution of fingers over time. They wanted to track the concentration of the displacing fluid at the outlet of the cell through time. This elution function is important to those who are flushing the displaced fluid from a porous medium such as soil. They found that a slow flow rate (1.6 ft/Day) produced a single finger, the outline of which became blurred over time, by diffusion and dispersion of the fluids across the interface. The width of the finger was about 40% of the width of the cell. A fast flow rate (29 ft/Day) produced many small

fingers which grew into a few large ones. These fingers also showed blurred edges over time. Their average widths were only 12% of the cell width in the later photograph. These findings tended to confirm what Saffman saw in immiscible systems, making the point that miscible and immiscible fingering flows are variations on the same phenomenon.

In this paper, Slobod and Thomas also report that for their system, fingering is entirely eliminated if the viscosity of the displacing fluid is varied so as to decrease continuously as it is injected. Thus, they argue that a viscosity gradient may be necessary, but is not sufficient to cause viscous fingering in miscible fluid flow systems. The continuously varying viscosity injection scheme would provide a viscosity gradient in the flow direction similar to that anticipated in RTM, and the finding that fingering is prevented by this sort of viscosity gradient would tend to reinforce the idea that there is a criterion that RTM flows must meet to display viscous fingering.

Later work by Gorell and Homsy (1985) shows that although the displacement of a more viscous fluid by a less viscous fluid is more stable if the viscosity varies as a function of gradient, instead of a viscosity jump, it cannot be made unconditionally stable, and fingering can still occur.

Perkins and Johnston (1965) lay down an empirical treatment of finger dimensions in rectilinear and radial flows. They propose a new measure for finger width; λ = width/spacing, as shown in Figure 1.2. This measure lends itself to single and multi-finger systems, whether or not contained by the walls of a flow cell. It is easily conceptualized into the wavelength of the interface.

Perkins and Johnston treat both miscible and immiscible flows, noting that in the interface, the concentration of fluid 2 in fluid 1 changes with time due to both molecular diffusion and mechanical dispersion. The concentration profile follows the complementary error function:

$$C(x,t) = \frac{1}{2}\left[1 - \mathrm{erf}\left(\frac{x - Ut}{2\sqrt{D_L t}}\right)\right] \qquad (1.5)$$

where C is the concentration of fluid 2 in fluid 1, U is the flow velocity, and D_L is the longitudinal dispersion coefficient, given as:

$$D_L = \frac{D_o}{\mathcal{F}\varepsilon} + 0.5 U d_p s$$

$$D_T = \frac{D_o}{\mathcal{F}\varepsilon} + 0.0157\ U d_p s \qquad (1.6)$$

These expressions for the transverse (D_T) and longitudinal (D_L) dispersion coefficients were derived empirically in a previous paper (Perkins and Johnston, 1963), for granular porous media of particle size d_p, porosity ε, formation factor $\mathcal{F}$, and consistency of packing s. The porosity refers to the fraction of the flow area which is open to flow, and ranges from 0 to 1. The formation factor is a measure of the connectivity of the pores, that is, how many flow paths are continuous through the medium, compared to how many are dead ends. $\mathcal{F}$ also ranges from 0 to 1. s, the consistency of the packing, is about 3.5 for a typical random pack of particles, and is never less than 1 (Perkins, 1963). The first term in Eq. (1.6) is the molecular diffusion term, and since the molecular diffusion coefficient is generally on the order of 1×10^{-5} cm^2/sec, Perkins neglects it in comparison to the second term. When neglecting the first term, Eq. (1.6), shows that the dispersion coefficients are proportional the velocity of the fluid and some properties of the porous medium such as porosity or particle size. The numerical coefficients of the second terms were derived for packed particles (Perkins, 1963), and are not valid for fibrous porous media. In Chapter 3 of the present work, D_L and D_T are measured for 2 kinds of fibrous porous media, using the approximation of $D_L \propto U$, without investigating the nature and sensitivity of the dependence of the dispersion coefficients on the physical characteristics of the porous media.

Perkins and Johnston observe that there is a short initial time in a flow experiment where fingering does not occur, and that fingers tend to grow in such a way that widths are close to the minimum width that is able to grow for a given the amount of dispersion which is characteristic of the system. This corresponds to the observation that fingers tend to lengthen while growing to a characteristic width, then will split before lengthening further. If transverse dispersion serves to enlarge the characteristic width of fingers, it may serve as a suppression mechanism by lowering the viscosity gradient which is driving the fingers.

Saffman and Taylor and Slobod and Thomas noted that for low fluid velocities, single fingers tended to form, but multiple fingers would form if the fluid velocity was increased. The transition from a single finger to multiple fingers involves the creation of a large amount of interface. If interface is determined to be detrimental to the finished RTM part, it will be important to minimize the formation of multiple fingers. Park and Homsy (1985), treating immiscible flows, offer insight into the finger splitting phenomenon by showing that a modified capillary number (Ca) is a dimensionless group, the value of which corresponds to the qualitative fingering patterns observed.

$$Ca = \frac{\mu U}{\gamma}\left(\frac{b}{2h}\right)^2 \qquad (1.7)$$

Where μ is the viscosity of the displaced fluid, b is the width of the flow cell, and h is the thickness of the flow cell. It was found that a single finger would grow in width and length, then split into two finger tips during the course of the injection into a Hele-Shaw cell, and that the timing of the tip splitting depended upon Ca. When $Ca < 100$, the finger remained single, but as Ca was raised above 100, the tip would begin to split at regular intervals in the injection. This splitting produced regular, self-similar patterns. When Ca became much greater than 100, the tip splitting became unpredictable in time, and the resulting fingers were irregular and unpredictable. This is part of the basis for describing

viscous fingering as a chaotic phenomenon. There is some literature available, but the subject of chaos in fingering flows is beyond the scope of this paper.

This discussion of the capillary number, Ca, is based on immiscible flows. However, it shows that large viscosity differences and large fluid velocities as well as small cell thickness tend to increase the tendency of fingers to branch. Narrow flow cells (small b) and high surface tension tend to discourage branching. Similarly, in miscible systems, we expect increased viscosity and increased velocity to increase the instability of the flow. The stabilizing factor would be dispersive mixing of the two fluids, which would tend to reduce the viscosity gradient, and the sharpness of the transition from one fluid to another at an interface. Since it has been shown that increased fluid viscosity tends to increase dispersive mixing, it is expected that there will be some optimum fluid velocity in RTM flow, which would damp fingers by dispersion as quickly as they were formed. Also, Tan and Homsy, as discussed below, evaluate theoretically the stabilizing effect of increased dispersion in fingering flows, and show that anisotropic porous media with $D_T > D_L$ have greater finger-dampening effects than isotropic porous media. (Remember, transverse and longitudinal refer to the coordinates of flow, not to the coordinates of the preform.) Thus, when RTM is practiced with an anisotropic porous medium, the location of the resin inlet should be taken into account, so as to orient the flow direction with the coordinate of the preform which has the lower dispersion coefficient, and maximize the finger-damping ability of the preform.

Gorrell (1983) shows that the displacement of crude oil toward an extraction well can be stabilized if the viscosity of the displacing fluid is decreased as the displacement progresses due to the addition of a solute. However, it is also shown that the interface cannot be made unconditionally stable.

In further work of Gorell and Homsy (1985), it was noted that predictions could be made of the most dangerous wavenumber (reciprocal finger width) for a given flow.

Fingers with widths corresponding to the most dangerous wavenumber will be the fastest growing fingers in the system. In a later paper, Tan and Homsy (1986) used a stability analysis of the equations of motion and Fick's law of diffusion to derive the dependence of the most dangerous wavenumber on the viscosity ratio of two miscible fluids. Fick's law was introduced to account for the movement of a solute in the fluids due to diffusion and used analogously to account for the effects of dispersion. Since the viscosity of the fluid depends on the concentration of the solute in this analysis, the local viscosity in the flow can be accounted for, and it is shown that the transverse dispersion is primarily responsible for determining the most dangerous wavenumber (or characteristic width) of fingers.

The analysis of Tan and Homsy produced a stability criterion that is depicted in Figure 1.4. The vertical axis is a dimensionless growth constant, which is directly related to the change in the length of the finger over time. The horizontal axis is the dimensionless wavenumber of the fingers. Suppose a flow which has a viscosity gradient increasing in the flow direction, before fingers have arisen. Then, some disturbance gives rise to a number of 'ripples' on the interface. There will be a distribution of widths to the ripples, some being wider than others. According to Figure 1.4, differences in wavenumber lead to differences in growth rate. Very wide fingers (wavenumber $\cong 0$) have zero growth rate. Very narrow fingers (high wavenumber) have zero or negative growth rates. Fingers which have widths corresponding to the most dangerous wavenumber will be the fastest-growing fingers in the system. Thus, they are the fingers most likely to be observed. It is possible that flow conditions in a Hele-Shaw cell of limited extent may dictate a characteristic finger width which is wider than the dimension of the cell, and this may serve as a stabilizing mechanism. This in turn implies that fingering flow experiments carried out in laboratory flow cells may be more stable than similar experiments carried out in field (unbounded) conditions.

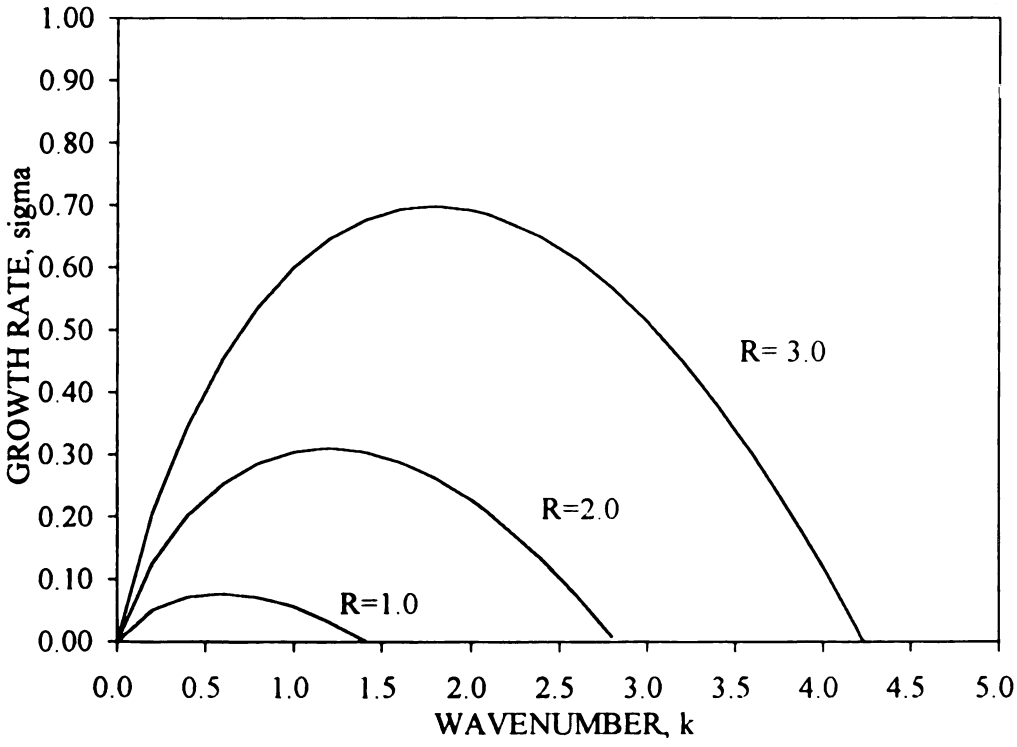


Figure 1.4: Dimensionless growth rate of fingers of various wavenumber (reciprocal width), after Tan and Homsy, (1985).

At short times after the fingers begin to grow, Tan and Homsy show that the growth rate (σ) of fingers in a miscible displacement flow, with dispersion which is anisotropic, is a function of the ratio of the viscosities of the fluids far from the interface(R), the wavenumber (k), and the ratio of the transverse to the longitudinal dispersion coefficients (e):

$$R = ln\frac{\mu_1}{\mu_2}$$

$$e = \frac{D_T}{D_L}$$

$$\sigma = \frac{1}{2}\left[\left(Rk - k^2\right) - k\left(k^2 + 2Rk\right)^{1/2}\right] + (1-e)k^2 \qquad (1.8)$$

This is the equation graphed in Figure 1.4. The most dangerous wavenumber (k_m) is thus:

$$\frac{d\sigma_m}{dk} = 0$$

$$-8\left(e^2 - e\right)k_m^3 - 4\left(4e^2 - 5e\right)Rk_m^2 + 8eR^2k_m - R^3 = 0 \qquad (1.9)$$

Figure 1.5 shows how k_m is influenced by R and e. As the transverse dispersion increases with respect to the longitudinal dispersion, the most dangerous wavenumber decreases, i.e., the most common finger width increases. As the viscosity ratio increases, the most common finger width decreases.

In RTM flows, the structure of the preform will influence the ratio of the dispersion coefficients. Compared to fingering flows in the absence of preform (i.e. in the Hele-Shaw cell), a particular preform may produce a larger characteristic finger width because of an increase in D_T/D_L. The dispersion coefficients for the Hele-Shaw cell and two kinds of preform were measured in Chapter 4. The random swirl mat has e = 0.031, which is 40% of e for the Hele-Shaw cell, and 10% of e for a woven glass preform. Thus, it is expected that the characteristic fingers will be widest in the random swirl mat, and very narrow in the woven fabric.

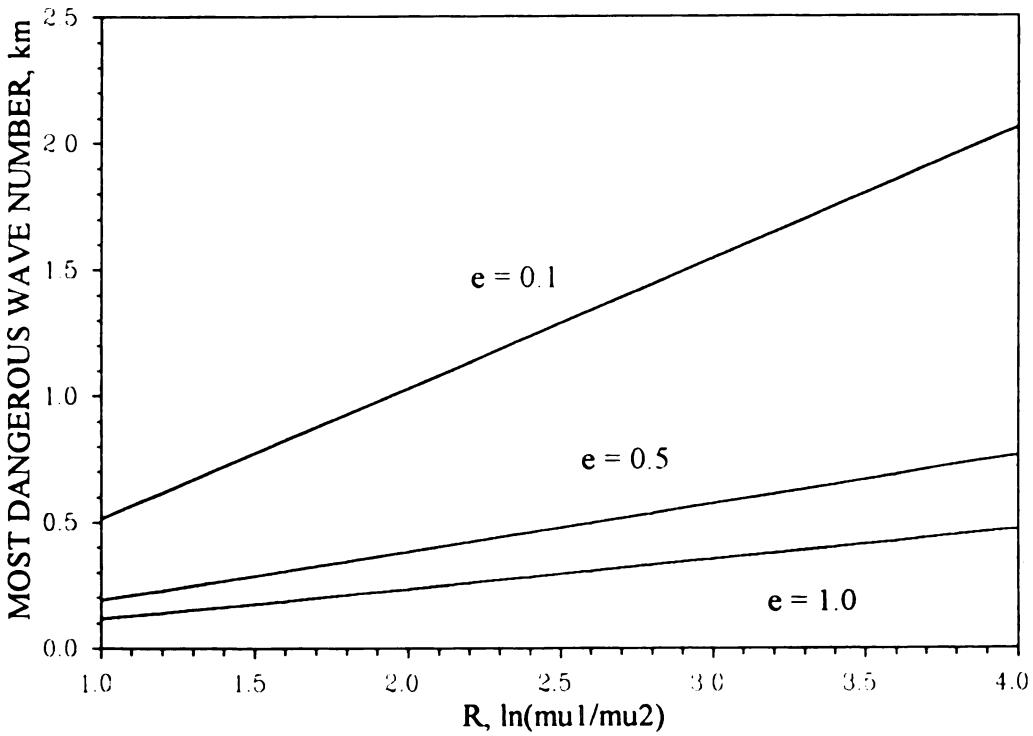


Figure 1.5: Most dangerous wavenumber as a function of viscosity ratio.

The subject of viscous fingering in reacting resin flows has not been reported in the literature. Thus, it is necessary to point out the similarities and differences to be expected between miscible fingering flows between two flat plates, and reactive resin flows in a mold containing fibrous preform.

First, all above discussions assume two discrete fluids, which are either miscible or immiscible in each other. As depicted in the lower two profiles in Figure 1.6, these fluids have distinct viscosities, and the interface between the fluids involves a jump in viscosity over a short distance, at least initially. If the fluids are miscible, the jump will decay over time due to both diffusion and mechanical dispersion of fluid (or a solute) across the interface. However, far from the interface, the viscosities are unaffected. The stability criteria for these two situations, as shown in Eqs. (1.2) and (1.9). The gradual decrease of viscosity with distance into the cell, due to the metered addition of a solute to the flow, is depicted as the uppermost profile in Figure 1.6. As discussed above, this profile has been found to be the most stable manner of displacing a more viscous fluid from a flow cell with a less viscous fluid, but is not unconditionally stable.

In RTM, the resin is mixed just prior to entering the mold, and the viscosity rises exponentially according to the time from mixing (age) of the fluid. Thus, there is only one fluid, and the question of miscibility is a meaningless one. If the injection of the resin into the mold is not interrupted, there will be no jump in the viscosity, but a gradient from the oldest fluid (highest μ) to the youngest (lowest μ), such as is depicted as the exponentially rising curve in Figure 1.6. It is proposed that since μ is a function of time, and the local gradient grows with time, any instability in the flow will grow too, regardless of the stabilizing influence (if any) of dispersion.

Thus it is expected that fingering flows will occur in RTM when the injection conditions are such that a viscosity gradient in the mold is sufficiently large, and the flow rate sufficiently high. There may be conditions under which fingering will be delayed until

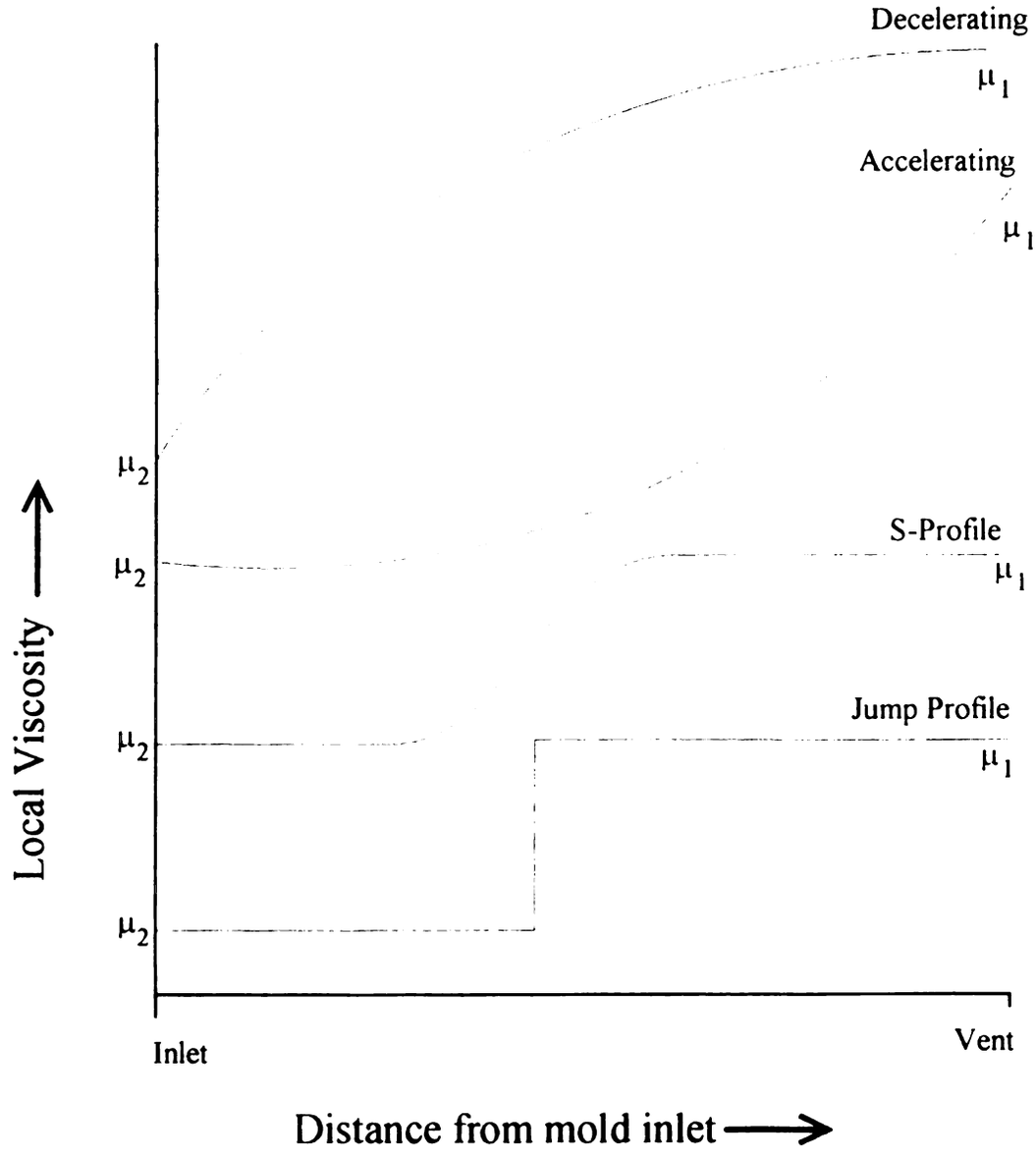


Figure 1.6 Viscosity profiles in a flow cell, various types of fluids.

a critical value of the viscosity ratio or velocity is reached. It is expected that the viscous fingering criterion will be based on a viscosity ratio or contrast which depends on the extent of reaction of the resin as a function of time and temperature. The determination of the viscous fingering criterion for an RTM mold and an epoxy resin system is reported in Chapter 6, and the fingering flow criterion is applied to an RTM moldability diagram in Chapter 7.

As a contrast to the above discussion of what constitutes viscous fingers, it is perhaps instructive to discuss some situations which have the appearance of viscous fingers, but which do not fit the definition, i.e., instabilities at the interface between two fluids, in a flow where a less viscous fluid is displacing a more viscous fluid from a porous medium.

The term 'channeling ' refers to the tendency of fluid to flow faster through portions of a packed bed where the permeability is locally greater than elsewhere. Channeling can be distinguished from viscous fingering by noting that channeling can take place when there is no viscosity gradient, or when a fluid is displacing air from the porous medium. To the extent that channeling allows resins of different age to come together in a mold, the effect of channeling flow on a finished part may be similar to the effect of viscous fingering, and so the results of studying viscous fingering may well be applied to the problem of channeling flow in RTM.

Air entrainment occurs at the flow front of a resin which is being injected into a preform at such a high velocity that the flow front does not stay coherent, but froths, and encloses air bubbles. Air entrainment is very detrimental to the properties of a finished part, and can best be avoided by injecting at lower flow rates. (Macosko, 1989). Air entrainment occurs at the air/resin interface, and is not the result of an unfavorable viscosity gradient.

Resins of different age may come together in the mold when multiple gatings are used, or when a flow front divides and meets again behind an insert. The locale of the merger of the two flow fronts may be likened to a weld line, and may have the same kind of effect on the properties of a finished part that the interface between fluids of different ages may have when it is caused by viscous fingering or channeling. The meeting of two flow fronts may also give rise to viscous fingering, if one fluid is more viscous than the other, and they flow together for some distance after the fronts merge. However, flow around an insert is not necessarily identified with viscous fingering.

Finally, there is the possibility that instabilities or secondary flows may arise which are due to density differences, whether because of uneven temperature distributions, or because of volume changes during reaction. These flows are not identified with viscous fingering per se, although again, they may have the same effect of bringing together resin packets which have different ages.

Although the subject of this study is viscous fingering flows, it should be noted that the flow situations mentioned above may be responsible for the same sort of artifact in a finished RTM part, i.e. a region of the part where packets of resin of different ages came together, and presumably formed a bond. In studying the effects of viscous fingering on a finished RTM part, we are also studying the effects of channeling and flow around inserts on a finished RTM part.

CONSEQUENCES OF FINGERING FLOWS IN REACTIVE RESIN SYSTEMS

One result of fingering flows is that an interface forms between a packet of the more viscous fluid and a packet of the less viscous fluid at the edges and tips of the fingers. In reactive resin systems, this interface will become embedded in the finished part. Will the existence of the interface weaken the RTM part in which it is embedded? This question is not addressed in the literature, but related topics are adhesion and welding and weld-lines in thermoplastic resins. This section will explore the applicability of this literature to the

problem of fingering interfaces in RTM. Experiments designed to test the properties of the interface formed in RTM are described in Chapter 4 for a Derakane resin system, and in Chapter 5 for an epoxy system.

In thermoplastic injection molding, the molten polymer is forced into a mold, then solidified by cooling. The strength and appearance of the finished part depend in large degree on the details of the flow field, and on the cooling process. When two molten fronts meet, either from multiple gatings, or from flow around an insert, they form an interface which may or may not be detrimental to the part. This interface may be deficient in reinforcement particles such as glass fibers and may include surface blemishes such as shrink marks. These effects combine to decrease the tensile strength at the interface by 50% in glass filled polypropylene (Fisa, 1991). The loss of strength is less severe in parts with no glass reinforcement, but is still significant. This loss of strength is partly due to an absence of fibers in the weldline, but air trapped in the weldline as the flow fronts come together may also contribute. The loss of strength in the weldline can be minimized by cooling the part slowly enough that there is plenty of time for chain ends of the molecules to diffuse across the weldline. In un-filled resins, this may result in regaining strength equal to the bulk strength of the polymer, although in filled systems, slow cooling alone will not move the fibers into the weldline.

When one solid thermoplastic part is applied to another, with pressure and heat, welding of the parts may take place. The mechanism of welding is described in Wool (1984 and 1989), and in Vakula and Voyutskii (1963). Both welding of solid polymer surfaces and the healing of a weldline in fluid surfaces depend upon the ability of the molecules to partially diffuse across the weldline, to provide entanglements. The most common model is called the "reptation" model, due to the likeness of molecules diffusing, despite being confined by their neighbors, to the movement of a snake (reptile) in a hole. The development of strength in a weld depends on the thermodynamic compatibility of the

polymers, i.e., whether they are 'soluble' in one another, and on the time and temperature of the contact. The final strength depends weakly on the pressure of the contact, as long as the pressure is sufficient to bring the surfaces into close contact. The effort of making close contact is reduced if the surfaces to be welded are softened, or even molten. Because of this, and because molecule ends become much more mobile when the polymer is above the glass transition temperature, it is of great advantage to weld thermoplastics above their T_g if possible. Welding below T_g is feasible, but may require hundreds of minutes (Wool, 1989).

None of the welding literature investigated deals with polymers which form crosslinks across the weldline, but the adhesion literature treats the formation of an adhesive bond with the reptation model (c.f. Voyutskii and Vakula, 1963) similar to the treatment of thermoplastic welding.

Logically, the strength of the weld or adhesion between two thermosetting materials would depend upon the number of crosslinks which form across the interface. Miller and Macosko (1988) give a discussion of the statistical nature of a cross-linked network, but they assume that the polymer is homogenous, i.e., the degree of reaction throughout the domain where the cross-linking is taking place, does not depend on location. This is plainly not the case when resins of different histories come together at an interface.

Let us consider the following situation: a batch of epoxy resin has been mixed together and injected into a mold. The first moment of mixing will be taken as $t = t_0$. At some time, $t_0 + \Delta t$, a second batch of resin is mixed and injected. The second batch will meet the first batch at an interface. At the moment of meeting, the resins will begin to mingle. Small molecules will diffuse across the interface, and larger ones also. Crosslinks will also be formed. An amine or epoxide site on a growing polymer chain in Resin I, say, can react with a monomer, with a branch of a chain belonging to the bulk of Resin I, or

with a chain from Resin II. Since the monomers are (relatively) mobile, it does not matter if the reacting monomer is from Resin I or Resin II, initially. However, a chain in Resin I reacting with a chain "anchored" or originating in Resin II will be creating a crosslink across the interface. The more crosslinks of this sort which are formed, the stronger we expect the interface to be when the part is fully cured. When a chain in Resin I reacts with another chain from Resin I, the link is not expected to add to the strength of the interface, except inasmuch as either of them goes on to react with chains from Resin II. Thus, the strength of the fully cured interface depends on the number of links formed between the Resin I and Resin II. This, in turn, depends upon the number of unreacted sites still available when the resins were brought together, and on the ease with which the chains from either resin can diffuse to each other and react. These factors in turn depend upon the details of the stoichiometry, timing and temperature of the molding operation.

Throughout the reaction of the resins, the extent of reaction (α) at any time and temperature can be modeled. At the time that the two resins meet, their respective extents of reaction can be designated α_I and α_{II} respectively. When the two resins contact each other, each will have a proportion of its sites unreacted that amounts to $(1-\alpha)$. Since Resin I is more advanced in its cure, it will have fewer unreacted sites than Resin II. Thus, the maximum number of crosslinks that can form depends on $(1 - \alpha_I)$. However, only a portion of these free sites will be able to form crosslinks. There will be some back-biting, and some steric hindrance. And, even at stoichiometric ratios, not all sites will ultimately react. Therefore, the strength of the interface when fully cured should not be compared to some theoretical strength, assuming full reaction of every site, but to the strength of a sample of the bulk material, cured under the same conditions, but containing no interfaces (or other flaws).

Given the existence of interfaces in RTM parts, whether due to fingering flows or flow fronts meeting behind inserts, the question arises as to whether the finished part is

affected in any way. If α_I is low when the interface forms, the ultimate number of crosslinks may be comparable to those in the bulk resin. Thus the interface may be as strong as the bulk resin, and the resin may be said to be forgiving of interfaces. If the extent of reaction is very high, or other factors prevent cross-links from forming, the significant numbers of 'network defects' may cause the interface to be weaker than the bulk resin. In this case, the tensile strength and flexural stiffness of a part may be decreased, and there would be motivation to avoid allowing interfaces to form. If interfaces are adhesive joints which are as strong as the bulk of the resin, then they can be tolerated in RTM parts.

Shrinkage of the resin as it polymerizes may also lead to residual stresses in the part, if different regions of the part shrink to different extents while they are bonded together. This differential shrinkage may cause stresses at an interface which may be inconsequential, or which may be great enough to warp a finished part. In Chapter 4, experiments are described in which fingering flows were induced in RTM plaques, so that the molded-in fingers could be tested for their effect on the physical properties of the finished plaque. Chapter 5 describes experiments wherein plaques were deliberately made with extensive interfaces which could be sampled and tested for strength.

INTRODUCTION TO RESIN TRANSFER MOLDING

Resin transfer molding is a process by which reinforced plastic parts are manufactured. Like other liquid molding techniques, it involves forcing low viscosity resin (less than 1 Pa·sec) into a closed mold which contains reinforcing material. The injection of the liquid resin must be complete before the viscosity of the resin rises too high for further flow, and this may lead to the need for quite high injection pressures, to provide the necessary flow velocities to fill large parts in short times. High injection pressures in turn, lead to higher tool cost, as the mold must be able to withstand the injection pressures without deforming or leaking.

RTM, S-RIM and RIM are all liquid molding techniques. They differ in their areas of application according to the production rate (parts per hour) that can be achieved. Figure 1.7 shows the relative areas of application of RTM, S-RIM, and RIM (S-RIM without preform) in terms of the clamping pressure required and the mold filling times generally used. In general, S-RIM is a high speed, high pressure drop, and low to moderate V_f operation which requires high clamping pressures. In contrast, RTM operates at low clamping pressures and higher fill times, and can accommodate a wide range of fiber volume fractions. The division of RTM from S-RIM is not so much a physical limitation as an economic one. High clamp pressure means high cost, precision tooling, which must be operated at high production rates in order to justify its cost, and this is usually defined as the S-RIM area. RTM can be economical for low part rates or short production runs because the tooling can be less substantial, but it can also be scaled up to produce large production runs at high rates. Thus, the results of RTM flow studies may be applied to S-RIM as well, if scaling arguments are well-considered. Keeping this in mind, further discussion will be limited to RTM.

The low pressures characteristic of RTM make it suitable for flow visualization studies of reactive resin flows by making it possible to construct transparent molds. Thus, the shape of the advancing resin front can be observed, as well as the dynamics of the penetration of the fiber tows by the resin. There is a large body of literature which explores the modeling of the resin flow front in the mold, so that mold designers may explore methods of increasing production rates in RTM.

THE MOLDABILITY DIAGRAM

In general, liquid molding techniques may be described by a moldability diagram such as Figure 1.8, which is adapted from Macosko (1989). This diagram illustrates the interplay of the injection conditions dictated by the molding equipment and the nature of

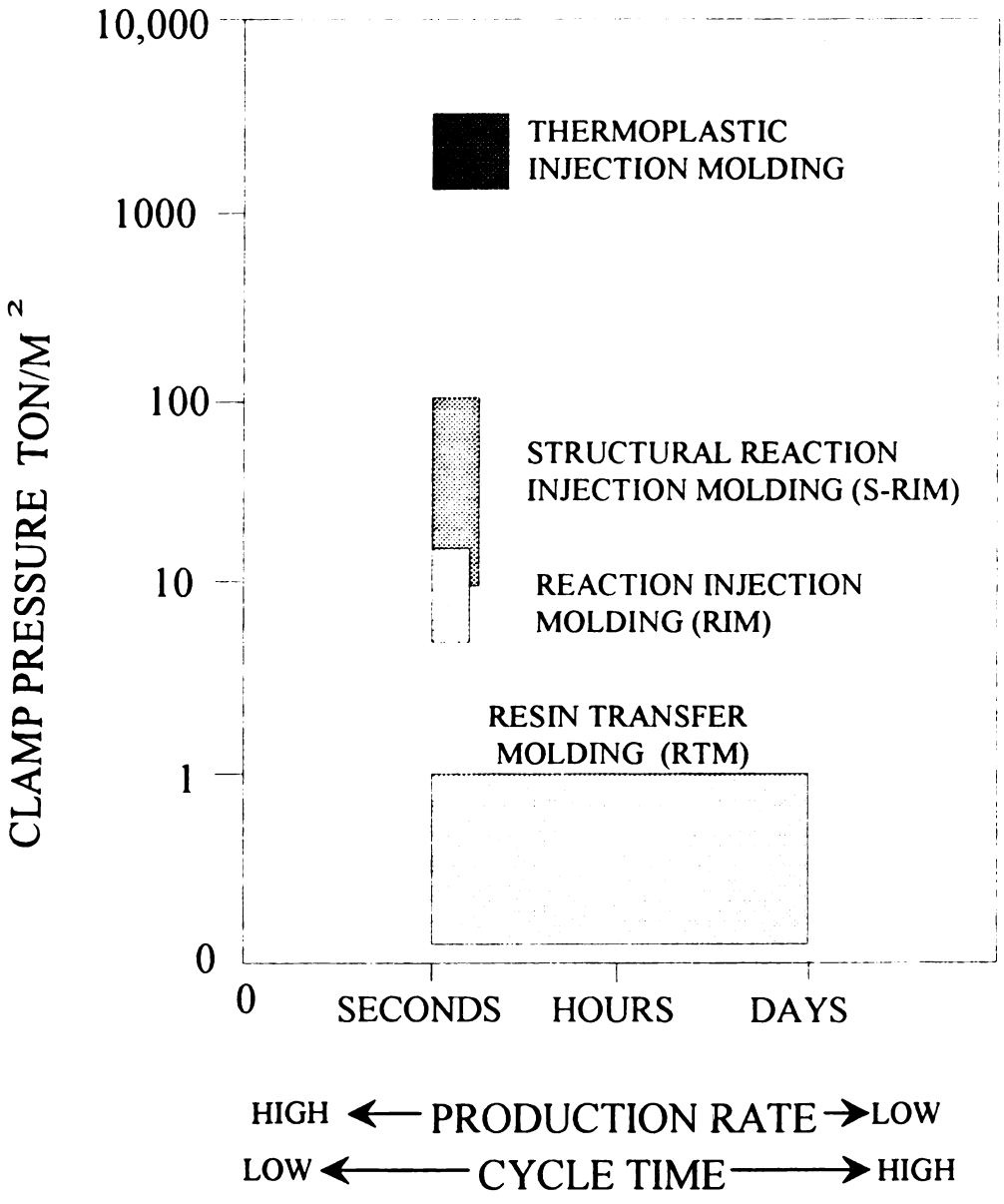


Figure 1.7: Relative operating areas of Reaction Injection Molding (RIM), Structural-RIM, and Resin Transfer Molding.

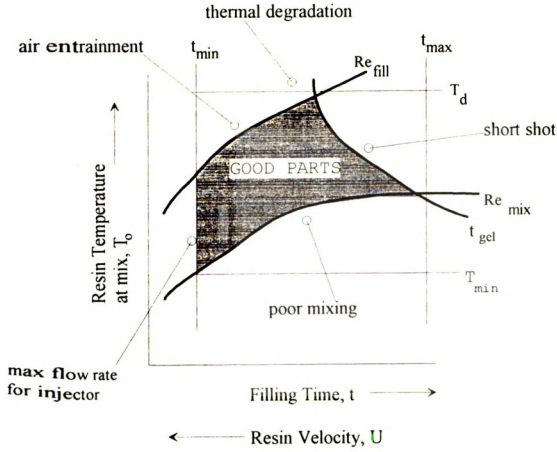


Figure 1.8: Moldability diagram for RTM, after Macosko, (1989, pg. 128).

the resin at hand. Figure 1.8 is a general diagram shown here for discussion. A diagram specific to the RTM process described in this work will be presented in Chapter 7.

The goal of RTM, as in any industrial process, is to make parts economically. This means making parts of acceptable quality in the shortest time possible. Thus, Figure 1.8 shows the operating conditions necessary to make good parts in the injection step. Constraints on the "good parts envelope" may be physical, chemical, or economic, as will be discussed in the following.

Referring to Figure 1.8 then, we see that the vertical axis is the temperature of the resin being injected into the mold. In general, higher material temperature leads to higher reaction rates, and faster part production. However, there is a temperature beyond which undesirable property changes in the resin occur. This is known as the degradation temperature of the resin, and is given as a horizontal line in Figure 1.8, labeled T_d. The actual degradation temperature of the resin is a characteristic of the resin, but the choice of a limit on the resin inlet temperature is influenced by the character of both the resin and the mold. Polymerization reactions are generally highly exothermic. A given mass of reacting resin is capable of raising its own temperature to well above its degradation temperature if the heat is not absorbed by its surroundings. Thus, if the mold is adiabatic, then the operating temperature limit must be lower than the actual degradation temperature of the resin, or the exotherm of the reaction will cause degradation in the mold. On the other hand, an isothermal injection and mold system will allow the limit on the inlet temperature to be chosen more nearly equal to the resin degradation temperature. The line on Figure 1.8 must represent the limit of the inlet temperature which, given the molding conditions, will not allow the resin temperature to rise beyond the degradation temperature *at any time* during the mold cycle.

A lower temperature bound is designated as T_m. At temperatures below T_m, the resin may have too high a viscosity to mix well, or to flow into the mold well. This value

is also influenced by the permeability of the preform, and its ability to resist being dislodged in the mold by the drag of the flowing resin.

The horizontal axis of Figure 1.8 is given as the time to fill the mold, and is inversely related to the flow velocity in the mold. Other things being equal, a large mold takes longer to fill than a small one. Any given injection machine will have a maximum flow rate, and this is the left-hand bound labeled t_{min}. The maximum time possible for filling is bounded by the need to make parts at a rate which will be economical. These four bounds, two of inlet temperature, and two of filling time, make a rectangle within which further limits will be set by other considerations.

Good parts do not contain air bubbles, so the filling time must be greater than that which will cause the resin front in the mold to froth or to entrain air. Macosko (1989, pg. 128) argues that the Reynolds number of filling, based on the mold thickness should be less than 30 to insure that air entrainment does not occur.

$$Re_{\text{filling}} = \frac{\rho v h}{\mu(T_o)} < 30 \qquad (1.10)$$

Where h is the thickness of the mold, v is the velocity of resin flow, and ρ and μ are the density and viscosity of the resin.

Since the viscosity decreases as T_o rises, the bound marked "air entrainment" in Figure 1.8 is inclined to the right, that is, the lower the viscosity, the higher the fill time must be to avoid air entrainment. Note that this bound is shown as a more stringent limitation on the injection step than the capacity of the injection machine. This may not be true if another injection machine were used with the same resin and mold.

Good parts contain resin that is fully cured and homogeneous. To achieve both homogeneity and full cure, good mixing of the resin components is essential. Two common methods of mixing resin components prior to injection are batch mixing and continuous mixing.

When the resin components are mixed together in a vessel by stirring, then injected as a batch, the resin is all the same age. If it is kept isothermal, then any aliquot of the resin will have the same degree of reaction and viscosity at a given time as any other. Non-isothermal viscosity profiles are more complex, as reaction rate depends upon both temperature and time (as described in Chapter 2), and viscosity depends on the degree of reaction. High viscosity due to low temperature or impurities in the components will hinder good mixing, so the lower bound, T_m, of Figure 1.8 still stands. The pot life, that is, the length of time the batch of resin will remain liquid enough to be injected, is also a consideration, and will be discussed below as the gel time.

For high production rates, the preferred method is continuous mixing of the resin components in the injection nozzle, just prior to the mold inlet. One continuous injection unit can serve several molds, and no resin components are wasted, as all mixed resin ends up in the mold. Good continuous mixing requires that the streams to be mixed be of similar viscosity, and that the streams impinge with sufficient velocity. Macosko (1989, pg. 127) has found that keeping the mixing Reynolds number above 300 will provide good impingement mixing.

$$Re_{\text{impingment}} = \frac{4\rho Q}{\pi d \mu(T_o)} > 300 \qquad (1.11)$$

The Reynolds number is based on the volumetric flow rate of one of the components through a tube of diameter d, into the mix head. Other continuous mixing methods, such as static mixers, may have different critical Reynolds numbers. Since the viscosities of the components increase with a decrease of temperature, the boundary labeled Re_{mix} on Figure 1.8, describes a lower limit to T_o which can be used to make good parts. The limit to T_o increases with increasing fill time, because increasing fill time decreases Q in Eq. (1.11).

Continuous mixing of the resin at the inlet of the mold results in resin flows where each packet of the resin has a different age, and thus variations in degree of reaction, viscosity, and temperature may arise in the mold during the fill time. In particular, a viscosity gradient may arise in the mold, with the oldest resin in the mold being significantly more viscous than the newest resin.

If the fill time is a significant portion of the gel time (as defined in Chapter 2), the viscosity of the oldest resin in the mold may rise high enough to stop flow in the mold before the mold is full. The part thus made is termed a "short shot" and is generally scrap. The gel time is temperature dependent, as it depends on the extent of reaction. Thus, higher values of T_O require shorter fill times, as illustrated in Figure 1.8 in the line labeled t_{gel}.

The shaded area in Figure 1.8 is the operating envelope. Operating outside of the envelope virtually assures that no good parts will be made. However, operating inside the envelope does not insure that good parts will always result. Further investigation of the process may lead to more stringent boundaries than those outlined in Figure 1.8. For example, it may be found that the fibrous reinforcement in the mold may be dislodged by the drag induced on it by high resin velocities, and the critical velocity may be less than that which will cause air entrainment. Thus, the operating envelope would be reduced in area to assure that the preform is not disturbed by the flow.

In addition, there may be some extent of reaction, short of gel, beyond which two resin flow fronts coming together will not form an interface which will be fully as strong as the bulk of the part. The need to avoid weak interfaces of this kind would lead to a more stringent condition of the left boundary than that shown on Figure 1.8 as t_{gel}.

Other conditions may exist which may further limit the boundaries of the operating envelope, and it is proposed that fingering flow may be one of them. Chapter 6 contains the description of the experiments which were performed to delineate the viscous fingering

criterion. Chapter 7 shows how the moldability diagram for the RTM system described in Chapter 6 was constructed to include the viscous fingering criterion.

THE STRUCTURE OF THE PREFORM

In RTM, the reinforcing material is usually a glass or carbon fiber fabric which is packed tightly enough in the mold to stay in place despite the drag of the resin as it flows through the mold. The fabrics are generally made of very fine fibers (less than 10 microns) which have been bundled together in tows, then used like yarn in weaving and other fabric construction techniques. This hierarchy of dimension scales: fiber to tow to fabric, is illustrated in Figure 1.9.

Preform fabric can be obtained in many forms, from felt made of chopped fibers which have been lightly bonded together, to complex triaxial weaves. Some preforms are three dimensional structures built up from various fabrics, then stitched together to hold their shape. All preforms must be robust enough to be handled in the manufacturing process without falling apart. Yet they must conform to the mold contours, allow resin to flow through them and wet them thoroughly, and provide the designed reinforcement to the finished part. Much study has been directed to the flow of resin in various kinds of preforms, focusing on the transport of resin through the inter- and intra-tow spaces through convection and wicking. However, there are no studies of fingering flows in fibrous preforms. It is expected that the construction of the preform will dictate the widths of fingers through the size of the inter-tow spaces, where convection flow takes place, and through the dispersive effect discussed above. Chapter 3 describes the characterization of the permeability and dispersion coefficients for two preforms used in the fingering flow experiments described in Chapters 4 and 6.

PHYSICAL PROPERTIES OF COMPOSITE MATERIALS

Two tests of physical properties of materials are the 3-point bend test, and the tensile test. These tests yield information on the properties of materials which are of use

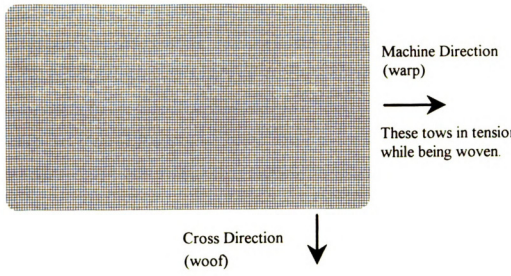


Figure 1.9: Structure of a woven preform.

to designers of parts. What follows is a short introduction to the tensile test and 3-point bend tests, and a discussion of their relevance in testing composite parts.

The tensile properties of a sample bar may be described as follows. Consider Figure 1.10. A rectangular bar of width b, thickness h, and length L is subjected to a force or load, F, acting along its long axis, and applied evenly across the end face of the bar. The stress applied, is calculated as the load, F, applied over the original cross-section, $b_o h_o$.

$$\sigma_x = \frac{F_x}{b_o h_o} \tag{1.12}$$

Under the load, the bar will lengthen a bit, and will shrink in the width and thickness directions also. The deformation of the bar can be expressed as the strains in the longitudinal (ε_x) direction, and the width (ε_y) direction:

$$\varepsilon_x = \frac{\Delta L}{L}$$

$$\varepsilon_y = \frac{\Delta b}{b}$$

$$\nu = \frac{\varepsilon_y}{\varepsilon_x} \tag{1.13}$$

ν is Poisson's ratio, which can range from 0 to 0.5, and is typically 0.34 for rigid, cured epoxy resins (Handbook of Epoxy Resins, pg. 6-24). The volume change (ΔV) of the bar due to a tensile stress, σ_x, can be expressed as

$$\frac{\Delta V}{V_o} = \frac{\sigma_x}{E_t}(1-2\nu) \tag{1.14}$$

Figure 1.10 also shows the relationship between the stress and strain for a typical material. At low strains, the relationship is linear, with the slope defined as the tensile, or Young's modulus, E_t:

$$E_t = \frac{\sigma_x}{\varepsilon_x} \tag{1.15}$$

This linear region is called the elastic region of the stress-strain curve. At higher strains,

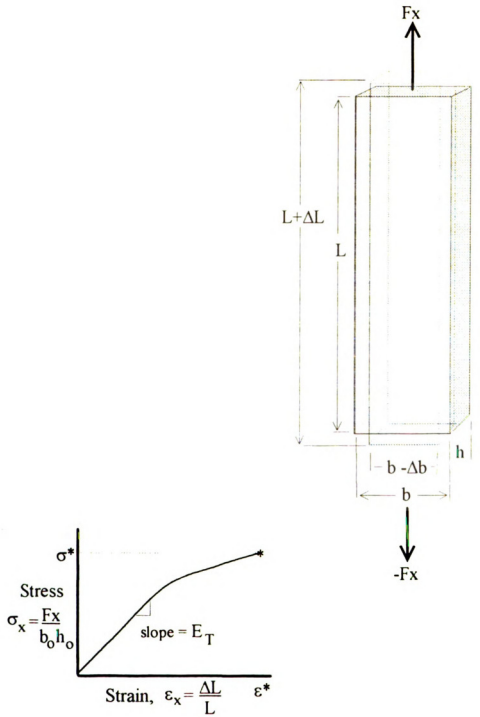


Figure 1.10: Tensile deformation of a rectangular prism.

the stress-strain relationship ceases to be linear. This part of the stress-strain diagram is known as the plastic deformation curve. As the load is increased, eventually the tensile strength, σ^*, is reached, and the material fails.

For isotropic, homogenous materials, the Young's modulus is the same whether the test is performed in tension or in compression. However, the tensile strength of a material may be very different from the compressive strength. Furthermore, the tensile strength of any particular sample of material is very dependent upon the presence of flaws such as cracks or bubbles of air. A specimen will generally fail at the flaw, and so the tensile test may provide information about the number and nature of flaws present in a sample population of the material. Good practice when choosing samples for the tensile test is to avoid those samples which are obviously flawed, and to provide at least 5 samples which are putatively identical for purposes of averaging.

The 3-point bend test is used to measure the properties of a material in bending. Figure 1.11 shows a test bar in the 3-point bend test fixture. The bar rests on two lower supports, a distance L apart, and a load is applied to the top, halfway between the two supports. As the load is increased, the bar will be deformed as in part B of Figure 1.11.

The top and bottom of the bar become arcs of a circle of radius r, and all material planes which were parallel to the top and bottom stay parallel by deforming in like manner. Material planes which were originally cross-sections of the bar, that is, normal to the longitudinal axis, remain planar in the deformed bar, but now are parallel to radii of the circle, rather than being parallel to each other. Note that the top of the bar is in axial compression, while the bottom is in axial tension. In the center of the bar is a plane which is under neither tension nor compression. This is called the neutral axis, and falls at y=0 in the coordinates given, when the cross-section is symmetrical about y = 0.

These observations are true for isotropic materials in the elastic region of the stress strain curve, which is depicted as part C of Figure 1.11. The deflection, d, is defined as

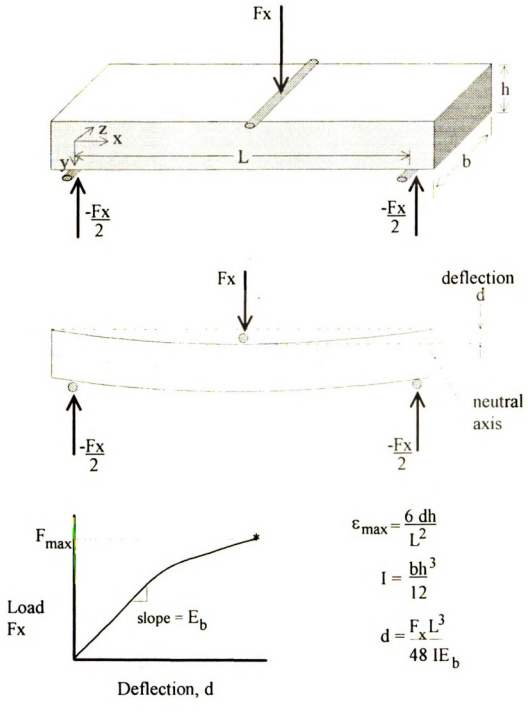


Figure 1.11: Bending deformation of a rectangular prism.

the distance that the loading point has traveled in applying the load. Other values of interest are the flex or bending modulus, E_b, and the strain in the 'outermost fiber' of the bar, ε_{max}:

$$d = \frac{F_x L^3}{48 I E_b}$$

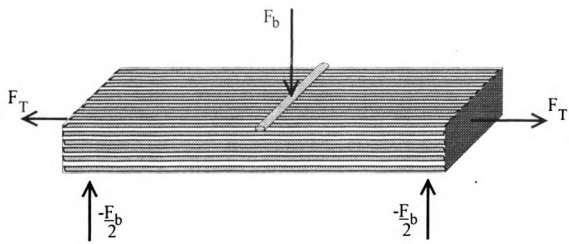
$$I = \frac{bh^3}{12}$$

$$\varepsilon_{max} = \frac{6dh}{L^2} \qquad (1.16)$$

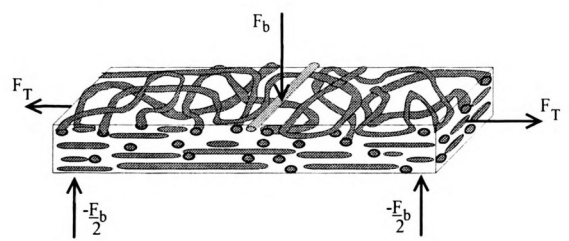
I is the moment of the cross-section. In 3-point bend testing, the maximum strain is kept small enough (3-5%) that it is assumed that the shear stress generated within the bar is small compared to the tensile stress at the outer fiber. The short beam shear test uses large deflections to test the shear strength of the material, and will be described in detail in Chapter 5.

It is generally assumed that successive cycles of loading and unloading of the material will produce the same value of E_b, if the strains are kept small. This assumption may not be valid where the stress applied during a cycle is sufficient to damage the material, perhaps by exacerbating existing flaws. For an isotropic, homogeneous material at small strains, the tensile modulus (E_t) and the flex modulus (E_b) are the same. However, this is not true when testing a composite material, as the addition of fibers, complicates the picture, as will be discussed below.

Figure 1.12 shows two kinds of fiber reinforced materials. The upper bar has fibers aligned in the x direction, and distributed evenly throughout the y-z plane. When this bar is stressed by tensile loads, P_t, the fibers bear the load in proportion to their volume fraction in material. Since the fibers generally are much stronger than the resin, the tensile modulus and tensile strength are strongly influenced by the volume fraction of fibers. See Table 1.1 for typical physical properties of glass fibers and thermosetting resins. In simple



Uni-directional fiber composite material



Random Swirl mat preform.

Figure 1.12: Two kinds of fiber-reinforced composite bars.

terms, the resin is present to bind the fibers together so they can bear the load; the resin does not greatly contribute to the tensile strength of the bar, and a flaw in the resin is of (comparatively) little consequence.

Table 1.1: Typical physical properties of fibers and resins. (After Hull, 1981).

	Young's modulus (GPa)	Tensile strength (GPa)	Elongation to fracture (%)	Poisson's ratio ν	Shrinkage on curing (%)
E glass	76	1.4 - 2.5	1.8 - 3.2		
Glass fiber/polyester $V_f = 0.50$, unidirectional parallel to fibers perpendicular to fibers	35-40 8-12	650-750 20-50	1.8	0.26 0.26	
Glass fiber-polyester $V_f = 0.20$, planar random continuous fibers	8.5	110	2		
Neat polyester resin	2 - 4.5	40 - 90	2	0.37 - 0.39	4 - 8

The flex modulus is also influenced by the presence of fibers. When the bar is loaded in bending, half the fibers will be in tension, and half will be in compression. The polymer resin between them will serve to transfer load from one fiber to another, and will mainly be in shear. If the resin fails to transfer the load adequately, the bar will buckle. The properties of the resin in shear are thus critical to the bending properties of the bar, and so flaws in the resin will tend to be detected by the bend test more readily than the tensile test for unidirectional fiber reinforcement.

Figure 1.12 also shows a sample bar containing random swirl mat at $V_f = 0.20$. The fibers in this sample all lie parallel to the x-z plane, but they are randomly distributed in the plane. Very few fibers will run continuously from one end of the bar to the other, and so the tensile properties are not as strongly dependent upon the fibers, since only those which run parallel to the x direction will be bearing tensile loads. The strength of the resin, and

the presence of flaws is much more important in this kind of composite bar than in the uni-directional bar. Likewise, the bending properties of the bar as a whole are strongly influenced by the flexural properties of the resin, because the fibers occupy only 20 % of the volume of the bar, and because the configuration of the fibers does not allow the tensile and compression stresses to be borne along the axis of the majority of the fibers. On a large scale (several square centimeters) the swirl mat is random, but on a small scale (say the width of the bar), it is expected that the flex modulus will not equal the tensile modulus, as it cannot be assured that the section of the bar in tension is similar in fiber content and orientation to the section of the bar which is in compression.

In both cases, if it is desired to test the physical properties of the resin in the composite bar, the 3-point bend test will be more revealing than the tensile test because the dominance of the fibers in the tensile test may obscure any changes in properties due to the resin. However, the tensile test will be useful if the manner of failure reveals the presence of flaws in the resin associated with some feature of the resin, such as interfaces due to fingering flow.

SUMMARY

The preceding discussion has been an introduction to the phenomena of viscous fingering flows and an explanation of their possible role in resin transfer molding. The next two chapters detail the characterization of the thermosetting resins and fibrous preforms used in experiments with viscous fingering flows in RTM. Chapters 4, 5 and 6 detail the actual viscous fingering flow experiments, and Chapter 7 interprets the results of Chapter 6. Chapter 8 contains a summary of the conclusions drawn in this work, and the recommendations for further work. Bon Voyage.

CHAPTER 2

CHARACTERIZATION OF THE RESIN SYSTEMS

INTRODUCTION

There were two reactive resin systems used in the main body of this work. Details of the structures, properties and sources of the components of both resins are given in Appendix A.

The Derakane® 411 resin is a polyvinyl ester resin from Dow Chemical Co. This resin system has a short gel time (~18 min) and can be fully cured at room temperature. The Derakane resin system consists of three liquid componenets, and is easy to mix as a batch, but it does not lend itself to in-line mixing due to the large disparity in volume fractions of the three components.

The other resin was diglycidyl ether of bisphenol A (DGEBA) epoxy monomer with triethylene tetramine (TETA) hardener. The DGEBA/TETA epoxy resin system was chosen because the components are relatively non-toxic, the cure could be achieved at low temperatures, and the pot life was relatively long. These components are available in high purity grades, so that the chemistry is relatively simple. In addition, the viscosity of the resin rises gradually with time, and this is expected to facilitate the observation of fingering flows due to viscosity gradients in the mold. Also, the two components are similar enough in volume fraction so that in-line mixing can be used for injection of the resin into a mold.

This chapter documents the work done to characterize the viscosity, reaction kinetics, gel time, exothermic temperature rise, and specific volume profile of the DGEBA/TETA resin system, as well as the viscosity, gel time, exothermic temperature

rise, and specific volume profile of the Derakane 411 system. Tables 2.4 and 2.5 show the resin recipes used throughout this work, and summarize the properties of the DGEBA/TETA and Derekane 411 resins which were determined as follows.

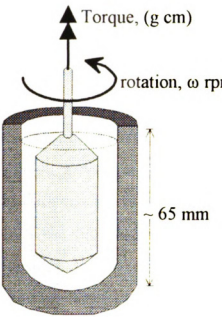
VISCOSITY OF DGEBA/TETA EPOXY

The viscosity of the DGEBA/TETA resin system was characterized at a temperature of 50° C, which was chosen as a convenient molding and cure temperature. In addition, the DGEBA is consistently a liquid at 50° C, but at room temperature it has a tendency to crystallize over the course of 3 to 7 days. Thus, the room temperature viscosity of the DGEBA is unpredictable, and it is best to work with it at an elevated temperature. The crystallization of the DGEBA is promoted by the presence of water which has been absorbed from the atmosphere. For the viscosity characterization, no effort was made to remove moisture from either the DGEBA or the TETA.

The viscosity of the DGEBA/TETA was measured on two instruments, which had overlapping ranges of measurement. For the low viscosity/short time measurements, a Brookfield Digital Viscometer Model DV-II was used, with a temperature-controlled cell. This couette flow instrument gave valid readings in the range of 0.1 to 7.0 Pa·sec. For the higher viscosity measurements, a Rheometrics Mechanical Spectrometer, model RMS8000 was used in the parallel plate configuration. Valid readings were obtained in the range of 10 to 10,000 Pa·sec. Schematics of the two instruments are given in Figure 2.1.

MEASUREMENTS

The Brookfield Viscometer calculates viscosity readings from a knowledge of the spindle configuration (couette flow, shown in Figure 2.1) and rotation rate, and from a reading of a load cell which measures torque exerted on the spindle shaft by the drag of the fluid being measured. The load cell has a limited range in which readings are valid. In the case where a viscosity is increasing over time, the range of valid data can be widened by decreasing the rotation rate when the load cell approaches its maximum. In these



Couette Viscometer

Cell is temperature controlled.

Spindle radius: 11.8 mm

Cell radius: 19 mm

Spindle driven at constant rotation rate, ω.

Torque measured at spindle shaft.

Parallel Plate Viscometer

Enclosed in temp. controlled oven.

Plate Radius: 2.5 cm
Gap Width: 0.13 mm

Torque measured at top shaft.

Bottom Plate driven with frequency ω rad/sec.

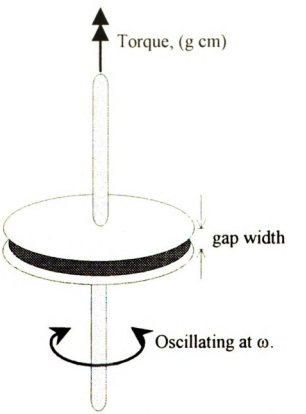


Figure 2.1: Viscometer configurations, Brookfield (couette) and Rheometrics (parallel plate).

measurements, Spindle #27 was used, and the rotation rates used were 100, 50 and 20 rpm.

The measurement procedure using the Brookfield Viscometer was as follows: DGEBA was brought to 50° C, but the TETA was left at room temperature. DGEBA was weighed into a beaker, and TETA was added at the weight ratio of 12.9 g TETA/ 100 g DGEBA. Timing was begun when the DGEBA and TETA were first weighed together, and stirring took approximately 4 minutes. The viscometer cell, which had been preheated to 50° C was then loaded with resin, and the controller quickly equilibrated the temperature. Viscosity measurements began at 4 minutes from mix, and continued at intervals until the viscosity had increased beyond the range of the viscometer. The cell was then dismounted and cleaned. The basic data are presented in Appendix C. Figure 2.2 shows the results graphed together with the high viscosity results discussed below.

The Rheometrics RMS8000 was used to measure the complex viscosity of the reacting resin by loading the resin between two parallel plates, and subjecting it to an oscillating rotation. The torque generated on the shaft of the top plate was then measured, and the complex viscosity was calculated by the software. The radius of the plates was 25 mm, and the gap between them was 0.13 mm. The load cell in the RMS8000 is not accurate at readings below 2.0 g·cm, which was reached at 32 minutes into the run, with timing being started when the actual measurements began. Mixing time was approximately 4 minutes, and time to load the RMS8000 was approximately 3 minutes more. The data from the RMS8000 run appear in Appendix C. Figure 2.2 contains the viscosity data, and the shear modulus data are graphed in Figure 2.5 , which will be discussed below, in the section on the determination of the gel point.

DISCUSSION

Both sets of viscosity data are shown in Figure 2.2. The Brookfield data end at 25 minutes, 6.2 Pa·sec. The Rheometrics data begin at 32 minutes, 8.7 Pa·sec, and end where

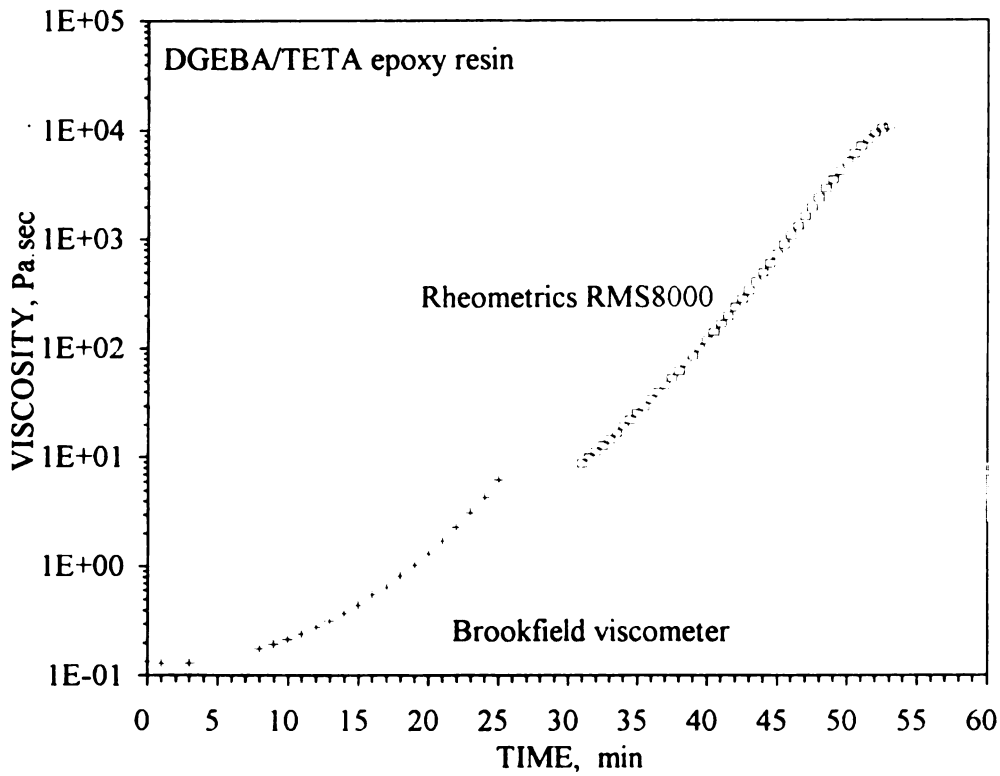


Figure 2.2: Viscosity data of the DGEBA/TETA resin system.

the load cell reached its limit, at 10,000 Pa·sec. As discussed above, the zero time on the Brookfield data occurred at the mix time of the resin, while the zero time on the Rheometrics data began at the first measurement, which actually occurred about 7 minutes after the resins were mixed. There is some uncertainty in the actual amount of time between the mixing of the resin and the first measurement on the Rheometrics, and small differences in weighing the components may also contribute to the viscosity curve being shifted a minute or two, so in order to obtain a single curve, the Rheometrics data were shifted in time approximately 7 minutes to the left, as shown in Figure 2.3. This curve was not amenable to a linear fit at small times, so the entire curve was fit with a polynomial using a least-squares regression subroutine. The solid line in Figure 2.3 is the result of the regression, which can be given as:

$$log_{10}\mu = log_{10}\mu_o + Bt + Ct^2 + Dt^3 + Et^4 \qquad (2.1)$$

$T = 50°C$

$log_{10}\mu_o = -0.8416$

$B = -3.519 \times 10^{-2}$

$C = 5.466 \times 10^{-3}$

$D = -6.22 \times 10^{-5}$

$E = 2.043 \times 10^{-7}$

where t is time in minutes, and μ is the viscosity in Pa·sec. The fitting coefficient, R^2 is 0.999.

Despite the small coefficients, none of the higher order terms in Eq. (2.1) is insignificant at large times, because of the large number of minutes involved. This equation will be used as the relationship between time and viscosity where needed. The viscosity data will also be used to obtain a relation between the viscosity and the extent of reaction, as discussed below. All resin properties are summarized in Table 2.4.

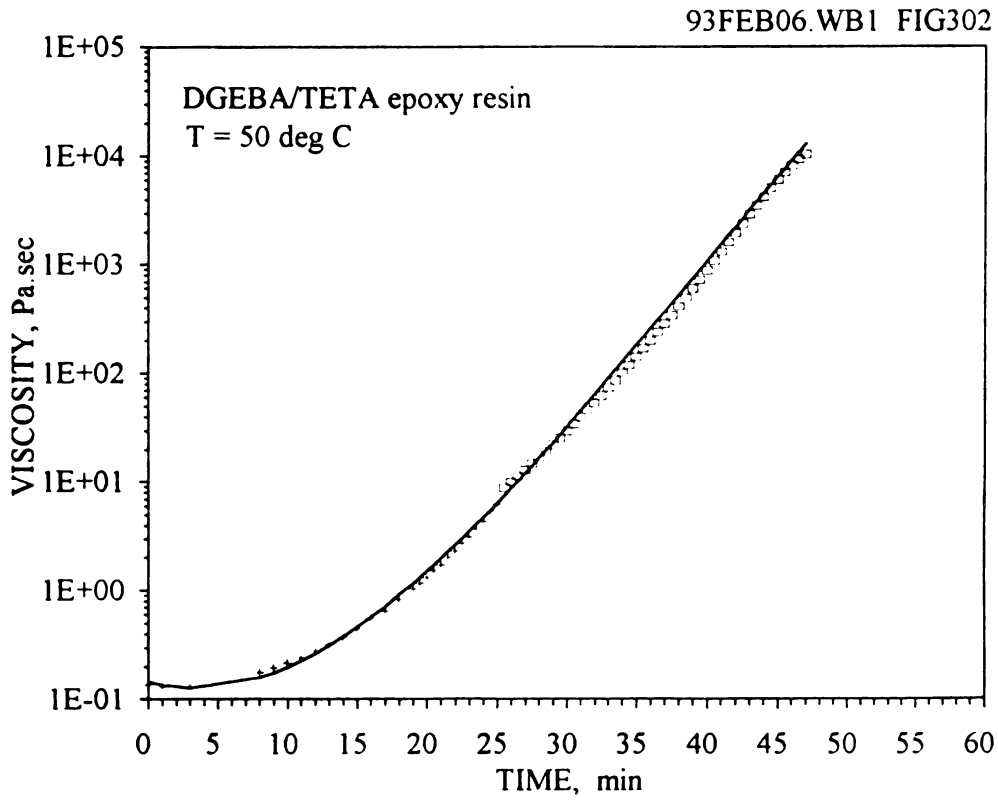


Figure 2.3: Viscosity model for DGEBA/TETA resin system: polynomial

Alternatively, the viscosity can be fit to an exponential similar in form to that used below to relate viscosity to the extent of reaction:

$$\mu(t) = \mu_o A t \left[\frac{t_c}{t_c - t}\right]^{(B+Ct)} \qquad (2.2)$$

$T = 50°C$
$\mu_o = 0.1096 \ \ Pa \cdot sec$
$t_c = 65 \ \ min.$
$A = 1.7069 \ \ min^{-1}$
$B = -109.63$
$C = 1.1922 \ \ min^{-1}$

The fit coefficient of this model is 0.9988. Figure 2.4 shows that this expression for viscosity fits just as well as that above, and the choice of which one to use will be made based upon which form is easiest to work with on any given task.

Eq.'s (2.1) and (2.2) were derived from data taken isothermally. It is assumed that the initial viscosity (μ_o) has an Arrhenius dependence on temperature, but no data were taken to confirm this.

VISCOSITY OF DERAKANE 411 RESIN

Viscosity measurements for the Derakane resin took place at 25 °C, using the Brookfield viscometer, as described above. The RMS8000 was not used to show the high-viscosity portion of the Derakane reaction. The results are shown in Figure 2.5. Note that the viscosity is almost constant at 0.45 Pa·sec in the early part of the reaction. After 12 minutes, the viscosity rises rapidly, to a practical gel point at 18 minutes. Thus, in using Derakane resin for RTM, care was taken to keep the injection time below 16 minutes. The viscosity can be modeled in a similar form to Eq. (2.2) above:

$$\mu = \mu_o + At + B\,ln\left(\frac{t_c}{t_c - t}\right) + Ct\,ln\left(\frac{t_c}{t_c - t}\right) \qquad (2.3)$$

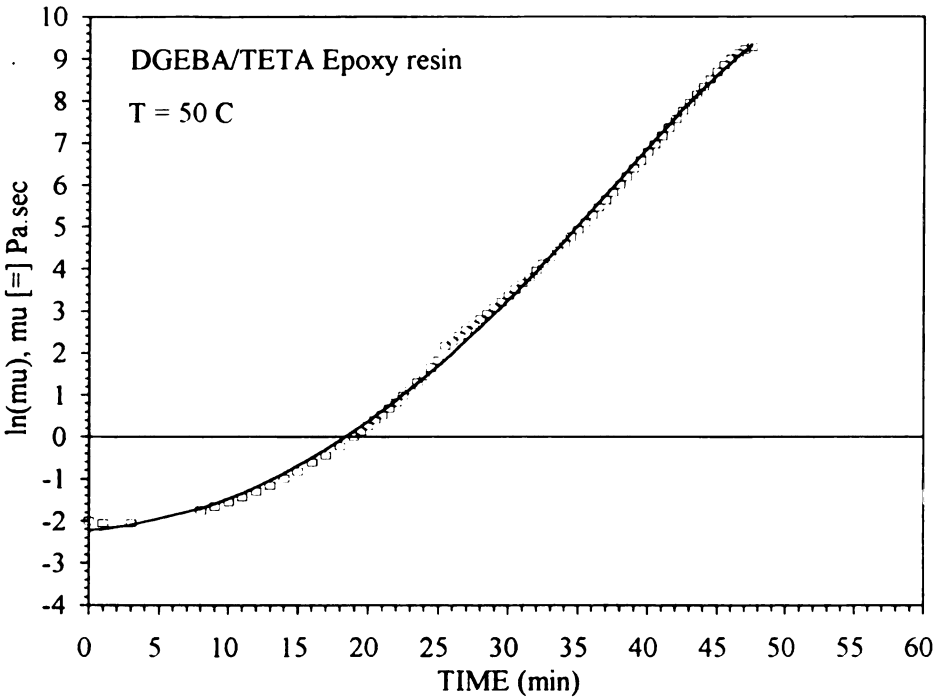


Figure 2.4: Viscosity model for DGEBA/TETA resin: power law.

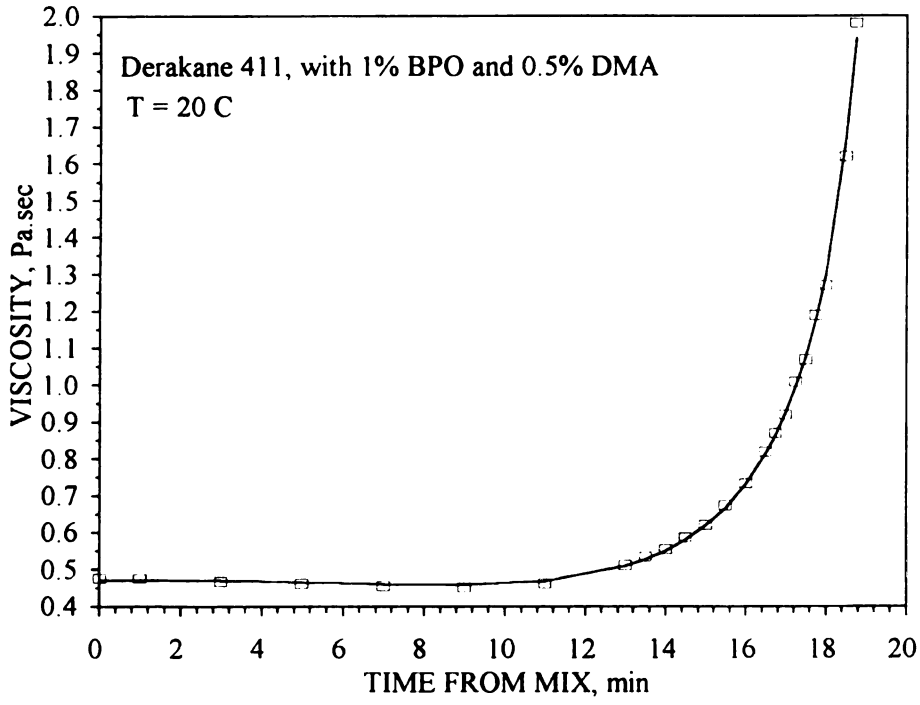


Figure 2.5: Viscosity profile for Derakane resin system.

$T = 20°C$
$t_c = 19.5$ min
$\mu_o = 0.4713$ Pa · sec
$A = -0.1536$ Pa · sec / min
$B = 3.0254$ Pa · sec
$C = -0.09017$ Pa · sec / min

Note that Eq. (2.3) is based on the viscosity, instead of the natural logarithm of the viscosity. For these low values of the viscosity, this method provided a much better fit, as can be seen in Figure 2.5.

REACTION KINETICS OF DGEBA/TETA RESIN

Molecular configurations for DGEBA and TETA can be found in Appendix A. DGEBA is a symmetrical molecule of basically linear plan, containing two phenyl groups in the backbone. At each end is an oxirane ring, and these are the active sites for the polymerization reaction. TETA is a straight-chain molecule, having four nitrogen molecules in the backbone. There are two secondary amines in the backbone, and two primary amines on the ends of the molecule. Thus, the DGEBA has two active sites per molecule, and the TETA has six. The stoichiometric ratio for this reaction is 12.9 parts TETA per 100 parts DGEBA by weight. This ratio is calculated such that there is one oxirane per active hydrogen, so the overall molecular ratio is DEGBA:TETA = 3:1.

The epoxidation reaction is illustrated in Appendix A. A primary amine attacks the oxirane ring, adding the nitrogen to the last carbon on the DGEBA backbone, and providing a hydrogen to the oxygen, which then becomes an hydroxyl group on the second carbon in the DGEBA backbone. Once a primary amine is reacted, it becomes a secondary amine, capable of another reaction to become a tertiary amine (Horie, 1970). Since primary amines have a greater reaction rate than secondary amines (as much as a factor of 50) it is expected that this reaction would have two steps. That is, nearly all primary amines would react before secondary amines began to react. As there are effectively two primary and four secondary amines, it is expected that the change in

reaction rate or dominating mechanism would occur when the extent of reaction is about 0.33.

In order to model the reaction between DGEBA and TETA, we will consider a reaction occurring at constant volume between the components A and B, producing product P.

$$A + \upsilon B \xrightarrow{\mathcal{R}} P \tag{2.4}$$

Where υ is the stoichiometric coefficient. This is a very simplified picture, since P participates in further reactions to form polymer. The reaction rate, $\mathcal{R}$, is defined as the moles of A consumed per volume, per time, or as the change in concentration of A over time, since volume is constant.

The reaction rate can be defined as the disappearance of component A per unit volume per time.

$$\mathcal{R} = -\frac{dC_A}{dt} \tag{2.5}$$

If the concentration of A at any time is C_A, and the concentration at zero time is C_{Ao}, then the fraction of A reacted at any time is:

$$\alpha = \frac{C_{Ao} - C_A}{C_{Ao}} \tag{2.6}$$

α is known as the extent of reaction. Assuming that component A is the limiting component, then $0 \le \alpha \le 1$, because C_A goes to zero as the reaction approaches completion.

The relationship between the reaction rate and the extent of reaction is:

$$\frac{d\alpha}{dt} = -\frac{1}{C_{Ao}}\frac{dC_A}{dt} = -\frac{1}{C_{Ao}}\mathcal{R} \tag{2.7}$$

In general, the rate of reaction will depend on the initial concentrations of the reactants, the temperature of the reaction, and the extent of the reaction. Let us propose a model for $\mathcal{R}$ that includes these features:

$$\mathcal{R} = C_{Ao}^{p} C_{Bo}^{q} k_{\mathcal{R}} (1-\alpha)^{p+q} \qquad (2.8)$$

The reaction constant, $k_{\mathcal{R}}$, will be temperature dependent, and it is assumed that this manifests itself in an Arrhenius manner:

$$k_{\mathcal{R}} = k_A \, exp\left[\frac{-E_{\mathcal{R}}}{R_g T}\right] \qquad (2.9)$$

Where $E_{\mathcal{R}}$ is the activation energy of the reaction, R_g is the gas constant, and k_A is the pre-exponential factor. The rate of reaction in terms of the extent of reaction is thus:

$$\frac{d\alpha}{dt} = -\frac{1}{C_{Ao}}\mathcal{R} = -\left[C_{Ao}^{p-1} C_{Bo}^{q} k_A\right] exp\left[\frac{-E_{\mathcal{R}}}{R_g T}\right](1-\alpha)^{p+q} \qquad (2.10)$$

The method of Differential Scanning Calorimetry (DSC) was used to evaluate the constants in Eq. (2.10), by equating the rate of heat production during the reaction with the rate of reaction.

DSC is a widely accepted method of determining the kinetics of a reaction (Abolafia 1969, Peyser 1977, Prime 1973, Fava 1968, Mijovic 1984). The DSC measures the heat input necessary to control the temperature of two sample pans, one of which contains reacting materials, and one of which is a blank. The difference in heat input between the two samples is taken to be due to the heat evolved by the reaction. A record of this heat flow over time can be interpreted as representing the rate of reaction. The total heat given off during the reaction can be calculated from the integral of the heat flow curve, and these data can be used to fit kinetic rate laws.

The Dupont Thermal Analysis System used in this study has built-in software to use the method of Borchardt and Daniels to fit the kinetic equation:

$$\frac{d\alpha}{dt} = k_o \, exp\left[\frac{-E_a}{R_g T}\right](1-\alpha)^{n} \qquad (2.11)$$

Where:

t is time (min)

k_0 is the pre-exponential factor of the Arrhenius temperature dependence (1/min)
E_a is the activation energy (J/mole)
R_g is the gas constant (8.314 J/mole·°K)
T is the temperature (°K)
n is the reaction order
α is the extent of reaction, defined by:

$$\alpha(\tau) = \frac{\overline{H}(\tau)}{H_o} = \frac{\int_0^{\tau} Hdt}{\int_0^{\infty} Hdt} \qquad (2.12)$$

H is the heat flow measured by the calorimeter as a function of time (J/g·sec).

Note that the k_0 of Eq. (2.11) encompasses the initial concentration terms and the pre-exponential factor of Eq. (2.10). Thus, k_0 derived from the method of Borchardt and Daniels, and shown in Eq. (2.11), is specific to the stoichiometry used to derive it. If it is desired to alter the stoichiometry, then another value of k_0 must be derived. If a number of different stoichiometries are to be used, then all the constants in Eq. (2.10) should be evaluated, for the convenience of having one model to fit all stoichiometries. For the present study, however, only one mass ratio of DGEBA/TETA will be used, and the limited model, Eq. (2.11) will be deemed sufficient to our needs.

If the calorimeter is programmed to raise the sample temperature at a constant rate, the heat flow by time data can be fitted to Eq. (2.11) by the method of Borchardt and Daniels (TA Manual), which assumes that the specific heat is negligible in comparison with the heat evolved due to the reaction. (See Brown, 1988). The results of a typical temperature scan are given in Figure 2.6. The scan rate, β, is 10 °K/min. The curve has no features, such as extra peaks or shoulders which are indicative of side reactions. This appearance of a single reaction mechanism is in contradiction to the discussion above, which pointed out the possiblity tha the reaction may proceed in two or more steps because of differences in the reactivity of the primary and secondary amines. The total area under the curve corresponds to the value of H_o, the total heat of reaction.

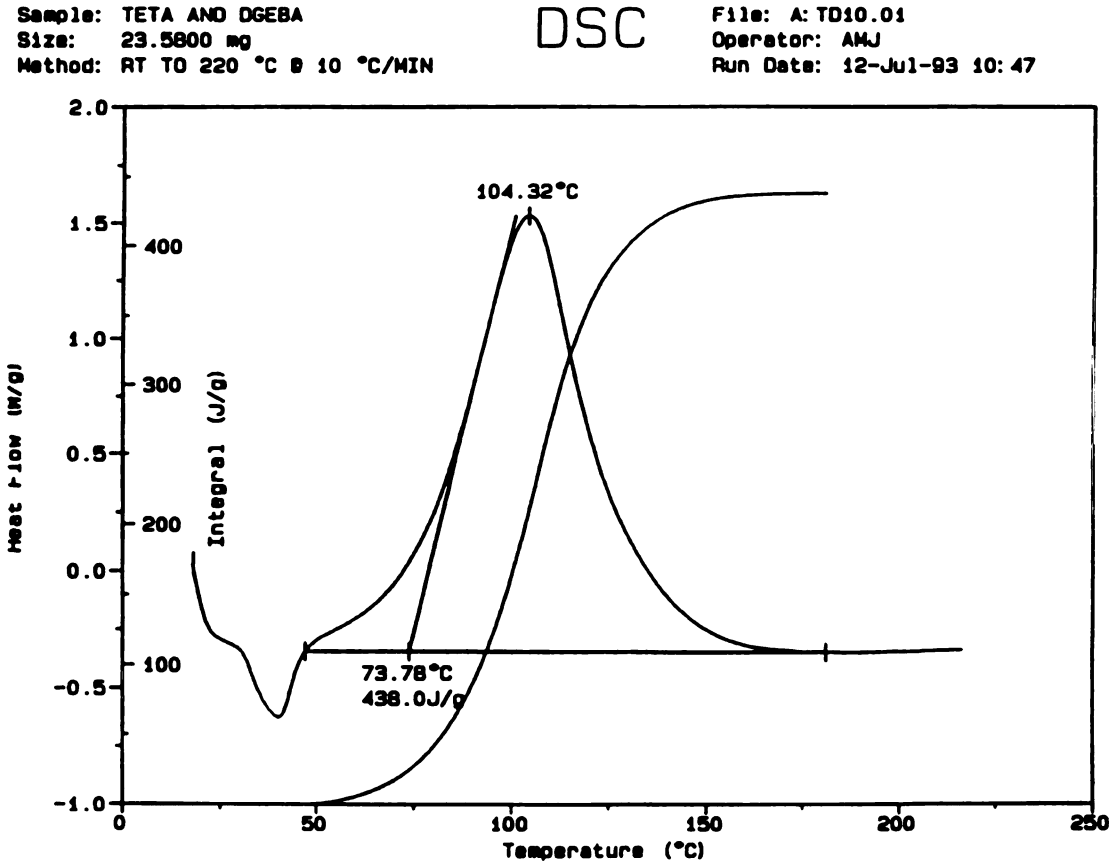


Figure 2.6: Differential Scanning Calorimetry scan of DGEBA/TETA resin system. **Scan** rate = 10° K/min.

The beginning and end of the reaction curve are joined by a horizontal line, the baseline. The fact that the baseline is horizontal indicates that the heat capacity of the reacting resin does not change significantly from the beginning to the end of the reaction. If the baseline were not horizontal, then the changing heat capacity of the sample resin would have to be accounted for in the heat balance. For this analysis, the change in heat capacity throughout the reaction will be ignored.

The DGEBA/TETA system, mixed in stoichiometric ratio of 100:12.9 parts by weight, was subjected to 8 temperature scans at various values of β. Both components were dried in the vacuum oven prior to mixing, and were mixed at 273 °K. Each scan represents a newly mixed batch.

The constants derived by the TA program for these scans are given in Table 2.1. Note that the parameters n, E_a, and k_o appear to vary with β in a systematic way, with the two lowest and two highest scan rates having much higher values for all three parameters than the middle four values of β. This leads to average values of the parameters which have large standard deviations, and which produce a model curve, according to Eq. (2.11), which fits only the reaction where β = 10 °K/min. Figure 2.7 shows the data from the β = 1 °K/min scan, along with the curve generated from the kinetic parameters for that particular scan, and the curve generated from Eq. (2.11), with the average values of the parameters. Other scan rates are depicted in Appendix C.

DISCUSSION

As can be seen in Figure 2.7, the parameters for the individual scan produces a curve which fits the lower half of the reaction very well, but tends to over-predict the heat flow after the peak has been reached. This may be an indication that the reaction is not entirely one mechanism; perhaps the first half of the reaction is dominated by the primary amine reactions, and the second half by the secondary amines, which have a different rate, although not so different as to produce separate peaks. If it is necessary that the kinetic

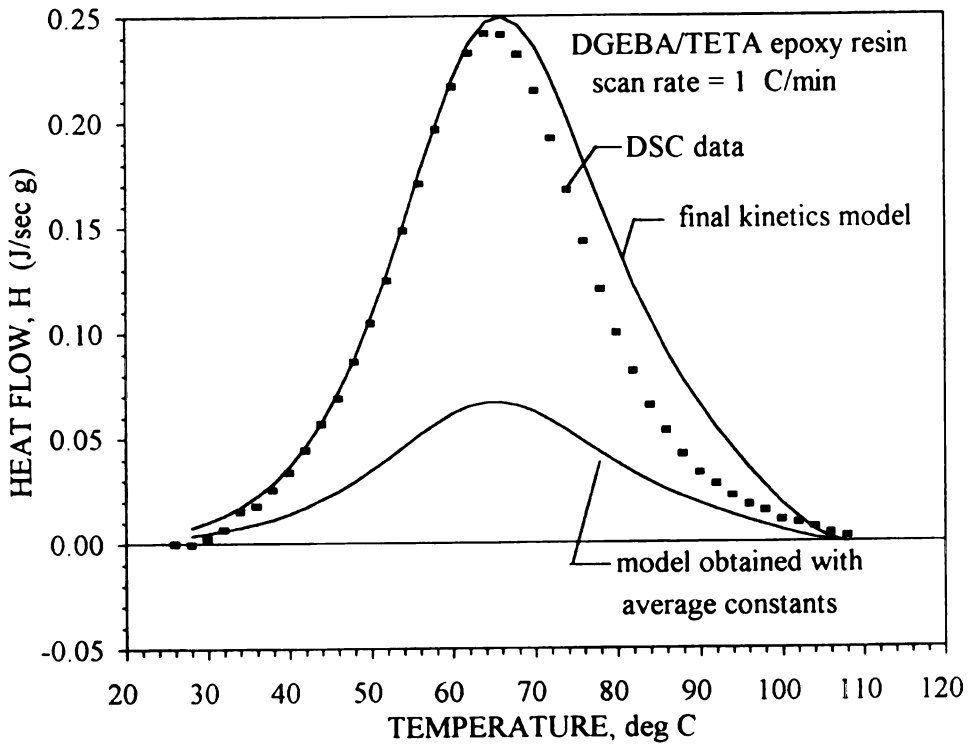


Figure 2.7: Kinetics data and model for DGEBA/TETA resin system.

expression fit the DSC data very well at all times of the reaction, an autocatalytic reaction rate expression might be a better fit:

$$\frac{d\alpha}{dt} = k_o \, exp\left[\frac{-E_a}{R_g T}\right](1-\alpha)^n \alpha^m \qquad (2.13)$$

The term, α^m, being added to express the fact that a secondary reaction becomes important at large values of α. However, since the interest in the present work is in the rate of reaction before the gel point, under isothermal conditions, the rate expression will be taken to be:

$$\frac{d\alpha}{dt} = k(1-\alpha)^n$$

$$\alpha = 1-\left[1-(1-n)kt\right]^{1/1-n}$$

$$k = k_o \, exp\left[\frac{-Ea}{R_g T}\right] \qquad (2.14)$$

$$T\,[=]^\circ K$$

$$k_o = 10^{14.99}\,min^{-1}$$

$$E_a = 103.5 \quad kJ/mole$$

$$R_g = 8.314 \quad J/mole\,^\circ K$$

$$n = 1.58$$

which involves the parameters from the lowest scan rate. This expression leads to a graph of α by time which is shown in Figure 2.8. The gel time of 50 minutes corresponds to α = 0.40.

The Handbook of Epoxy Resins (17-9) states that a typical heat of reaction for epoxy resins is 24,000 cal per mole of epoxy oxygen. For the DGEBA/TETA system, this would be equivalent to 524 J/g, which tends to confirm the finding of 438 J/g, reported above.

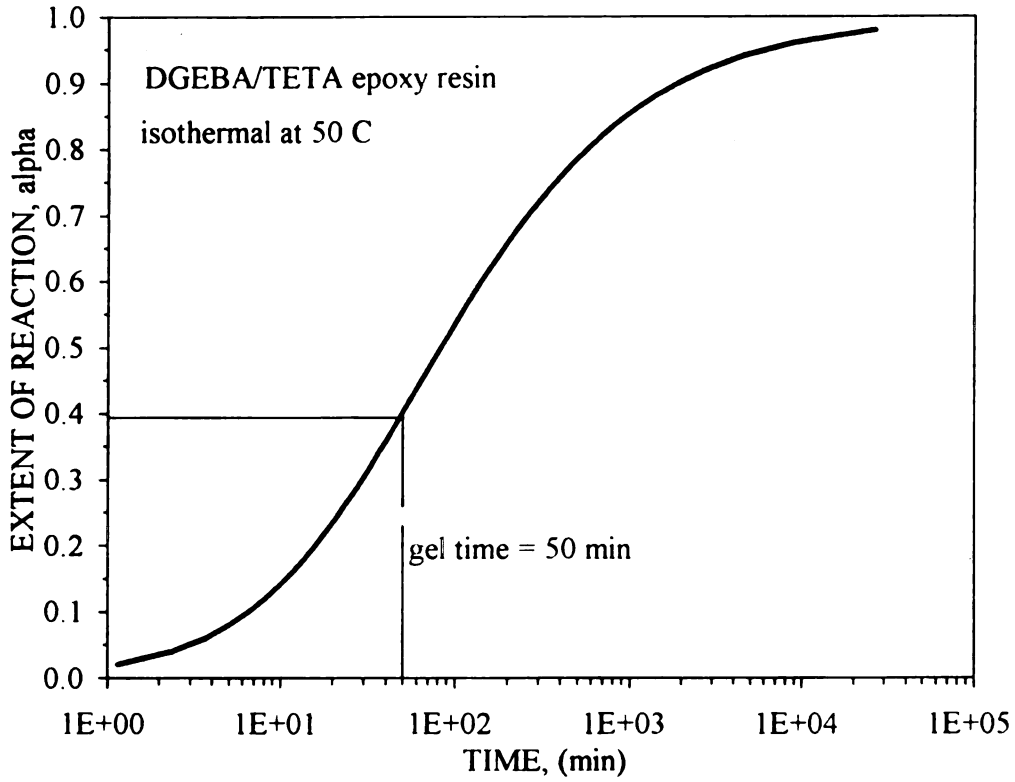


Figure 2.8: Conversion (α) versus time for DGEBA/TETA resin system.

Table 2.1: Kinetics Parameters from DSC temperature Scans.

Scan Rate (°K/min)	n	E_a (kJ/mole)	$\log_{10} k_o$ (1/min)	H_o (J/g)
1	1.58	103.5	15.0	441.4
2	1.56	92.7	13.2	421.0
5	1.08	83.3	11.4	457.2
10	1.11	80.8	10.9	434.6
20	1.02	77.4	10.2	459.8
30	1.04	78.1	10.2	430.1
40	1.58	82.9	10.8	447.3
50	2.05	88.4	11.4	415.2
average	1.38	85.9	11.6	438.3
standard deviation	±0.37	±8.8	±1.7	±16.1
literature values*	1.58	77.8	11.0	216.7

*Kim and Kim (1987).

Kim and Kim (1987) have derived the kinetic parameters of a DGEBA/TETA system of unstated weight ratio with the same method as above. Their values appear in Table 2.1. As can be seen, the values for n, k_o, and E_a are quite comparable to those from the present study. However, the value given by Kim and Kim for H_o is only 49% of that found above. This may be due to a mix ratio which differed from the stoichiometric ratio of the present study. Kim and Kim do not report their mix ratio, but Macosko (1998, pg. 204) states that it is 70% of the stoichiometric amount. This explanation is sufficient to make the value of H_o reported by Kim and Kim 60% (on an equivalent TETA basis) of that reported here. Otherwise, the discrepancy cannot be explained, unless by speculation that the materials used by Kim and Kim were not free of water, or that some heat was lost while mixing. Other investigations of the kinetics of this resin system proved that even when mixing takes place at low temperatures, significant heat can be evolved and lost before the sample is loaded into the DSC.

VISCOSITY OF DGEBA/TETA EPOXY AS A FUNCTION OF α

Macosko (1989) proposed that the viscosity of a reacting crosslinking polyurethane can be modeled as a function of the extent of reaction:

$$\mu = \mu_0 \left(\frac{\alpha_g}{\alpha_g - \alpha} \right)^{(C_1 + C_2 \alpha)} \tag{2.15}$$

where the initial viscosity, μ_0 is a function of temperature, and α_g is the extent of reaction at gelation. Taking the natural logarithm of Eq. (2.15) yields:

$$ln\,\mu = ln\,\mu_0 + C_1\, ln\left(\frac{\alpha_g}{\alpha_g - \alpha} \right) + C_2\, \alpha\, ln\left(\frac{\alpha_g}{\alpha_g - \alpha} \right) \tag{2.16}$$

Using Eq. (2.14) and the data for viscosity as a function of time, discussed above, both at 50 °C, gives a table of data from which the constants C_1, C_2, and α_g can be found through a least-squares regression. The result is:

$$\begin{aligned} \mu_0 &= 0.1011 \quad Pa \cdot sec \\ \alpha_g &= 0.68 \\ C_1 &= 0.417 \\ C_2 &= 17.51 \end{aligned} \tag{2.17}$$

The regression coefficient, $R^2 = 0.998$ indicates that the fit is excellent, and Figure 2.9 echoes this. Note that the extent of reaction at gel is given here as 0.68, which is much higher than that determined from experience, where the gel time is about 50 minutes at 50 °C, which corresponds to $\alpha = 0.40$. This is an indication that the kinetic gel time is not the same as the practical working gel time. Determination of the gel time of the DGEBA/TETA resin is described in more detail below.

THE GEL POINT OF DGEBA/TETA EPOXY

The gel point of a thermosetting material is defined as the reaction conversion at which the weight average molecular weight diverges to infinity. This is chemical gelation, and depends upon irreversible formation of chemical bonds. At this time the viscosity of

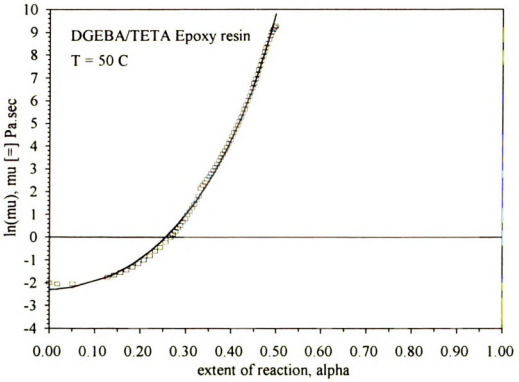


Figure 2.9: Viscosity as a function of extent of reaction for DGEBA/TETA resin system.

the reacting resin also diverges to infinity, but viscosity is a macroscopic phenomenon, and involves reversible physical associations as well as irreversible chemical gelation. Thus, the viscosity may become very high before actual chemical gelation, and physical gelation may produce a weak gel which can be broken up by applying shear.

The gel point is often defined as the point in the reaction when the storage modulus, G' is equal to the loss modulus, G". The complex modulus, G^* is (Tanner, 1985):

$$G^* = \frac{\hat{\sigma}}{\hat{\gamma}} = G' + iG'' \tag{2.18}$$

where shear stress is applied to a sample in a sinusoidal manner, with oscillation frequency, ω, and such that the shear strain, shear stress, and strain rate are given by:

$$\begin{aligned} \gamma &= \hat{\gamma}\, exp(i\omega t) \\ \tau &= \hat{\sigma}\, exp(i\omega t) \\ \dot{\gamma} &= i\omega\hat{\gamma}\, exp(i\omega t) \end{aligned} \tag{2.19}$$

The complex modulus is also related to the complex viscosity:

$$\eta^* = \eta' - i\eta'' = \frac{G''}{\omega} - i\frac{G'}{\omega} \tag{2.20}$$

G'(ω) is known as the storage modulus, and indicates the elastic part of the response of a viscoelastic material to shearing stress. G"(ω) is the loss modulus, and represents the viscous response. As a thermosetting resin develops a molecular network, both the viscous and the elastic response should increase. Since the resin is undergoing a change from a liquid (purely viscous) to a solid (purely elastic) then one would expect that G' should become equal to, and eventually surpass G". The point where it does so is called the crossover point, and is usually taken as the gel point of the system.

Winter (1987) disputes that the crossover point is a reliable indicator of gel point in all cases, saying that the gel point occurs at the G', G" crossover only in stoichiometrically balanced network polymers far away from their glass-transition temperatures. The DGEBA/TETA system was used at the stoichiometric ratio. However, the glass transition

temperature of the system rises throughout the reaction (Wisanrakkit, 1990), and the reaction temperature of 50 °C probably does not exceed the glass transition temperature later in the reaction. Figure 2.10 shows G" data from the RMS8000, taken at the same time as the viscosity data. The G' data are not shown, because they were below the detection limit of the RMS8000 throughout the run. Thus, the G' curve cannot be said to cross the G" curve, and the gel point of this resin system is undetectable by this method.

The gel point of the resin is of interest in designing RTM experiments so that the mold is full before the resin becomes too viscous to flow through the piping and preform. One method of finding the gel time of a given resin system is to find when the surface of the resin will support a certain weight. Alternatively, the surface can be periodically probed with a rod. When the rod can draw long threads of resin from the surface, the gel point is imminent When the surface does not adhere to the rod, gel point is just past. This method was used to determine the gel time as 50 minutes at 50°C, for a plaque kept at constant temperature in an oven. For a resin sample in an aluminum pan, starting at room temperature, the gel time is 65 minutes, as discussed below.

The viscosity of the resin at 50 minutes and 50°C corresponds to 3.7×10^4 Pa·sec calculated by Eq. (2.1). This viscosity is too high for pumping resin through piping or molds, and a more practical working value of gel time might be 30 minutes at 50°C, which corresponds to a viscosity of 32.2 Pa·sec.

THE EXOTHERMIC TEMPERATURE OF EPOXY AND DERAKANE RESINS

The adiabatic temperature rise is defined as the temperature attained by a sample of reacting resin if no heat is transferred to the surroundings. If the heat of reaction (H_o) and the heat capacity (C_p) are known for a reaction system, calculation of the adiabatic temperature rise (ΔT_{AD}) is straightforward:

$$\Delta T_{AD} = \frac{H_o}{C_p} \qquad (2.21)$$

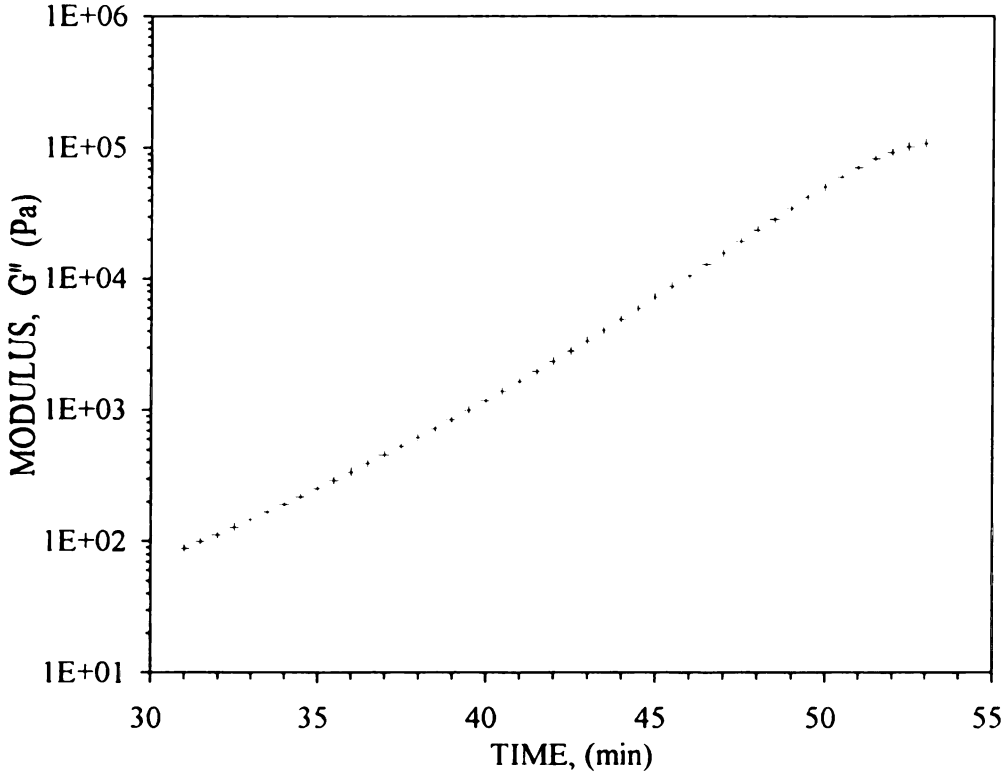


Figure 2.10: Complex shear modulus for DGEBA/TETA resin system.

The Handbook of Epoxy Resins (pg. 17-9)gives a rule-of-thumb value of C_p = 0.3 cal/g °C. If the heat of reaction is 438.3 J/g, as determined below, the adiabatic temperature rise is expected to be 349 °C. However, adiabatic conditions are difficult to produce, so the practical measure of the heat given off by a mass of reacting resin is the exothermic temperature rise. The exothermic temperature rise (as distinct from ΔT_{AD}) of the DGEBA/TETA system and the Derakane system were determined experimentally according to ASTM standard D 2471-71.

To determine ΔT_{exo} experimentally, the resins were mixed at ratios given in Table 2.4, with components starting at room temperature, which was 27 °C. Timing started at first contact of the components, and mixing was carried on through the first three minutes. The reaction vessel was a rectangular aluminum pan, 15.25 cm by 8.9 cm, and the resin stood in the pan to a depth of 2.5 cm. The pan was placed in still air on a sheet of rock wool insulation 2.5 cm thick. A type J thermocouple was embedded in the center of the reacting resin mass, and the temperature was recorded at intervals. In addition, the surface was probed, and the gel point was noted. The resulting data are graphed in Figures 2.11 and 2.12, and results are summarized in Table 2.2.

Table 2.2: Exothermic temperatures for Epoxy and Derakane resins.

Resin components	Total Mass (g)	Peak Temp. (°C)	Gel Time (min)
DGEBA 161.6 g TETA 20.9 g	182.5	215	65
Derakane DMA BPO emulsion	200.2	170	16.5

DISCUSSION

The peak temperatures and gel times for the epoxy and Derakane systems are given in Table 2.2. Note that the epoxy system has a higher exotherm, and longer gel time than the Derakane, although the test parameters were similar. The graph of the reaction temperature by time for the epoxy system (Figure 2.11) shows that the reaction accelerates at about the gel time, and seems to stop producing heat shortly after reaching a peak. The Derakane, on the other hand, gels well before the temperature curve becomes steep.

The adiabatic temperature rise is an intrinsic property of a reacting resin system. However, the exothermic temperature, which is the maximum that may be attained in a mold or other container of resin during reaction, is strongly dependent on the rate of heat transfer to the surroundings. Heat is transferred to surroundings via the surface of a sample of resin, but is generated within the volume of the sample. Therefore, a resin sample with a low surface to volume ratio, or which is insulated from its surroundings will tend to heat up. This rise in temperature will cause the reaction to accelerate, shortening pot life; perhaps causing thermal degradation. Therefore, molding operations cannot be assumed isothermal unless there is large surface area and heat transfer from the resin is good. Thick sections and samples in beakers may generate enough heat to discolor the finished part, or to disfigure plastic containers and mold surfaces. The gel time measured by this method is unlikely to be the same at that of an isothermal reaction, and is given here largely as a measure of useful pot life of the resin.

In Chapter 5, plaques of DGEBA/TETA epoxy were made for the purpose of testing mechanical properties of the finished plaque. These plaques were made approximately 13 mm thick, and were made in a temperature-controlled convection oven. An unsteady heat transfer calculation was made using an implicit finite difference method described in Patankar (1980) to find that if the initial temperature of the reacting mixture

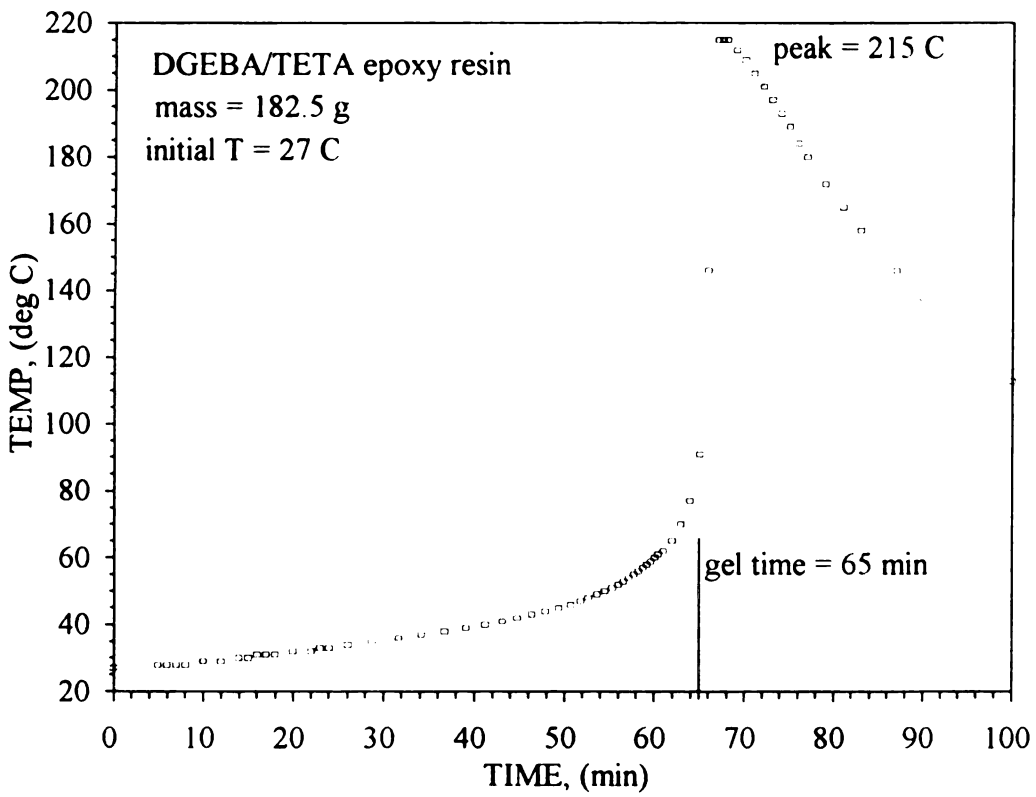


Figure 2.11: Exotherm of DGEBA/TETA resin system.

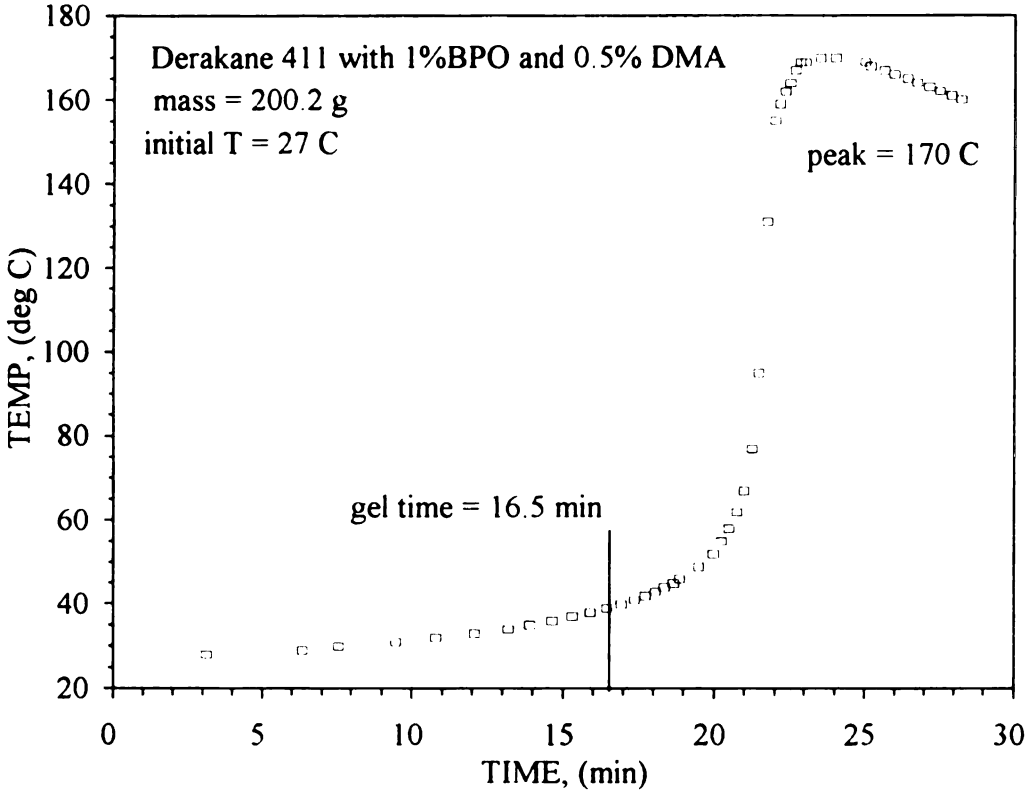


Figure 2.12: Exotherm of Derakane® resin system.

is 50 °C, and the edges of the plaques are all kept at 50 °C, then the temperature at the center of the plaque peaks at 59 °C, about 4 minutes into the reaction. This temperature excursion was deemed unlikely to be detrimental to the plaques.

DETERMINATION OF A SUITABLE CURE CYCLE FOR DGEBA/TETA

The Dow Chemical Co.'s literature on the DGEBA/TETA system gives the recommended cure cycle as 2 hours at 100 °C or several days at room temperature. This implies that full cure is achieved even at low temperatures, given sufficient time. Wisanrakkit (1990) shows that when the glass transition temperature of the system (which increases as the resin cures) equals the reaction temperature, the reaction becomes diffusion limited, and the reaction rate becomes very low, though not zero. Thus, it is necessary to determine an acceptable cure cycle for a resin system to achieve fully cured parts. The extent of cure of the DGEBA/TETA resin system after 3 different cure cycles was determined using the Differential Scanning Calorimeter (DSC).

DGEBA and TETA were mixed in the weight ratio of 100:12.9, and three groups of four DSC sample pans were made up. The first group of samples was stored at room temperature (≈25 °C) for two days, then subjected to a temperature scan of 10 °C/min in the DSC. The heat evolved by the samples during the temperature scan was calculated from the DSC run, and used to calculate the extent of cure of the resin as follows:

$$\alpha_{residual} = 1 - \frac{\int_{2\,days}^{\infty} H dt}{H_o} \qquad (2.22)$$

Where H_0 is the heat of reaction, 438.3 J/g, as discussed above, and the integral in the numerator represents the heat evolved during the DSC scan.

The second group of samples was put into the oven at 50 °C for 2 hours, then stored at room temperature for 2 days, and the third group was cured at 100 °C for three hours before the DSC scan. Results of these runs are presented in Table 2.3.

Table 2.3: Residual cure of DGEBA/TETA resin.

Cure Cycle	T_g (° C)	Heat evolved (J/g)	Extent of cure $\alpha_{residual}$
2 days @ 25 °C	44.6 ± 0.16	97.54 ± 3.1	0.78 ± 0.007
2 hrs @ 50 °C, plus 2 days @ 25°C	60.3 ± 0.93	35.38 ± 2.58	0.92 ± 0.006
3 hrs @ 100 °C	92.1 ± 6.1	undetectable	1.00

Figure 2.13 shows a typical thermogram from the second group of samples. There is an endothermic event with an onset temperature of 60.87 °C, and this is interpreted as the glass transition temperature of the partially cured sample. Note that T_g is greater than 50 °C, thus showing that the T_g can exceed the reaction temperature, given time. Or, alternatively, showing that the reaction advances despite diffusion limitation. The first group also shows a T_g that exceeds its reaction temperature, but the third group shows a T_g that is less than the reaction temperature, at 92 °C.

Table 2.3 shows that the cures can advance at room temperature, since the first group of samples achieved 78% cure in two days. However, the second group had not achieved full cure 2 days after their treatment at 50 °C, and so samples used for mechanical testing should be either post-cured at 100 °C, or allowed at least a week at room temperature to complete the cure, and achieve final mechanical properties.

MEASUREMENT OF VOLUME CHANGE DURING REACTION FOR DGEBA/TETA AND DERAKANE RESINS

Epoxy resins in general undergo a net decrease in volume from the beginning to the end of the reaction. This volume change is typically 3 to 5%, and must be accounted for when designing molds for high precision parts. (Handbook of Epoxy Resins, pg. 17-12). Cured epoxy resins also undergo volume changes due to temperature changes. The thermal coefficient of expansion for epoxy resins is given as 0.001 in/in of length (ibid., pg. 6-31). When materials with dissimilar coefficients of thermal expansion are bonded to one another, changes in temperature will cause them to exert stress on one another, as

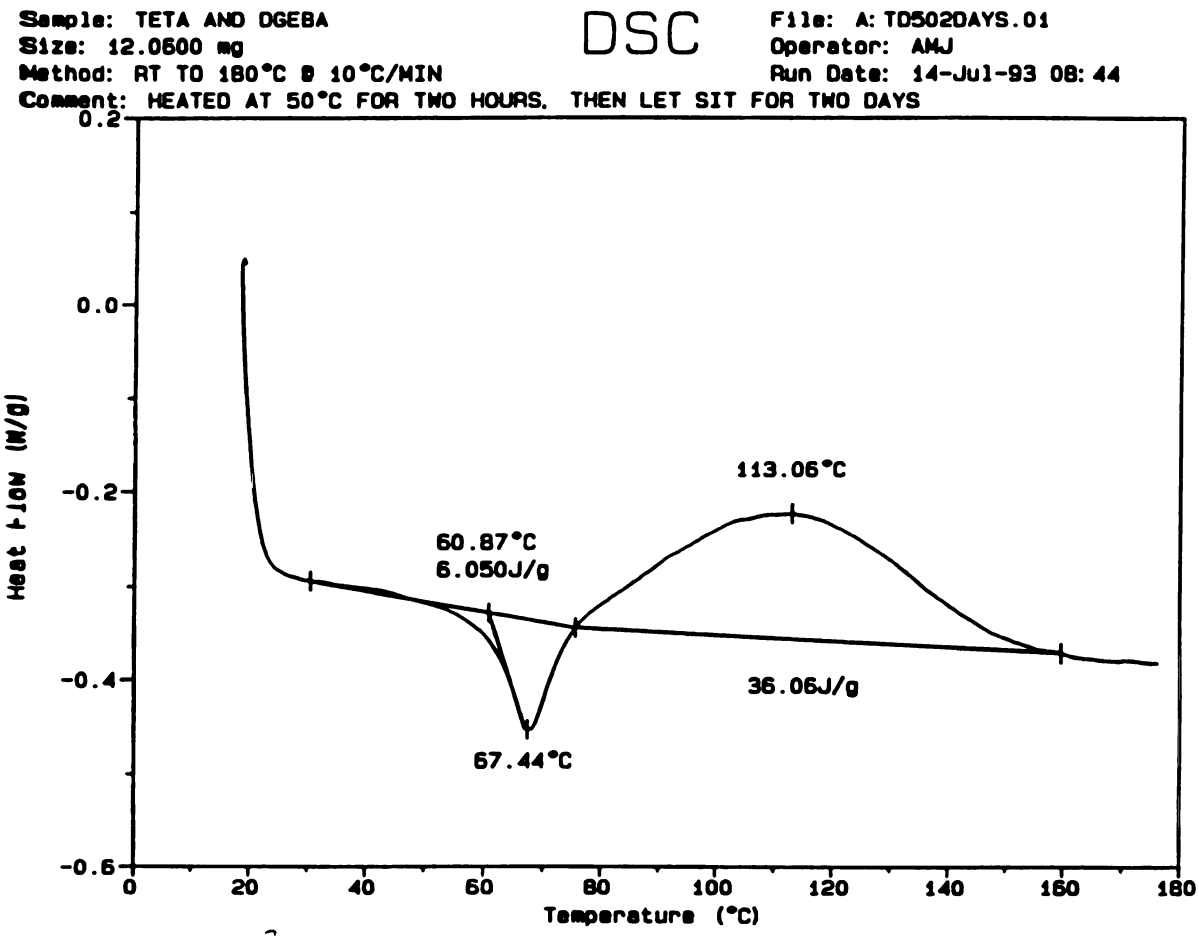


Figure 2.13: DSC scan of DGEBA/TETA sample cured for 2 hours at 50° C.

their volumes do not change at the same rate. Bi-metallic thermometers take advantage of this phenomenon. However, the stresses that arise can be so great between thermosetting resins and glass or carbon fiber reinforcements as to degrade the strength of the bond between them, leading to lower mechanical properties.

The specific volume of DGEBA/TETA and Derakane systems was measured throughout the curing reaction by means of a modified dilatometer, shown in Figure 2.15. The resins were mixed according to Tables 2.4 and 2.5, then each sample was loaded into a latex rubber balloon, which was closed and weighed. Each balloon was then enclosed in a dilatometer with a known mass of distilled water, the height of which was read on the pipette immediately. Dilatometers were then suspended in a thermostat bath (50 °C for DGEBA/TETA, and 25 °C for Derakane), and readings of the height of the water in the pipette were taken at timed intervals. The balloon served as a flexible container so that the volume of the resin could change freely, without the resin adhering to the glass container, or being contaminated by the working fluid. Each set of samples included a blank containing only water, so that the effects of the volume change of the working fluid could be calculated out. The height of the water in the pipette was recorded to ± 0.05 cmby means of a vertical cathetometer. Temperature of the thermostat bath was kept to within 0.2 °C of set point by a temperature controller.

Figures 2.15 and 2.16 show the results given as specific volume, normalized to the original volume of the resin, as a function of time. In the case of the Derakane resin, the normalized volume of the blank is also shown. This is constant at 1.00. The blank in the DGEBA/TETA run leaked during the run, and volume changes due to the volume of water inside the dilatometers were subtracted out by using handbook values of the density of water.

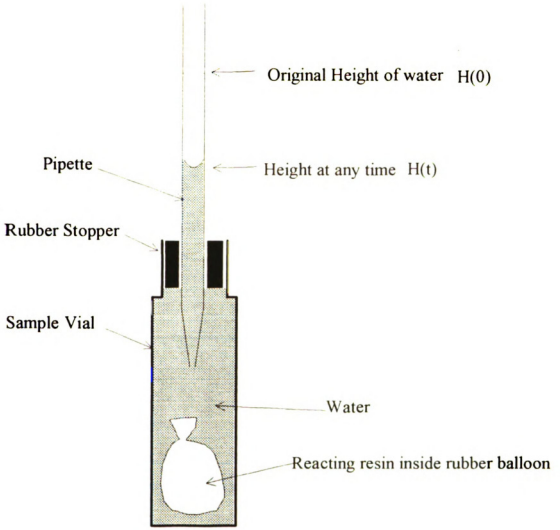


Figure 2.14: Dilatometer, an apparatus for measuring volume of reacting resin.

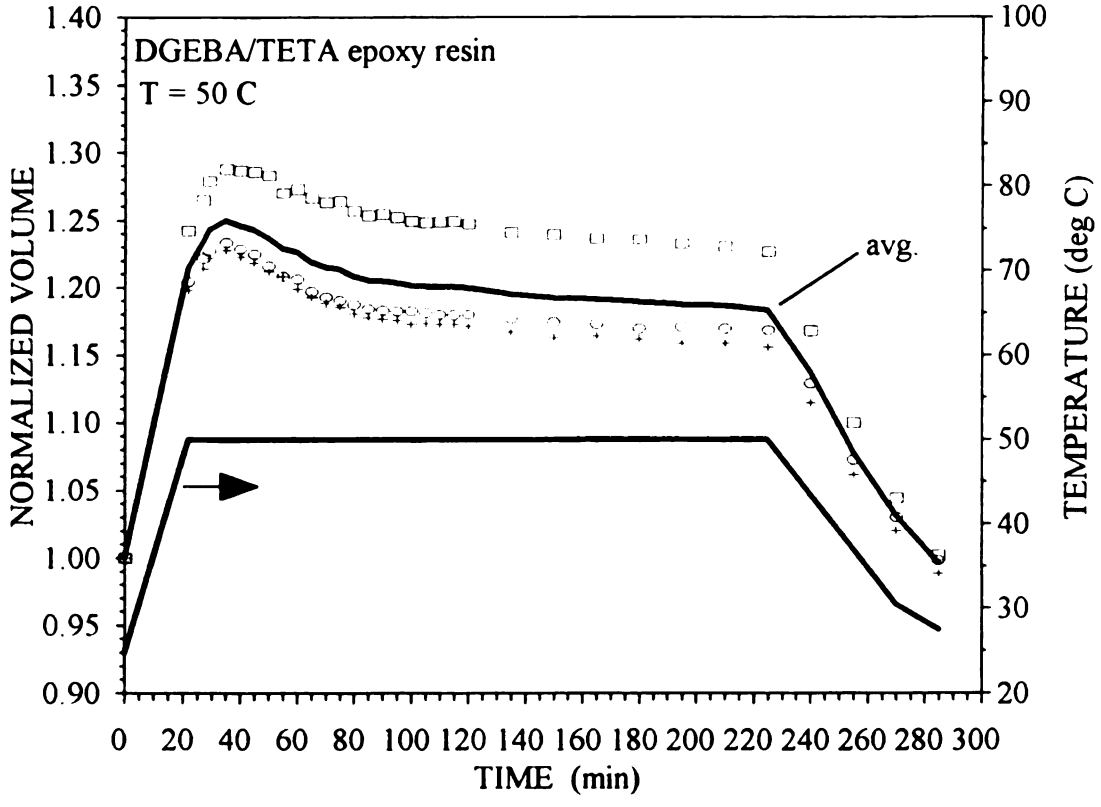


Figure 2.15: Volume profile of DGEBA/TETA resin system during cure.

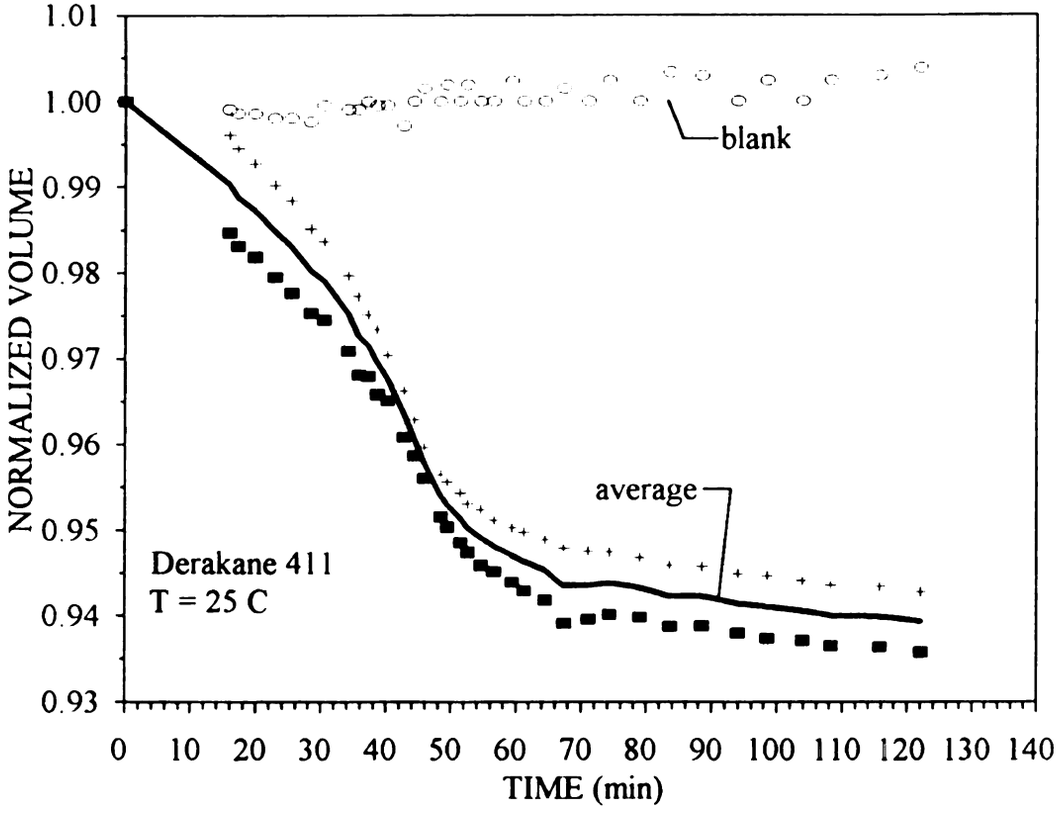


Figure 2.16: Volume profile of Derakane® resin system during cure.

RESULTS

The DGEBA/TETA system shows an increase in specific volume due to the resin coming to 50 °C. The volume then further increases during the first part of the reaction, until just before the gel point. Then the volume decreases steadily until the temperature of the bath begins to drop. The overall volume change, from fluid resin at room temperature to solid resin at room temperature is -0.3%. However, during the reaction, the specific volume increases as much as 25%, and this is compensated for by some polymerization shrinkage, and by about 18% shrinkage due to temperature drop at the end of the run. The coefficient of thermal expansion can be calculated from the part of the specific volume curve where the temperature is decreasing by first calculating the volume shrinkage (S_V) over the temperature range, using that to find the linear shrinkage (S_L), and then dividing by the associated temperature change.

$$S_V = \frac{V_2 - V_1}{V_1}$$

$$S_L = -1 + \sqrt[3]{1 + S_V}$$

$$C_t = \frac{S_L}{T_2 - T_1} \qquad (2.23)$$

Where C_t is the coefficient of thermal expansion, (cm/cm/ °C). For the DGEBA/TETA system, the value of C was measured as 0.0023 cm/cm/°C.

The Derakane reaction was run at 25 °C, so there was no opportunity to measure the coefficient of thermal expansion. Figure 2.16 shows the profile of the specific volume by time. The specific volume decreases monotonically through the reaction, although the rate of decrease changes at around 45 minutes. The net volume change is 6% from liquid reactant to solid resin.

Thus, the DGEBA/TETA system is a low shrinkage system, at -0.3% volume change, in comparison with the Derakane resin, at -6% volume change.

Table 2.4 summarizes the findings of the characterization of the DGEBA/TETA resin system. These results will be used to calculate viscosity gradients and mobility ratios in Chapter 6, and will be used to compare material testing results in Chapter 5. Derakane properties are reported in Table 2.5, and are used in Chapter 2 where fingering flow experiments with Derakane resin are reported. Some of the material properties in Tables 2.4 and 2.5 are obtained from the literature, and sources are noted where applicable.

Table 2.4: Summary of results of DGEBA/TETA epoxy resin characterization.

Resin property		Source
Recipe	100 parts by wt. DGEBA (Diglycidyl Ether of Bis-phenol A) 12.9 parts by wt. TETA (Tri-Ethylene Tetramine)	
viscosity, $\mu(t)$ t in minutes μ in Pa·sec.	$\mu(t) = \mu_0 A t \left[\frac{t_c}{t_c - t}\right]^{(B+Ct)}$ $T = 50°C$ $\mu_o = 0.1096 \ \ Pa \cdot sec$ $t_c = 65 \ \ min.$ $A = 1.7069 \ \ min^{-1}$ $B = -109.63$ $C = 1.1922 \ \ min^{-1}$	Measured, Ch. 2
Kinetics, $\alpha(t,T)$ t in minutes T in °K	$\frac{d\alpha}{dt} = k(1-\alpha)^n$ $\alpha = 1 - \left[1 - (1-n)kt\right]^{1/1-n}$ $k = k_o \, exp\left[\frac{-Ea}{R_g T}\right]$ $T\,[=]°K$ $k_o = 10^{14.99} \, min^{-1}$ $E_a = 103.5 \ \ kJ/mole$ $R_g = 8.314 \ \ kJ/mole\,°K$ $n = 1.58$	Measured, Ch. 2
Gel time, t_g, min.	50 min @ 50 °C, isothermal 65 min @ exotherm 25 to 215 °C	Measured, Ch. 2

Table 2.5: Continued.

Resin property		Source
Viscosity, $\mu(\alpha(t,T))$	$\mu = \mu_o \left(\frac{\alpha_g}{\alpha_g - \alpha} \right)^{(C_1 + C_2\alpha)}$ $\mu_o = 0.1564$ Pa · sec $\alpha_g = 0.59$ $C_1 = -4.902$ $C_2 = 40.47$	Measured, Ch. 2
Exotherm, °C.	215	Measured, Ch. 2
Specific volume change, liquid to solid	-0.3% -3 to 5%	Measured, Ch. 2 Handbook* pg. 17-12
Specific volume, solid	1.2 - 1.3	Handbook* pg. 6-33
Specific volume, liquid	0.988 @ 50° C 1.087 @ 25° C	Calculated, Ch. 2
Thermal coefficient of expansion, cm/cm ·°C	0.0023 0.001	Measured, Ch. 2 Handbook* pg. 6-31
Heat capacity C_p, cal/g·°C	0.3	Handbook* pg. 17-19
Thermal conductivity cal/(sec·cm^3·°C)	0.500×10^{-3}	Handbook* pg. 6-32
Tensile strength σ^*, MPa	60. ± 4.8 62.1	Measured, Ch. 5 Handbook* pg. 7-10
Young's modulus E_t, GPa	0.92 ± 0.03 3.27	Measured,Ch. 5 Handbook* pg. 7-10
Flexural modulus E_b, GPa	2.4 ± 0.10	Measured, Ch. 5
Strain to break ε^*, %	6.3 ± 0.66	Measured, Ch. 5
Possion's ratio ν, cm/cm	0.34	Handbook* pg. 6-25

* Handbook of Epoxy Resins (1967)

Table 2.5: Results of Derakane 411 resin characterization.

Resin Property		Source
Derakane 411 (vinyl ester resin)	98 parts by weight Derakane® 411 resin 2.5 parts by weight BPO emulsion (40 wt% Benzoyl Peroxide in reactive diluent) 0.1 parts by weight DMA (DiMethyl Aniline)	
Viscosity, μ(t) t in minutes μ in Pa·sec.	$\mu = \mu_o + At + B ln\left(\frac{t_c}{t_c - t}\right) + Ct\, ln\left(\frac{t_c}{t_c - t}\right)$ $T = 20°C$ $t_c - 19.5$ min $\mu_o = 0.4713$ Pa · sec $A = -0.1536$ Pa · sec / min^{-1} $B = 3.0254$ Pa · sec $C = -0.09017$ Pa · sec / min^{-1}	Measured, Ch. 2
Gel time, minutes	18 min @ 25 °C, isothermal 16.5 min @ exotherm 25 to 170 °C	Measured, Ch. 2
Exotherm, °C	170	Measured, Ch. 2
Volume changes, liquid to solid, %	-6 -4 to -8	Measured, Ch. 2 Hull (1981)
Tensile strength σ*, MPa	76 to 83	Dow product lit.
Young's modulus E_t, GPa	3.38	Dow product lit.
Flex modulus E_f, GPa	3.90 3.10	Measured, Ch. 4 Dow product lit.
Poisson's ratio, ν, cm/cm	0.37 to 0.39	Hull (1981)
Elongation at failure %	5.0 to 8.0	Dow product lit.

CHAPTER 3

CHARACTERIZATION OF THE POROUS MEDIA

INTRODUCTION

The nature of a porous medium will have a strong role in the formation or suppression of fingers in fluids flowing through it, inasmuch as the porous medium will 1) increase the tendency of the fluid interface to finger by increasing the interstitial flow velocity of fluid, 2) tend to mitigate the viscosity gradient through dispersion, thus suppressing fingers and 3) determine the shape and size of fingers through the size and connectivity of the pore structure.

For example, in fused rock, where pores are twisty little tubes with few interconnections, fingers will tend to have widths on the order of a tube diameter or two, with little transverse dispersion. On the other hand, where the porous medium is basically one big flow channel criss-crossed with fiber bundles, the finger can have larger widths, and there will be comparatively more transverse dispersion. As discussed in Chapter 1, Tan and Homsy (1986) have shown that the tendency of miscible flows to form viscous fingers is damped when the transverse dispersion is large compared to the longitudinal dispersion. Literature values for dispersion coefficients exist mainly for particulate porous media, and are not assumed, a priori, to have application to fibrous porous media.

It is expected that the permeability and dispersiveness of a preform will have a strong influence on the tendency of viscous fingers to form in RTM flows. For this reason, the measurement of the permeability and dispersion coefficients for three porous media are herein described. These porous media are the Hele-Shaw cell (no preform), the Unifilo random swirl mat, and the Hexcel woven glass mat. These three porous media are

identical to those used for the experiments described in Chapters 4 and 6. The sources and particulars of the glass preforms are given in Appendix A. The Hele-Shaw cell is described as a porous medium, because, as described below, flow through two flat plates spaced close together (the Hele-Shaw cell) is described by an equation identical to Darcy's law.

The following sections consist of physical descriptions of the fiber mats, including the calculation of the fiber volume fraction, then the discussion of the permeability measurements, and finally the discussion of the dispersion coefficient measurements.

DESCRIPTION OF POROUS MEDIA

Figure 3.1 is a schematic of the structures of the random swirl and the plain weave fiber mats. The random swirl mat consists of long tows of E-glass fibers laid down in a swirl pattern, and held together at tow junctions by a binder which is more or less soluble in the resin. For the present work, the binder was known to be slightly soluble in styrene, which is a major component of Derakane resin. The solubility in the DGEBA/TETA resin system was unknown, but was presumed to be slight. The tows are laid down in a random pattern in the x-y plane, but the z direction is made up of layers of tows deposited one onto another, and has a layered appearance when viewed from the edge. Interstitial spaces are large compared to the tow diameters, and there are few dead-end flow paths. It is expected that the permeability of this mat will be isotropic in the x-y plane, if the tow pattern is truly random. The permeability in the z direction will not be measured.

The woven mat consists of E-glass fiber tows laid parallel to each other, then woven with similar tows. The weave pattern is plain, or simple one over, one under. The warp, or machine direction, contains 16 tows per inch, and the woof, or cross direction, contains 14 tows per inch. The inter-tow spacing is about 1 mm, by inspection, and is about the same as the widths of the tows. Since the two fabric directions contain different numbers of tows, it is expected that the fabric will have permeability that is not isotropic,

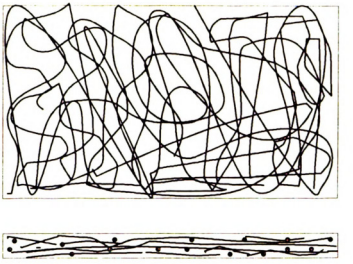


Figure 3.1: Schematic of glass mats for preform.

but which will be orthotropic with the two principle directions coinciding with the tow directions in the fabric.

DETERMINATION OF THE FIBER VOLUME FRACTION

The fiber volume fraction (V_f) is a measure of the volume of the mold or the finished part that is occupied by the material of the preform, in this case, glass. The porosity of the preform is the volume of the mold not occupied by the fiber, $\varepsilon = 1\text{-}V_f$. Likewise, volume occupied by the resin in the finished part is $V_r = 1\text{-}V_f$, if there are no voids.

$$V_f = \frac{\text{mass of preform}}{(\text{volume of mold})\ (\text{density of fiber})} \qquad (3.1)$$

The density of the glass fiber used in this study was taken as the handbook value for E-glass: 2.56 grams/cm^3.

Each preform is compressible in the mold to some degree. The maximum V_f attainable varies with the preform according to how tightly the preform can be compressed in the mold, without causing the mold to be deformed or to leak. In the mold used in the present work, the Plexiglas top was apt to bow if there was too much preform in the mold. Typical fiber loadings in the mold are shown in Table 3.1.

Table 3.1: Typical preform volume fractions.

Preform type	No. plies	Volume fraction of fibers, V_f (mold = 0.3 cm thick)	Porosity, ε (mold = 0.3 cm thick)
None	0	0	1.0
UNIFILO RANDOM SWIRL MAT	3	0.20	0.80
HEXCEL WOVEN MAT	12	0.45	0.55

DETERMINATION OF THE PREFORM PERMEABILITY

The most common description of flow through a porous medium is Darcy's Law, which states that the velocity of flow through a porous medium is proportional to the pressure drop acting to drive the fluid, and inversely proportional to the viscosity of the fluid. Darcy's Law can be inferred from the equations of motion, using the assumptions that the flow is steady and fully developed, gravity forces are unimportant, and that the fluid is Newtonian.

$$v_x = -\frac{\kappa}{\mu}\frac{dP}{dx} \tag{3.2}$$

Where v_x is the interstitial velocity, μ is the fluid viscosity, and P is the pressure.

The factor, κ, is the permeability of the flow channel. In the open rectangular channel, $\kappa = h^2/12$, but in porous media, the permeability depends upon the area open to flow, and specific details of the flow paths.

The Blake-Kozeny Equation is another expression for the velocity of flow in a packed bed of porosity ε. (Bird, et al, 1965)

$$v_o = \bar{v}_x\varepsilon = -\frac{d_p{}^2\varepsilon^3}{150(1-\varepsilon)^2}\frac{(P_2 - P_1)}{\mu L} \tag{3.3}$$

Where d_p is a particle diameter based on the ratio of the surface to the volume of the particle, and ε is the porosity of the packed bed. The Blake-Kozeny Equation is a valid predictor of the value of the permeability of a packed bed when the packing has a particle nature, the flow is laminar, and the porosity is less than 0.5. The first term of Eq. (3.3) can be likened to the permeability in Darcy's Law, so that where the Blake-Kozeny equation is valid, the permeability of the porous medium can be expressed as:

$$\kappa = \frac{d_p{}^2\varepsilon^2}{150(1-\varepsilon)^2} \tag{3.4}$$

However, in liquid molding flows, the porous medium is generally fibrous, and the porosity is anywhere from 0.20 to 0.70. The requirement of laminar flow is easily met in

liquid molding flows, but the Blake-Kozeny equation is inadequate for describing the permeability of complex fibrous porous media, which usually have a macroscopic, or intra-tow length scale as well as a microscopic or inter-tow length scale. Thus, permeability of the preforms used in this study were determined empirically, following the method of Chan (1991), as described hereinafter.

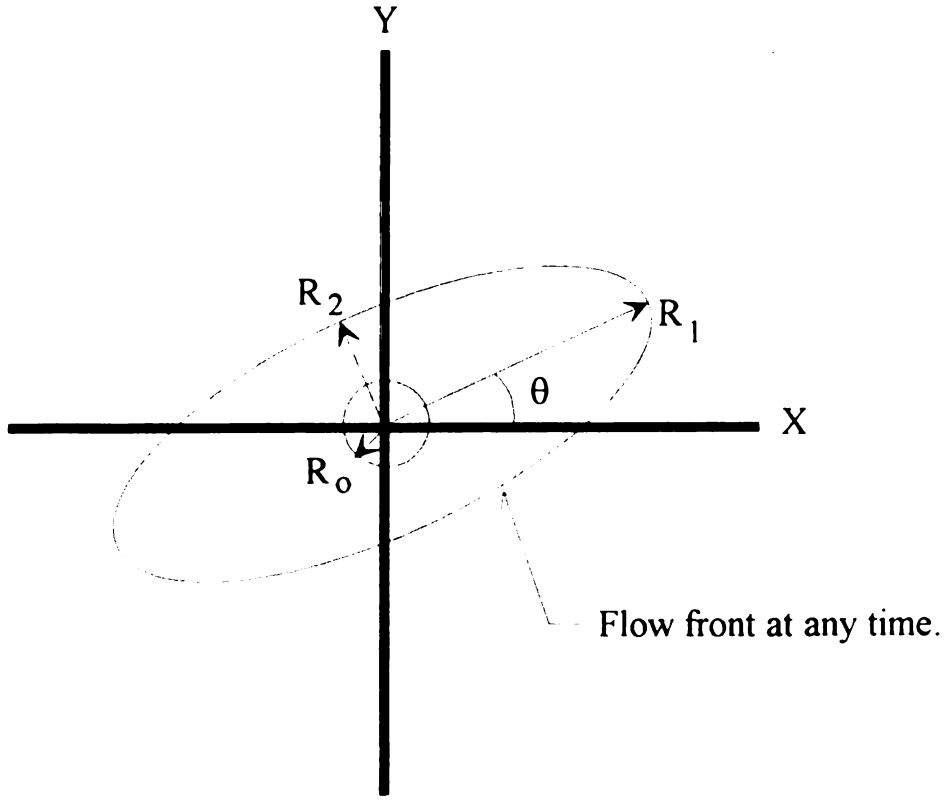
If the flow is two-dimensional, or the porous medium is anisotropic in two dimensions, the above equations can be expanded into matrix form, and the permeability tensor becomes:

$$\kappa = \begin{pmatrix} K_{xx} & K_{xy} \\ K_{yx} & K_{yy} \end{pmatrix} \tag{3.5}$$

The permeability can also be expanded to three dimensions, if required, but the nature of the preforms treated below allows the use of two dimensions by virtue of the fact that the thickness of the mold is small, and there is no z-component to the flow.

The permeability tensor is symmetric, and if the x-y coordinate system coincides with the principle axes of the porous medium, then the off-diagonal terms are zero, and only the principal components of the permeability tensor must be sought (Chan 1991).

Chan describes a method of determining the components of the permeability tensor for preforms that are isotropic, orthotropic, or anisotropic. They also give the standard method of rotation if the principal axes of the preform do not coincide with the laboratory coordinate system. The method is based on obtaining data on the major and minor axes of an oval flow front of fluid into the preform, as a flat plaque mold is filled from the center. Figure 3.2 shows the nomenclature and the most general situation: anisotropic, with principal axes of flow not coincident with laboratory axes. Special cases occur if the flow front is oriented such that the angle, θ, is zero, when the preform is orthotropic; and if the



Special Cases:

Isotropic: $R_1 = R_2$ and $\theta = 0$

Orthotropic: $\theta = 0$

Anisotropic: $R_1 \neq R_2$ and $\theta \neq 0$

Figure 3.2: Permeability measurement, coordinates and definitions.

flow front is circular, when the preform is isotropic. Appendix B gives the details of the derivation of the method of measuring the permeability which is described below. The result is a relation between an equivalent permeability and observable experimental quantities. The equivalent permeability can then be related to the components of the permeability tensor, K_{xx} and K_{yy}. The method involves measuring the major and minor axes of an oval flow front at several time intervals in a permeability run. Data of the length of the axes (D_x and D_y) taken in a flow experiment represent matched sets of x, y, t data. A graph of D_x versus D_y should be a straight line, passing through zero, and having a slope of $m_1 = (K_{yy}/K_{xx})^{1/2}$, as shown in Figure 3.3.

The equivalent permeability, K_e can be found through a graph of $F(D_x)$ versus t data, where $F(D_x)$ is defined as:

$$F(D_x) \equiv \left(\frac{D_x}{D_o}\right)^2 \left(2\,ln\left(\frac{D_x}{D_o}\right) - 1\right) + 1 = \frac{16 K_e \Delta P}{\varepsilon \mu \left(K_{yy}/K_{xx}\right)^{1/2} D_o^{\,2}} t \qquad (3.6)$$

Where D_o is the diameter of the inlet port. This graph, shown in Figure 3.4 should yield a straight line with a slope, m_2, equal to the first term on the right hand side, and an intercept passing through zero if t = 0 when $D_x = D_o$. If the other quantities are known experimentally, then K_e can be calculated from the slope, m_2, and the components of κ are:

$$K_{xx} = \frac{K_e}{m_1}$$
$$K_{yy} = K_e m_1 \qquad (3.7)$$

The permeabilities of two preforms were measured according to the following procedure.

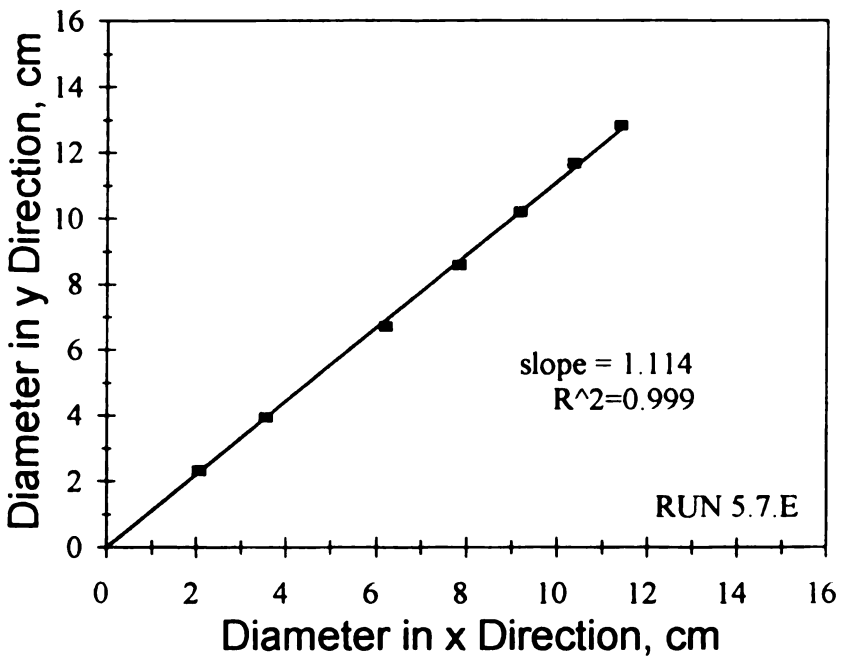


Figure 3.3: Data from permeability run 5.7.E, graphed as radius in x direction versus radius in y direction.

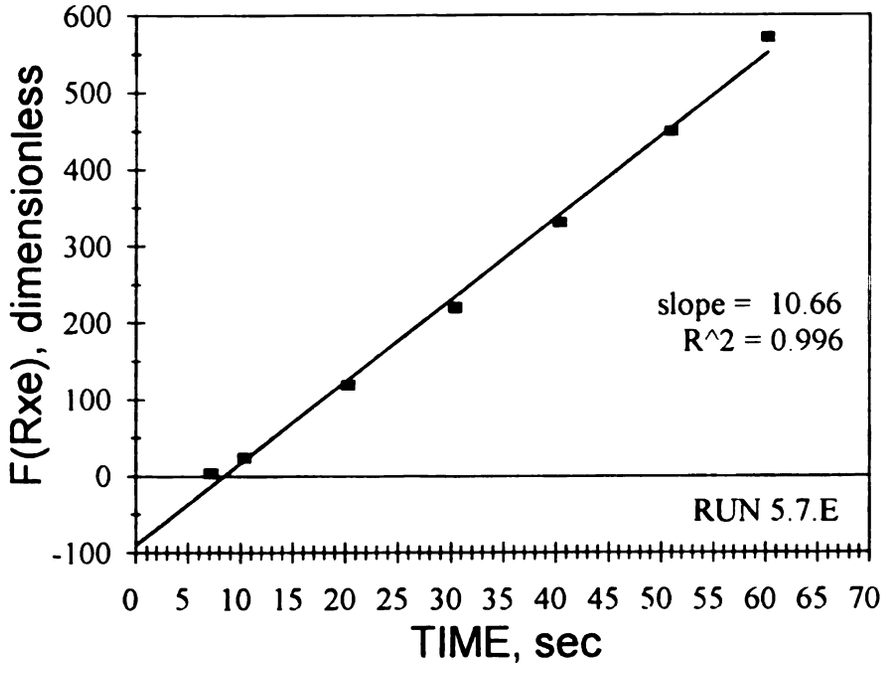


Figure 3.4: Data from permeability run 5.7.E, graphed as $F(R_{xe})$ versus time.

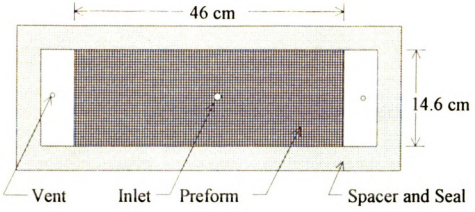
MEASUREMENT PROCEDURE

A flow cell consisting of two flat plates separated by a narrow gap was filled with a porous medium. See Figure 3.5. Fluid of known viscosity was injected into the cell, normal to the bottom plate, under a known pressure drop. The fluid spread in an oval centered on the injection port, (R_0 = 0.476 cm) and a time series of photographs of the flow front was made through the transparent top plate of the cell. From the photos, the major and minor axes of the oval were measured. The timer was not started in such a way that zero time was marked when the fluid first entered the cell.

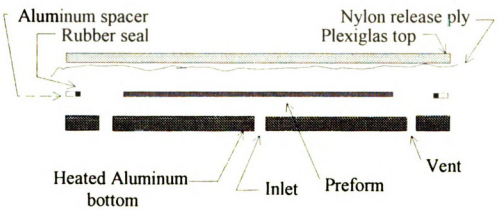
The fluid used was Indopol L-50, a polybutene from Amoco. Full specifications may be found in Appendix A. The viscosity of the polybutene was measured both before and after the flow measurements, using a Brookfield Viscometer, at a lab temperature of 22° C, and was found to be 0.290 Pa·sec. The viscosity was measured at multiple rotation rates to show that it was not affected by the magnitude of the shear rate, and so could be considered a Newtonian fluid for these experiments. Polybutene was chosen because it does not absorb water from the atmosphere, as glycerol does, so that the elaborate drying procedures necessary when using glycerol were avoided. The polybutene was dyed with Oil Red, an oil-soluble dye from Aldrich Chemical Co.

The air pressure in the fluid reservoir was controlled through a regulator. The pressure of the fluid in the tubing was measured just up-stream of the cell inlet by a pressure transducer. The transducer was accurate to 0.2 psig (1.38 kPa). The pressure did not vary noticeably throughout any given run, once the valve to the flow cell was open. The pressure pot and valves are shown schematically in Figure 3.6

Measurements were made in a flow cell which contained no preform, as well as with preforms consisting of 3 plies of random swirl mat from Unifilo, and 12 plies of a woven glass mat from Hexcel Corp. All plies were oriented in the cell with the machine direction of the fabric coincident with the long (x) axis of the mold. Fiber volume fraction was determined by weighing the plies before they were placed in the cell, then calculating the



Plan View



Exploded Cross Section

Figure 3.5: Schematic of flow cell for permeability measurements.

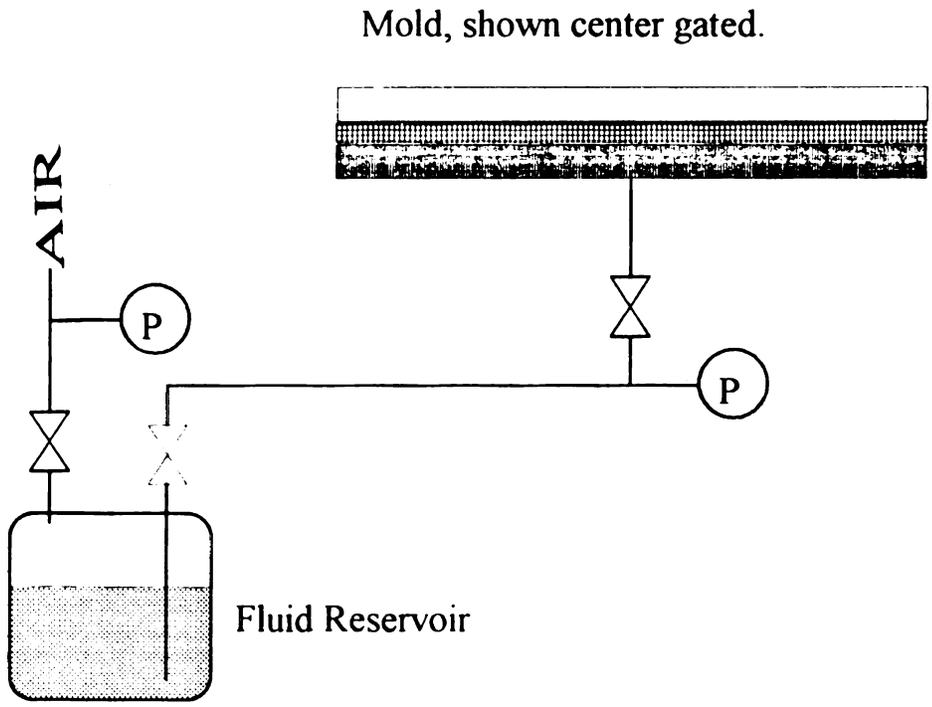


Figure 3.6: Apparatus for constant pressure injection.

volume which they occupied with the cell fully clamped according to Eq. (3.1). The cell thickness was measured using a micrometer inserted between the top and bottom plate when the mold was fully clamped. Ten measurements yielded and average of 3.00 mm ± 0.12. Plies were cut to have dimensions of 14.6 cm width and 22.9 cm length. Again, full specifications on the preform fabrics is available in Appendix A.

DATA COLLECTION AND SAMPLE CALCULATIONS

Figure 3.7 shows a photograph which is typical of the measurement runs. The fluid is visible as a dark area at the center, and superimposed on the cell face are the run number, the timer face, and a grid of 1 cm squares. The rubber seals are visible at the top and the bottom of the photograph, and the x direction is parallel with these.

It was found that the enlargement of the photograph in the x direction was not to the same scale as the enlargement in the y direction, so, for each series of photographs, scale factors were formulated using the 1 cm grid as a basis. Values are reported as diameters rather than radii, because of the difficulty of reproducing the location of the center of the cell from one photo to another.

The data table from the run depicted in Figure 3.7 is presented in Table 3.2. It contains the time versus diameter data, and the results of the linear regressions are also given. These values are plotted in Figure 3.3. Table 3.2 also contains a column of values of $F(D_x)$. These were calculated using the diameter data, and the diameter of the inlet. These values were also subjected to a linear regression, and the results are summarized in Table 3.2 and graphed in Figure 3.4. The regression for the $F(D_x)$ by t graph was not forced through zero, because the timer was not started exactly as the fluid filled the inlet port. The fitting constant, R^2, is greater than 0.99 in both cases, indicating that this flow is consistent with the theory discussed above.

RESULTS AND DISCUSSION

Table 3.3 is a summary of the data from all the permeability measurement runs. Each kind of preform was measured twice, and the average values are given in Table 3.4.

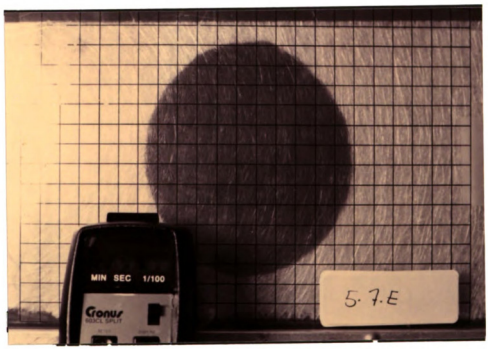


Figure 3.7: Photograph from permeability run 5.7.E; polybutene flowing through random glass preform.

The ratio of K_{xx} to K_{yy} is also given, which confirms that the empty cell is isotropic, as expected. The random glass mat, however, is not truly random, as the flow front spreads in an oval, giving a K_{xx} to K_{yy} ratio of 0.85. The woven glass had a thread count of 14 x 16 ends per inch, and so was not expected to be isotropic. As expected, the woven fabric was orthotropic, with a K_{xx} to K_{yy} ratio of 1.36.

Table 3.2: Data from permeability run 5.7.E. ΔP = 0.3 psig, D_O = 0.95 cm, preform: swirl mat, V_f = 0.18.

TIME (sec)	D_x (cm)	D_y (cm)	$F(D_x)$
7.2	2.07	2.33	3.6
10.4	3.56	3.94	23.9
20.3	6.22	6.71	118.6
30.4	7.85	8.60	219.9
40.4	9.19	10.21	330.4
51.0	10.37	11.67	449.1
60.2	11.41	12.83	570.9

Results of linear regression:

$D_y = 1.114 \times D_x$ $\quad R^2 = 0.999$

$F(D_x) = -89.67 + 10.65 \times D_x$ $\quad R^2 = 0.996$

Table 3.3: Summary of permeability experiment data.

RUN ID	ΔP kPa	μ mPa·s	$\varepsilon = 1-V_f$	m_1	m_2 1/sec	K_e $m^2 \times 10^{10}$	K_{xx} $m^2 \times 10^{10}$	K_{yy} $m^2 \times 10^{10}$
5.7.B	3.4	290	1.00	0.982	42.21	198.	201.	194.
5.7.C	3.4	290	1.00	0.990	39.47	186.	188.	184.
5.7.D	2.1	290	0.81	1.061	13.51	92.6	87.2	98.2
5.7.E	2.1	290	0.82	1.114	10.66	77.5	69.6	86.4
5.7.F	3.4	290	0.62	0.888	2.77	7.26	8.18	6.45
5.7.G	24.1	290	0.63	0.827	21.35	7.56	9.14	6.25

For comparison, note here that $h^2/12 = 7.5 \times 10^{-7}$ m^2 for the empty cell, as compared with the measured value of $K_{xx} = 0.192 \times 10^{-7}$ m^2. This large discrepancy is almost certainly due to fluctuations in pressure, which, though undetectable by the pressure transducer, may have been a significant fraction of the injection pressure of 0.3 psi. Permeability runs with preforms had higher injection pressures, and so should suffer from lower possible discrepancies. Greater accuracy in the pressure measurement would be desirable in future work.

The Blake-Kozeny equation, Eq. (3.4), gives a value of 10.0×10^{-8} m^2 for $\varepsilon = 0.55$ and $d_p = 0.1$ cm. This is two orders of magnitude larger than the measured value of the permeability in the woven mat, 7.4×10^{-10} m^2.

Table 3.4 also contains, for comparison, the results of Chan and Hwang for a woven glass fabric identical to that used in the present work. Their value of K_{yy} for this fabric is only 2% different from the value reported here, but their value of K_{xx} is different by 27%. This may perhaps be explained by very low pressure conditions of the first run of the woven fabric, as the value of Chan and Hwang is only 17% different from that obtained when the pressure drop was raised to 3.5 psig (24.1 kPa). The run with woven fabric and 0.5 psig (3.4 kPa) lasted 360 seconds, and may have been so slow as to not provide a consistent flow front throughout the thickness of the preform. The possibility of capillary action being great enough to contribute to this flow front is discounted because the capillary action would tend to increase the apparent permeability, not decrease it as seen here. Also, Chan recommends (personal communication, May 1993) cutting a hole through the preform of radius R_0, so as to eliminate the z direction permeability as a factor. This was not done in the present work.

Since both the preforms have preferred flow directions, i.e., the permeability is anisotropic, we would expect to see fingers from a radial injection grow fastest in the direction of greatest permeability. Thus, in the orientation of the above experiments, finger growth in the $\pm x$ direction should outstrip finger growth in the $\pm y$ direction. This is

indeed observed in the plaques made with center injection of Derakane resin, which were described in Chapter 4. For injection from an end gating, as was used for the fingering flow experiments described in Chapter 6, only the K_{xx} is expected to come into play, because the velocity is uni-directional in x.

Table 3.4: Permeability of preforms.

PREFORM TYPE	V_f	K_e $m^2 \times 10^{10}$	K_{xx} $m^2 \times 10^{10}$	K_{vv} $m^2 \times 10^{10}$	K_{xx}/K_{vv}
NONE	0.0	192. ± 8.0	195. ± 9.2	189. ± 6.8	1.03
UNIFILO RANDOM STRAND	0.18	85.0 ± 10.6	78.4 ± 12.5	92.3 ±8.4	0.85
HEXCEL WOVEN MAT	0.38	7.41 ± 0.21	8.66 ± 0.68	6.35 ± 0.14	1.36
HEXCEL WOVEN MAT*	0.31		11.0	6.48	1.70

* Results of Chan and Hwang, 1991.

DETERMINATION OF THE DISPERSION COEFFICIENTS

When two fluids of different compositions are brought together, molecules from each fluid will naturally diffuse into the other fluid, thus tending to mix the two fluids over a period of time. This molecular diffusion can be described by Fick's law:

$$\frac{DC}{Dt} = \mathcal{D}_o \nabla^2 C \qquad (3.8)$$

$$\frac{DC}{Dt} = \frac{\partial C}{\partial t} + v_x \frac{\partial C}{\partial x} + v_y \frac{\partial C}{\partial y} + v_z \frac{\partial C}{\partial t}$$

Where C is the concentration of the migrating component, and $\mathcal{D}_o$ is the molecular diffusion coefficient. If the interface between the two fluids is initially sharp, and the diffusion coefficient itself does not depend upon C, then the concentration can be

expressed as a function of distance from the interface (x) and time (t), as (Perkins and Johnston, 1963; also see Appendix B):

$$C(x,t) = \frac{1}{2}\left[1 \pm \mathrm{erf}\left(\frac{x}{2\sqrt{\mathcal{D}_o t}}\right)\right] \qquad (3.9)$$

The sign inside the brackets is negative if the concentration initially steps up (i.e. at t=0, $C(0^+)=1$, and $C(0^-)=0$). If the concentration steps down, the positive sign is appropriate. Figure 3.8 shows a schematic of diffusion across an interface between two fluids. The original location of the interface is taken as x=0, and for subsequent times, the location of the interface is taken to be the (x,y) coordinates at which the concentration is half of its original value. Note that in an ordinary flow, the mixed zone is growing in both the x and y directions simultaneously. Flow situations will need to be contrived to isolate the effects of the longitudinal from the transverse dispersion for accurate measurements to be made.

If the diffusion is taking place in a fluid moving at a steady interstitial velocity, U, then the location of the interface is also moving at U, and the location of the interface at any time t is $x_I = x_O + Ut$, where the interface was located at x_O when t=0.

If the two fluids are flowing through a porous medium, then the concentration profile will change not only due to diffusion, but also due to dispersion. Perkins (1963) defines dispersion as "the increased mixing (over and above that caused by diffusion) caused by uneven fluid flow or caused by concentration gradients resulting from fluid flow". Perkins further notes that there will be, in general, two types of dispersion: that occurring in the same direction as the gross fluid movement, and that occurring transverse to the flow direction.

An effective dispersion coefficient will be defined in an analogous manner as the diffusion coefficient, and will have the same effect on the concentration gradient.

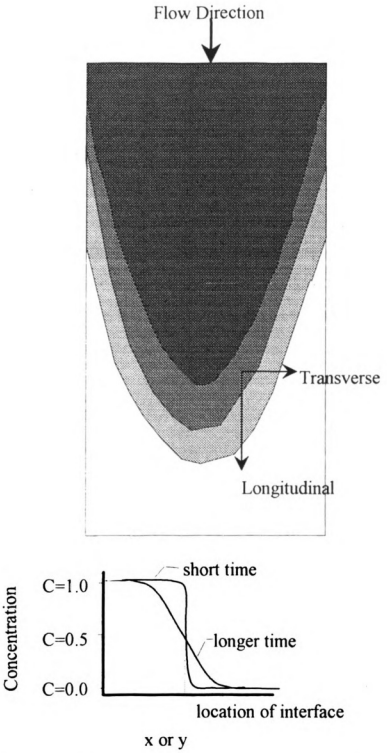


Figure 3.8: Schematic of diffusion across an interface between two fluids.

$$\frac{DC}{Dt} = \mathcal{D}_e \nabla^2 C \tag{3.10}$$

With boundary conditions:

$$C(-\infty, t) = 1$$

$$C(+\infty, t) = 0$$

$$C(0, t) = 0.5$$

The effective dispersion coefficient will contain two components; D_L, which is the dispersion in the x-direction due to flow in the x-direction, and D_T, which is the dispersion in the y-direction due to flow in the x-direction. It is possible to construct flow situations where D_L and D_T can be measured in isolation. Figure 3.9 shows the flow situation for measuring D_L, and Figure 3.10 shows the flow situation for measuring D_T. Given flow in the x-direction, and assuming that there are no concentration gradients in the z-direction, then Appendix B shows that the following are similarity solutions for Eq. (3.10):

$$C(x,t) = \frac{1}{2}\left[1 - \operatorname{erf}\left(\frac{x - x_I}{2\sqrt{D_L t}}\right)\right]$$

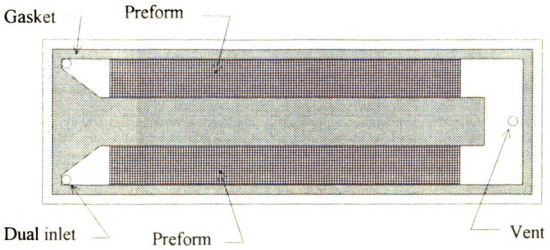
$$C(y,t) = \frac{1}{2}\left[1 - \operatorname{erf}\left(\frac{y - y_I}{2\sqrt{D_T t}}\right)\right] \tag{3.11}$$

Where y_I is the location of the interface, that is, the y coordinate where the value of the concentration is 0.50. The x coordinate of the interface, x_I, moves in the mold at velocity U, so x_I = Ut. If U is not constant, Eq. (3.11) will not be solutions to Eq. (3.10). The value of t at any given x or y is derived from a knowledge of U, and the x coordinate at which the concentration is known.

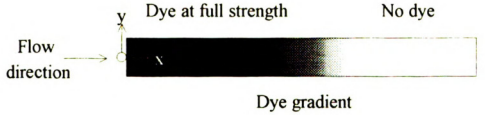
Perkins proposes that the longitudinal (D_L) and transverse (D_T) dispersion coefficients take the form below, where each contain a molecular diffusion term.

$$D_L = \frac{\mathcal{D}_o}{\mathcal{F}\varepsilon} + 1.75 U d_p$$

$$D_T = \frac{\mathcal{D}_o}{\mathcal{F}\varepsilon} + 0.055 U d_p \tag{3.12}$$

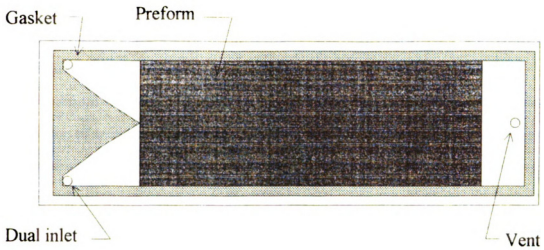


Plan view of mold configuration.

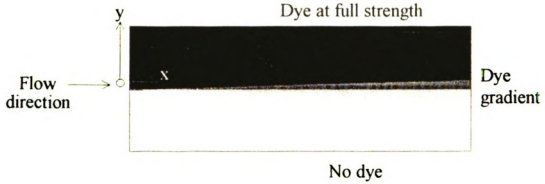


Finished plaque has dye concentration which can be measured as a function of location.

Figure 3.9: Resin injection scheme for determining longitudinal dispersion coefficient.



Plan view of mold configuration.



Finished plaque has dye concentration which can be measured as a function of location.

Figure 3.10: Resin injection scheme for determining transverse dispersion coefficient.

Eq. (3.12) are empirical fits from data taken by Perkins and others for flows through porous media which are granular in nature, with a particle size of d_p, porosity of ε, and formation factor, $\mathcal{F}$. The formation factor is the fraction of the flow paths that are connected from one end of the porous medium to another, and is sometimes measured as the fraction of an imposed electrical current that is transmitted across the porous medium by a conductive fluid. Thus, $\mathcal{F} = 1$ for a completely connected porous medium, and $\mathcal{F} = 0$ for a porous medium with no open flow paths.

If the molecular diffusion coefficient, $\mathcal{D}_o$, is taken on the order of 10^{-5} cm^2/sec, then the first terms of Equations 3.12 become small in relation to the second terms, because $\mathcal{F}$ and ε range from 0 to 1. Then the dispersion coefficients are proportional to the fluid velocity by a constant which encompasses physical details of the porous medium, such as d_p. Then the ratio of D_L to D_T in Eq. (3.12) is:

$$\frac{D_L}{D_T} = \frac{1.75}{0.055} = 31.82 \qquad (3.13)$$

This value of D_L/D_T means that the mixing due to flow through an isotropic porous medium is not isotropic. The mixed zone in the longitudinal direction grows much faster than the mixed zone in the transverse direction.

Koch and Brady (1986) show that for theoretically isotropic packings of fibers,

$$D_L \propto U \quad \text{if } Pe > 1$$
$$D_T \propto U \quad \text{if } Pe > 10 \qquad (3.14)$$
$$Pe = \frac{Ur}{\mathcal{D}_o}$$

Where r is the radius of the fiber. Given a molecular diffusion coefficient, $D_o \cong 1\times10^{-5}$ cm^2/sec, the Peclet numbers for the flows achieved in the fingering flow experiments described in Chapter 6 ranged from 150 to 3000. Thus, we expect that the dispersion coefficients will be linear with U. The constant of proportionality will have units of length, and will involve a length scale characteristic of the porous medium. For ease of

comparison of dispersion coefficients between preforms identical except for small differences in the porosity, the dispersion coefficients will be reported as:

$$D_L = \frac{L_L U}{\varepsilon}$$

$$D_T = \frac{L_T U}{\varepsilon} \qquad (3.15)$$

$$\frac{D_L}{D_T} = \frac{L_L}{L_T}$$

Where L_L and L_T are constants with units of length. The dependence of L_L and L_T on an observable characteristic of the porous medium, like tow diameter or inter-tow spacing is beyond the scope of this work.

Koch and Brady also find that for $10 \leq Pe \leq 1000$, $D_L/D_T \cong 100$, for fibers which are aligned in one dimension, but which are randomly arranged in the other two dimensions. This is only three times the value that Perkins and Johnston found for isotropic beds of particles. If these two situations are considered to be at two ends of the range of values of D_L/D_T , it may be that the range is only an order of magnitude or two wide.

Tan and Homsy (1986) show that the growth rate of fingers is increased almost tenfold when $D_L/D_T \rightarrow \infty$, compared to the case of $D_L/D_T = 1$, while the length scale of the fingers is decreased by a factor of $(D_L/D_T)^{-1/3}$. On the other hand, when $D_L/D_T \rightarrow 0$, i.e., transverse dispersion is very large, the growth rate of fingers is decreased to the order of D_L/D_T, and the length scale of fingers increases to the order of $(D_L/D_T)^{-1}$. Thus, Tan and Homsy conclude that large transverse dispersion stabilizes the fluid flow by suppressing the fingers.

It will be of interest to measure the dispersion coefficients in the fibrous porous media, and to compare the ratio D_L/D_T to that for random packs of particles. If the ratio is larger, we expect the tendency for fingers to grow to be increased due to the nature of

the fibrous porous medium, as compared to the particulate porous medium, other things being equal.

PLAQUE PRODUCTION

Plaques from which to measure the dispersion coefficients were produced in the constant pressure molding apparatus depicted in Figure 3.6, with the resin injection point at one end of the mold instead of the center. Gaskets were modified so as to produce plaques as depicted in Figure 3.9 for measurement of D_L and Figure 3.10 for measurement of D_T. Note that for the longitudinal runs, two plaques were made simultaneously.

For both kinds of plaques, the DGEBA/TETA resin system was used. Two batches, one dyed and one undyed, were mixed at the same time, and injected either serially (for D_L) or simultaneously (for D_T) into the mold. Since the resin batches were the same age, it was expected that their viscosities would not differ through the run. All mixing and injection took place at room temperature with resin that was liquid at room temperature due to low water content.

At the end of the injection, plaques were cured at 50 °C for 3 hours, then stripped from the mold. No postcure was done, as physical properties were not of interest. However, plaques were at least 30 days old when the dye concentration measurements were made, so it is assumed that the cure was well advanced, as discussed in Chapter 2.

Injection pressure varied with the progress of the injection, from less than 1 psig to 10 psig for the random swirl mat, and >12 psig for the woven mat. Front velocity was not derived from the pressure trace, but from a time series of photographs.

COLORIMETRY

It was assumed that since the dye was as soluble in one batch of resin as in the other, that the movement of dye was equivalent to the movement of dyed resin. Thus the concentration of the migrating species, the dye, was taken as an indicator of the dispersion of the displacing fluid in the displaced fluid. Therefore, the dye concentration was measured in the cured plaques by colorimetric means.

The Noritsu Model 810 Photometric Densitometer operates by passing light of a known intensity through a transparent sample, and evaluating the intensity of each of three wavelengths of the transmitted light. It is ordinarily used in calibrating photographic processing machinery. The area sampled on any given measurement is a circle 0.5 cm in diameter. The readout of the densitometer is digital, but lacks any units, so for each plaque, enough readings were taken where the dye concentrations were maximum and minimum to establish the values corresponding to the C = 1 and C = 0. In general, readings ranged from 2.2 to 0.5, but varied with each plaque. Since the dyed resin was red, and the undyed resin was light yellow, only the reading for the absorbance of cyan light was noted and used for calculations, although greater accuracy might have been had by adding all three readouts for any single measurement.

Each plaque was overlaid with a grid of 0.5 cm squares in order to provide a coordinate system for measurement of the dye concentration by photometric densitometry. Origins of the coordinate systems are noted in Figures 3.9 and 3.10. Since the readings were taken inside any given grid square, the coordinate of the reading was considered to be the center of the square.

DATA COLLECTION AND SAMPLE CALCULATIONS

LONGITUDINAL DISPERSION

The velocity of the flow front for each of the three longitudinal runs was derived from a time series of photographs of the injection, and all three are shown in Figure 3.11. In each instance, the velocity is constant throughout the injection. Use of Figure 3.11allows the deduction of t_I, the age of the interface, given the x-coordinate of the interface in the finished plaque.

In each of the six plaques made, the interface between the undyed and dyed fluid was not straight in the y direction, but was somewhat bowed. In order to avoid large corrections to the location of the interface, concentration data were taken only at the center 2 cm of each plaque. Each of these four C(x) profiles was then treated as follows.

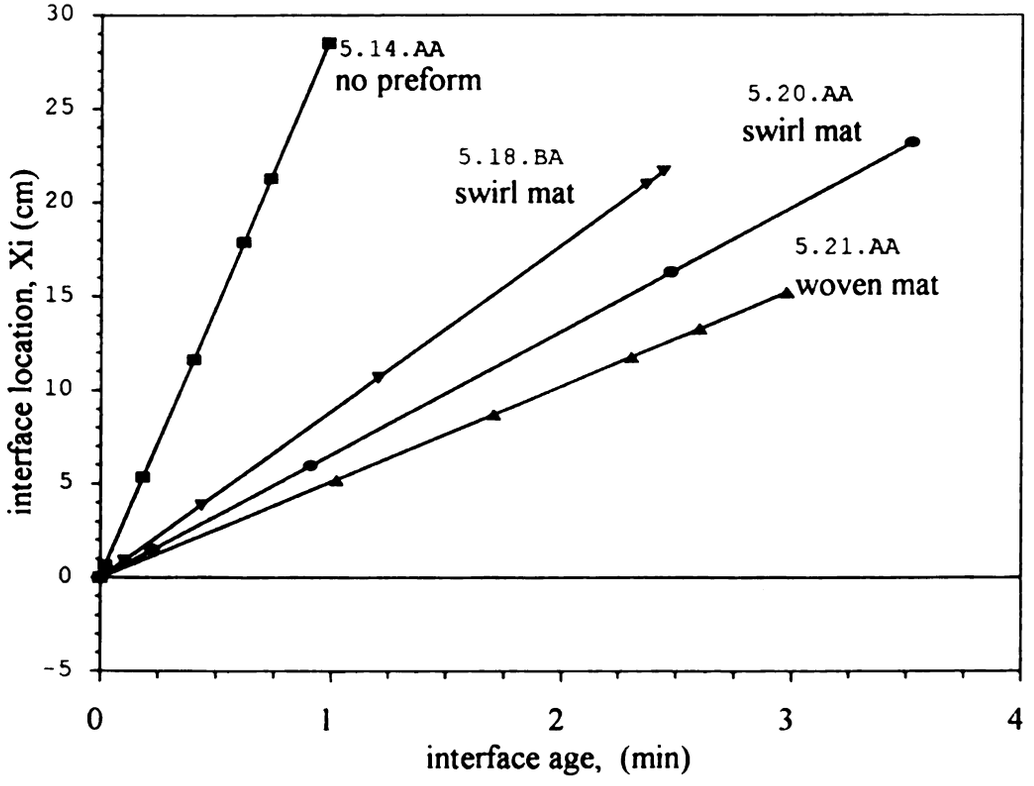


Figure 3.11: Flow front velocities in plaques for longitudinal dispersion measurements.

1. The densitometer readings for maximum and minimum concentration were noted, and readings were corrected to yield concentration data in the range: $0 \leq C \leq 1$.
2. x_I was taken as the x coordinate of the plaque where $C = 0.5$, interpolating where necessary.
3. The average of x_I for the four profiles was found, and the corresponding t_I from Figure 3.11 was noted.
4. Each concentration profile was then shifted so that the 50% value of the concentration fell at x_I.

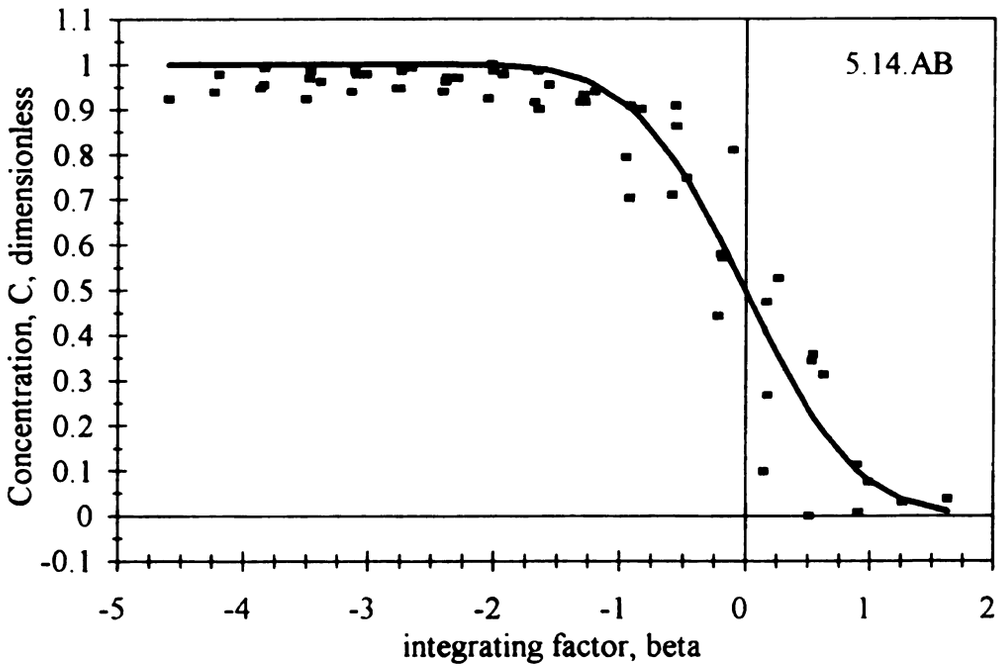
This data treatment yielded tables of concentration by location data which are included in Appendix C. These data could then be fit to Eq. (3.9) with the regression method detailed in Appendix B. Table 3.5 contains the values for x_I, t, and D_L derived for the eight plaques. R^2 is the fitting coefficient, where a value of 1 indicates that the model fits the data perfectly. The last column in Table 3.5 shows the length scale, L_L defined in Eq. (3.15). Figure 3.12 shows a typical set of concentration data on a similarity plot, which shows that though there is scatter in the data, the similarity solution is the proper form.

TRANSVERSE DISPERSION

Plaques for the determination of the transverse dispersion coefficient were made with the mold configuration pictured in Figure 3.10. The injection scheme was similar to that described above, except the dyed and undyed fluid were injected simultaneously, rather than serially. Three plaques were made, one with no preform, one with swirl mat, and one with woven mat, as before. The velocity of the fluid was determined from a timeseries of photographs, and is shown in Figure 3.13 for all three plaques. The data were fitted with a least squares routine to obtain the velocity functions:

$$\begin{aligned} U &= 20.7 && \text{cm/min (no preform)} \\ U &= 4.95 + 13.87(1 - exp(-t)) && \text{cm/min (swirl mat)} \\ U &= 2.57 + 8.20(1 - exp(-t)) && \text{cm/min (woven mat)} \end{aligned} \tag{3.16}$$

Note that the velocity for the plaque with no preform is constant in time, but in the two plaques with preforms, the velocity decreases with time. This was due to the



$$\beta = \frac{x - x_I}{\sqrt{4 D_L t}}$$

Figure 3.12: Typical concentration data on similarity plot for longitudinal dispersion plaque. No preform.

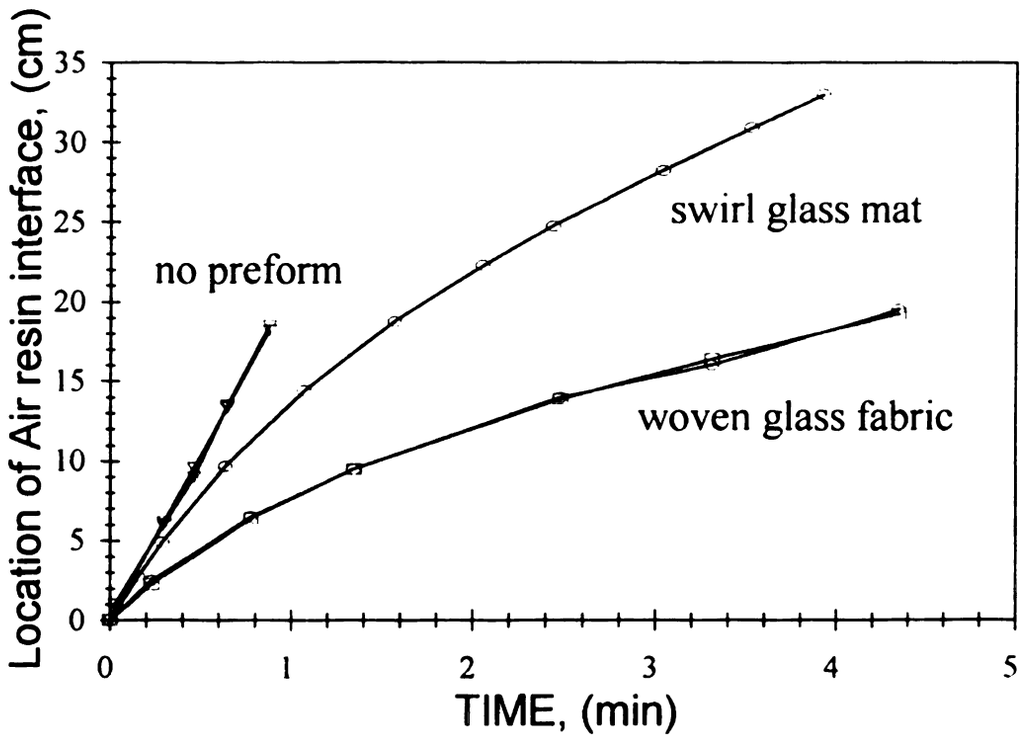


Figure 3.13: Flow front velocities in plaques for transverse dispersion measurements.

increasing amounts of drag being generated in the preform as it is filled with resin. When the preform is completely saturated with resin, the velocity will become steady. It is this asymptotic velocity which will be used to find L_T from Eq. (3.15).

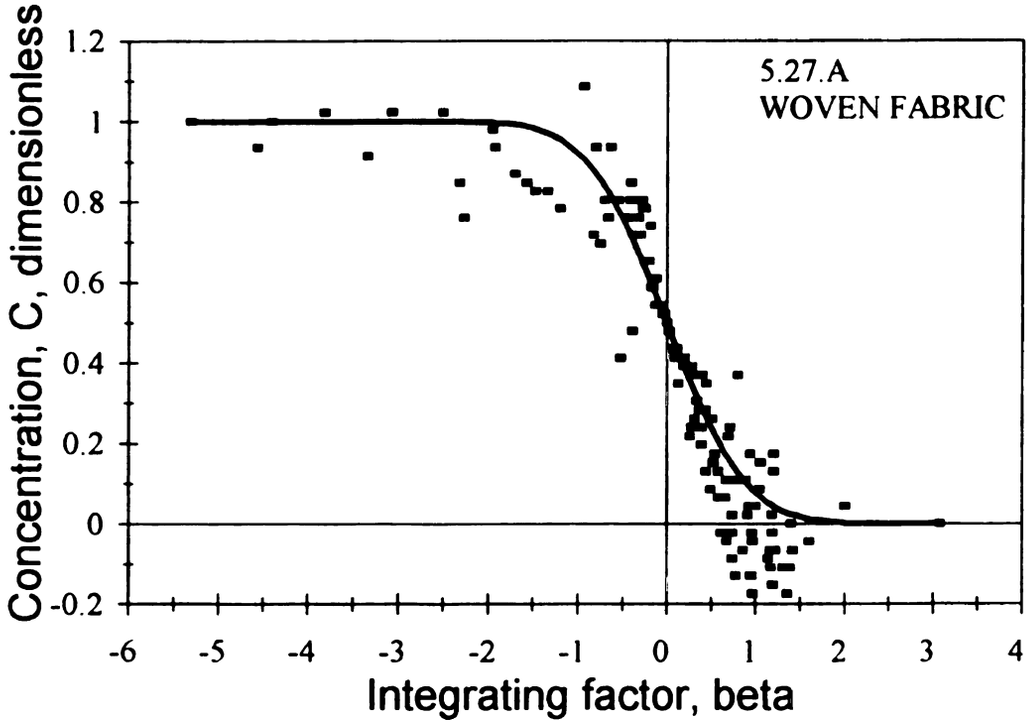
Colorimetric data were taken in the y direction along 15 lines of constant x for each plaque. At each line of constant x, an associated time was derived from Figure 3.13.

As before, the concentration data were normalized with the maximum and minimum values of the absorption for each plaque. These data are tabulated in Appendix C. Again, C(x,y,t) data were fitted by the least squares regression detailed in Appendix B, and the results are in Table 3.6, and a similarity plot is shown in Figure 3.14 .

RESULTS AND DISCUSSION

Table 3.5 shows that despite the very good fitting coefficients for the individual plaques, the values for the longitudinal dispersion coefficients are not very reproducible. Figure 3.12 shows that the data have considerable scatter in them, and this is probably the cause of the discrepancies between values for L_L. The regression routine for D_L forced the remainder to be less than 0.0005, and the solution was not substantially improved by requiring the remainder to be less than 0.0001. The cause of the scatter is probably the fact that the dyed front was not straight across the plaque, but was bowed in the y direction. It was attempted to minimize this effect by taking data only very near the center (y = 0) of the plaques, but since readings each encompassed a square 0.5 cm on a side, four profiles of constant y, variable x were needed to provide the necessary density of data. A colorimeter with a smaller objective would be desirable in future work.

Figure 3.14 shows that the broader profiles of the transverse dispersion plaques were measured with much less scatter to the data, especially near the end of the plaque where the profiles were broadest. The fit coefficients, as shown in Table 3.6 are also excellent.



$$\beta = \frac{y - y_I}{\sqrt{4 D_T t}}$$

Figure 3.14: Typical concentration data on similarity plot for transverse dispersion plaque. Woven mat preform.

Table 3.5: The longitudinal dispersion coefficients.

Plaque	Preform	U (cm/sec)	D_L (cm^2/sec)	R^2	L_L (cm)
5.14.AB	none $\varepsilon = 1.0$	0.461	0.0147	0.992	0.0318
5.20.AA	swirl mat $\varepsilon = 0.82$	0.148	0.0178	0.982	0.0984
5.20.AB	swirl mat $\varepsilon = 0.82$	0.121	0.0134	0.988	0.0906
5.21.AA	woven mat $\varepsilon = 0.55$	0.085	0.0117	0.989	0.0755
5.21.AB	woven mat $\varepsilon = 0.55$	0.064	0.0067	0.990	0.0576

Therefore, Table 3.7 shows the averages of values of L_L, and the ratio of L_L/L_T for each kind of preform. Despite the imprecision of the value of L_L, it can be seen that the dispersion coefficients are at least 3 orders of magnitude larger than a typical diffusion coefficient, which would have a value on the order of 10^{-5} cm^2/sec.

Table 3.6: The transverse dispersion coefficients.

Plaque	Preform	U (cm/sec)	D_T (cm^2/sec)	R^2	L_T (cm)
5.25.A	none $\varepsilon = 1.0$	0.345	0.000845	0.961	0.00245
5.26.A	swirl mat $\varepsilon = 0.82$	0.087	0.001364	0.966	0.0129
5.27.A	woven mat $\varepsilon = 0.55$	0.045	0.001819	0.914	0.0221

Perkins and Johnston report $D_L/D_T = 31.8$ for beds of packed particles. Note that this is nearly equal to $D_L/D_T = 32.4$ reported here for random swirl mat, despite the obvious differences in structure between a particulate and a fibrous medium. Thus, we

might conclude that a swirl mat of $\varepsilon = 0.79$ is about as dispersive as a packed bed of particles. It may be, however, that this result is more due to the quantity and nature of the open spaces in the swirl mat, than the presence of fibers. As the fiber volume fraction increases, the similarity of the ratios may disappear.

Table 3.7: Dispersion coefficient results.

Preform	L_L (cm)	L_T (cm)	L_L/L_T
none $\varepsilon = 1.0$	0.0318	0.00245	13.0
swirl mat $\varepsilon = 0.82$	0.0919	0.0129	32.4
woven mat $\varepsilon = 0.55$	0.0666	0.0221	3.0

Koch and Brady, (1986) find that $D_L/D_T \cong 100$ for fibrous porous media consisting of fibers which are random in two dimensions, but which are aligned in the remaining directions. This is the same order of magnitude as the ratio reported here for swirl mat, but it is an order of magnitude larger than that for woven preform, which has fibers aligned in all three dimensions.

Table 3.7 contains the values of L_L and L_T which will be used for scaling purposes in Chapter 6 where fingering flow experiments are described. In comparing the longitudinal dispersion constants for the three porous media, we see that the Hele-Shaw cell has the smallest value of $L_L = 0.032$. The woven mat has double the value of L_L, and the swirl mat has triple the value. Thus, the longitudinal mixed zone will be widest in the swirl mat, and shortest in the Hele-Shaw cell. In contrast, the transverse mixed zone will be widest in the woven mat, and smallest in the Hele-Shaw cell. Thus, other things being equal, we expect fingering to be damped in the woven mat, compared to the Hele-Shaw cell, but exacerbated in the swirl mat, based on the predictions of Tan and Homsy that

large ratios of D_L/D_T will tend to increase the dimensionless growth constant of fingers which arise in miscible displacement flows.

CHAPTER 4

INVESTIGATION OF THE EFFECT OF A DISTRIBUTION OF RESIN AGE IN RTM PLAQUES

BACKGROUND

Resin transfer molding involves the injection of a reacting polymer system into a flow channel, the mold, where it is expected to gel, solidify, and cure into a useful polymeric article. Commercially, the resin is mixed as it enters the mold, and gels shortly after the mold is filled. Thus, the first resin which has been injected into the mold may be considerably older than the last resin, and consequently will be more viscous, and have fewer molecular sites still open to crosslinking reaction. As discussed in Chapter 1, and below, this age gradient may give rise to fingering flows because of the viscosity gradient that arises. One consequence of fingering flows is that resin 'packets' of different ages will come together in the mold. Because the extent of reaction differs between the two packets, there may be less crosslinking between them than there would be inside the packets themselves. The interface between the two packets may thus be weaker than the bulk resin, and may also contain bubbles or other impurities which were trapped in the interface by the flow. Fingering flows are not the only situation wherein resin packets with different ages will meet in an RTM mold. Flow around inserts or from multiple gatings may form an interface where resin packets of different age come together. Interruptions in the injection, as when two shots are needed to fill an especially large mold cavity, and channeling of flow through preforms or along mold edges also may cause a distribution of resin age in the mold.

It is of interest to study the consequences of the age distribution of resin in RTM, to determine whether the traces left in a finished part by fingering flows are detrimental to the physical properties of the part. It is speculated that if the age difference is great enough, the interface itself will be weak due to insufficient crosslinking. If the interface occurs where two bulk flows come together, then the interface may be weakened by trapped bubbles, or by an excess of binder dissolved from the preform. The fact that the resin on either side of the interface will have different volume changes (shrinkage) associated with its age differences may also tend to put residual stress on the interface, tending to weaken it. "Weakness" may be manifested by a loss of tensile strength or flexural stiffness. Also, the presence of air bubbles or pockets of binder may increase the vulnerability of the part to solvent attack, as well as serving as crack initiation sites.

This chapter describes the production and testing of RTM plaques which contain age distributions due to fingering flows. Plaques were made without preform, and with two kinds of glass preform: a random swirl mat, and a woven fabric. The plaques were cut up for test samples so as to sample areas with interfaces of several different geometries. 3-point bend testing showed that specific kinds of interfaces seem to decrease the flexural modulus of the sample bar by as much as 15%.

DESCRIPTION OF FINGERING FLOWS DUE TO AGE DISTRIBUTION IN RTM

Saffman and Taylor (1958) showed that fingering flows would occur when a less viscous fluid was displacing a more viscous fluid from a porous medium. Saffman discussed fluids which were immiscible in each other, but others (Gorrell, 1985, Tan, 1986) have shown that miscible fluid displacements also will give rise to viscous fingering if the viscosity gradient is great enough, and the stabilizing influences such as dispersive mixing are not too great. The literature, as discussed in Chapter 1, has mainly investigated viscous fingering flows in clear channels (Hele-Shaw cells) and in porous media which are granular in nature. Viscosity gradients investigated in the literature arise

because of the presence of two fluids of distinct viscosity. Not discussed is the case of the viscosity gradient arising because of an age distribution in a reacting fluid whose viscosity rises with age, although Bakkes (1993) discusses fingering flow which arises because of the differential dissolution of a binder which is present in limited quantitiy in the preform and which is soluble in the resin. It was found that the concentration gradient gave rise to a viscosity gradient, which gave rise to fingering, in a resin system which was not reactive. This situation may be analogous to the viscosity gradient caused by the differences in ages of the resin in the mold.

Four types of viscosity profiles are shown in Figure 4.1. The jump profile would be typical of a displacement flow with immiscible fluids. Each fluid has a definite viscosity, and no mingling takes place. Saffman showed that this type of flow will produce fingers if the velocity is high enough to overcome the stabilizing influence of density difference. The S-curve profile is the result of a displacement flow where the bulk of each fluid has a definite viscosity, but the two fluids have mingled at the interface to produce a continuous transition from one fluid to another. Tan and Homsy (1986) have shown that fingering instabilities arising because of a viscosity difference are damped by this kind of dispersive mixing. A gradual transition such as that labeled 'decelerating' was proposed by Gorrell and Homsy as the most stable profile for displacing a viscous fluid like crude oil with a less viscous fluid like water. In practice the 'decelerating' profile would be achieved by adding a polymeric thickening agent to the displacing fluid in decreasing amounts as the displacement proceeded.

All of these profiles can be produced in resin transfer molding, with manipulation of the injection scheme. However, the typical profile in RTM would be the continuous increase in the direction of flow (labeled 'accelerating' on Figure 4.1), not because of an additive, but because the viscosity is increasing with time due to reaction. It is expected that this additional dimension of time may serve to exacerbate the fingers by increasing in time the

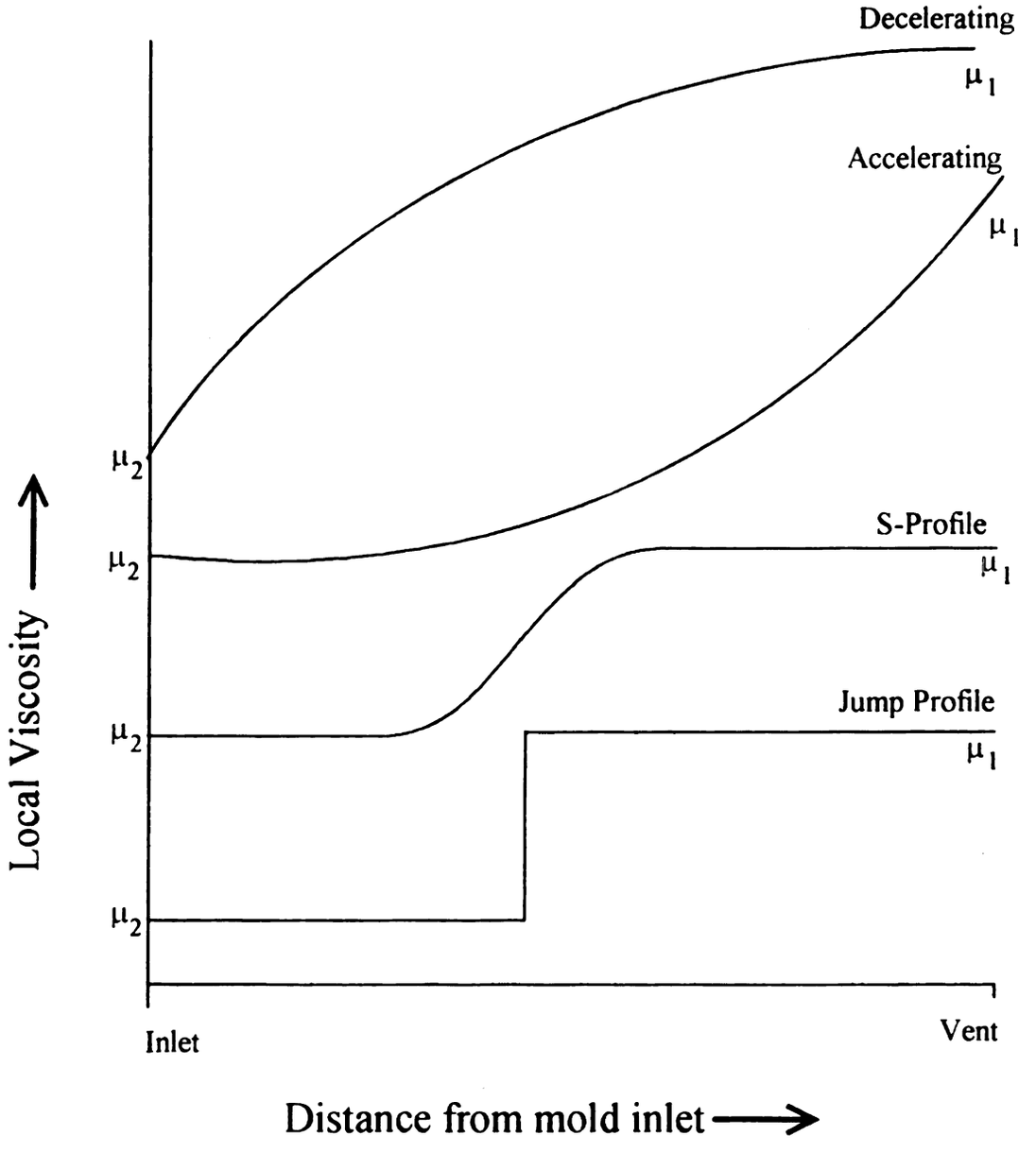


Figure 4.1: Viscosity profiles in RTM which may be accomplished by the manipulation of the injection protocol.

spatial viscosity gradient which is driving the propagation of the fingers. In effect, the slope in the viscosity profile gets larger with time.

It seems clear that viscosity gradients can arise in RTM and cause fingering flows. Yet, there may also be stabilizing influences in RTM flows, as compared to fingering flows in clear channels or granular porous media. For example, the typical RTM preform has higher porosity, higher connectivity, and larger pore spaces than the typical granular medium, a sand pack. Preforms also tend to be anisotropic, unlike sand packs, which are assumed to be isotropic. Tan and Homsy have shown that anisotropic dispersion in a porous medium will have an effect on the tendency of fingers to grow. If the dispersion transverse to the flow direction is much greater than the dispersion parallel to the flow direction, then the fingers will tend to be damped. The anisotropy of preforms may either dampen or exacerbate the fingering flow and will play a defining role, through the size of the intertow pore spaces, on the widths of fingers and the shapes of their tips.

The presence of the preform is expected to affect the generation of fingers and their final shapes, but it will also affect the performance of the final part in which interfaces are embedded. As discussed in Chapter 1, the presence of fibers in a finished part may mask any loss of properties caused by the presence of an interface.

EXPERIMENT PROCEDURES

PLAQUE PRODUCTION

The resin system chosen to produce plaques with resins of different age was Derakane® 411 vinyl ester resin from The Dow Chemical Co. The resin was formulated with 0.5% N,N-Dimethylaniline (DMA), and 1% Benzoyl peroxide (BPO) by weight. The BPO was used in paste form to shorten the mix time to 4 minutes, in contrast to a mix time of greater than 10 minutes for the pure BPO powder. The dye used with this system was Oil Red, available from Aldrich Chemical Co., and was added at the rate of 0.5% by weight. Specifications and suppliers of all materials are listed in Appendix A. The initial

viscosity of the resin was 0.45 Pa·sec, and the gel time was approximately 18 minutes at room temperature. See Chapter 3 for resin characterization procedures. Figure 4.2 illustrates the viscosity by time curve of this formulation. The viscosity stays very low for a significant fraction of the gel time, then rises steeply just before gel. Derakane® 411 resin contains a significant amount of styrene monomer, which helps keep the viscosity low during the early part of the reaction. In order to provide a viscosity difference between two batches of resin in the mold, the age difference will have to exceed 11 minutes or so, but be less than 18 minutes, which is designated as the gel time.

Plaques were produced in an RTM mold with a narrow (0.3 cm) gap with a clear channel, i.e. no preform, to produce a neat resin plaque, and with two kinds of preforms. Continuous strand swirl fiberglass mat was obtained from Vetrotex Certainteed. Its designation was Unifilo U816, and it contained a binder that was slightly soluble in the Derakane® resin. Three plies of the mat were used to achieve a fiber volume fraction (V_f) of 0.21. This could not be increased to the more commercially viable $V_f = 0.30$ because of clamping pressure limitations in the mold. Hexcel Corporation supplied the woven glass fabric, designated #7532. It is plain weave with 16 warp and 14 woof ends per inch. This is not quite balanced, so care was taken to stack the plies so that the machine direction was laid along the lengthwise axis of the mold. This was intended to preserve the anisotropy which the fabric would induce in the flow. Twelve plies of this fabric were used to obtain $V_f = 0.45$.

Figure 4.3 shows a schematic of the RTM mold used for this study. The mold produces a rectangular plaque 46 cm long, 14.6 cm wide, and 0.3 cm thick. The top of the mold is Plexiglas®, which is protected from the styrene in the resin by a sheet of clear nylon film. A layer of light machine oil between the Plexiglas® and the nylon film keeps the film from wrinkling while the mold is assembled. The bottom of the mold is an

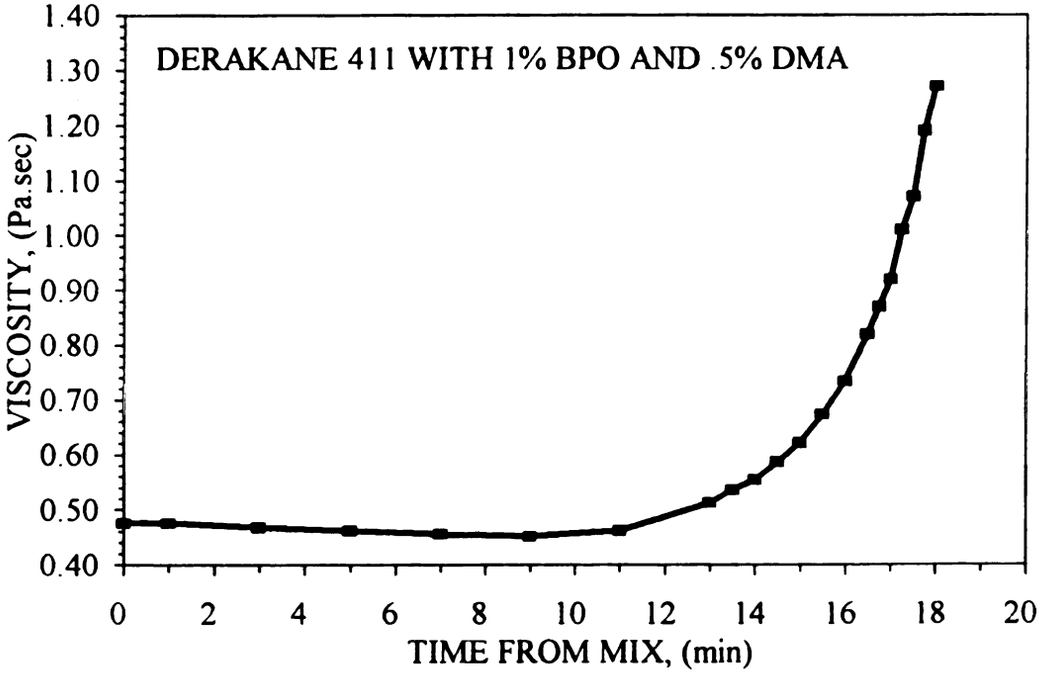
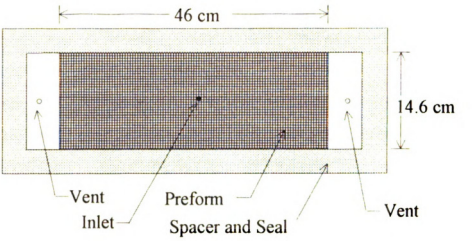


Figure 4.2: The viscosity of Derakane resin as a function of time, at 20°C.



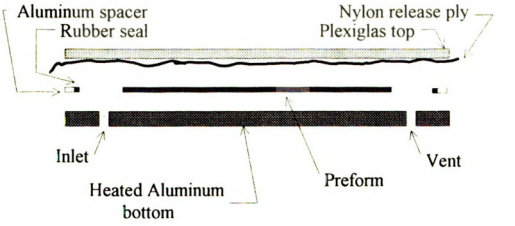


Figure 4.3: The RTM mold used to produce plaques with resins of different ages.

aluminum plate, with heaters attached. The edges of the mold are sealed with a flat silicone rubber gasket, which is kept in place by an aluminum frame. The frame also acts as a spacer between the top and bottom when clamps are applied. The mold is fed through a central gate by a piston which can be driven at a constant rate, so as to give a constant volumetric flow rate of resin into the mold cavity. The progress of the resin front through the mold was recorded with a video camera.

The effect of an age distribution in the resin on the flow was investigated as follows. The age of a batch of resin was counted from the time the peroxide initiator was mixed with the Derakane base resin. Plaques with age differences were made by mixing the required resin in two batches. Half the resin (Batch 1) was mixed and injected, then a time of 11 to 14 minutes was allowed to pass before the second half of the resin (Batch 2) was mixed and injected. The age difference of 11 to 14 minutes is a significant portion of the gel time of 18 minutes. However, the entire injection time of both resins was kept to under 16 minutes, so as to avoid the possibility of gelled particles interfering with the fingering flow. The injection procedure was as follows:

1. Prepare mold.
2. Mix Batch 1. Mix time approximately 4 minutes.
3. Load Batch 1 into the piston and inject into mold at 0.67 cm^3/min.
4. When the mold is over 1/2 full, stop the injection, close the inlet valve, and clean out the piston and the tubing.
5. Start mixing Batch 2 at 9 minutes after start of Batch 1. Mix time approximately 4 minutes.
6. Load Batch 2 into the piston and inject at 0.67 cm^3/min.
7. When mold is full, close inlet valve and vents. Heat mold to cure temperature (40 °C or 70 °C) for 1 hour. Then strip plaque from mold and postcure for 1 hour in 100° C convection oven.

Three plaques were also made with a single batch of resin each, so that there would be no age difference. No fingering flow was observed in these plaques. Table 4.1 gives the a summary of the plaques which were produced. All plaques were made with a

volumetric flow rate, Q, of 0.67 cm^3/min. This resulted in an interstitial velocity, U, characteristic of each preform type, given a constant thickness of the mold. The interstitial velocities were calculated as: 0.18 cm/sec in the clear channel mold, 0.23 cm/sec in random glass preform, $V_f = 0.21$, and 0.33 cm/sec in woven glass preform, $V_f = 0.45$.

Table 4.1: Plaque production variables.

Plaque #	Preform	Δt (min)	T_{cure} (°C)
9.22.A	none	0	40
10.07.B	none	0	70
9.18.A	none	11	40
9.21.A	none	14	70
10.06.A	random glass $V_f = 0.21$	0	40
9.17.A	random glass $V_f = 0.21$	14	40
9.16.A	random glass $V_f = 0.21$	14	70
10.12.A	random glass $V_f = 0.21$	11	70
9.15.A	woven glass $V_f = 0.45$	14	40
9.11.A	woven glass $V_f = 0.45$	13	50

PLAQUE SAMPLING AND TESTING

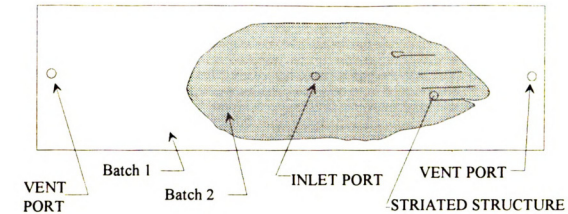
Because of the low number of finger structures per plaque, it was not considered feasible to reserve half of the plaque for flexural testing and half for tensile testing. Therefore, only flex testing results are reported here. Measurement of the flexural modulus of sample bars cut from the plaques was accomplished using a United Testing Systems (UTS) testing frame in accordance with ASTM standard D-790. The cross-head speed was 1 mm/min, the test span was 80 mm, and the maximum strain in the sample was

kept to less than 3%. The load cell had a capacity of 88 N, and was deemed accurate to ± 5% of its full scale reading. Dimensions of the test bars were measured to the nearest 0.1 mm.

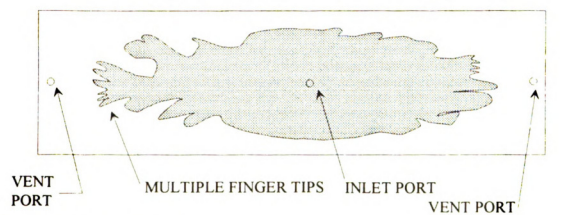
Plaques were cut up into sample bars taken across the width of the mold to yield approximate dimensions of 14.6 cm length, 1.4 cm width, and 0.3 cm thickness. Figure 4.4 depicts three typical plaques, while Appendix C contains a diagram of each plaque, showing the shape of the interface, and the location of each sample bar. Dark areas in these diagrams represent dyed or Batch 2 fluid, and light areas represent Batch 1 fluid. Bars were taken so as to represent areas of the plaque which contained Batch 1 (undyed) only, and Batch 2 (dyed) only, as well as various types of finger shafts and tips. Bars were prepared and tested at ambient temperature and humidity conditions.

All sample bars were tested centered in the 3-point bend fixture, then many were removed from the fixture, and repositioned eccentrically for another test. Figure 4.5 shows a schematic of a sample bar loaded centered and eccentrically. In the example shown, the centered position tests the 6 interfaces of 3 narrow regions of dyed resin surrounded by undyed resin. When the bar is tested eccentrically, 4 of the interfaces are in the test span. The difference between these two tests should show the cumulative effect of interfaces on the flexural modulus of the sample bar.

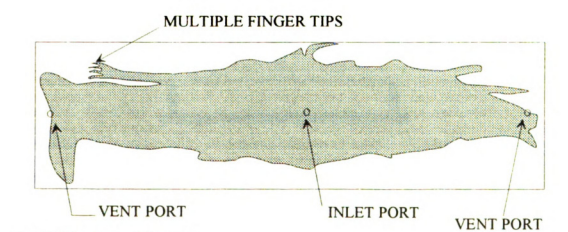
The ASTM standard states that to obtain reproducible numbers, 5 identical samples must be tested, and the average value reported. Given the random patterns of the fingering flows, it was not possible to obtain 5 samples with identical features from any plaque. Therefore, it should be accepted that the numbers reported here may represent less than five sample bars each, due to the difficulty of obtaining multiple samples of similar interface structures.



PLAQUE 9.18.A Vf = 0.0

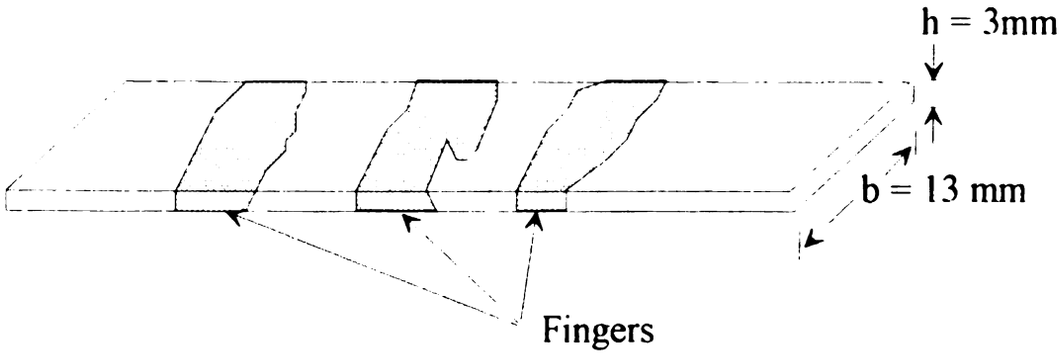


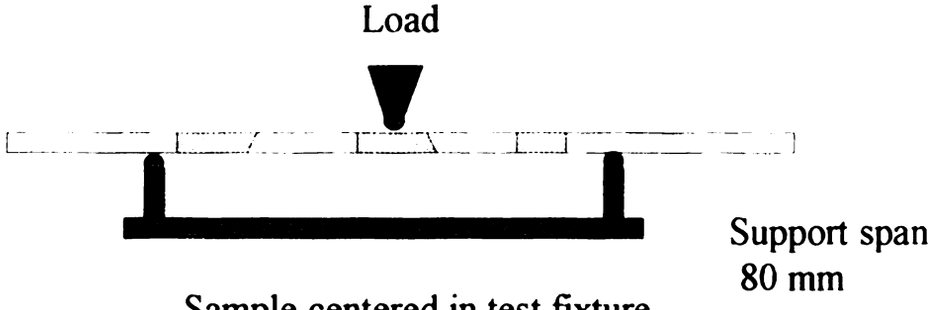
PLAQUE 9.17.A Vf = 0.21



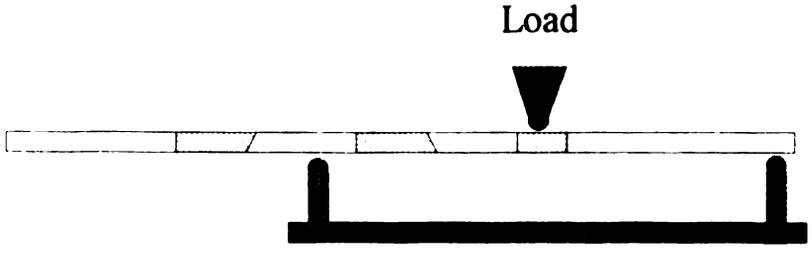
PLAQUE 9.15.A, Vf = 0.45

Figure 4.4: Typical finished plaques showing Batch 1 as light and Batch 2 as dark.





Sample centered in test fixture.
6 interfaces are in test span.



Sample eccentrically loaded in test fixture.
4 interfaces being tested.

Figure 4.5: Position of the test bars in the 3-point bend test fixture.

RESULTS

VISCOUS FINGERING FLOW PATTERNS

Three plaques with interfaces due to viscous fingering are illustrated in Figure 4.4. In all plaques, Batch 1 is the undyed resin that ends up at the outer edges of the plaque. Batch 2 is dyed, and occupies the center of the plaque. During the cure and post-cure, the dye tended to fade, but did not spread into the undyed resin, so it gave a good indication of the position of the interface between the two batches both during the flow and in the final plaque.

The flow front of the dyed resin in the neat resin plaque (Figure 4.4A) was circular at the beginning of the injection, but became oval as the dyed resin neared the sides of the mold. The flow was slow enough that no distinct fingers developed at the flow front, but several long thin inclusions of the undyed resin appear behind the flow front of the dyed resin. These striations are not fingers, but they are structures where resins of different age came together at an interface, so they were sampled for flex testing.

The flow front in the random glass preform (Figure 4.4B) plaques is also circular until the resin nears the edge of the mold, after which the front becomes oval, with fingers superimposed. The fingers, which arise stochastically, as discussed in Chapter 1, are not symmetrically distributed on the main oval interface. The right end shows three fingers, one with a rounded end, one with a few branches at the end, and one with many small fingertips at the end. The left side of the plaque shows a more rounded profile, with small fingers superimposed upon it. Sample bars were cut from the plaque to include all these features.

The early flow front in the woven preform (Figure 4.4C) was not circular, but rather cross-shaped, as the resin flows preferentially parallel to the fiber tows in the fabric. Fingers also showed a preference to grow parallel to the fiber direction, and to channel to the end of the mold with almost no spreading. Still, this plaque displays fingers which

have rounded ends as well as multiple small fingertips, which again, were sampled for testing of physical properties.

The neat resin plaques ($V_f = 0$) are assumed to be isotropic, since they have no fibers. The average flex modulus, E_b, for these bars is approximately 4.0 GPa, compared to the value of 3.10 GPa, given by Dow literature as being typical of this Derakane formulation.

The results of the properties testing appear in Appendix C, and are summarized in Table 4.2. Table 4.2 lists the flex testing results for each kind of finger structure being tested. Definitions of finger structures are as follows: "all Batch 1" and "all Batch 2" have no interfaces in the test span, and are taken from Batch 1 and Batch 2 areas of the plaque, respectively. Samples labeled "shafts-3" are bars cut perpendicularly across the shafts of the fingers behind the tip. The number (3) indicates the number of interfaces in the test span. Samples labeled "smooth tips" and "multiple tips" are likewise cut to include the rounded part of the fingertip. The designation "striations" refers to the striated structures seen only in the neat resin plaques, as discussed above.

DISCUSSION

Figures 4.6, 4.7 and, 4.8 show the results of the flex modulus testing. In each graph, the average and standard deviations of the flex modulus are segregated according to the type of finger structure that was represented by the sample bar, according to the description above. In cases where only one sample was tested, the standard deviation was taken to be zero.

NEAT RESIN PLAQUES

Figure 4.6 shows the results of the flex testing of neat resin plaques. Each sort of finger feature that was sampled and tested appears with the average and standard deviation bars. The overall average of the flex modulus was 3.9 GPa, and the dark bar at the left of Figure 4.6 represents 3.9 ± 5%, which is the accuracy of the test. All the bars

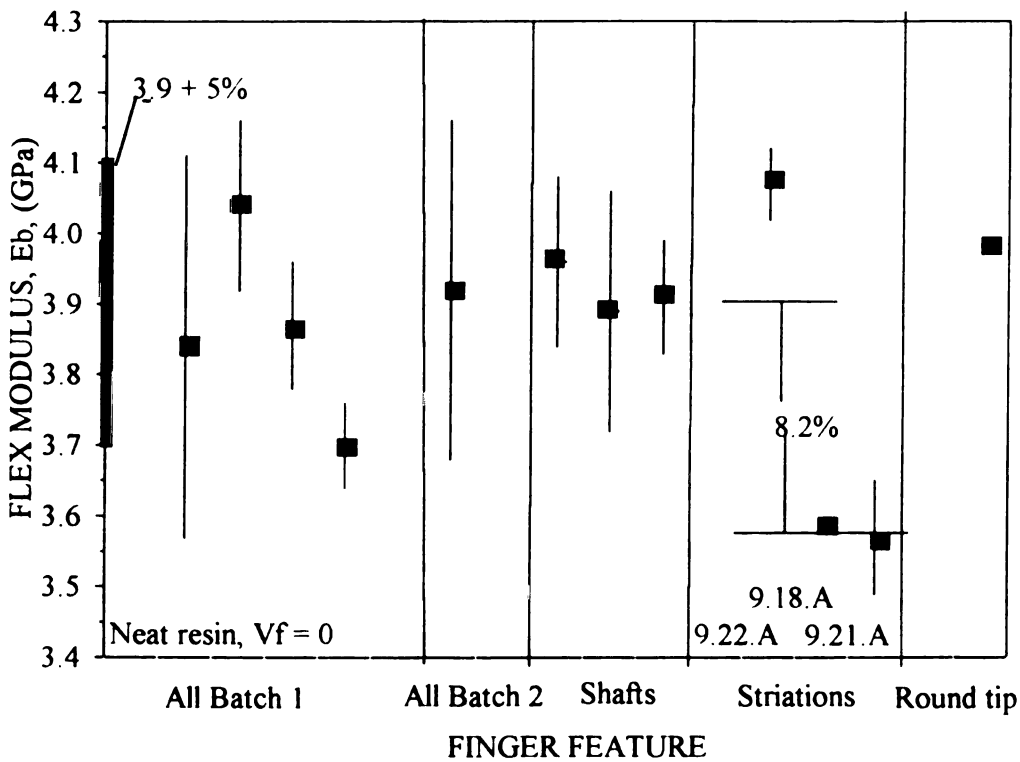


Figure 4.6: Results of the 3-point bend testing, neat resin plaques.

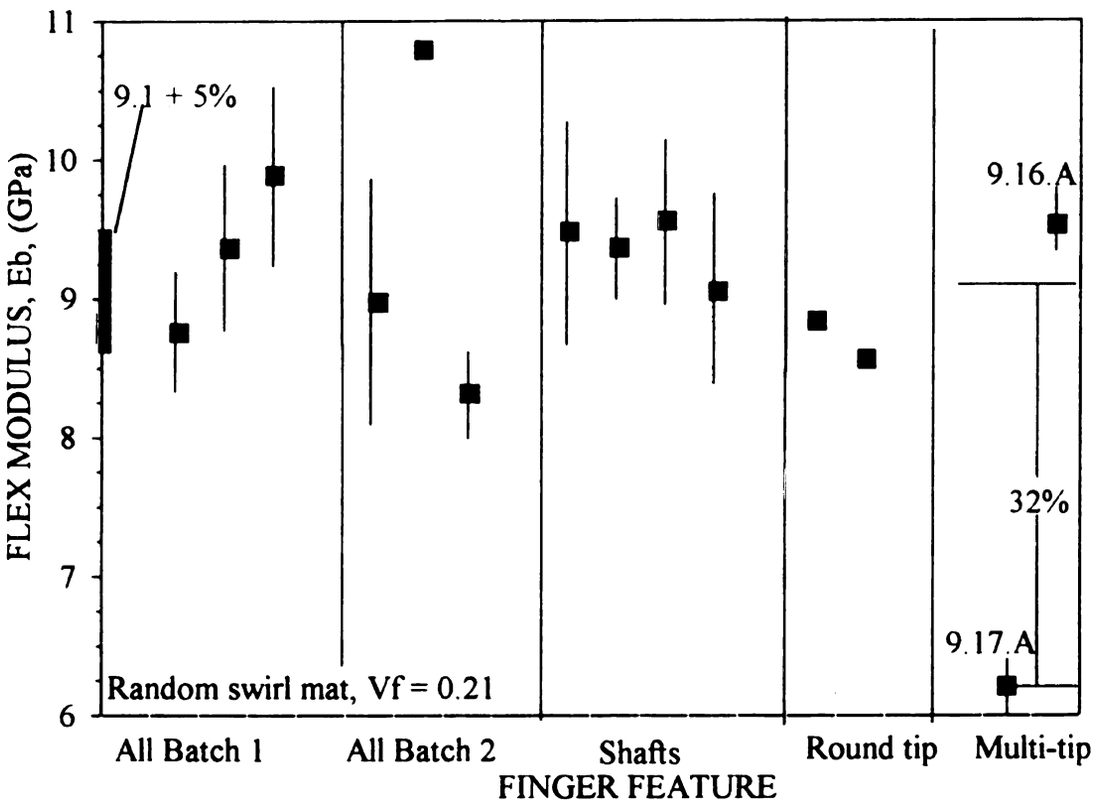


Figure 4.7: Results of the 3-point bend testing, random swirl glass preform, $V_f = 0.21$.

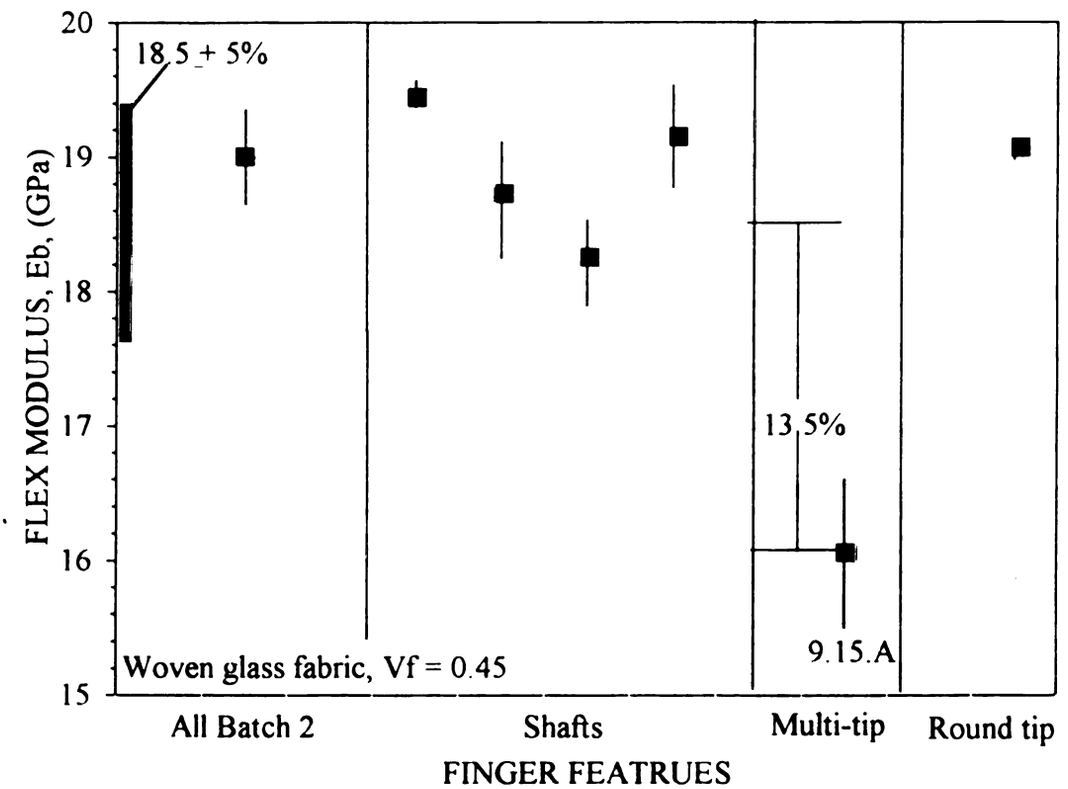


Figure 4.8: Results of the 3-point bend testing, woven glass preform, $V_f = 0.45$.

which had only one kind of resin (All Batch 1 or All Batch 2) or had simple interfaces (shafts) fall within the accuracy of the test. The single sample bar that contained a broadly rounded finger tip also falls inside the accuracy of the test. However, only some of the sample bars containing striations fall within the accuracy range. Striated samples from two other plaques have values of flex modulus which are lower by 8.2%, at 3.58 GPa.

The fact that the Batch 1 and Batch 2 samples all fall within the accuracy of the test is as expected. The only differences between Batch 1 and Batch 2 are dye content and mix time. Since the reaction is complete throughout the entire plaque by the time that the sample bars are tested, one packet of flawless resin should be as strong as another.

However, it was hypothesized that the presence of an interface between two resins of different ages would tend to decrease the flex modulus. This is contradicted by the results in Figure 4.6 that indicate that samples with a few (2 to 5) interfaces present have flex moduli which are well within the accuracy of the test. Perhaps the interface reaches the full strength of the resin because the resin packets have low conversion when they come together (according to literature, Derakane 411 resin gels at very low conversion, about 3%) or perhaps each interface is only incrementally detrimental to the flex modulus, and a larger number of interfaces will give lower values for E_b.

The rightmost column in Figure 4.6 represents the single instance of a broadly rounded finger tip that was sampled. The value of E_b for this sample fell well within the accuracy of the test.

The samples labeled "striated" were taken from areas where long thin areas of Batch 1 resin were trapped behind the flow front of the Batch 2 resin. The boundaries between the two batches were revealed by the presence of red dye in Batch 2. In Plaque 9.22.A, the boundaries of the striations were very faint, and only 5 or so were countable. This corresponds with the average value of E_b of 4.07 GPa. However, in Plaque 9.21.A, 17 interfaces were counted in the test span, and some had sharp boundaries (as delineated

Table 4.2: Summary of physical properties by type of fingering feature.

Plaque	Preform type	Finger feature	Flex modulus (GPa)
9.22.A	no preform $V_f = 0$	all Batch 1 all Batch 2 shafts striations	3.84 ± 0.27 3.92 ± 0.24 3.96 ± 0.12 4.07 ± 0.05
10.07.B (no age difference)	no preform $V_f = 0$	all Batch 1	4.04 ± 0.12
9.18.A	no preform $V_f = 0$	all Batch 1 shafts striations	3.87 ± 0.09 3.89 ± 0.17 3.59
9.21.A	no preform $V_f = 0$	all Batch 1 striations shafts round tip	3.70 ± 0.06 3.57 ± 0.08 3.91 ± 0.08 3.98
10.06A (no age difference)	random mat $V_f = 0.21$	all Batch 1	8.76 ± 0.43
9.17.A	random mat $V_f = 0.21$	all Batch 1 all Batch 2 shafts round tip multi-tips	9.37 ± 0.59 8.98 ± 0.88 9.47 ± 0.80 8.84 6.20 ± 0.20
9.16.A	random mat $V_f = 0.21$	all Batch 1 all Batch 2 shafts, 1 - 2 shafts, 4 + multi-tips	9.88 ± 0.64 10.80 9.55 ± 0.59 9.36 ± 0.36 9.57 ± 0.22
10.12.A	random mat $V_f = 0.21$	all Batch 2 shafts round tip	8.31 ± 0.31 9.07 ± 0.68 8.56
9.15.A	woven fabric $V_f = 0.45$	all Batch 2 shafts, 1 - 3 shafts, 4 - 6 round tip multi-tips	19.00 ± 0.35 18.68 ± 0.43 19.47 ± 0.10 19.05 ± 0.07 16.05 ± 0.55
9.11.A	woven fabric $V_f = 0.45$	shafts, 1 - 2 shafts, 4	18.21 ± 0.32 19.15 ± 0.38

by the red dye) between Batch 1 and Batch 2 fluid. Similarly, Plaque 9.18.A about 11 interfaces were counted in the test span. None of the interfaces was very sharp, but the variation between dyed and undyed resin was easy to see.

Thus a large number of distinct interfaces seems to tend to reduce flex modulus in neat resin samples, while interfaces which are few in number or indistinct in boundaries does not.

PLAQUES WITH RANDOM MAT PREFORM

Figure 4.7 shows the flex modulus values for plaques with 3 plies of random swirl glass mat, $V_f = 0.21$. At the left of Figure 4.7, is the average and the ± 5% error bars. The average value of E_b for these plaques is 9.1 GPa, over twice the value for neat resin plaques. Thus, it is expected that any loss of modulus caused by flaws in the resin will be at least partly masked by the presence of the preform.

As in the neat resin plaques, the samples which contain all Batch 1 or all Batch 2 resin fall on the average, with one exception of Plaque 9.16.A, where the single sample of Batch 2 resin had a value of E_b = 10.8 GPa. This is 19% higher than the average of 9.1 GPa, and close inspection of the actual sample bar did not reveal any likely reason. It is possible that that particular point of the plaque had more glass fibers than average, but this explanation is discounted because 8 samples of a plaque made with identical reinforcement were incinerated to find the average fiber fraction, and the results showed that among the eight samples, the weight fraction of glass varied by only 3.4%.

Again, the sample bars containing up to 4 interfaces had average values of the flex modulus, and the two samples with broadly rounded finger tips also had average values of E_b.

The rightmost column in Figure 4.7 gives the flex modulus found for two sample bars which had multiple thin, pointed finger tips present. Each of these two bars was tested centered and eccentrically, as discussed above, and the two tests were averaged to

give the error bars shown. Since both finger structures were only about 3 cm wide, and centered in the bar, a large part of the finger structures could not be eliminated from the span in the eccentric test, so it is not known whether testing only half of the fingered structure would yield a different value for E_b. What the error bars do show, is that the flex modulus is reproducible on a single sample, when deformations are kept small.

The observation that these two bars, both labeled as having multiple finger tips, have such different values for E_b, leads to a close examination of the sample bars themselves. The bar with the higher value of E_b came from Plaque 9.16.A. The finger structure consists of many sharply pointed finger tips superimposed on a broader (approximately 3 cm wide) region of Batch 2 fluid. The tips themselves are about 1 mm wide, and the whole structure gives the impression of a paintbrush. As can be seen in Figure 4.9, the edges of the fingers are 'feathery' rather than sharp. The bar from Plaque 9.17.A had a value of E_b that was 32% lower than the average. The finger structure of this bar also looks like a paintbrush, but the finger boundaries are much sharper, as if there was less dispersive mixing at the edges of the fingers. Figure 4.10 contains a photo of this bar.

The fact that one fingered structure has indistinct boundaries and one sharp boundaries may be accounted for by differences in the transverse dispersive mixing of Batch 1 and Batch 2 resin during the injection of the resin. However, as discussed in Chapter 4, dispersive mixing depends upon the interstitial velocity of the resin, the details of the flow paths in the preform, and the time during the flow over which mixing could take place. These two plaques were made with identical preforms at identical volumetric flow rates. The sample bars were taken from areas in the plaques at similar distances from the inlet. The difference in dispersive mixing must have arisen because of the local velocity difference associated with the fingering flow, where a growing finger by definition advances faster than the bulk fluid.

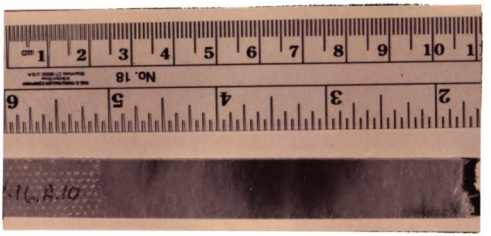


Figure 4.9: Multi-tip finger structure from Plaque 9.16.A. Note feathery edges to fingers.



Figure 4.10: Multi-tip structure from Plaque 9.17.A. Note sharp edges to fingers on bar number 1.

These results show that a multiplicity of tips is not sufficient to lower the flex modulus of a sample bar in which they appear. Tips with indistinct boundaries do not seem to be detrimental to the flex modulus, but multiple tips with distinct boundaries have lowered the flex modulus by 32%.

PLAQUES WITH WOVEN GLASS PREFORM

Figure 4.8 shows the flex moduli measured for the plaques which had 12 plies of woven glass fabric, $V_f = 0.45$. At the left of the graph is the average and ± 5% error bar. As discussed above, the presence of the preform is expected to mask to some extent the changes in the flex modulus which may have been caused by the fingering flow.

There were no sample bars which contained all Batch 1 resin. The sample bars with all Batch 2 resin, and 1 to 6 interfaces taken across finger shafts accord with the average value of 18.5 GPa, ± 5%. A single sample bar containing a broadly rounded tip also conformed with the average value of E_b for these plaques with woven fabric preform.

However, the sample which had multiple fingertips superimposed on a wider finger front suffered a 13.5% decrease in the flex modulus from the values prevalent elsewhere in the plaque. This sample was also tested centered and eccentrically. The fingered structure lay far enough from the center of the sample bar that eccentric testing could detect an increase in the value of E_b of 1 GPa by excluding about half of the fingered structure.

This finger structure also resembled a paintbrush, in that multiple thin finger tips protruded from a broader mass of resin, similar to the paintbrush structure discussed above. However, in the case of the woven fabric preform, each finger was more or less sharply delineated because it occupied the space between two tows in the preform, and transverse dispersive mixing was hindered by the presence of the tows. In other parts of the plaques with woven fabric preforms, fingertips were observed to span several intertow spaces, but in this case, each finger appeared to occupy a single intertow space. It may be that in this region of the mold, the 12 plies of preform were aligned perfectly one over the



other, so that each finger seen at the surface occupied a narrow intertow space which was continuous throughout the thickness of the mold, while other fingers occupied several intertow spaces at the surface because the spaces were not aligned in the thickness direction.

Again, simple interfaces and broadly rounded tips are not detrimental to the flex modulus of the plaque. Fingering structures with large numbers of fingers (at two interfaces each) which have sharply defined edges show a 13.5 % decrease in E_b from the average value in unfingered regions of the plaques.

CONCLUSIONS

RTM plaques with Derakane 411 resin were produced in which injection of resin with age differences ranging from 60% to 80% of the gel time produced viscous fingering flow. The interfaces formed by the fingers were sampled and tested in 3-point bend, to find whether the presence of interfaces between packets of resin which had different ages when they came into contact would be detrimental to the flexural modulus of the finished plaque. Plaques were made with no preform, with random swirl mat ($V_f = 0.21$) and woven glass fabric, ($V_f = 0.45$). In all three kinds of plaques it was found that interfaces which were few in number, or which had indistinct edges (as delineated by a gradient in the dye content across the interface) were not detrimental to the flexural modulus. However, sample bars which contained greater than 10 interfaces which could be characterized as sharp, or well-defined, lowered the flexural modulus significantly. Specifically, in the plaques with no preform, striated structures containing 11 to 14 interfaces decreased the flex modulus by 8.2%. In plaques with random swirl mat preform, a finger structure with greater than 20 interfaces which could be characterized as distinct suffered a 32% loss of modulus, while a similar structure with indistinct interfaces suffered no loss of modulus. In plaques with woven fabric reinforcement, a multiple finger structure with distinct edges had a decrease in flexural modulus of 13.5%.

Thus, it can be concluded that interfaces between resin packets of different ages are not detrimental to the flexural modulus of the plaques in which they occur, unless the interfaces are very numerous in any given locale, and have distinct edges. Interfaces which show some mixing between the two resins, and thus have indistinct edges do not show decreases in flexural modulus compared to the values typical for a plaque.

CHAPTER 5

INVESTIGATION OF THE STRENGTH OF THE INTERFACE FORMED BETWEEN RESINS OF DIFFERENT HISTORIES

INTRODUCTION

The experiments reported in Chapter 4 showed that samples of RTM plaques that include several finger tips had reduced flex modulus compared to monolithic samples, or to samples with few and simple interfaces. If it is postulated that the interface at the tips of the fingers is the cause of this loss of modulus, then the next logical step is to test the strength of the interface that is formed when two resins with different histories come together.

Therefore, this chapter describes the production and testing of 2-ply plaques which contain large areas of interface, made by pouring resin into a flat plaque mold in two stages. The time lag between the first and second pour was varied from zero to twice the gel time. The interface that was formed between the two plies was then tested in short-beam shear to evaluate the effect of the age difference between the two plies on the shear strength of the interface. It was expected that plaques made with a small age difference would show greater interfacial strength than plaques made with a large age difference, for reasons discussed below. If the presence of the interface in the plaque proves detrimental to the physical properties of the plaque, then the rationale for avoiding fingering flows in RTM will have been established.

THEORY

Thermosetting resins are transformed from a liquid or a weak solid to a strong solid by the crosslinking polymerization reaction. In the case of the DGEBA/TETA system, the

primary and secondary hydrogens on the amine groups of the TETA react with the oxirane groups in the DGEBA to form ester linkages. Each TETA molecule can make six links, and each DGEBA can make two links. When stoichiometric amounts of the two resins are mixed and fully reacted, it is presumed that all the possible sites of reaction have reacted. Practically, this is not true, as some percentage of active sites will have been prohibited from reacting through steric hindrance, the presence of impurities, or some such. However, it is the crosslinks that give the finished resin its strength, and anything which interferes in large measure with the formation of crosslinks will lead to loss of strength in the finished part. In some cases, this is desirable, and reactive rubber molecules are included to add toughness to the finished part at the expense of lowering the tensile strength (Raghava, 1988). In any case, as the reaction proceeds, large molecules are built up from smaller units, the viscosity rises, and the volume may change. When some percentage of the active sites has been reacted, the reacting mass of resin gels, and becomes a weak solid. Prior to gelation, the liquid resin would have been unable to sustain strain when subjected to stress. After gelation, however, the resin can support stress, and stress may become molded-in, if it is not relieved.

When two masses of resin are brought together before the reaction is complete, the ultimate strength of the interface will be due to the formation of crosslinks across it. In thermosets, these crosslinks are chemical in nature, and may form from the first contact until the cure is complete. The rate of bond formation is limited by reaction kinetics before the gel, and limited by diffusion of the monomers through the polymer after gel. Crosslink density is limited by the number of unreacted sites near (molecularly speaking) the interface at the time of contact. Thus, we expect interfaces formed at low conversion to be as strong as the bulk of the resin, but interfaces formed late in the reaction to be weaker. If the reaction is poisoned at the interface, for example by the presence of oxygen, then we expect that the interface will be quite weak compared to the bulk of the resin.

Residual or molded-in stresses may weaken a thermoset part by giving rise to micro-cracks. They may also cause a material to behave anisotropically when subjected to externally applied stress. Very severe molded-in stresses can cause parts to warp when they are removed from the mold (Hull, 1987).

One common source of residual stress in a composite part is the mismatch of the coefficients of thermal expansion between the fiber and the resin. As the composite is heated or cooled, the resin and fibers swell or shrink volumetrically at different rates. If the resin is well bonded to the fiber, the interface between them is subjected to a good deal of stress (Hull, 1987). Thermosetting resins are also known to undergo volume changes during the polymerization reaction. These volume changes have been measured for the DGEBA/TETA epoxy resin and Derakane systems and the results reported in Chapter 2. Since some of the volume changes occur after the gel point of the resin, it is postulated that the difference in total volume change between two regions of resin which are bonded together at a time which corresponds to different points in their volume profiles may give rise to molded-in stresses which may have an adverse effect on the strength of the bonded interface.

The discussion below will focus on the effects expected when two samples of resin which are bonded together experience differential shrinkage. This will be followed by a discussion of the short beam shear test, as it applies to testing this kind of two-ply sample, then a description of the production and testing of the 2-ply plaques.

DISCUSSION OF STRESSES ARISING DUE TO SHRINKAGE

Figure 5.1 shows a schematic of a plaque which has an interface, similar to the plaques made for the study detailed below. The plaque was made by pouring a batch of resin into a mold, then waiting some number of minutes (Δt) to pour another freshly mixed batch of resin onto the first batch. This treatment causes an interface to be formed halfway through the thickness, parallel to the bottom of the plaque. When a material

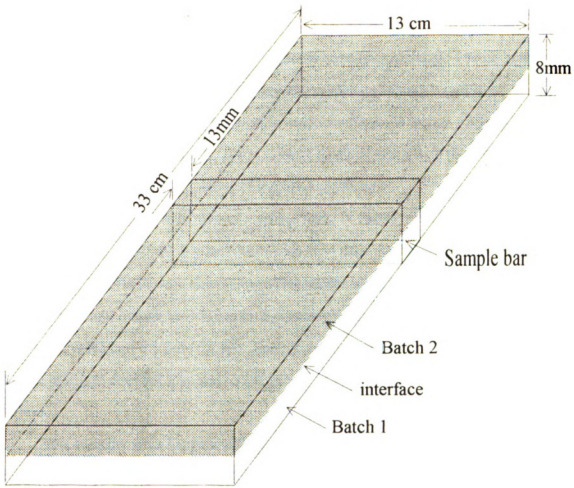


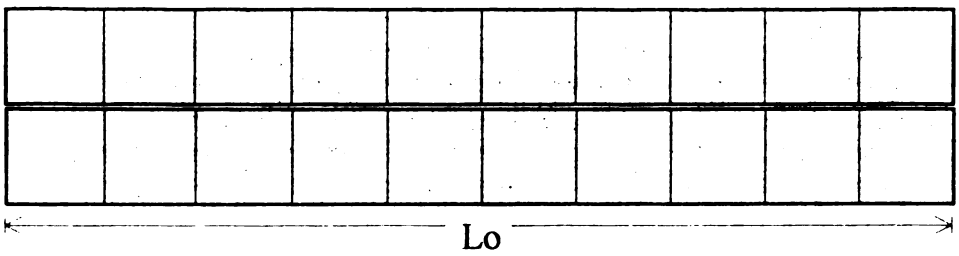
Figure 5.1: Schematic of a two-ply plaque.

shrinks volumetrically, there may be a preferred dimension in which the volume change takes place, depending on the constraints imposed on the material by adhesion to mold walls and the like. If two materials are bonded together before undergoing a volume change, they will influence each other through the bond (or interface). The net result will be molded-in stresses, which may cause physical properties of the plaques to be anisotropic with regard to the orientation in which the plaque is tested. Differential shrinkage in three different geometries is discussed below, along with the effect that each would have on observable properties of the finished plaque.

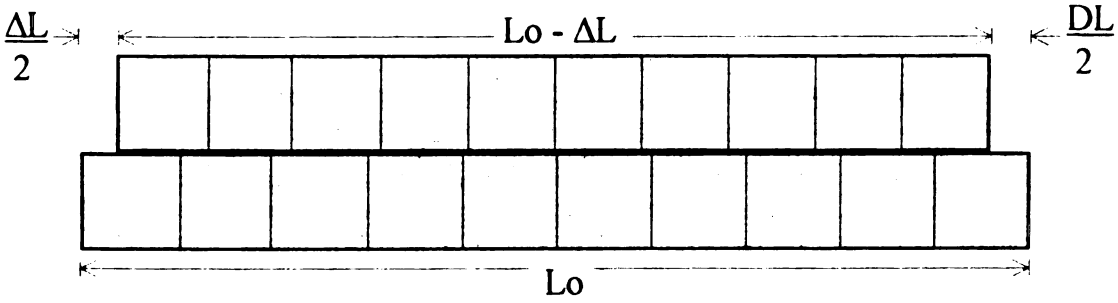
Figure 5.2 shows a side view of a plaque made of two layers of material in which top layer shrinks longitudinally and the bottom layer does not. Both layers are the same length initially. If there were no bonding at the interface, then the length of the top layer of material would change from L to $L(1-S_L)$, where S_L is the shrinkage, or the change in length expressed as a fraction (or sometimes a percentage) of the original length. This change in length does not give rise to any stress, because the bar is unconstrained as it shrinks.

Now consider what happens if the top layer is bonded to the bottom layer before it begins to shrink. The bonded interface between the two layers acts to constrain the two layers to move together. Because of this, the shrinkage of the top layer will act to shorten the bottom layer as well. If the layers are thin, warpage as shown in Figure 5.2C will result. Note that the final shape is an arc of radius r, under the assumption that all differential elements of the resin shrink the same amount. Also note that cross-sections which were planar in the undeformed sample remain planar in the deformed sample. If one were now to use force to flatten the sample, it becomes evident that in the flat configuration, the top layer is in tension, and the bottom layer is in compression. This means that the interface is in shear, and the shear stresses may become great enough to cause the adhesive bond at the interface to fail. The length of the flattened sample will be

Two plies initially same length.



Top ply shrinks; plies not bonded together.



Top ply shrinks; plies bonded together at interface.

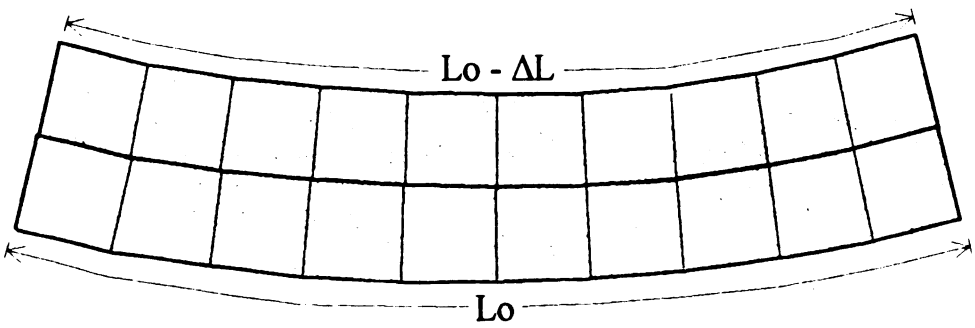


Figure 5.2: Schematic of a two-ply bar where shrinkage of top ply causes curvature

a compromise between the unconstrained length of the top layer, $L(1 - S_L)$, and the unconstrained length of the bottom layer, L. If both layers have the same thickness and modulus of elasticity, then the final length would be the average of the two, $L(1 - 0.5S_L)$.

If the layers are thick enough that no curvature is apparent, the stresses are nonetheless present. The net result of this kind of shrinkage would be that the top layer is in tension, and the bottom layer is in compression. If this plaque were tested in 3-point bending, as described in Chapter 3, then it would be found that the value of flex modulus obtained when the plaque was placed in the test fixture such that the load was applied to the top layer, and the bottom layer rested on the supports, would be greater than the value obtained if the plaque were placed in the other orientation.

Figure 5.3 shows a schematic of a situation where the volume shrinkage of the two layers takes place entirely in the thickness direction. The series depicts the steps in producing a two-ply sample in a flat rectangular mold with an open top. The resin for bottom layer is poured in and assumes the shape of the mold on the bottom and sides. Since it is a liquid at this stage, the resin forms a flat, level upper surface. As the resin begins to shrink due to reaction, the surface will become somewhat concave, if the resin at the sides of the mold adheres to the mold wall, and is constrained by it. At this point, liquid resin for the top layer is poured in. It, too, begins with a flat level top surface, which begins to become concave. However, in this case, the concavity is caused by the further shrinkage of the bottom layer added to the shrinkage of the top layer. If the layers were thin enough, this situation would lead to the warpage seen as the last of the series of Figure 5.3 . Note that this warpage is opposite in sense to that of the longitudinal shrinkage case above, i.e., if the sample is flattened, the top layer is in compression, and the bottom layer is in tension. When this plaque is tested in 3-point bend, the value of the flex modulus will be somewhat greater when the top layer is uppermost in the test fixture.

If, in the manufacture of the plaque described above, the top surface were not free to move, but was constrained by a top mold surface, then the shrinkage of the resin might

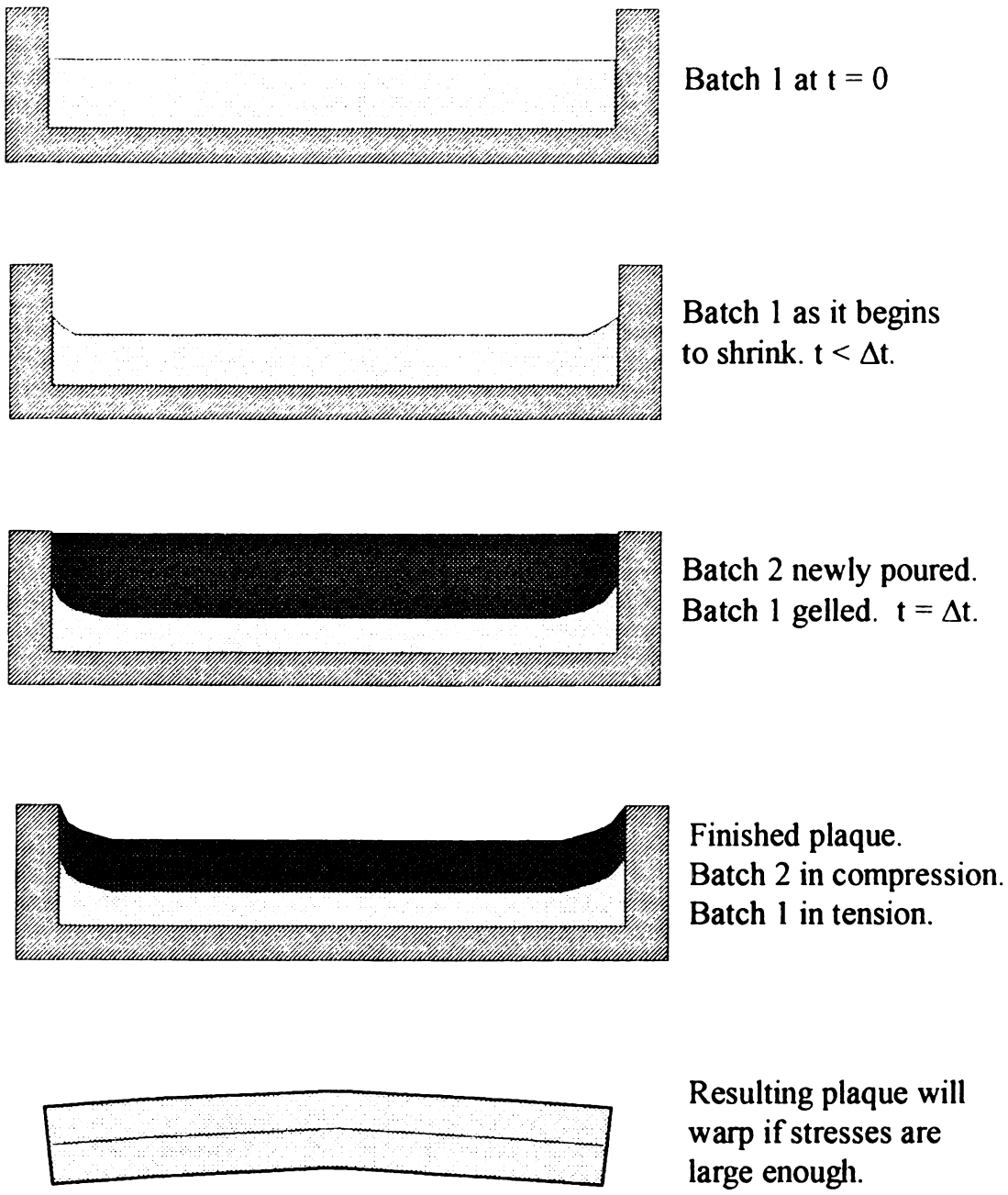


Figure 5.3: Schematic of a two-ply bar where shrinkage causes a change in thickness.

act to pull one or both plaque surfaces away from the mold wall. If the adhesion to the mold wall is good, and the adhesion at the interface is poor, the shrinkage may act to cause gaps in the resin at the interface. Consider Figure 5.4. A two-ply plaque is shown in cross-section. The resin is constrained on all sides by the mold wall. If it is considered that the shrinkage of each ply tends to put the interface in tension, then the tensile stress on a differential element of the interface may be calculated through the following argument.

The application of a tensile stress (σ_{xx}) to an elastic solid will cause a volume change that depends on the material properties:

$$\frac{V_f - V_o}{V_o} = \frac{\sigma_{xx}}{E_t}(1 - 2\nu) \qquad (5.1)$$

Where V_f is the final volume, V_o is the original volume, E_t is the Young's modulus, and ν is the Poisson's ratio. If the volume change is taken as that measured in Chapter 2, i.e. -0.3%, and handbook (Handbook of Epoxy Resins) values of the material properties are used

$$\sigma^* = 62.1 \quad \text{MPa}$$
$$E_t = 3.27 \quad \text{GPa}$$
$$\nu = 0.34$$

then the stress on the differential element is 31 MPa. This is about half of the tensile strength of the resin, and molded-in stresses of this magnitude would almost certainly be detrimental to the part in which they occur. In practice, the bond between the resin and the mold wall is weak, and the resin will tend to pull away from the wall before undue stress is applied to the interface.

The three examples of differential shrinkage on either side of a flat interface discussed above show how different boundary conditions between the resin and the mold may give rise to molded-in stresses in the finished part. In the two situations with a free

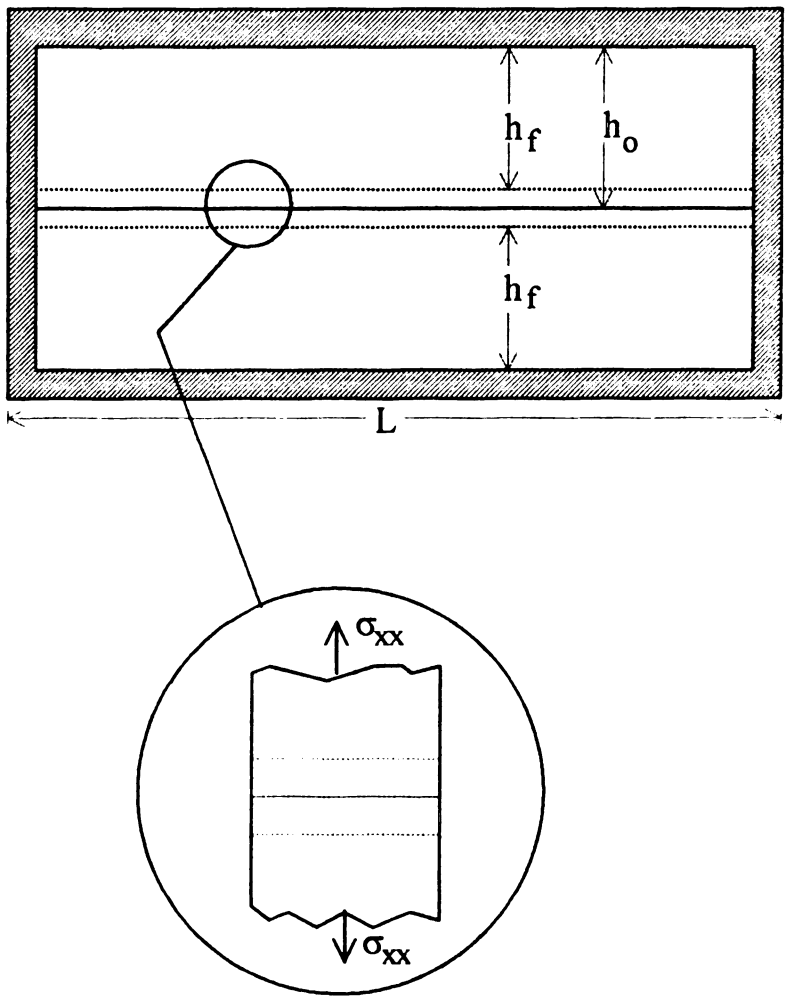


Figure 5.4: Internal stresses in a two ply plaque enclosed in a mold on all sides.

surface at the upper surface of the resin, there is shear stress on the interface. In the situation with a closed mold, there is tensile stress on the interface. The flat boundary conditions discussed above may be argued to be analogous to the shafts of fingers, or the tips of broad fingers, where the curvature is not very great. However, the tips of narrow fingers will have widths on the order of a few millimeters, and so a discussion of shrinkage at a curved interface is in order.

Consider Figure 5.5. A square plate of resin A contains a circular inclusion of resin B. The edges of the plate of A are considered to be fixed, so that all the area change due to shrinkage is manifested at the circular interface, if shrinkage in the thickness direction can be ignored. The situation depicted may be considered as either looking down the length of a finger, so that the thickness dimension of the plaque would be the vertical dimension of the figure, or as looking down onto a fingertip which has been doubled from a semi-circle to a circle to take advantage of the symmetry of the system to make the geometry easier. In this case, the finger width would be 2 R_o, and the root to root distance of fingers would approximate L.

At zero time, resin A and resin B meet at an interface which is circular with radius R_o. If the resins are not bonded at the interface, then the shrinkage of each resin will tend to pull it away from the interface, and the final result will be an annular gap, as shown by the dashed lines in the figure. The final radius of resin B will be R_B, and the final radius of the hole in resin A will be R_A. The initial and final volumes of the resins can be expressed as:

$$V_{A_o} = h\left(L^2 - \pi R_o^{\,2}\right) \tag{5.2}$$

$$V_{A_f} = h\left(L^2 - \pi R_A^{\,2}\right)$$

$$V_{B_o} = h\left(\pi R_o^{\,2}\right) \tag{5.3}$$

$$V_{B_f} = h\left(\pi R_B^{\,2}\right)$$

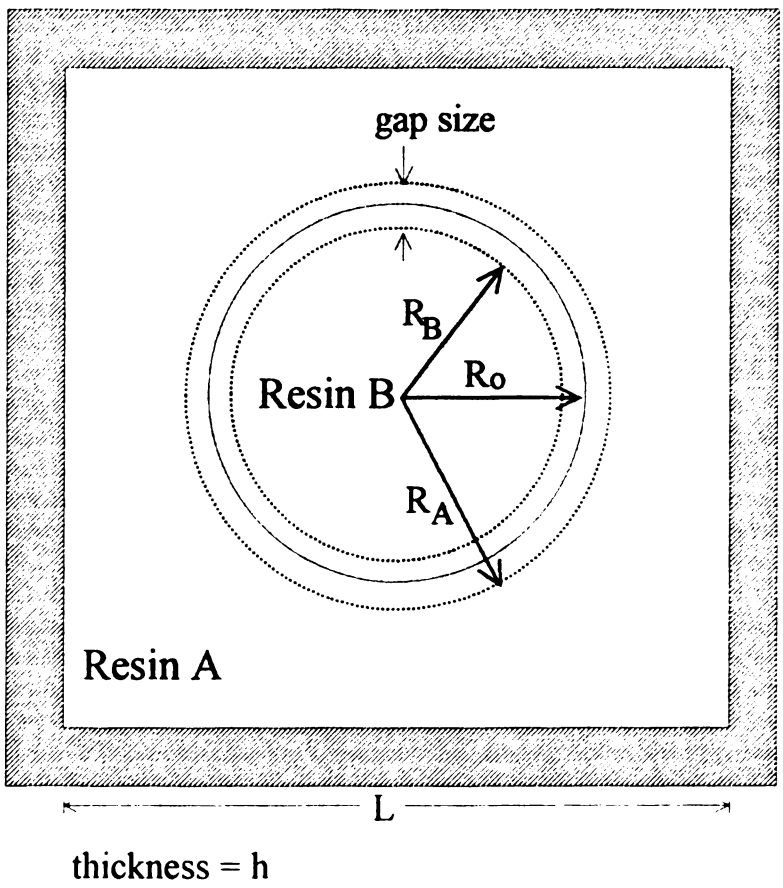


Figure 5.5: Schematic of volumetric shrinkage in a system with a curved interface.

Where h is the thickness, and the subscripts (o) and (f) denote the initial and final conditions.

If the two resins are bonded together, then they exert stress on each other through the interface, and neither resin will actually change volume. The stress at the interface can be estimated through the following argument.

Hydrostatic pressure, that is stress acting on a body normal to its surface at every point, will cause the volume of the body to shrink by an amount which depends on the magnitude of the pressure, and on the material properties. (Gere and Timoshenko, 1984, pg. 322)

$$\frac{V_f - V_o}{V_o} = \frac{\underline{\underline{\sigma}}(1-2\nu)}{E_t} \qquad (5.4)$$

$$\underline{\underline{\sigma}} = \left(\sigma_{xx} + \sigma_{yy} + \sigma_{zz}\right) = 3\sigma_{xx}$$

E_t is the Young's modulus of the material, and ν is Poisson's ratio. The hydrostatic pressure causes the volume to decrease. If the sign of the stress were changed, then the stress would be applied normally outward from the surface, tending to increase the volume. The magnitude of the stress needed to expand resin B from R_B to R_o, or equivalently, to keep resin B from shrinking from R_o to R_B is:

$$\sigma_B = \frac{h\pi\left(R_o^{\,2} - R_B^{\,2}\right)}{h\pi R_o^{\,2}} \frac{E_B}{3(1-2\nu_B)} \qquad (5.5)$$

Similarly for resin A:

$$\sigma_A = \frac{h\pi\left(R_o^{\,2} - R_A^{\,2}\right)}{h\left(L^2 - \pi R_o^{\,2}\right)} \frac{E_A}{3(1-2\nu_A)} \qquad (5.6)$$

These two stresses act to place the material at the interface in tension. If the material properties of the resins (E and ν) are alike, then the stress which the interface must withstand is:

$$\sigma_A = \sigma_B = \frac{E_t S_{VA}}{3(1-2\nu)} \qquad (5.7)$$

$$S_{VA} = 1 - \frac{V_{A_f}}{V_{A_o}}$$

$$S_{VB} = 1 - \frac{V_{B_f}}{V_{B_o}}$$

where S_{VA} and S_{VB} are the volume shrinkage of resins A and B. Note that the relative sizes of R_o and L do not explicitly affect the stress experienced by the interface. This is because the shrinkage occurs isotropically throughout the volume of the resin.

If the stress at the interface is greater than the tensile strength of the material at the interface, we would expect the interface to crack, delaminate or otherwise fail. As noted above, the Handbook of Epoxy Resins supplies physical properties:

$$\sigma^* = 62.1 \quad \text{MPa} \qquad (5.8)$$
$$E = 3.27 \quad \text{GPa}$$
$$\nu = 0.34$$
$$S_V \cong 0.03 \text{ to } 0.05 \quad \text{(literature)}$$
$$S_V = 0.003 \quad \text{(as measured in Chapter 3)}$$

Using Equation 5.7 and the first three values above, the total shrinkage which will cause failure of the interface can be calculated as 0.0167. This is larger than the shrinkage measured in Chapter 2, and one magnitude smaller than the literature values cited above. The value of S_V measured in Chapter 2 is only 0.003, and this would probably not cause failure, according to the analysis above, but the interface may be under so much stress that the addition of a comparatively small stress will cause it to fail.

The situation described above is probably the worst case. In an RTM molded plaque which contains fingers, some of the shrinkage will occur in the thickness direction, and will not put stress on the curved interface at the fingertip. Also, fibers which cross the interface will take some of the stress, and the interface may not fail. However, the above result indicates that even if the material at the interface is as strong as the bulk resin, the shrinkage at the fingertips will likely cause small cracks, and this will lead to a loss of physical properties, such as was observed in Chapter 4.

INTRODUCTION TO SHORT BEAM SHEAR TEST

The experiments with two-ply bars which are described below were intended to show whether the interface between two layers of resin which meet at different ages is as strong as the bulk of the resin, which is not involved with the interface. As discussed above, it is expected that differential shrinkage may cause detectable anisotropy in the sample bars cut from the two-ply plaques. The interface strength was tested in shear by means of the short beam shear test described below.

The short beam shear test measures the shear strength of an interface located in the center of a test specimen by applying a load at a point centered between two support points. A sketch of the test specimen and the test fixture is shown in Figure 5.6. When a load is applied at the center of the specimen, it will tend to be deformed into a section of an arc, with cross-sections which were planes staying planar, in the same manner as discussed above. Using this assumption, the shear and tensile stresses inside the specimen can be calculated as:

$$\sigma(x,y) = -\frac{6F}{bh^3}(L-x)y \qquad (5.9)$$

$$\tau(x,y) = \pm\frac{3F}{bh^3}\left(\left(\frac{h}{2}\right)^2 - y^2\right) \qquad \begin{cases} \text{positive if } 0 \le x \le L/2 \\ \text{negative if } L/2 \le x \le L \end{cases}$$

Where: F = load applied [N]
b = width of specimen [mm]
h = thickness of specimen [mm]
L = distance between support points [mm]
x, y and z are defined in Figure 5.6

)

Eq. (5.9) is valid throughout the sample bars for small deflections, but not for large deflections.

Figure 5.7 depicts the tensile and shear stress profiles experienced by the material of the specimen. The maximum shear stress occurs at the geometric center of the specimen, so an interface located at the center of the bar is tested in pure shear, with no tensile

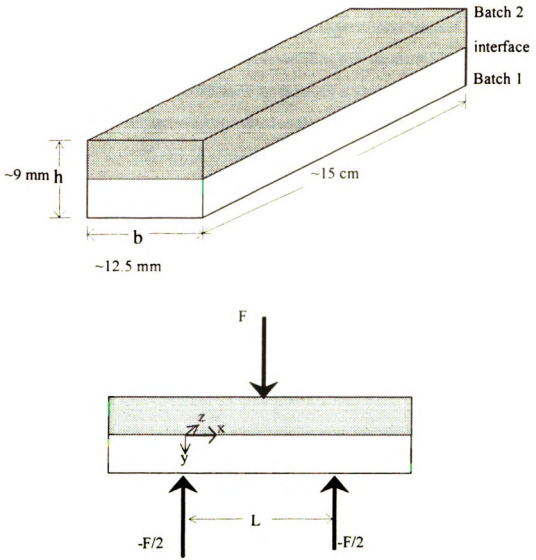


Figure 5.6: Sample bar and test coordinates for short beam shear test.

component. The tensile stress is maximum at the bottom "outer fiber" at the center of the specimen, and the maximum compressive stress is at the top "outer fiber".

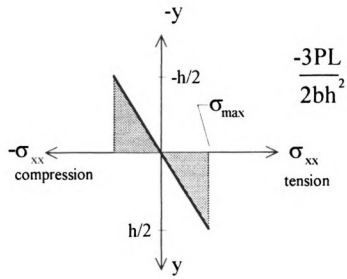
The short beam shear test involves loading the test specimen until it breaks, then noting the breaking load and the failure mode. [SACMA standard SRM 8-88] The breaking load may be used to calculate the breaking stress from the above equation, but it is not the tensile strength, which is defined as the breaking stress of a specimen loaded in pure tension, and which may be calculated as:

$$\text{tensile strength} = \sigma^* = \frac{F_{break}}{b_o h_o} \tag{5.10}$$

The stress in a specimen loaded in pure tension is uniform throughout the cross-section and throughout the test length of the specimen, whereas the tensile stress in a beam in bending is not uniform in either in the x or y direction, when deformations are large. The calculation above for the maximum stress in the specimen due to the short beam shear test does not give a value of the tensile strength of the material, only a maximum tensile stress value which can be used to compare results among similar specimens tested in a similar manner. The maximum shear and tensile stresses present in the specimen just as it fails can be calculated from the load which caused it to fail:

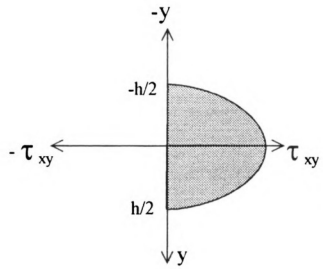
$$\sigma_{max} = 1.5\frac{F_{break} L}{bh^2}$$
$$\tau_{max} = 0.75\frac{F_{break}}{bh} \tag{5.11}$$

The maximum tensile stress calculated above is that which is calculated to be present when the specimen fails. Only a thin layer of material at the bottom of the specimen will have experienced this stress. All other material in the specimen will have experienced less stress due to the load, F. σ_{max} at break is inversely proportional to square of the thickness of the specimen bar. Thus, it is not considered valid to compare the maximum tensile stress at break between two samples of very different cross sections. For samples



$$\frac{-3PL}{2bh^2} = \sigma_{max} \quad \text{at } y=h/2$$

Tensile stress profile



$$\tau_{max} = \frac{.75P}{bh} \quad \text{at } y = 0$$

Shear stress profile

Figure 5.7: Tensile and Shear stresses within bar under 3-point bending.

of very similar cross sections, the test is considered to be accurate to ± 5%, if the samples are carefully made, and multiple samples are tested so that values are repeatable.

A two-ply plaque is assumed to be weaker than a monolithic plaque of identical dimensions, due to the presence of the interface. The upper bound of σ_{max} at break of two-ply plaques will therefore be equal to σ_{max} at break for a monolithic plaque. The lower bound can be calculated by considering the σ_{max} at break when two plies which have no bond whatever, not even friction, are tested in short beam shear. Each ply is of thickness h/2, for a total of h. The two are positioned in the test fixture as before, and the load is applied to the top ply at x = L/2. It is assumed that the load on the top ply is transmitted to the bottom ply as a distributed load instead of as a point load. Taking into account the thickness of the bottom ply as h/2, the maximum tensile and shear stresses a due to the distributed load on the bottom ply can be expressed as:

$$\sigma_{max} = 6\frac{FL}{bh^2} \quad \text{at} \quad x = \frac{L}{2} \quad \text{and} \quad y = \frac{h}{2}$$

$$\tau_{max} = 1.5\frac{F}{bh} \quad \text{at} \quad x = 0 \quad \text{and} \quad x = L \quad \text{and} \quad y = \frac{h}{2} \qquad (5.12)$$

The shear stress is a maximum at y = h/4, directly above the supports of the bar. This is due to the nature of the vertical shear stress profile in the distributed load configuration.

Note that for any given F short of break, the maximum tensile stress in the bottom ply of an unbonded pair is four times the maximum tensile stress in the bottom of a monolithic bar of thickness h. Thus, it is expected that whatever load is required to break a monolithic specimen will be four times the load needed to break a two-ply specimen with zero bond strength. This calculation will provide a convenient way to compare the strength of a weak interface with a theoretical lower limit.

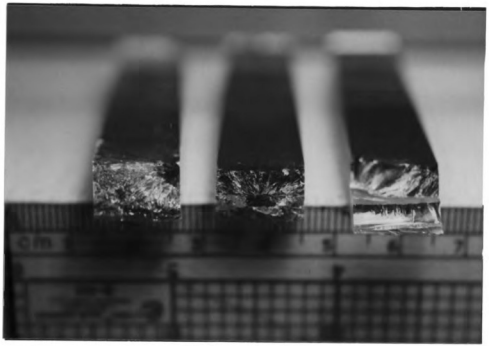
Much insight into the nature of the specimen can be obtained by examining the failure surfaces of the specimens. Brittle failures can be distinguished from crazing and

creep rupture by visual inspection. In brittle failures, the initial location of the crack, and its mode of propagation can be deduced (Morgan, et al., 1982). Figure 5.8 is a photograph of typical fracture surfaces of the two-ply specimen bars. The location of the initial crack can be seen as a small pit from which rays of craze marks emanate. There is also a region where the resin surface is as smooth as glass, taking up perhaps a quarter of the area. One specimen shows some delamination at the interface, as well. These phenomena will be discussed in more detail in the results section below.

Since neither the normal stresses (tensile and compressive) nor the shear stress is uniform throughout the cross-section of the specimen, it is expected that in an isotropic material, the failure will be initiated at a location where the stress is highest, i.e. tensile and compressive failure should be initiated at the tensile or compressive surfaces, but shear failure should be initiated at the center of the specimen. Even an isotropic material may be stronger in compression than in tension, so we expect to see either tensile or compressive or shear failures predominate. But, an isotropic material should have the same breaking stress whether it is tested "right side up" or "upside down" in the test fixture.

If the material is not isotropic, then the location of the crack initiation, and the values of the breaking stress when the material is tested in different orientations will yield clues to the nature of the material. For example, if substantial delamination occurs at a molded-in interface, then the interface may be judged to be the weak link of the material. If the failure occurs in the bulk of the resin, then it is likely that the failure occurred because of a defect, such as a bubble, because the bulk of the resin, away from the center and the surfaces, is carrying less stress than they are, and should not fail before they do.

The experiments described below were designed to produce plaques which had large areas of interface where two batches of resin of different histories had come together, thus emulating what might happen at the interface formed by fingering flow in RTM over large enough areas that statistically significant numbers of tests can be made.



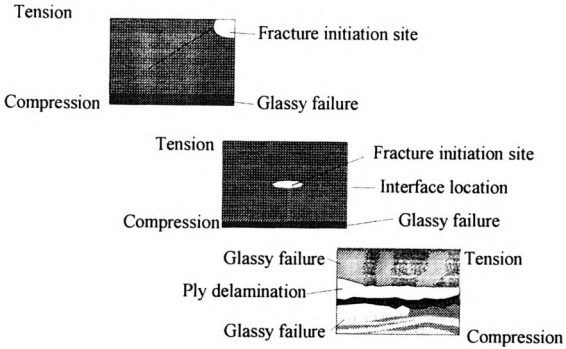


Figure 5.8: Typical fracture surfaces of two-ply bar specimens.

DESCRIPTION OF PLAQUE PRODUCTION

In order to produce large areas of interface for testing, plaques were cast in a horizontal rectangular mold by pouring one batch of resin onto the surface of another, older batch. The mold was open to the atmosphere at the top, and was heated by being placed in a forced-air oven. Figure 5.9 is a schematic of the plaque mold, including dimensions. The interior of the mold was sprayed with Teflon mold release before each plaque was cast. The casting was made in two batches: Batch 1 was mixed and poured into the mold at $t = 0$, and Batch 2 was mixed and poured at $t = \Delta t$. The first batch was mixed at room temperature and poured into a room temperature mold. The oven set point was then raised to 50° C. The resin components for the second batch were raised to 50° C before mixing, so that there would be no density difference due to temperature between the two resins when Batch 2 was poured in the mold. After Batch 2 was poured, the plaque was cured in the oven at 50° C for two hours before being stripped from the mold.

The resin used was the DGEBA/TETA epoxy system characterized in Chapter 2 and summarized in Table 3.5. The Batch 2 resin of some of the plaques also contained a small amount (<0.5%) of Oil Red dye, available from Aldrich Chemical Company. The dye was added so that the location of the interface between the two batches would be known. All plaques were duplicated with and without dye, and no differences due to the dye content were detected in the short beam shear testing.

Plaques with age differences (Δt) ranging from zero to 120 minutes were produced. The plaque with $\Delta t = 0$ gave samples to be tested in both short beam shear and pure tension. This "monolithic" plaque served as an example of the theoretical maximum short beam shear strength obtainable, and the theoretical minimum strength of a two-ply plaque was calculated as being 25% of the maximum strength, as discussed above.

Since the gel time of the resin was approximately 50 minutes at 50° C, $0 \leq \Delta t \leq 120$ minutes constitutes a wide range of age differences. Two plaques were made at each age difference except zero. Two plaques were also made with interfaces contaminated by

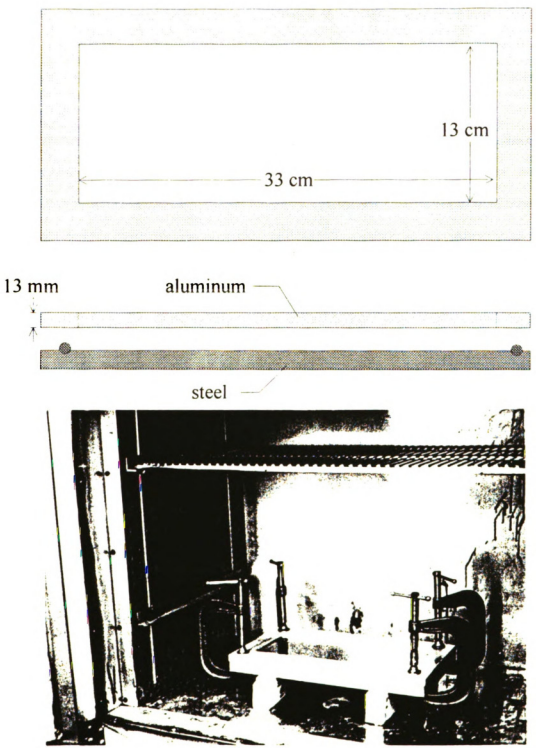


Figure 5.9: The horizontal plaque mold.

Teflon mold release spray. The spray was applied to the surface of the first batch after it had gelled, then was allowed to dry before the second batch was poured in. These plaques were to serve as controls. Their intentionally weak interfaces were expected to delaminate easily in the short beam shear test.

It was assumed that the polymerization in all plaques was complete, as all plaques were either post-cured for 2 hours at 100 °C, or were at least 20 days old at room temperature before being cut into specimen bars. The kinetics work reported in Chapter 2 shows that these measures should have been sufficient to assure that the reaction was complete.

The mold material was steel (i.e. good thermal diffusivity), and the plaque production took place in a convection oven with thermostatically controlled air circulated through it. It was assumed that these measures were enough to assure that the surfaces of the resin would remain near 50 °C throughout the cure cycle of the plaque. However, as discussed in Chapter 2, thick sections of curing resin may be unable to dissipate heat rapidly, and internal temperatures may be quite high. Therefore, a heat balance calculation was carried out using the handbook values of 500×10^{-6} cal/sec/cm^3/°C for thermal conductivity, and 0.3 cal/g/°C for heat capacity. The heat of polymerization was assumed to be generated as discussed in Chapter 2, with the total heat produced being 104.7 cal/g. An implicit finite difference method following Patankar (1980) was used, with a source term linearized to mimic the heat production as a function of temperature and reaction extent at any time. The result was that the maximum temperature of the plaque was calculated to be 9 °C above the surface temperature of 50 °C, peaking at 255 seconds into the reaction. This indicates that the plaques were produced under nearly isothermal conditions, and no dangerous exotherms were experienced.

DESCRIPTION OF PLAQUE TESTING

Plaques were cut into specimen bars, the dimensions of which were approximately: L = 15 cm, b = 12.5 mm, and h = 9 mm. Obvious flaws such as cracks and bubbles were

avoided when selecting sample locations. The samples were tested in short-beam shear using a United Testing Systems test frame, according to SACMA standard SRM 8.88. The distance between the supports was 31.8 mm (1.25 in) and the crosshead speed was 1.27 mm/min. (0.05 in/min.). The load cell was rated for 4448 N (1000 lb_f), and was accurate to ± 5%. Dimensions of specimens were measured to ±0.01 mm.

From each plaque, five specimens were tested with Batch 1 in tension while in the test fixture. Five more specimens from each plaque were tested with Batch 2 in tension (i.e. upside down), so that in all ten specimens were tested per plaque. As per standard, the load on the test fixture was increased until the specimen fractured. Then the value of the load at break was recorded, and specimen fragments were collected for visual inspection of the fracture surfaces. Manual notes were made of the stress/strain curves, and a majority were linear, but a few samples showed a small amount of plastic deformation before failure. Numerical results are presented in Table 5.1. The table containing the results of the visual inspection of the specimen fragments appears in Appendix C, and is summarized below in Table 5.2.

PLAQUE TESTING RESULTS

Table 5.1 summarizes the shear stress (τ_{max}) and tensile stress (σ_{max}) in the specimens at break. Each entry is the average of five specimens. Seven values of Δt are represented, as well as two plaques in which the interface was contaminated with Teflon mold release spray. As discussed later, visual inspection showed that nearly all of the sample bars failed in tension. The values of τ_{max} recorded indicate the shear stress present at the interface when failure occurred, but since the failures were not due to shear stress τ_{max} is not indicative of the strength of the interface. Therefore, it is the values of the maximum tensile stress (σ_{max}) in the bar at failure which will be discussed below.

Table 5.1: Numerical results of short beam shear testing.

			Batch 1 in tension		Batch 2 in tension	
Plaque ID	Δt (min)	$\Delta t/t_{gel}$	σ_{max} (MPa)	τ_{max} (MPa)	σ_{max} (MPa)	τ_{max} (MPa)
2.15.A	0	0	140	19.1	158	19.9
3.1.A	0	0	128	16.2	140	17.7
2.15.B	15	0.3	156	20.6	159	20.6
7.16.B	15	0.3	154	17.8	158	19.5
2.18.B	45	0.9	168	19.4	152	18.7
7.15.B	45	0.9	162	18.9	171	20.9
2.19.B	60	1.2	154	15.6	178	21.9
7.20.B	60	1.2	156	17.0	166	20.0
2.12.A	75	1.5	153	18.4	161	20.7
7.16.A	75	1.5	159	18.2	173	20.7
2.25.A	90	1.8	153	18.6	166	20.4
7.20.A	90	1.8	127	14.9	165	20.4
2.18.A	120	2.4	115	13.5	159	19.6
7.19.A	120	2.4	142	16.1	165	19.7
2.19.A	75 TEFLON	1.5	127	14.8	84	10.9
7.19.A	75 TEFLON	1.5	101	12.2	36	4.4

Figure 5.10 shows the average and standard deviation values of σ_{max} obtained from 5 specimens from each plaque when the specimens were loaded in the test fixture with Batch 1 intension, i.e. on the bottom. Note that the error bars indicate that the test is quite reproducible within a plaque. Also note that the average of σ_{max} tended to be highest when Δt was on the same order as the resin gel time of 50 minutes, but lower when Δt was much higher than t_{gel}.

Figure 5.11 shows the values of σ_{max} for specimens which were loaded in the test fixture with Batch 2 in tension. (i.e. upside down from their orientation in the mold.) Note that the error bars are narrower than before, and that the averages are also higher. Again, the highest values occur where Δt was comparable to t_{gel}.

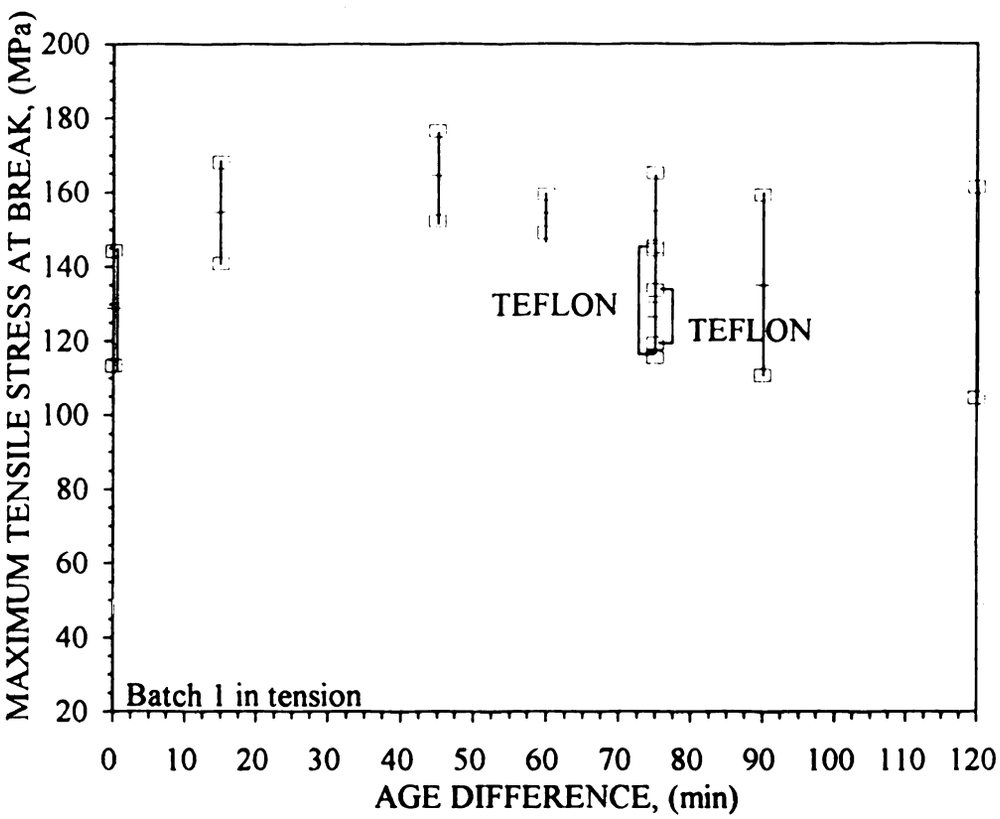


Figure 5.10: Maximum tensile stress in 2-ply specimen bars, tested with Batch 1 in tension.

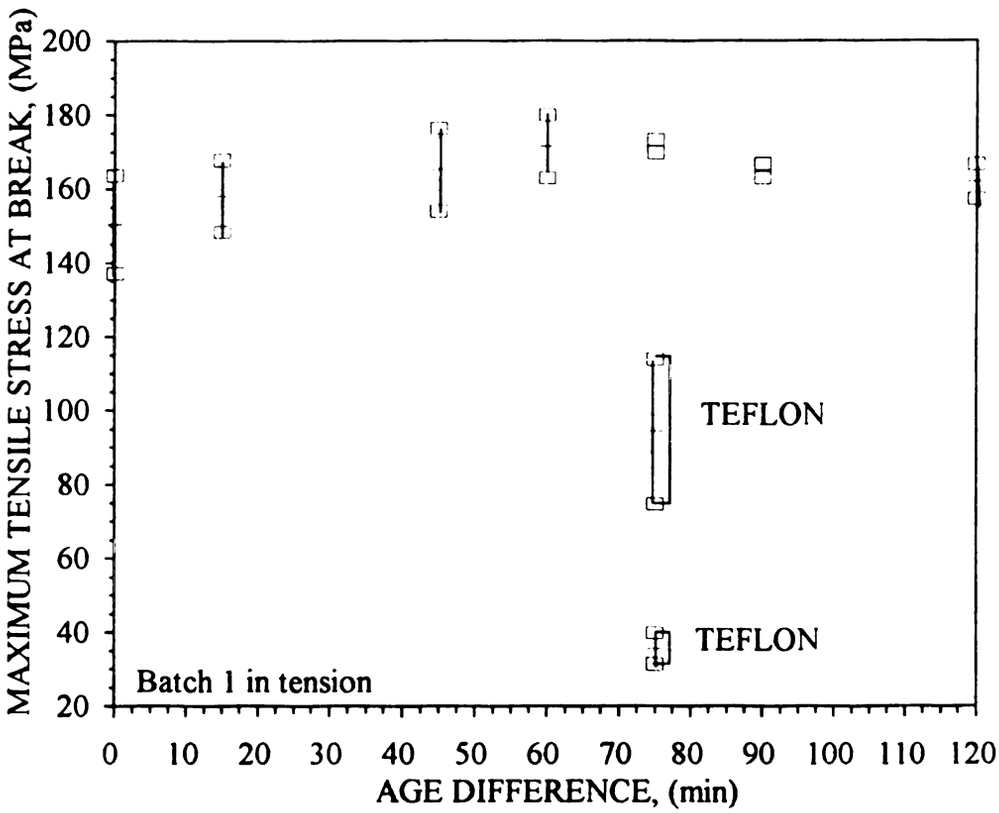


Figure 5.11: Maximum tensile stress in 2-ply specimen bars, tested with Batch 2 in tension.

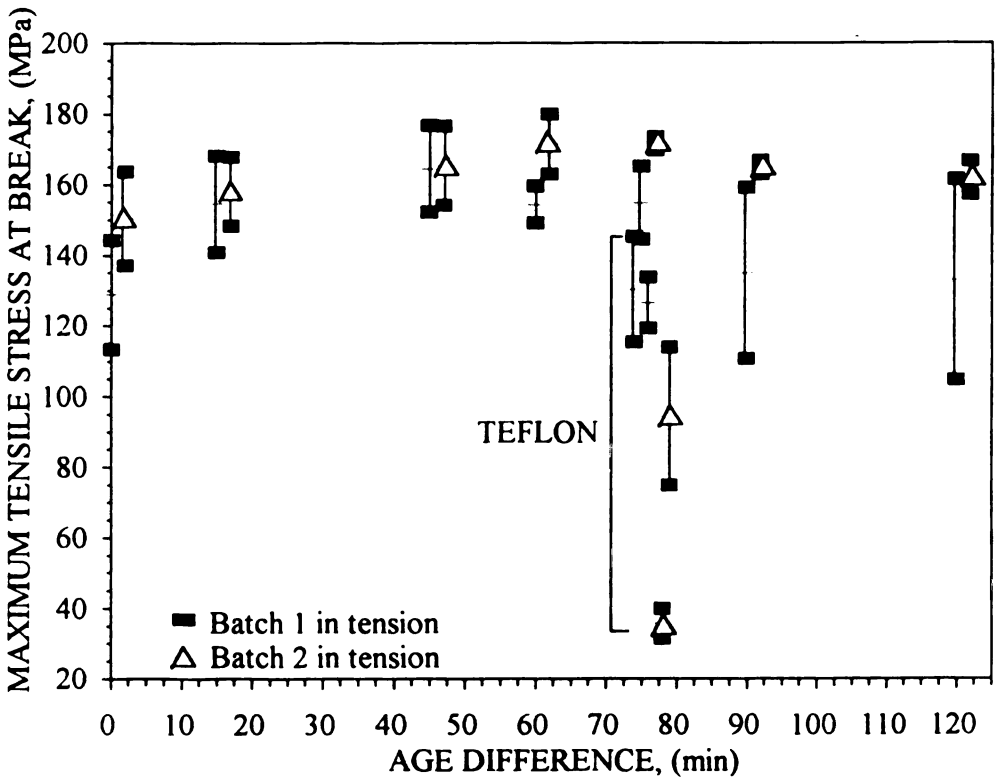


Figure 5.12: Comparison between the two test orientations.

Figure 5.12 compares the average values and error bars from Figures 5.10 and 5.11. In all but one plaque, the average σ_{max} was higher when Batch 2 was tested intension than when Batch 1 was in tension. In Figure 5.12 the error bars for the two conditions do overlap, indicating that the difference between the two orientations may not be statistically significant. However, there were distinct values of the load to break specimens in each orientation, and the differences were seen in all plaques but one. This slightly anisotropic behavior indicates that Batch 1 is prestressed in tension and Batch 2 is prestressed in compression, since resin which is prestressed in tension would show a lower value for the tensile strength than it would if there were no internal stress. This condition shows that the shrinkage of the resin in the thickness direction must be the primary cause of the residual stress, as discussed above. Indeed, when viewed in cross-section, the specimens look very much like Figure 5.3.

As expected, the specimens which had interfaces contaminated with Teflon spray were weaker than the uncontaminated specimens. The difference between the two plaques made with Teflon consists of a deliberate attempt to apply a light coat to one and a heavy coat to the other. This difference shows up quite clearly in Figures 5.10, 5.11, and 5.12, and confirms that a weak interface should be detected by this test. If the load to break a monolithic sample is 150 MPa, then the theoretical minimum for 2-ply plaques is 37.5 MPa, and some of the Teflon contaminated plaques achieve this. However, the average value of σ_{max} for these plaques is approximately three times the theoretical minimum.

Figures 5.10, 5.11, and 5.12 show that there is a small effect on the strength of the specimens due to the age difference between batches (Δt). However, the nature of the failure is not evident in these figures. Therefore, each specimen was inspected to evaluate the type of failure and the locus of the initial failure. It was expected that specimens which had weak interfaces would be distinguishable from those where the interface was as strong as the bulk resin.

The specimens for Δt's of zero and 15 minutes had no clear interfaces, as Batch 1 was still liquid when Batch 2 was added to the mold. All other specimens had clear interfaces, which were distinguishable visually, even in specimens which contained no dye.

Table 5.2: Summary of visual inspection of specimen fracture surfaces.

PLAQUE	Δt (min)	TENSILE SURFACE	TENSILE BULK	INTERFACE	COMPRES. FAILURE
2.15.A	0	8	0	0	0
7.15.A	0	7	2	0	0
3.01.A	0	10	0	0	0
2.15.B	15	6	3	0	0
7.16.B	15	9	1	0	0
2.18.B	45	4	5	1	0
7.15.B	45	9	1	0	0
2.19.B	60	3	7	0	0
7.20.B	60	8	2	0	0
2.12.A	75	8	1	0	0
7.16.A	75	8	1	0	0
2.25.A	90	4	5	0	0
7.20.A	90	9	0	0	0
2.18.A	120	4	1	3	0
7.19.A	120	9	1	0	0
2.19.A	75 TEFLON	3	0	6	0
7.19.B	75 TEFLON	2	0	8	0

Three typical patterns of brittle fracture were observed among the specimens. They are depicted in Figure 5.8, and Table 5.2 contains the summary of fracture types. All three specimens in Figure 5.8 are shown with the surface that was tested tension on top, that is, they are shown upside down from their actual test orientation. The locus of the crack initiation can be seen as a relatively smooth circle from which a pattern of cracks radiates. The left-hand specimen shows that the crack was initiated in the upper right corner. Thus, this specimen failed at the tensile surface, and cracks propagated directly

across the interface, parallel to the y-z plane. The center sample shows evidence that the failure initiated at the interface, and cracks radiate in both directions, i.e. toward both the tensile and compressive surfaces. The third sample shows glassy surfaces, and a large region where the crack propagated along the interface. This was from one of the plaques with an interface contaminated with Teflon.

Specimens from plaques with $\Delta t \leq 75$ minutes commonly failed at the tensile surface, or from within the bulk of the resin, on the tensile side of the interface. Only 10% of the specimens failed near the interface. This indicates that the interface is as strong as the bulk resin for these samples.

For the specimens where $\Delta t > 75$ min, failures at the interface, as depicted by the center sample in Figure 5.8, became 47% of the total. Thus, the interface may be considered the weakest point in 47% of these bars. That is, the interface is on average just as strong as the bulk resin for these samples.

CONCLUSIONS

The two-ply plaques were made and tested to show whether the interface formed when resins of different history are brought together is affected by the magnitude of the age difference between the two resins. It was concluded that the interface formed when Δt is less than $1.5 \times t_{gel}$ is at least as strong as the bulk resin, but that the interface formed when Δt is greater than $1.5 \times t_{gel}$ is approximatly as strong as the bulk. These results are based on inspection of the fracture surfaces of the specimens, and on the fact that the maximum tensile stress withstood by the specimens during the short beam shear test was not significantly affected by the magnitude of Δt.

Plaques with interfaces contaminated by Teflon, however, were only three times of the theoretical minimum of the short beam shear strength, instead of the factor of four expected of a plaque with a perfectly bonded interface. This indicates that it is possible to make interfaces which are weak enough to cause significant loss of short beam strength.

The fact that the specimens showed slightly different values of σ_{max} at break depending on their orientation in the test fixture indicated that the shrinkage of the resin in the thickness direction of the plaque as it cured was enough to cause some residual stress to arise in the plaques. These differences were within the accuracy of the test, but were consistent and repeatable nonetheless.

The fact that the residual stress caused by differential shrinkage across a plane interface was sufficient to cause a noticeable anisotropy in the short beam shear strength of the two-ply plaques lends weight to the argument made above that shrinkage across a curved interface may be sufficient to cause degradation of physical properties such as flex modulus at the locus of a finger tip. This would be a strong argument for avoiding fingering flows in RTM, and Chapter 6 explores the conditions under which fingering flows may arise in RTM situations.



MICHIGAN STATE UNIV
312930102

MICHIGAN STATE UNIVERSITY LIBRARIES
3 1293 01028 1834

LIBRARY
Michigan State
University

PLACE IN RETURN BOX to remove this checkout from your record.
TO AVOID FINES return on or before date due.

DATE DUE	DATE DUE	DATE DUE

MSU is An Affirmative Action/Equal Opportunity Institution

c:\circ\datedue.pm3-p.1

CHAPTER 6

ESTABLISHMENT OF FINGERING FLOW CRITERION FOR RTM

INTRODUCTION

As has been discussed in Chapter 1, several authors have investigated the stability of flows with viscosity gradients. The consensus is that any unfavorable viscosity gradient (i.e. viscosity increasing in the direction of flow) will tend to cause the fluid interface to develop fingers. However, fingers can be damped or prevented by density effects (in flows with a vertical component), or by dispersion effects (in flows where the two fluids are miscible). The surface tension between the two fluids does not tend to stabilize the interface against fingers, but it does influence the shape and size of the finger. All previous work focuses on flows where the viscosity of each fluid does not change with time, except locally at the interface, where dispersive mixing tends to flatten the viscosity gradient.

Chapter 4 showed that the viscosity gradients arising from the age difference of a reacting resin are sufficient to cause fingering flows. Chapters 4 and 5 showed that it is desirable to avoid fingering flows in RTM, to avoid loss of physical properties in the finished part. Therefore, it is the purpose of the present chapter to delineate a stability criterion for reacting resin flow such as might be found in RTM. Like the Saffman stability criterion, we expect the RTM fingering stability criterion to involve the flow velocity and the viscosity gradient, and we expect that the stability criterion will have the following features. Given a viscosity gradient which increases in the direction of the flow, an increase in the velocity of the flow is expected to both increase the tendency of the fluid interface to finger, and to increase the dispersive mixing which will tend to damp the

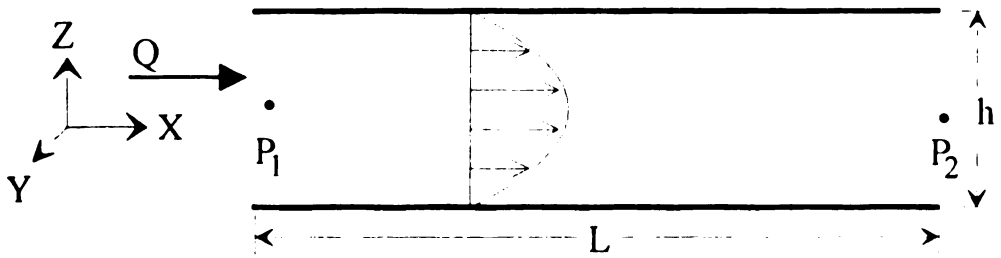
fingers. Thus, we expect fingers when the fluid velocity is between two critical values: the lower critical velocity will be great enough to cause fingers while the dispersive mixing is still small, and the higher critical velocity will be the value at which the dispersive mixing wholly damps out the viscosity gradient.

The stability criterion will also depend upon the viscosity gradient, and how it changes with time. Given a constant velocity, it is expected that there will be a minimum value of the viscosity gradient which will result in fingering. As the viscosity gradient increases, so will the tendency of fingers to grow. We do not expect an upper limit to the viscosity gradient, above which fingers will not appear, short of gelation. It is hypothesized that a stability criterion involving the flow velocity and the viscosity gradient can be formulated for the flow of a reacting fluid through a porous medium, and that the important factors will be the velocity of the flow, the magnitude of the dispersive mixing, and the magnitude of the viscosity gradient.

The theory section below describes the derivation of the important dimensionless quantities used for the analysis of the data from the fingering flow experiments. The fingering flow experiments were performed as described in the Experiment Description, which is followed by a discussion of the results and conclusions.

THEORY

Figure 6.1 defines the coordinate system and dimensions of the flow between two flat plates on which the following discussion is based. The resin enters at the left end, with a constant volumetric flow rate, Q. In the preform, the interstitial velocity is $U = Q/(bh\varepsilon)$. The flow in the RTM mold is assumed to conform to Darcy's law, and the fluid is considered incompressible, even though the volume is changing with the extent of reaction, as discussed in Chapter 2. The viscosity is also changing with the extent of reaction, thus the pressure drop through the mold is not constant with time.



$$V_y = V_z = 0$$

$$V_x = -\frac{\Delta P}{2\mu L}(y^2 - hy)$$

$$V_x = Q/A$$

Figure 6.1: Schematic of flow between two flat plates.

Suppose the reaction between the components of the epoxy resin involves components A and B and produces product P.

$$A + \upsilon B \xrightarrow{\mathcal{R}} P \tag{6.1}$$

Where υ is the stoichiometric coefficient. This is a very simplified picture since P participates in further reactions to form polymer. The reaction rate, $\mathcal{R}$, is defined as the moles of A consumed per volume, per time, or as the change in concentration of A over time, since volume is constant. Expressions for $\mathcal{R}$ have been derived in Chapter 2.

The concentration of reactant A in a unit volume at any time changes due to convection, diffusion, and reaction. The component balance is:

$$\frac{\partial C_A}{\partial t} + \underline{v} \cdot \nabla C_A = \mathcal{D}\nabla^2 C_A - \mathcal{R} \tag{6.2}$$

Taking the extent of reaction as the moles of A consumed over the moles of A at time zero, the concentration of A at any time can be expressed as:

$$\alpha \equiv \frac{C_{Ao} - C_A}{C_{Ao}} \qquad 0 \le \alpha \le 1 \tag{6.3}$$

Also, as discussed in Chapter 2 above, the reaction rate can be expressed as:

$$\left(\frac{d\alpha}{dt}\right)_{reaction} = \frac{\mathcal{R}}{C_{Ao}} = k_o \, exp\left[\frac{-E_a}{R_g T}\right](1-\alpha)^n \tag{6.4}$$

The component balance in terms of α is:

$$\frac{d\alpha}{dt} + \underline{v} \cdot \nabla \alpha = \mathcal{D}\nabla^2 \alpha + k_o \, exp\left[\frac{-E_a}{R_g T}\right](1-\alpha)^n \tag{6.5}$$

The equation of continuity and Darcy's law for this 1-dimensional flow are:

$$\nabla \cdot \underline{v} = 0$$

$$\underline{v} = -\frac{\kappa}{\mu}\nabla P \tag{6.6}$$

Where κ is the permeability, and P is the pressure. The viscosity is a function of the extent of reaction. Combining Eqs. (6.5) and (6.6) yields:

$$\nabla^2 P = \left(\frac{1}{\mu}\frac{\partial \mu}{\partial \alpha}\right)\nabla\alpha \cdot \nabla P \tag{6.7}$$

$$\frac{d\alpha}{dt} - \frac{\kappa}{\mu}(\nabla\alpha \cdot \nabla P) = \mathcal{D}\nabla^2\alpha + k_o \, exp\left[\frac{-E_a}{R_g T}\right](1-\alpha)^n \tag{6.8}$$

This pair of coupled, non-linear partial differential equations will now be non-dimensionalized by defining characteristic time and length scales. The time scale will be defined as the reciprocal of the kinetic coefficient (k^{-1} [=] time). This time is characteristic of the particular resin reaction being carried out, as discussed in Chapter 2. k has an Arrhenius dependence on temperature. In isothermal flows, however k may be considered a constant. The characteristic flow rate will be defined as the flow rate obtained from Darcy's law under initial conditions of the flow. The characteristic length scale is chosen as the thickness of the flow cell, h. In flows through porous media, the length scale is often taken as some characteristic length of the medium itself, instead of a characteristic of the mold. However, in this case, the flow through the preform is to be compared with the flow through a mold without preform, and the thickness of the mold, which is common to both flows, is the logical choice for a characteristic length. Thus, the characteristic quantities are:

$$k = k_o \, exp\left[\frac{-E_a}{R_g T}\right] \quad [=] \quad time^{-1}$$

$$U_o = -\frac{\kappa}{\mu_o}\nabla P_o \qquad [=] \quad length / time \tag{6.9}$$

$$h \qquad [=] \quad length$$

With use of these characteristic quantities, Eqs. (6.7) and (6.8) become:

$$\hat{\nabla}^2\hat{P} = \left(\frac{1}{\hat{\mu}}\frac{\partial\hat{\mu}}{\partial\alpha}\right)\hat{\nabla}\alpha \cdot \hat{\nabla}P \tag{6.10}$$

$$\frac{d\alpha}{d\hat{t}} - \frac{U_o}{kh^2}\frac{1}{\hat{\mu}}\left(\hat{\nabla}\alpha \cdot \hat{\nabla}\hat{P}\right) = \frac{\mathcal{D}}{kh^2}\hat{\nabla}^2\alpha + (1-\alpha)^n \tag{6.11}$$

Where the up caret (^) denotes a dimensionless quantity:

$$\hat{\mu} = \frac{\mu}{\mu_o} \qquad \hat{P} = \frac{P}{P_o} \qquad (6.12)$$

$$\hat{t} = tk \qquad \hat{\nabla} = h\nabla$$

Note that the permeability, κ, is not explicit in Eqs. (6.10) and (6.11) , as a consequence of the choice of a characteristic velocity.

The solutions of these equations will depend upon the dimensionless time and location coordinates, as well as the following dimensionless coefficients:

$$\frac{\mathcal{D}}{hU_o} = \text{Pe (Peclet number)}$$

$$\frac{1}{\mu}\frac{\partial \mu}{\partial \alpha} = \mathcal{M}\text{ (mobility ratio)}$$

$$\frac{U_o}{hk} = \mathcal{V}\text{(dimensionless velocity)} \qquad (6.13)$$

$$\frac{\mu}{\mu_o} = \text{viscosity ratio}$$

and any dimensionless quantities arising from the imposition of boundary conditions.

Table 6.1 gives values of the variables which are typical of the fingering flows discussed below. Given $\mathcal{D}$ as the molecular diffusivity, estimated at 1×10^{-5} cm^2/sec, the Peclet number ranges from 1.1×10^{-4} to 2.2×10^{-3}. Based on the dispersion constants measured in Chapter 3, $9.4 \times 10^{-3} \leq Pe \leq 3.27$. Thus, the diffusion is negligible with respect to the convection, but dispersion may or may not be.

The mobility ratio, as defined above, depends upon both extent of reaction and viscosity, which in turn depend upon the temperature and the age of the resin. Given $\mu(\alpha)$, derived in Chapter 2, $\mathcal{M}(\alpha(t,T))$ can be shown to be:

$$\mu(t,T) = \mu_0(T)\left[\frac{\alpha_g}{\alpha_g - \alpha}\right]^{(C_1 + C_2\alpha)}$$

$$\mathcal{M} = \frac{\partial(ln\,\mu)}{\partial\alpha} = \frac{C_1}{\alpha_g - \alpha} + \frac{\alpha C_2}{\alpha_g - \alpha} + C_2\, ln\left(\frac{\alpha_g}{\alpha_g - \alpha}\right) \qquad (6.14)$$

Thus, μ and $\mathcal{M}$ can be evaluated at any point of the mold for which the temperature and age of the resin are known.

Table 6.1: Ranges of dimensionless quantities for fingering flow experiments.

Quantity	Hele-Shaw	Random swirl mat	Woven fabric
porosity, ε	1.0	0.79	0.45
permeability, κ cm^2	1.92 x 10^{-4}	0.85 x 10^{-4}	0.74 x 10^{-4}
k min^{-1} @ 50 °C	0.0179	0.0179	0.0179
h cm	0.3	0.3	0.3
U_0 cm/sec	0.039 - 0.170	0.015 - 0.300	--
D_L cm^2/sec	0.0147	0.0134	0.0116
D_T cm^2/sec	0.000845	0.00136	0.00182
	Pe 1.4 x 10^{-6} to 2.9 x 10^{-4} (Based on dispersion)		
	Pe 1.1 x 10^{-4} to 2.2 x 10^{-3} (Based on diffusion only)		
	$\mathcal{V}$ 170 to 3360		
	$\mathcal{M}$ 2 to 60		

When the resin for an RTM process is mixed at time zero, the extent of reaction and the viscosity begin to increase, according to the relations for $\alpha(t)$ and $\mu(t)$ determined in Chapter 2. The interface of the fingering flow will be defined as the location where the fingers are being formed and/or can be observed. Figure 6.2 is a schematic showing that the reacting resin in an RTM mold will have a variety of ages, depending on the location of the resin in the mold. This is based on the assumption of plug flow in the mold, which

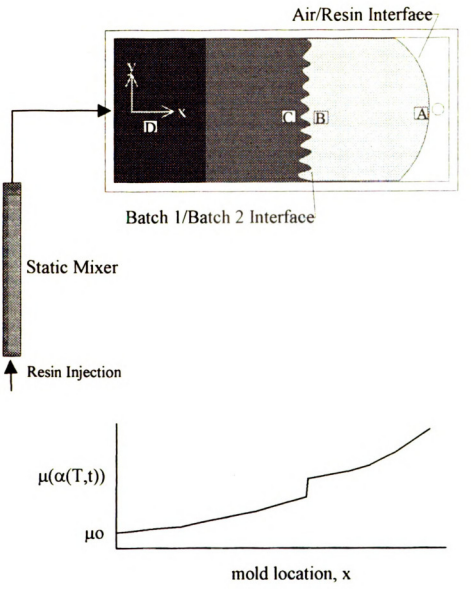


Figure 6.2: Illustration of resin ages in mold.

is observedly true for thin-section molds in absence of fingering. During the filling of the mold with resin, zero time is noted when the first resin enters the static mixer. The residence time (t_R) in the tube is determined as the time between the initial mixing of the resin, and the time it appears at the mold inlet. If the mixing of the resin is interrupted, i.e., the flow is stopped to differentiate between Batch 1 and Batch 2 resin, then the resins on each side of the interface so formed are different in ages by the delay time (t_D). Resin "packets" of interest in the present discussion are marked A, B, C, and D, and are discussed below.

Packet A is the resin at the interface between the first resin into the mold (Batch 1) and the air which it displaces. This will be the oldest resin in the mold, with the most advanced extent of reaction, and highest viscosity. This is the resin which will gel first, and the mold must be full before the gel time of this packet of resin is reached. The age ofthis resin at any time is simply the elapsed time since the resin entered the mixer, since that is taken as zero.

Packet B is the resin on the Batch 1 side of the interface. The interface location is (x_I, t_I), and moves with a velocity U_o. The age of the resin at B is calculated as:

$$B_{age} = t_R + t_D + \frac{x_I}{U_o} \tag{6.15}$$

Similarly, packet C is the resin on the Batch 2 side of the interface, and its age is:

$$C_{age} = t_R + \frac{x_I}{U_o} \tag{6.16}$$

The age of the resin at D is simply equal to the residence time of the resin in the mold inlet tube. This is the youngest resin in the mold, and it will have viscosity close to the viscosity of the resin feed just coming out of the mixer, μ_o.

Figure 6.3 shows viscosity of the resin in the mold versus mold location, calculated at several times during the filling of the mold. Points A, B, C and D correspond with the

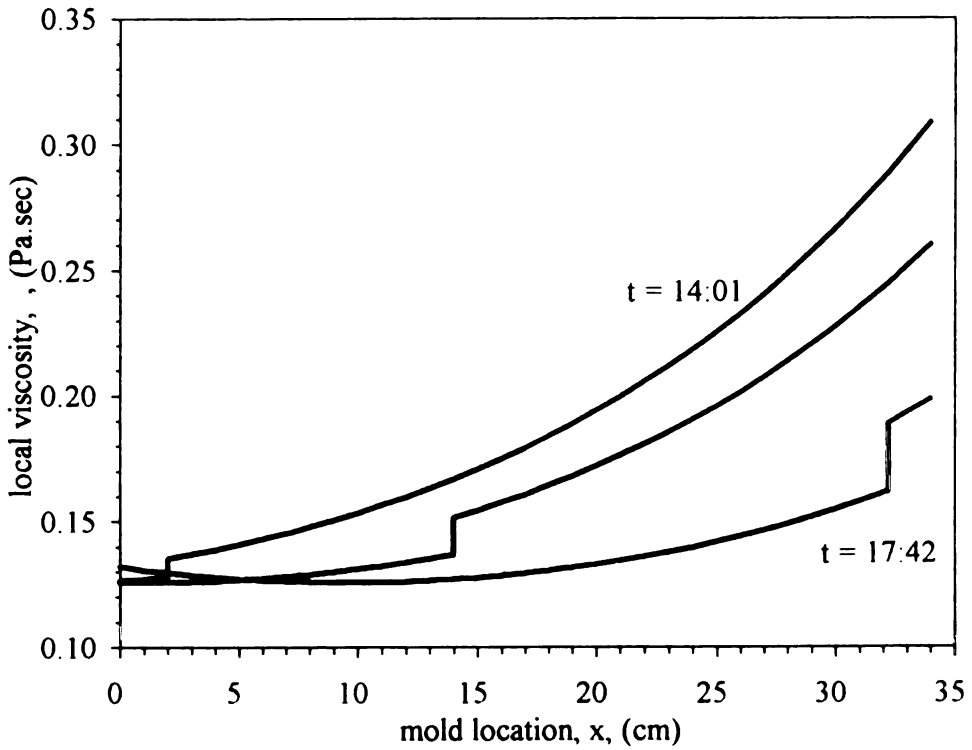


Figure 6.3: Viscosity profiles in the mold, calculated for resin temperature of 50° C, and several times.

resin packets A, B, C and D of Figure 6.2. Note that the viscosity jumps sharply between points B and C, and that the magnitude of the jump grows as time increases. This jump is due to the delay time between Batch 1 and Batch 2, as discussed above. In practice, the viscosity profile would tend to be spread out along some distance of the mold, due to dispersion. Over time, it would tend to take on an S-shape, rather than remaining a sharp jump. Based on the discussion of the literature given in Chapter 1, it is postulated that it is this rise in viscosity, locally at the interface between Batch 1 and Batch 2, that will give rise to the fingers.

The experiments described below were designed to emulate the flow rates, viscosities and fiber loadings typical of RTM. Table 6.2 compares typical values from literature with the experimental values. Due to the limitations of the molding equipment and the necessity of allowing fingers to form in the mold as opposed to the feed line, fiber volume fractions and resin velocities are on the low end of typical RTM values.

Table 6.2: Typical parameters for RTM processes.

	Present experiments	Typical RTM process
Mold thickness, h, (cm)	0.3	0.1 to 1.0
Resin velocity, U_0, (cm/sec)	0.01 to 0.3	
Resin viscosity, m, (Pa·sec)	0.144 to 100.	0.5 to 10
Fiber loading, V_f, (%)	18 to 21	15 to 60

Table 6.4 shows that the times involved in the injection of the resin into the mold for these experiments are quite long. In some cases, the injection time is more than 80% of the gel time. It was necessary to inject at low velocities to produce fingers which could be observed within the mold by the photographic methods at hand. It seems impractical to suggest that an actual RTM molding operation would see fingering flows in its operation,

as injection rates are so much higher. And yet, RIM and S-RIM operations routinely inject resin at such a temperature and velocity that the mold is full very shortly before the gel time. This is done to maximize production rates by minimizing the time that the resin must spend in the mold after the injection is complete. If the injection time is considered as a fraction of the gel time, the present experiments are comparable to actual RTM operations.

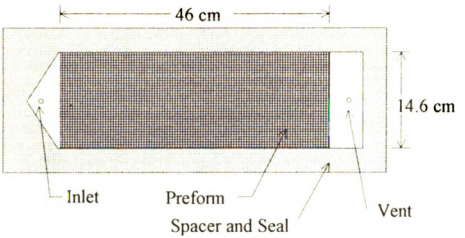
EXPERIMENT APPARATUS AND PROCEDURE

The resin system used for the fingering flow experiments was the DGEBA/TETA system formulated according to Table 3.1.

The mold used for the production of fingering flows is depicted in Figure 6.4. It is identical to the mold used in Chapter 3 for measuring the permeability of the porous media, except that for fingering flow experiments it was used end-gated instead of center-gated. The mold consists of an aluminum bottom plate, which has provision for being heated, an aluminum spacer with a silicone rubber gasket which sets the mold cavity thickness at 3 mm, and a Plexiglas® top. The Plexiglas is protected from the solvent action of the resin by a sheet of nylon release film.

The resin enters the mold from one end, spreads radially from the gate to fill the space between the gate and the preform, then enters the preform at its edge. The resin flow is thus rectilinear and parallel to the long axis of the mold, and the need to account for the z-direction permeability is obviated.

The resin is injected into the mold by the apparatus depicted in Figure 6.5. It consists of two pistons which feed into a static mixer, and thence into the mold inlet. The pistons are mounted in a frame which allows them to be driven by an Instron® mechanical testing frame. The Instron has cross-head speeds (S) which are listed in Table 6.3. The pistons are spaced in their frame such that each delivers a volumetric flow rate which corresponds to the mass flow rate necessary to deliver stoichiometric amounts of each



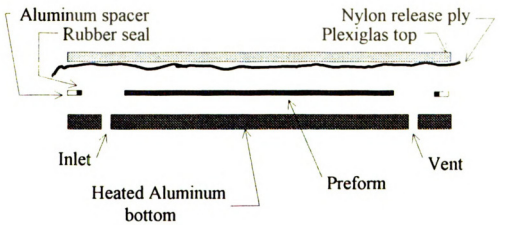


Figure 6.4: Schematic of the mold used in fingering flow experiments.

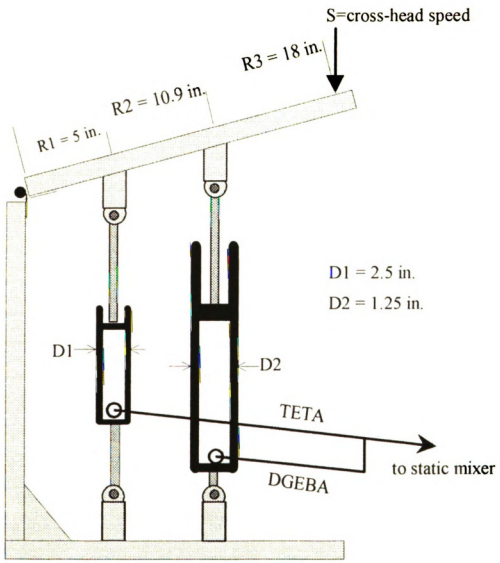


Figure 6.5: Apparatus for continuous in-line mixing and injection of resin.

component to the static mixer. The volumetric flow rates corresponding to S are also listed in Table 6.3.

Table 6.3: Injection speeds and volumetric flow rates used in the fingering flow experiments.

Instron speed S [=] in/min	Instron speed S [=] cm/sec	Volumetric flow rate Q [=] cm^3/sec	Mold fill time (min) $\varepsilon = 1$	Mold fill time (min) $\varepsilon = .85$
0.002	0.85×10^{-4}	0.0018	1849	2176
0.005	2.12×10^{-4}	0.0045	739	870
0.01	4.23×10^{-4}	0.0090	370	435
0.02	8.47×10^{-4}	0.0180	185	218
0.05	2.12×10^{-3}	0.045	74	87
0.10	4.23×10^{-3}	0.090	37	44
0.20	8.47×10^{-3}	0.180	18.5	22
0.50	2.12×10^{-2}	0.45	7.4	8.7
1.0	4.23×10^{-2}	0.90	3.7	4.4
2.0	8.47×10^{-2}	1.80	1.8	2.2
5.0	0.212	4.51	0.74	0.87
10.0	0.423	9.02	0.37	0.44

Experience showed that cross-head speeds of less than 15.2 cm/sec (0.1 in/min) produced flow rates which were not well-mixed in the static mixers, due to lack of momentum. A cross-head speed greater than 387 cm/sec (2 in/min) led to a pressure drop at the TETA nozzle great enough to cause TETA to leak by the piston seal. Thus, fingering flow experiments are limited to volumetric flow rates between 0.09 and 1.80 cm^3/sec due to the limitations of the apparatus. These limitations are noted on the moldability diagram presented in Chapter 7.

The piston containing the DGEBA was wrapped with heat tape, and the temperature controlled at 50 °C so that the viscosity of the DGEBA would be low enough to insure

good mixing in the static mixer. The TETA was used at room temperature, and was kept in a desiccator between runs to limit absorption of water.

The static mixer consisted of 7 sections, each 6 inches long, of 1/2 inch diameter static mixer units from Aldrich. Experience showed that the DGEBA and TETA were well mixed after the fourth section, when the volumetric flow rate was greater than 0.09 cm^3/sec.

PROCEDURE

The resin was injected in two stages. The first stage contained no dye, and was designated as Batch 1. When the mold was about half full of Batch 1, the injection was stopped and dyed TETA was substituted for the undyed TETA. The injection was then started again, so that the dyed resin of Batch 2 would displace the undyed Batch 1. The interruption of the flow of resin lasted about 2 minutes, and is called the delay time, t_{delay}.

The instant that the first resin in Batch 1 entered the static mixer was recorded as t = 0. The time was also noted when the injection was stopped, when it was restarted, and also when each photo was taken.

Photographs of the resin/air interface of Batch 1 were taken so as to establish the actual resin flow rate in the mold. Photographs of the interface between Batch 1 (undyed) and Batch 2 (dyed) resins were taken at intervals during the injection.

The experiment procedure can be summarized as follows:

1. Assemble mold. Heat mold and DGEBA cylinder to 50 °C.
2. Inject Batch 1 (containing undyed TETA). Note t = 0 when resin enters static mixer.
3. Stop injection and note time.
4. Drain undyed TETA from cylinder, add dyed TETA.
5. Restart injection and note time.
6. Observe and photograph flow fronts.
7. Stop injection. Close valves. Heat mold to 70°C, and cure resin.

EXPERIMENT RESULTS

Twelve runs were made with the above apparatus and procedure. Table 6.4 summarizes the conditions, including the type of porous medium (none or 3 ply Unifilo random glass mat), the injection speed, and the time of appearance of fingers. The 'residence time' is the time that it took the first resin to move from the static mixer to the inlet of the mold. As such, it is a measure of both the injection speed, and the length of the hose. The delay time is the time necessary to drain the undyed TETA from its piston, and substitute dyed TETA. This time will be taken as the age difference between Batch 1 and Batch 2 resin, and the viscosity gradient will be calculated from it.

The volume fraction of fibers was calculated from the mass of the glass mat and the dimensions of the mold, according to Eq. (4.1).

The velocity of the resin in the mold was calculated from the location of the advancing flow front observed in the photograph series for each run. This was taken to be a more accurate method than calculating the flow velocity from the volumetric flow rate, due to the possibility of short-circuit flow between the edges of the preform and the mold seals. Photographs do show that some short-circuiting is present, even though the preform was fitted as tightly into the mold as possible. A typical photograph series is shown in Figure 6.6, and is discussed in detail below.

Figure 6.6 consists of a series of 14 photographs taken during run 8.20.A. The mold inlet is visible as a dark circle on the bottom, and the flow direction is from bottom to top. The silicone rubber seal is visible as a broad V shape with its apex at the mold inlet, and running parallel to the flow direction at the left and right edges of the photos. There is no preform in this run, so the bottom of the mold, with round instrumentation ports, is directly visible through the clear resin. The timer in the photo reads in the format H MM SS ss. The small numbers are hundredths of seconds, and are not always resolvable by the camera, so time will be read as truncated to the second.

Table 6.4: Experimental parameters.

Run No.	S (in/min)	Preform	Residence time (sec)	Delay time (sec)	Velocity in preform (cm/sec)	Fingers (Y/N) (time in sec)
8.19.A	0.5	none	388	134	0.170	N @ 916
8.19.B	0.5	none	292	63	0.071	N @ 861
8.20.A	0.5	none	396	83	0.077	N @ 936 Y @ 975
8.20.B	0.2	none	462	87	0.044	N @ 2031 Y @ 2139
8.24.A	0.2	none	787	62	0.039	N @ 2102
8.24.B	0.2	random glass	818	52	0.036	Y @ 1871
9.9.A	0.5	random glass	442	120	0.100	Y @ 1135
9.9.B	0.5	random glass	347	240	0.100	Y @ 1292
9.17.A	0.1	random glass	1888	120	0.015	Y @ 3604
9.20.A	1.0	random glass	494	151	0.148	Y@ 1167
9.21.A	1.0	random glass	252	240	0.194	N @ 687
9.22.A	2.0	random glass	84	50	0.300	N @ 347

The grid laid over the mold is 1 cm square. Note that the grid in the photograph is not quite square due to the photographic printing process. Therefore, separate scale factors will be formulated for the x (with flow) and y (across flow) directions.

In photographs 1 through 4, the interface between air and the undyed resin of Batch 1 can be seen to be developing from circular to linear, thus showing that the bulk flow velocity becomes constant over the width of the mold. The line of the grid which passes over the mold inlet was taken as the reference line where x = 0. The distance from this line to the air/Batch 1 interface in photographs 3 and 4 was used to calculated the fluid

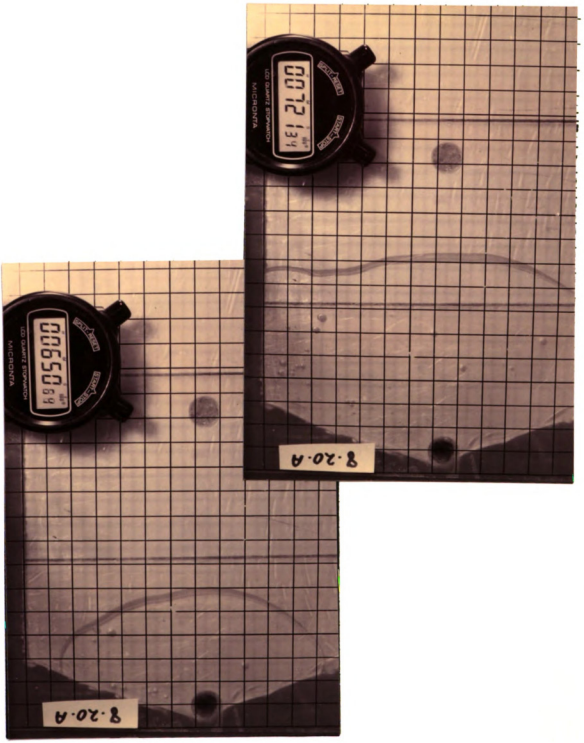


Figure 6.6: A typical series of photographs of a fingering flow experiment. Run 8.20.A, no preform, resin and mold temperatures 50° C.

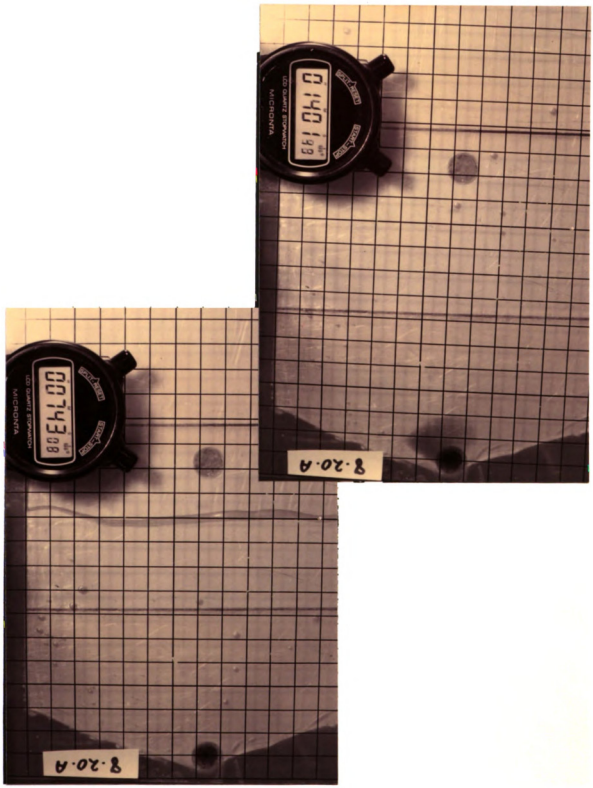


Figure 6.6 continued. Photographs 3 and 4.

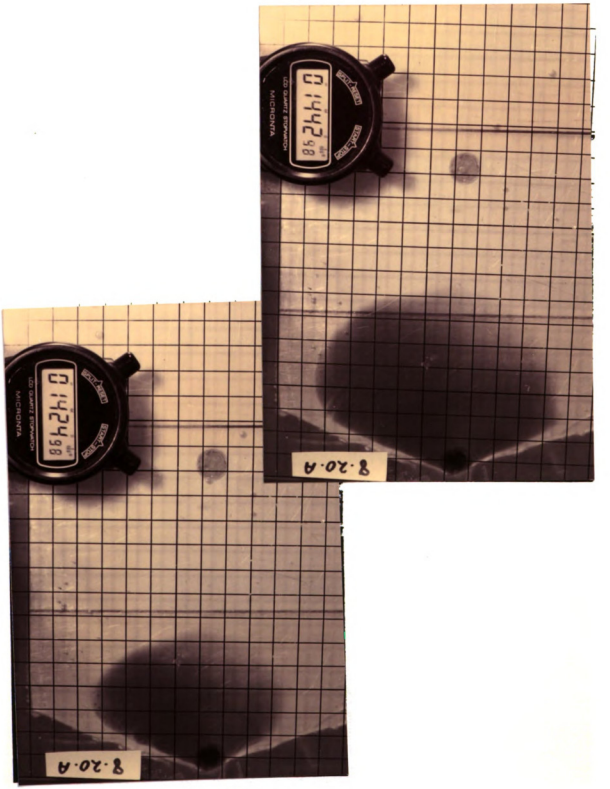


Figure 6.6 continued. Photographs 5 and 6.

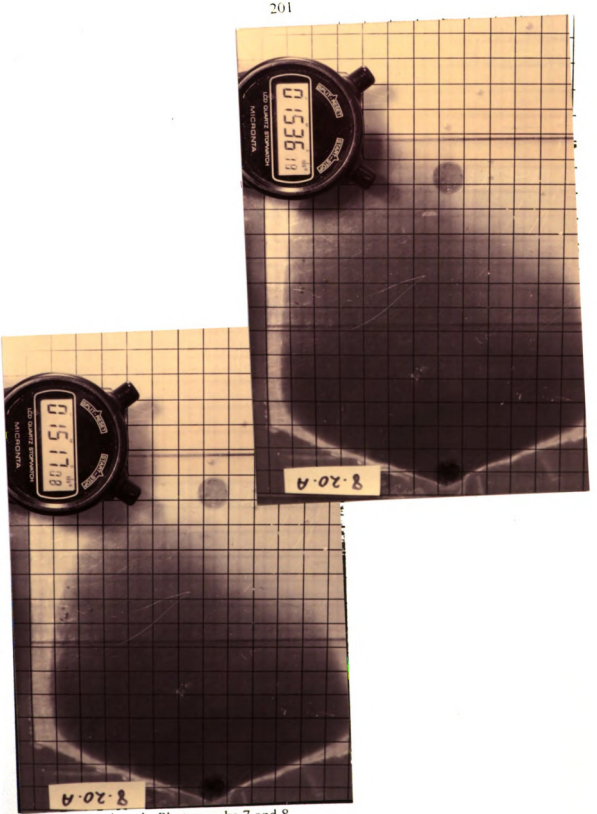


Figure 6.6 continued. Photographs 7 and 8.

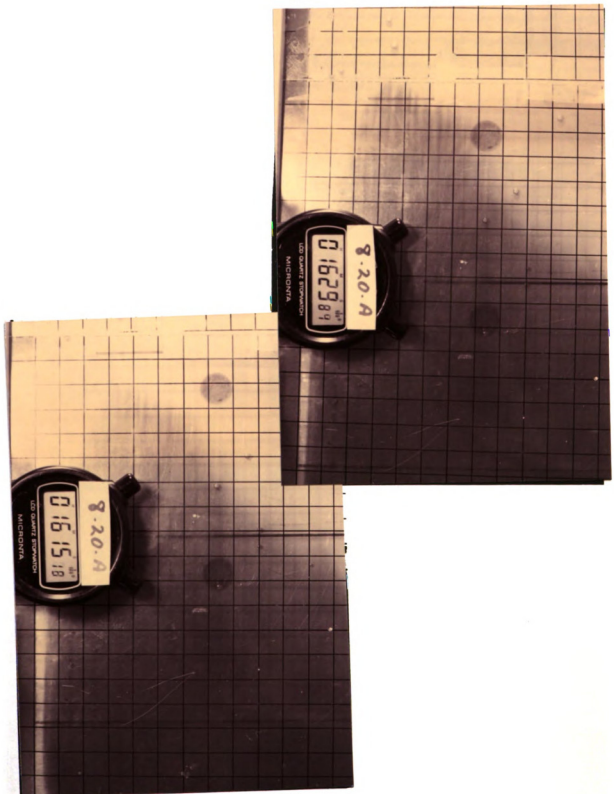


Figure 6.6 continued. Photographs 9 and 10.

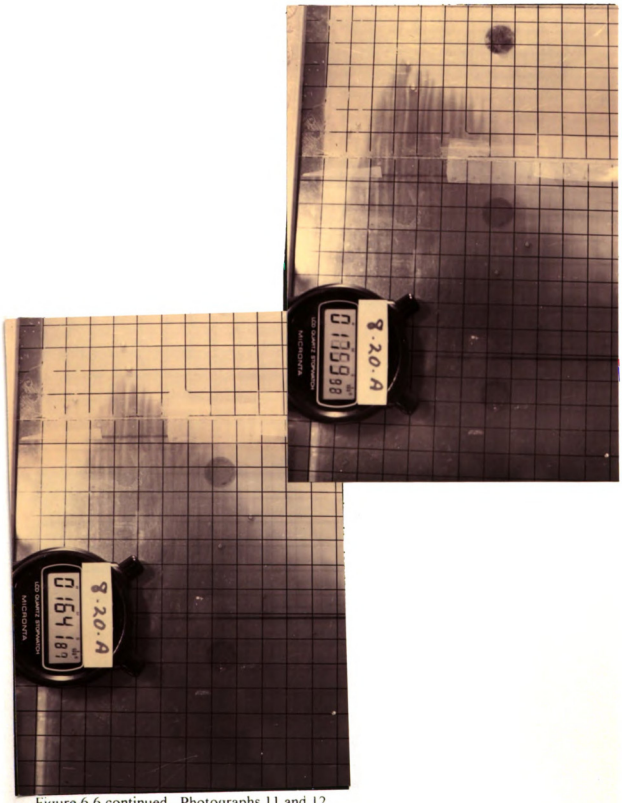


Figure 6.6 continued. Photographs 11 and 12.

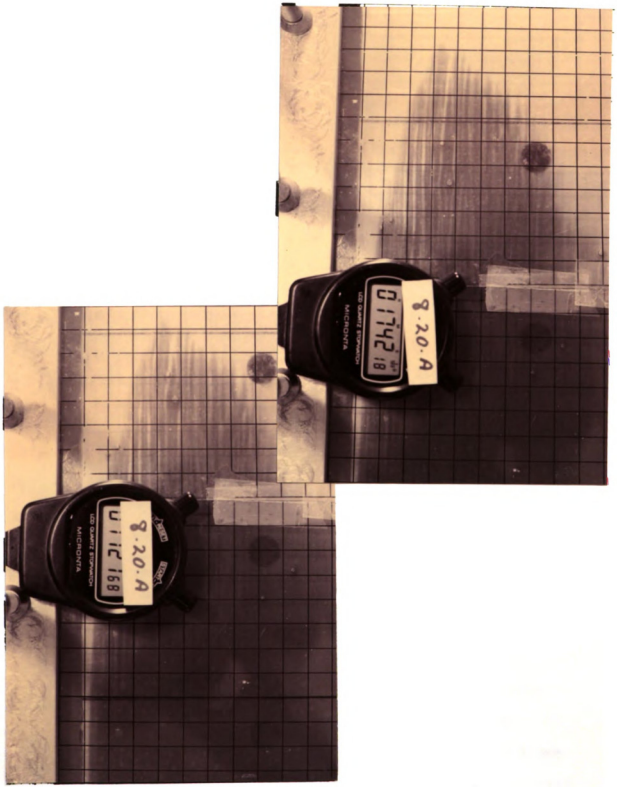


Figure 6.6 continued. Photographs 13 and 14.

velocity, which was assumed to be constant, because the volumetric flow rate was constant.

In photographs 5 through 14, the dyed resin of Batch 2 can be seen invading the clear resin of Batch 1. Batch 2 resin fans out from the inlet port, but does not come to occupy the entire width of the mold, as Batch 1 does. This failure to displace the fluid along the edge of the mold is a consequence of the no-slip boundary condition. Similarly, we expect the top and bottom sides of the mold to be thinly coated with Batch 1 resin. Saffman (1958) says that this boundary layer may be ignored in the analysis, if it is of constant thickness.

Photo 8 shows that the leading edge of Batch 2 has a concentration gradient, which is attributable to longitudinal dispersion, as discussed in Chapter 3. As of yet, no fingers are visible.

Fingers become visible in photo 10. They are superimposed on the oval outline of the interface between Batch 1 and Batch 2, and are not very well defined. However, the subsequent photo shows the fingers as having definite tips and widths, and these become more developed through the next three photos.

Each experiment run has such a series of photos, and all are present in Appendix C. It should be noted that several of the runs did not develop fingers, and that some runs did not have a fingerless period, but developed fingers as soon as Batch 2 entered the mold.

It was necessary to define the length and width of fingers as shown in Figure 6.7. Each finger was numbered and traced through the series of photographs, measuring its tip location in relation to the reference line. Scale factors were formulated for each set of photographs, and used to express tip location and tip width in units of centimeters. All identifiable fingers were measured, although those which were on the edges of the main flow front were ignored in later analysis. Fingers which grew wider during their careers

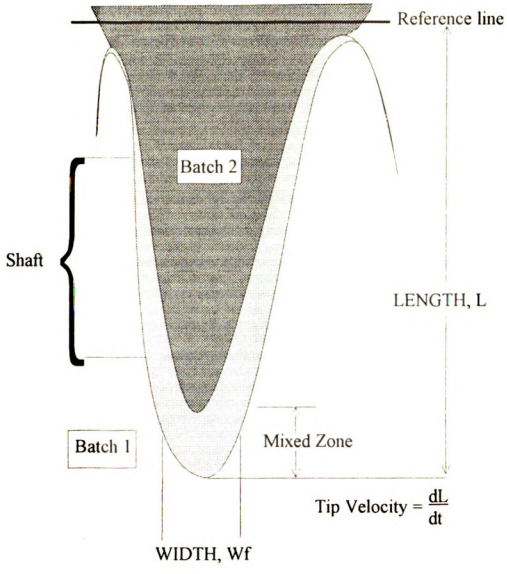


Figure 6.7: Definition of finger dimensions.

and then split into two or more fingers were also measured. They occurred infrequently, and are discussed below. Tables of measurements are to be found in Appendix C.

Figure 6.8 shows the results of the finger tip location measurements. For the run depicted in Figure 6.6, 15 fingers in all were measured. It is apparent that each finger tip moves at a constant velocity, and that velocities are similar across the width of the mold. (i.e. from 1 to 15 is equivalent to from left to right in the photographs in Figure 6.6).

DISCUSSION

Figures 6.9 through 6.12 show the data from the fingering flow experiments graphed according to the dimensionless quantities derived above. Of twelve runs, seven developed fingers, five did not. In two runs, fingers did not appear until well into the run: they appeared and began to grow between one photograph and the next. Reference to Table 6.4 will show which runs took place in Hele-Shaw cells, and which had random glass preforms. Each figure is discussed in detail below.

Figure 6.9 shows the relationship between the mobility ratio, $\mathcal{M}$, and the dimensionless velocity, $\mathcal{V}$, as defined in Eq. (6.13), and based on the age of the resin on the Batch 1 side of the interface (i.e., at point B in Figure 6.2). The rectangles represent the range of values of $\mathcal{M}$ and $\mathcal{V}$ for each run. Dark rectangles represent runs with fingers, while clear rectangles are runs with no fingers. Rectangles with a pattern inside represent runs which have random glass preform. There is no clear-cut value for $\mathcal{M}$ which represents a fingering criterion, although there is a general trend of decreasing $\mathcal{M}$ with increasing $\mathcal{V}$. This is contrary to the expectation that the viscosity jump at the interface would give rise to the fingering phenomenon.

Figure 6.10 shows the same relationship as Figure 6.9, but the values for $\mathcal{M}$ are calculated based on the age of the resin at the air/Batch 1 interface (i.e., point A on Figure 6.2). Now the rectangles fall on either side of a clear-cut line which has been drawn in. Runs whose values of $\mathcal{M}$ and $\mathcal{V}$ fall above the line showed fingers, without exception.

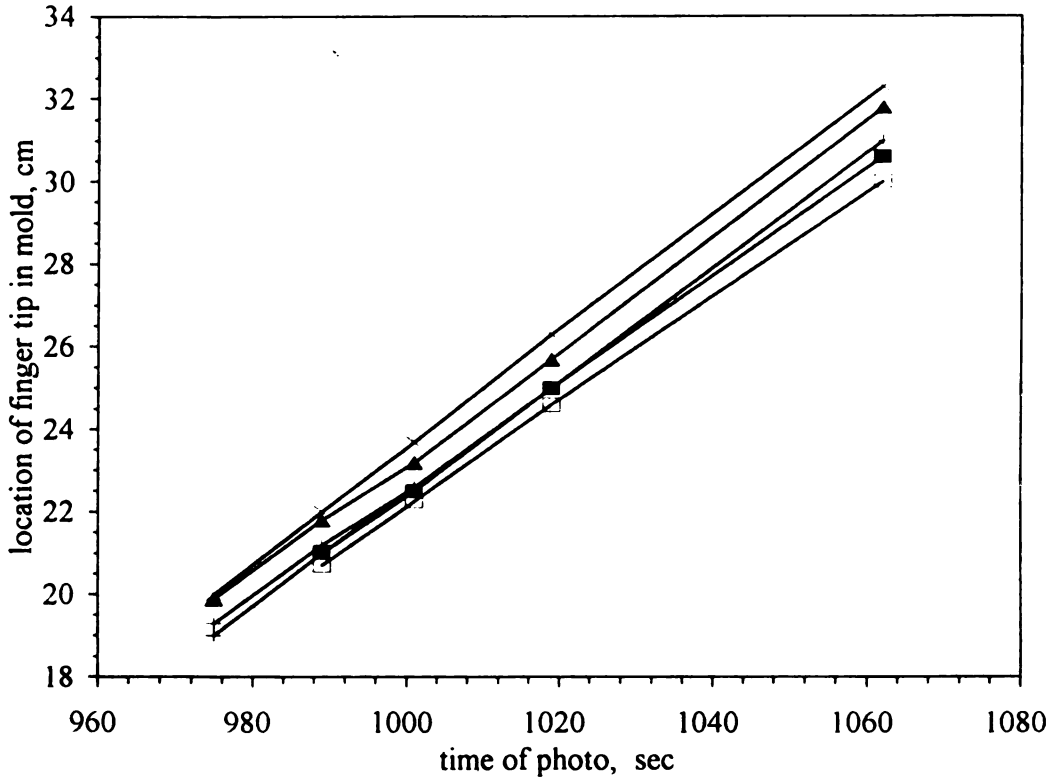


Figure 6.8: Finger tip locations in run 8.20.A.

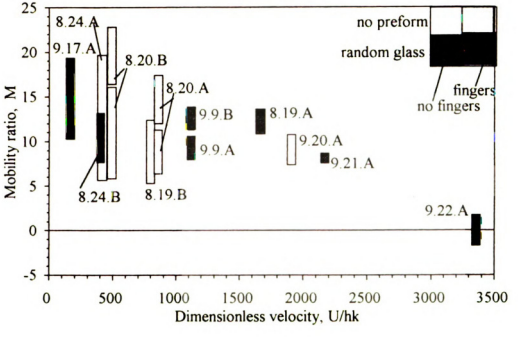


Figure 6.9: Mobility ratio, $\mathcal{M}$ versus dimensionless velocity, $\mathcal{V}$, based on age of resin at interface.

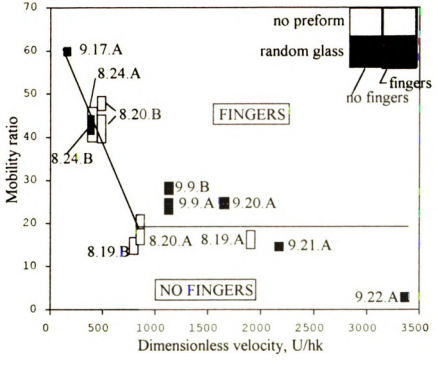


Figure 6.10: Mobility ratio, $\mathcal{M}$, versus dimensionless velocity, $\mathcal{V}$, based on age of oldest resin in the mold.

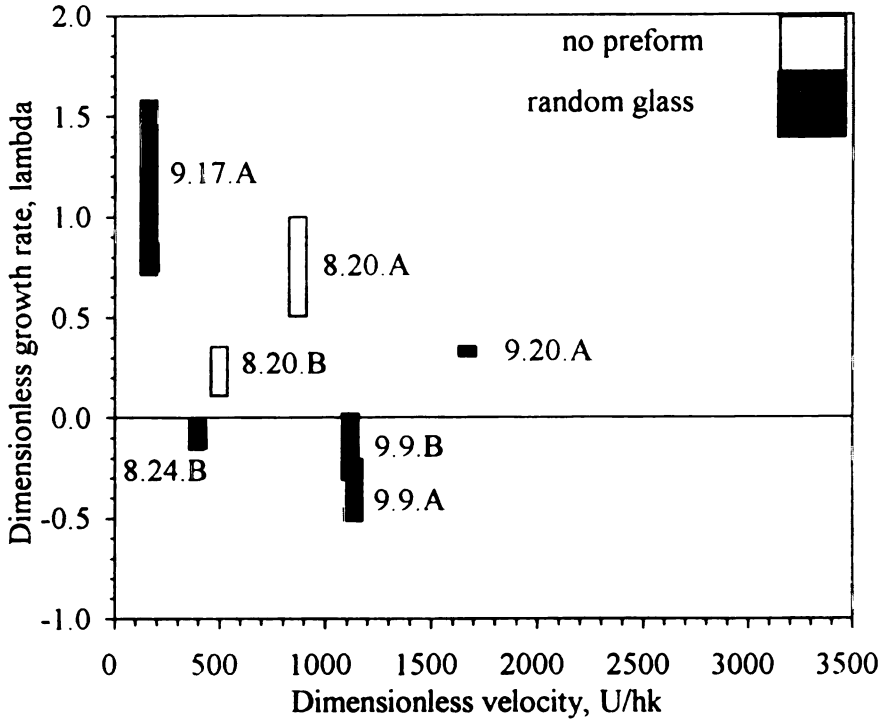


Figure 6.11: Finger growth rate versus dimensionless velocity.

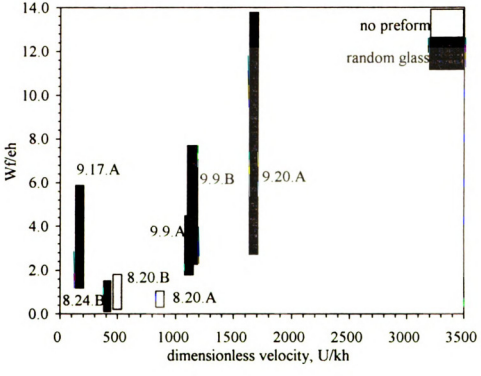


Figure 6.12: Finger width versus dimensionless velocity.

Those which fall below the line showed no fingers. In two cases, runs 8.20.A and 8.20.B, fingers appeared in the flow front between one photo and the next. The stability line thus must run right between the two rectangles representing each of these two runs.

At a value of $\mathcal{V}$ of about 490, run 8.24.A did not show fingers, although it lies very close to the stability line. Likewise, run 8.24.B, which did show fingers, lies just under the line. These two runs may serve as an illustration as to the accuracy of the experiment. The stability line may really be a 'stability zone' of finite width. Nevertheless, it seems clear that as $\mathcal{V}$ is held constant, $\mathcal{M}$ grows due to the advancing reaction until a critical value is reached, and fingers appear. The stability line depicted in Figure 6.10 is valid for runs with either no preform and random glass mat. It is also valid for the range of injection rates and delay times of the twelve experiments.

The line drawn as the stability criterion can be expressed as the critical value of the mobility ratio, $\mathcal{M}_c$, which is a function of the dimensionless velocity:

$$\begin{aligned} \mathcal{M}_c &= 70.0 - 0.060\mathcal{V} \qquad 170 \le \mathcal{V} \le 830 \\ \mathcal{M}_c &= 20 \qquad\qquad\qquad\quad 830 \le \mathcal{V} \le 3400 \end{aligned} \tag{6.17}$$

Note that this value of $\mathcal{M}$ is based on the age of the oldest resin in the mold, not on the difference of resin ages at the interface between Batch 1 and Batch 2.

This result shows that fingering depends on the magnitude of the rise in $\mathcal{M}$ in the mold as a whole, not on the length of an interruption of flow, such as will rarely arise in commercial RTM applications. It is the magnitude of the overall rise in viscosity inside the mold during filling which gives rise to the fingering flow. Thus, we expect that any mold with long enough flow paths or which is filled on a time scale such that the resin gels shortly after the mold is filled, may produce fingering flows. A jump in the viscosity with respect to time or location is not necessary. The applicability of the fingering criterion, Eq. (6.17), to the moldability diagram of an RTM system will be discussed in detail in Chapter 7.

Figure 6.11 shows the dimensionless growth rate of the fingers, λ, graphed against $\mathcal{V}$. λ is calculated from the velocity of the finger tip, as calculated for Figure 6.8:

$$\lambda = \frac{\frac{dL}{dt} - U_o}{U_o} \qquad (6.18)$$

The height of the rectangles represent the range of values which λ takes on during a run. Note that for some runs, λ is positive, meaning that the finger tip is advancing in the flow cell faster than the fluid in general. For some runs, the finger tip is advancing more slowly than the fluid, leading to negative values of λ. There seems to be no clear cut division between runs that have positive values of λ, and those with negative values. However, it should be noted that all the runs with negative values of λ contained random glass mat. The fingers in the random glass mat tended to be wider than those in the Hele-Shaw cells, as discussed below. It may be that fingers which grow in width as well as length will typically show negative values of λ.

Figure 6.12 shows the dimensionless finger width (W_f/h) graphed against $\mathcal{V}$. Each rectangle represents the range of values of the finger widths for each run. The averages are noted within the rectangles. For runs with no fingers, W_f is taken as zero. Each porous medium has a distinctive finger width. For the Hele-Shaw cell (no preform), finger widths are 0.2 cm on average, or about 0.67 x h. For random glass mat, finger widths average at about 1.0 cm, or about 3 x h. These results correspond with those of Slobod and Thomas (1963), who observe that the finger width for immiscible fluids in Hele-Shaw cells is on the order of the thickness of the cell. Also, as discussed in Chapter 1, Tan and Homsy (1986) show that for miscible fluids, there will a preferred finger width (expressed as wavelength), for a given ratio of viscosities and dispersion coefficients (D_L / D_T), which seems confirmed for the present experiments with reactive fluids.

CONCLUSION

The experiments described above were designed to emulate RTM in resin choice, superficial velocities, and mold fill time as a fraction of resin gel time. Fingers were observed in 7 out of 12 runs, thus showing that fingering flows can arise in RTM. A fingering/no fingering criterion was derived based on the mobility ratio, $\mathcal{M}$. This criterion was based on the viscosity and extent of reaction of the oldest resin in the mold, not on that near the interface. This implies that the fingering criterion will depend on the kinetics of the resin, and the dynamics of the mold filling, rather than on the presence or absence of an interruption in the mixing of the resin, or on the type of preform in the mold. This dependence on the viscosity gradient in the mold as a whole is in accord with the observation of Gorrell and Homsy (1985) that fluid flows with viscosity gradients which increase gradually in the direction of flow cannot be made unconditionally stable with regard to viscous fingering.

Although the presence or absence of preform does not seem to affect the value of $\mathcal{M}_c$, the width of the observed fingers is characteristic of the preform in which they occur. In Chapter 5, it was shown that it may be the effect of the differential shrinkage of resins across a curved interface which may be responsible for weakening the part in which the fingers occur. The effect does not depend upon the actual radius of curvature, so a characteristic finger width would not lead to a characteristic weakening of the part, except inasmuch as more individual finger tips will fit into the same span of mold, when each finger is narrower. Thus, fewer, wider fingers, such as are found in the random glass mat, will not cause as much weakening of an RTM part as many narrow fingers would do.

CHAPTER 7

THE MOLDABILITY DIAGRAM FOR FINGERING FLOW

INTRODUCTION

In Chapter 1, the moldability diagram of Macosko (1989) was described. As depicted in Figure 1.7, the area inside the polygon is the operating envelope where good parts can be made, with a given resin system and molding operation. While the diagram as a whole is unique to any given system, its boundaries can be delineated one at a time through known principles. This powerful tool allows engineers to predict from fundamentals what combination of molding conditions will result in acceptable finished parts for a particular molding operation. In Chapter 1, the general form of the moldability diagram was described. In this chapter, the moldability diagram for the DGEBA/TETA resin and injection system from Chapter 6 will be described. This moldability diagram will then be refined to include the stability criterion derived in Chapter 6, and show what conditions are necessary to avoid fingering flows.

DISCUSSION OF MOLDABILITY DIAGRAM BOUNDARIES

The moldability diagram shown in Figure 7.1 is the moldability diagram for the DGEBA/TETA resin system, without regard to fingering flows. The boundaries on this diagram are set in accordance with experience and practice with the injection set-up depicted in Figure 6.4 and 6.5.

The horizontal axis in Figure 7.1 is the time necessary to fill the mold. It is related to the mold volume and the resin velocity, in that a greater resin velocity shortens the fill time if the mold volume remains the same. The vertical axis is the injection and mold temperature, which is assumed to be isothermal throughout the injection, though the mold

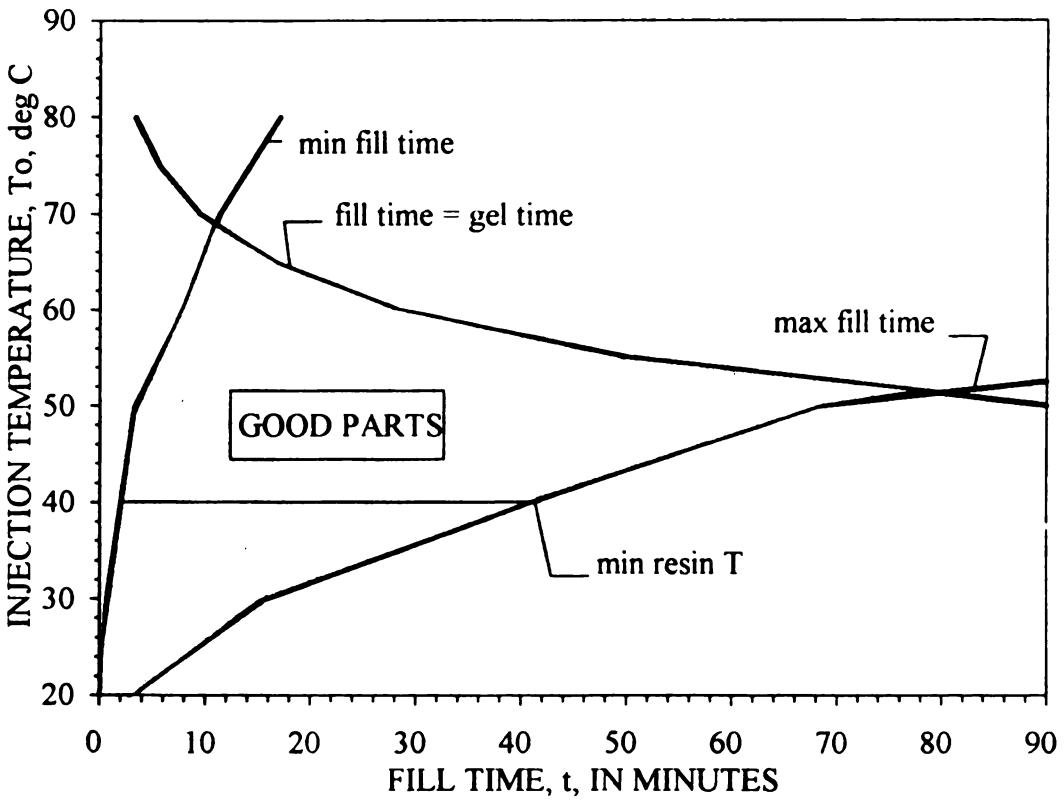


Figure 7.1: Moldability diagram for DGEBA/TETA resin system and injection molding apparatus of Figure 6.4 and 6.5.

temperature is raised during the cure step. This diagram is drawn for the specific resin system, mold and injection system described in Chapter 6.

The left and right boundaries represent mold fill rates at which the Reynolds number, based on the diameter of the static mixer, and the initial viscosity of the mixed resin is in the range of values which lead to good mixing. Specifically:

$$0.075 \leq Re \leq 1.49$$

$$Re = \frac{D_{mixer} U \rho}{\mu_o(T_o)} \qquad (7.1)$$

The upper constraint in Figure 7.1 is the line on which the fill time equals the time at which the resin would gel if the reaction were isothermal. The isothermal gel time was calculated as the upper bound of the diagram, instead of the adiabatic gel time because, the mold and injection system were run under nearly isothermal conditions, and because the adiabatic gel time for the DGEBA/TETA resin is very short, being approximately 10 minutes at a starting temperature of 40 °C.

Note that three of the boundaries in Figure 7.1 are mixing constraints. Choice of a different mixing system may effectively broaden the operating envelope for this system, by allowing good mixing at a broader range of fill times. The presence or absence of preform is not explicitly taken into account, as the fingering criterion derived in Chapter 6 is valid whether or not the mold contained preform. The experiments of Chapter 5 show that the presence of the interface is not detrimental to the epoxy part as long as the interface is formed before the gel time. Thus it is not necessary to restrict the moldability diagram by imposing a right boundary at $t_{weld\ line}$ as proposed in Chapter 1.

In order to add the constraints to the diagram that depend on the fingering flow criterion, $\mathcal{M}_c$, derived in Chapter 6, it will be necessary to convert $\mathcal{M}_c$ to coordinates of time and temperature. This can be done through Eq. (6.12), where $\mathcal{M}_c$ is a function of α, which in turn is a function of time and temperature. Because the initial value of the

viscosity drops out in the derivative, it not necessary to know the temperature dependence of the initial viscosity.

$$\mathcal{M} = \frac{C_1}{\alpha_g - \alpha} + \frac{C_2\alpha}{\alpha_g - \alpha} + C_2 \ln\left[\frac{\alpha_g}{\alpha_g - \alpha}\right]$$

$$\alpha = 1 - \left[\left[1 - (1-n)kt\right]^{(1/1-n)}\right] \qquad (7.1)$$

$$k = k_o \exp\left[-\frac{E_a}{R_g T}\right]$$

Where the coefficients are those derived in Chapter 3:

$C_1 = 0.417$

$C_2 = 17.511$

$\alpha_g = 0.68$

$E_a = 103500 \quad J/g\ mole$

$R_g = 8.314 \quad J/g\ mole\ °K$

$k_o = 10^{14.99}\ 1/min$

$n = 1.58$

Solving the above equations for the values of time and temperature which correspond to $\mathcal{M} = 20$ produces the numbers in Table 7.1. These numbers are then graphed in Figure 7.2. The curve thus obtained is the locus of time and temperature where $\mathcal{M} = 20$. Above this curve, we may expect fingering to occur. The goal of making parts without fingering narrows the operating envelope considerably.

Reference to Figure 6.10 will show that for values of the dimensionless velocity, $\mathcal{V} < 830$, $\mathcal{M}_c$ is greater than 20, and may be expressed as:

$$\mathcal{M}_c = 70 - 0.601\mathcal{V} \qquad (7.2)$$

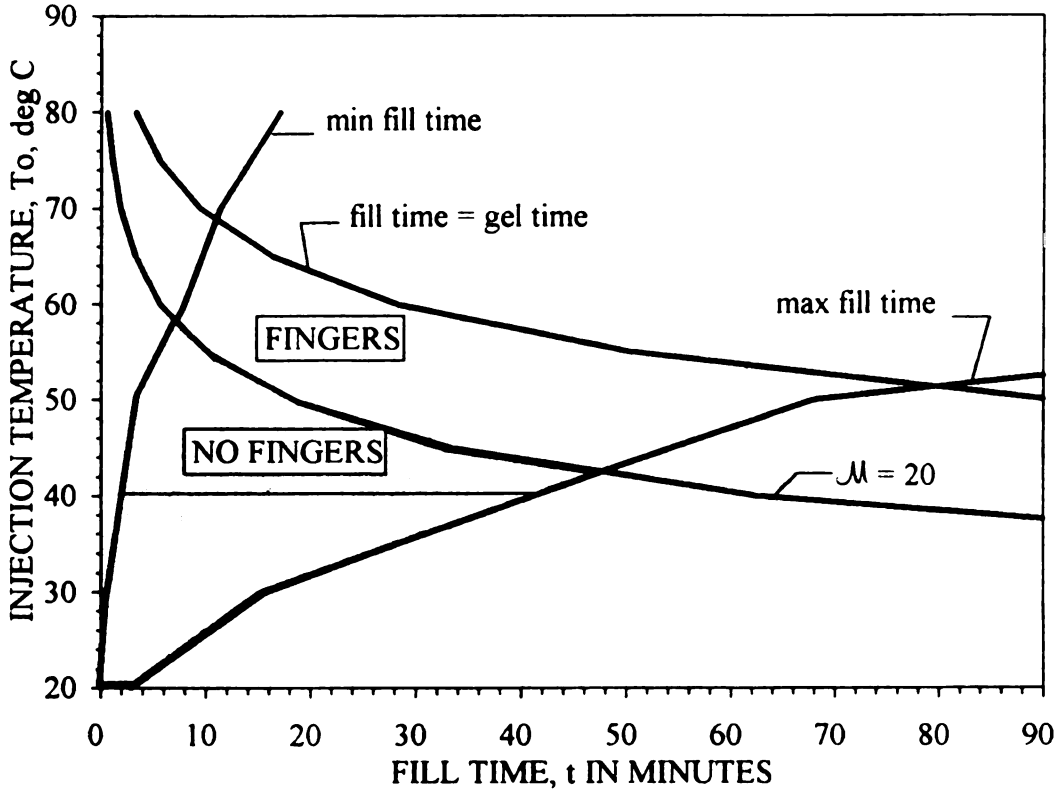


Figure 7.2: Moldability diagram of DGEBA/TETA system, with fingering criterion of $\mathcal{M}$ = 20 added.

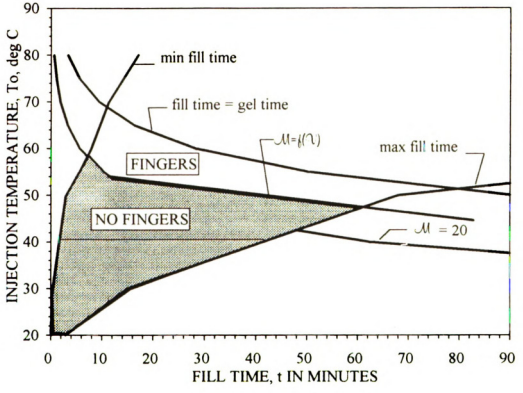


Figure 7.3: Moldability diagram of DGEBA/TETA system, with both branches of fingering criterion added.

Using the known fill times associated with the experiments that delineate $\mathcal{M}_c$, the last 5 values of Table 7.1 may be calculated by using Eqs. (7.1) to solve $\mathcal{M}(\alpha)$ for α. Then the known time is used to solve $\alpha(t,T)$ for T. These values form a straight line on Figure 7.3, labeled as $\mathcal{M} = F(\alpha)$. Applying this criterion, instead of the more stringent one of $\mathcal{M}_c$ = 20, enlarges the operating envelope at longer fill times. The shaded portion, then, of Figure 7.3, shows the region of the moldability diagram wherein fingers are not expected to occur.

Table 7.1: Values for moldability diagram.

T (°C)	$\mathcal{M}$	t_{fill} (min)	α	t_{gel} (min)
35	20	119.0	0.259	589
40	20	62.4	0.258	310
45	20	33.4	0.258	166
50	20	18.2	0.257	90.4
55	20	10.1	0.257	50.2
60	20	5.72	0.257	28.4
65	20	3.29	0.257	16.3
70	20	1.92	0.258	9.56
75	20	1.14	0.258	5.67
80	20	0.69	0..257	3.42
52	22	15.6	0.277	
52	40	25.0	0.392	
51	46	32.7	0.416	
50	46	34.8	0.416	
45	60	82.3	0.465	

CONCLUSION

The application of the fingering criterion to the moldability diagram considerably reduces the operating envelope of the process. This criterion confines the process to the lower temperature and shorter fill time region of the envelope, and shows that, as a rule of thumb, the fill time should be kept to less than 20% of the gel time. This finding will have

significance for parts manufacturers who wish to shorten their molding cycle time by shortening the gel time of the resin so that it gels shortly after the mold is full (i.e. $t_{fill} / t_{gel} \cong 1$).

Table 7.2 gives the values of the constants used to model $\mu(\alpha)$ for three resins. The first set of constants is for the DGEBA/TETA epoxy resin system used throughout the present work. The second set of constants is for a Derakane 8084 resin system similar to, but not identical with the Derakane 411 discussed in Chapter 2. The value of α_g for this resin is set artificially low so as to allow for a better fit to data. The actual extent of reaction at gel is about 3% (Larson, private communication). The third set of constants is for a phase-separating polyurethane system which is described in Macosko (1989, pg 59.). This resin is common in RIM operations, where the fill time is very nearly equal to the gel time.

Table 7.2: Values of viscosity model coefficients for three reactive resin systems.

Resin system	α_g	C_1	C_2
DGEBA/TETA epoxy	0.68	0.417	17.51
Polyurethane Macosko (1989)	0.85	3.50	-2.0
Derakane 8084 Larson (1993)	0.015	-0.656	221.3

Figure 7.4 is a graph of $\mathcal{M}(\alpha)$ for the three resin systems discussed above. Note that the epoxy resin curve rises steeply, and so reaches $\mathcal{M}_c = 20$ early in the reaction ($\alpha \cong 0.26$). On the other hand, the polyurethane has a much more gradual buildup of $\mathcal{M}$, and reaches $\mathcal{M}_c$ at $\alpha \cong 0.85$. The Derakane curve rises abruptly at very low extents of reaction, leading to the conclusion that fingering flows would be easily produced with Derakane 8084 resin, since $\mathcal{M}$ is greater than 20 through so much of the reaction.

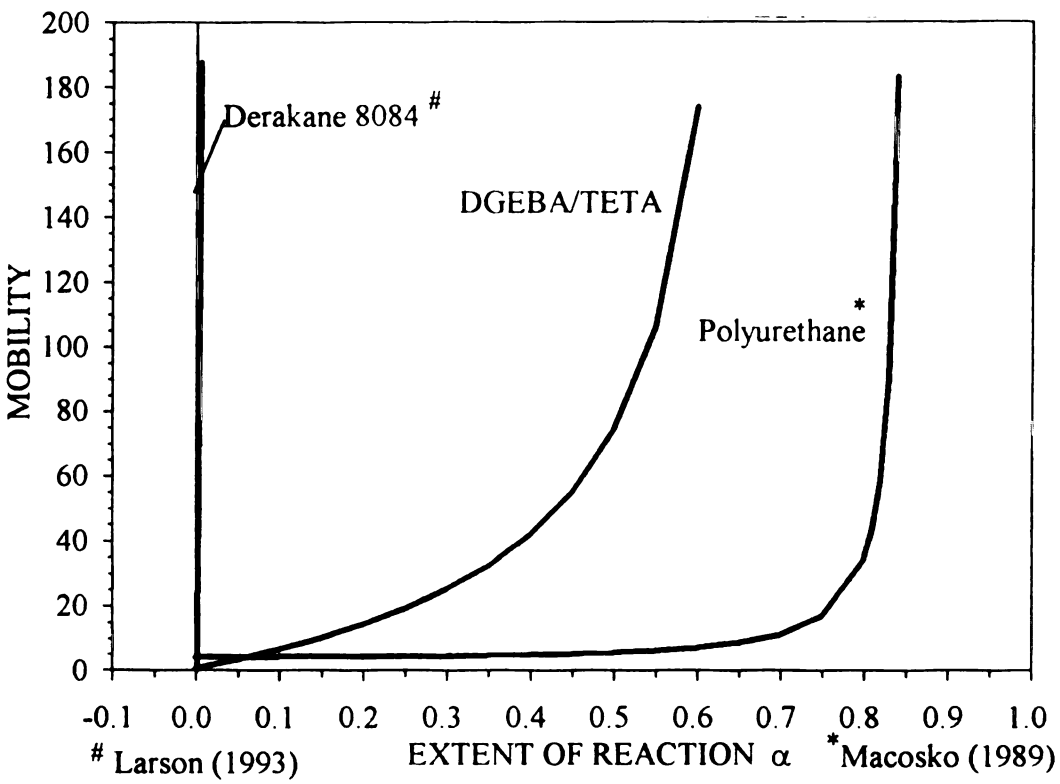


Figure 7.4: Mobility ratio, $\mathcal{M}$, as a function of α for several resin systems.

If the necessary condition to avoid fingering is $\mathcal{M} \leq 20$ for all three resins, it seems evident from Figure 7.4 that it would be very difficult to avoid fingering when using Derakane 8084 resin, because $\mathcal{M}$ becomes greater than 20 so early in the reaction that it would be impractical to try to fill a large mold before the reaction had proceeded beyond 1%. Contrariwise, it should be very easy to avoid fingering when using the polyurethane resin, because the value of $\mathcal{M}$ does not rise above 20 until late in the reaction.

If it proves valid for a variety of resin systems, this method of predicting the fingering behavior of a reacting resin system based on easily obtained viscosity and kinetics functions may be very useful in designing resin injection systems and mold gatings in parts where fingering flows must be avoided.

CHAPTER 8

CONCLUSIONS AND RECOMMENDATIONS

CONCLUSIONS

Viscous fingering flows have hitherto been studied in a variety of granular porous media, with a variety of fluid systems, miscible and immiscible. No literature has been found dealing with miscible displacements in fibrous porous media, nor has any been found dealing with fingering flows in fluids whose viscosity is changing in time due to reaction. This work describes viscous fingering flows which arise because of a viscosity gradient in the flow direction which is due to the polymerization reaction of the resin. It was speculated that fingering flows could arise in flow systems which emulated commercial RTM operations, and the results of the fingering flows could be detrimental to the physical properties of the finished parts. If so, then steps would need to be taken to design RTM molds, resin systems, and operating disciplines to avoid fingering flows in order to produce good quality parts. A clear fingering/no fingering criterion which could be applied to a given RTM process would be invaluable in this endeavor.

This work describes two resin systems in which fingering flows were observed; Derakane 411, a polyvinyl ester, and DGEBA/TETA epoxy resin. Porous media included two glass fiber preforms: random swirl mat, $V_f = 0.20$, and woven fabric, $V_f = 0.45$, as well as flows in molds without preform. No granular porous media were investigated.

The fingering flow experiments were used to derive a finger/no finger criterion that is a function of the kinetics of the DGEBA/TETA epoxy resin system through the mobility ratio, $\mathcal{M}$, and of the fluid mechanics of the RTM mold configuration through the dimensionless interstitial flow rate, $\mathcal{V}$. This criterion was transformed into a boundary for

the operating envelope of the moldability diagram for the RTM process, which appears as Figure 8.1. The area of the diagram where fingering flows do not occur is about half of the operating envelope for this particular RTM system.

Derakane 411 resin was used to produce finished plaques with fingers molded in. Injections with and without preforms produced fingering flows. Sample bars taken from the areas of the plaques which contained fingertips showed up to 15% loss of flex modulus, compared with samples from areas which had no fingertips. Furthermore, samples taken where fingering flow produced flat interfaces showed no loss of flex modulus. This was explained in terms of the stress caused by polymerization shrinkage on a curved interface as opposed to a straight one. Polymerization shrinkage of Derakane 411 was measured, and found through geometrical arguments to be sufficient to cause delamination if the interface is curved, but not if it is straight.

In order to test whether the interface where resins of different age come together is detrimental to a plaque when it is not associated with finger structures, plaques were made which had extensive areas of interface between two batches of resin of different ages. This interface was expected to emulate the interface formed at the sides and tips of fingers. The interface was expected to weaken the plaque in much the same manner in which a weldline or adhesive joint weakens the part in which it occurs. Samples from these plaques were tested in short beam shear to show whether the interface would fail in shear under lower loads than similar parts made with no interface. The tests show that the interface is at least as strong as the bulk resin, if the age difference between the resin on either side of the interface is less than the gel time of the resin. The interface is not as strong when the age difference exceeds the gel time, as indicated by the number of samples which failed at the interface rather that in the bulk of the resin. However, there is no significant difference in short beam shear strength between samples with any of the age

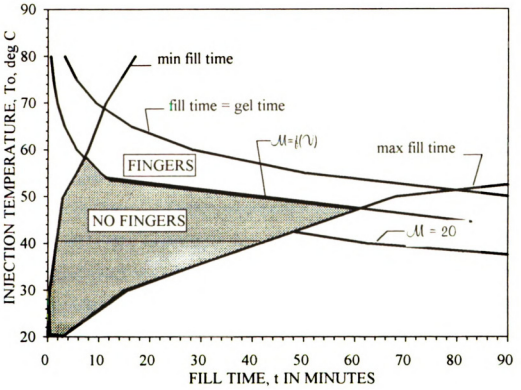


Figure 8.1: The moldability diagram for DGEBA/TETA epoxy resin in RTM, with the fingering criterion superimposed.

differences tested. A small anisotropy in the short beam shear test results when the bars were tested in different orientations was explained in terms of the molded-in stress produced by the polymerization shrinkage of the resin acting against the constraint of the mold while the resin was curing.

Measurements of the dispersion coefficient of a solute in a fluid flowing through a porous medium are not common in the literature. Perkins (1963) give values for dispersion coefficients in granular porous media, but the author is unaware of any dispersion coefficient measurements made in fibrous porous media. Chapter 4 describes a method of measuring the dispersion coefficient of flows in Hele-Shaw cells, random swirl glass mat, $V_f = 0.18$, and woven glass mat, $V_f = 0.45$. The method involves using RTM in a specially configured mold to make plaques in which a dyed resin is allowed to disperse into an undyed resin. The concentration of resin at various locations in the finished plaque are then measured with a photo-densitometer. The resulting C(x,y) data are then used to calculate the longitudinal and transverse dispersion coefficients, according to the method of Perkins (1963). This method gave data which were sufficiently good to calculate dispersion coefficients only to $\pm$ 12%. Future measurements should incorporate the use of a better-controlled pressure supply, and a photo-densitometer with finer spatial resolution.

Measurements of the permeability of a Hele-Shaw cell, random swirl glass mat, $V_f = 0.20$, and woven glass fabric, $V_f = 0.45$, were made with Polybutene as the working fluid. The use of polybutene avoided the problems with corn syrup and glycerol, which are the Newtonian model fluids of choice, to wit, changing viscosity due to absorption of water from the atmosphere. Again, future measurements should make use of a better-controlled pressure supply, as the permeability measurements are very sensitive to fluctuations in the driving pressure.

RECOMMENDATIONS

In Chapter 6 it was shown that it was the magnitude of the viscosity rise throughout the mold that was the basis of the finger/no finger criterion. Reaction is not the only way to produce viscosity gradients in a porous medium. Two other situations come to mind, both of which may be investigated to shed more light on the viscous fingering phenomenon, and both of which have implications in commercial RTM, as well as other unit operations, such as filtration and extraction.

If the temperature of a porous medium decreases in the direction of flow, the viscosity would rise in the flow direction. This viscosity gradient may be relatively large, as the viscosity of Indopol L-50, which is a low molecular weight polybutene, used in the present study as a fluid of constant viscosity for permeability measurements, is halved by a 13 °C rise in temperature. Polybutene flowing from a warm region of a porous medium to a cool one would probably give rise to fingering flows. The finger/no finger criterion in this case would depend on the viscosity as a function of temperature instead of as function of extent of reaction, $\mathcal{M}(T) \propto 1/\mu(T) * (\partial\mu/\partial T(x))$.

Alternatively, the flowing fluid may dissolve a thickening agent from the porous medium, such that the first fluid in the mold becomes more viscous than the last fluid in the mold, because the porous medium has been stripped of the solute by the passage of the resin. This situation arises in extraction problems, but also specifically in RTM, where the solute is a low molecular weight thermoplastic coating the fibers of the preform. (Bakkes, 1993). In this case, it would be necessary to know the viscosity as a function of binder concentration to formulate the finger/no finger criterion as: $\mathcal{M}(C) \propto 1/\mu(C) * (\partial\mu/\partial C(x,t))$.

In light of the above, it is recommended that viscous fingering flows be investigated in other situations where viscosity gradients arise not because one fluid is displacing a dissimilar fluid, but where the properties of a fluid flowing through a porous medium change locally within the porous medium.

It is not known if the fingering/no fingering criterion is valid for a variety of resins. The mobility ratio, $\mathcal{M}$, of the DGEBA/TETA epoxy resin system builds up gradually as the reaction advances. $\mathcal{M}$ of the Derakane system rises very rapidly as the reaction advances. Viscous fingering flows appear in both these resin systems. The fingering criterion derived in Chapter 6 is a critical value of $\mathcal{M}$ for the DGEBA/TETA system. If $\mathcal{M}$ of the resin in the RTM mold exceeds $\mathcal{M}_c$, then fingering is expected. On the other hand, $\mathcal{M}$ of a polyurethane resin does not rise above $\mathcal{M}_c$ until the resin is gelled. More study is needed to find if the numerical value of $\mathcal{M}_c$ is valid for many kinds of thermoset resins, or if the shape of the $\mathcal{M}(\alpha)$ curve is a determining factor in the value of $\mathcal{M}_c$. Giving the criterion broad applicability would be helpful to designers who must design molds and gating systems to avoid fingering.

All work with fingering flows in DGEBA/TETA resin system was done isothermally at T = 50 °C. The boundary of fingering/no fingering on the moldability diagram (see Figure 8.1) was derived from a fingering criterion obtained at 50 °C and the kinetics of the reaction. Further work should investigate other molding temperatures to confirm that the fingering criterion has the form depicted in Figure 8.1, for molding operations which are not isothermal. Due to the fact that increasing the temperature of the resin generally increases the rate of reaction as well, there may be competing effects between the decrease of viscosity due to increased temperature, and an increased viscosity due to increased reaction rate.

The resin injection system used for the fingering flow experiments was limited in the flow velocities it could deliver. Thus the flows in which fingers were produced were at the low end of what is typical of RTM. The injection/mixing system should be upgraded so that higher velocities can be investigated. The limit of dispersive dampening of the fingers could then be observed. Therefore, a logical extension of the work reported here

would be to use a highly dispersive medium, a very long mold, and high velocities to find if dispersion can overcome the tendency of reacting resin systems to finger.

It was speculated that the interface formed in an RTM part by a fingering flow would be detrimental in the same way that a weldline is detrimental to thermoplastic parts. It was shown that flat interfaces formed in plaques well before the gel time of the resin were not detrimental to the strength of the part. And, it was argued on geometric grounds that the shrinkage of a curing resin at an interface with another resin would not lead to significant weakening of the interface if it were flat, but could very well weaken a curved interface. Actual experiments with curved interfaces would shed more light on the mechanism whereby the curved interface at the tips of fingers seems to reduce the flexural modulus of RTM parts in which it occurs, and described in Chapter 4.

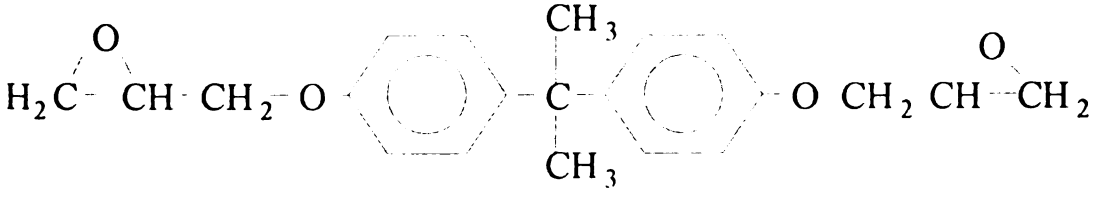
APPENDIX A

MATERIAL AND APPARATUS

EPOXY RESIN SYSTEM:

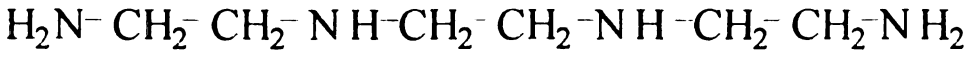
Monomer: Dow Epoxy Resin 332 (DER 332), a high purity grade of DGEBA (Diglycidyl ether of bisphenol A)

Density: 1.1 g/cm^3
M.W. : 340
Melting Point:
Viscosity at 20° C: 9.0 Pa·sec



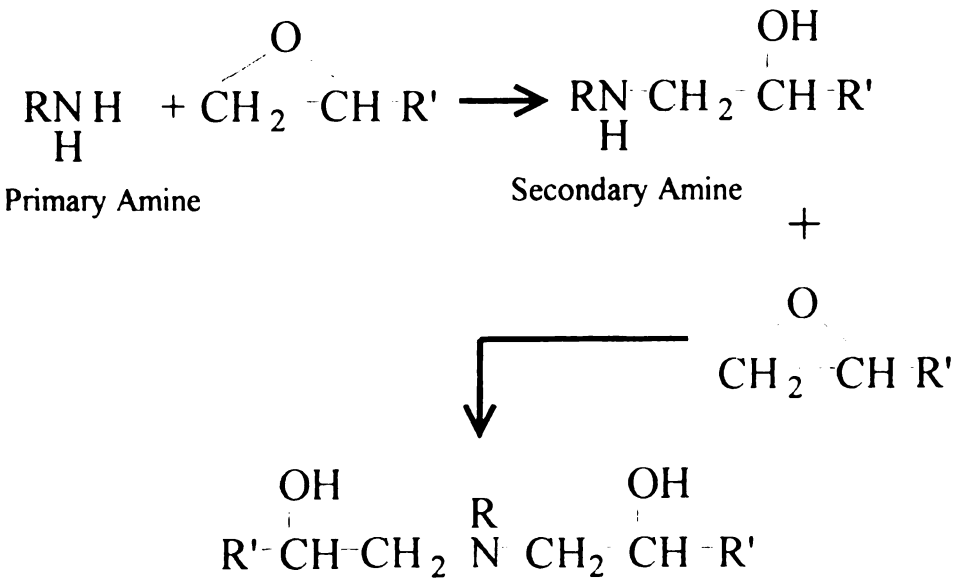
Hardener: TETA (triethylene tetramine), reagent grade, from Aldrich Chemical Co.

Density: 0.982 g/cm^3
M.W.: 146
Melting Point: 12° C
Boiling Point: 266° C



EPOXIDATION REACTION:

Stoichiometry: 100 parts DGEBA + 12.9 parts TETA = 112.9 parts formulated resin.
(88.57 wt%) (11.43 wt%) (100 wt%)



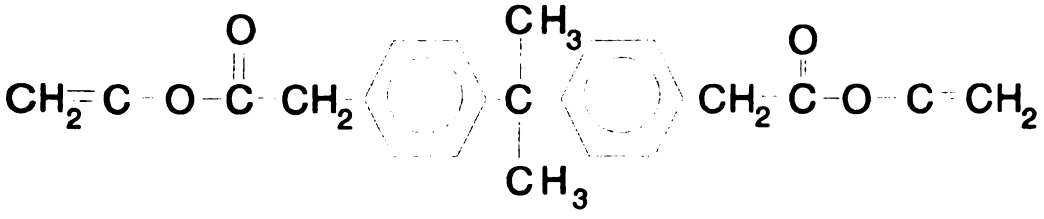
Recommended Curing Cycle: Gel at room temperature plus several days at room temperature, or 1-2 hrs at 100 ° C for full cure.

Reference: Formulating with DOW Epoxy Resins, Dow Chemical Co.;
Form No. 296-346-583

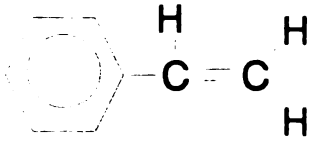
DERAKANE® RESIN SYSTEM:

Derakane 411-350 vinyl ester resin.
Consists of 40 to 50 % styrene monomer, balance vinyl ester resin.
Specific gravity: 1.020 to 1.060

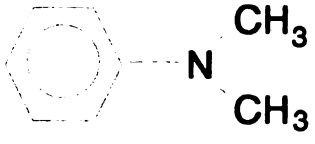
VINYL ESTER: 50 to 60% by weight.



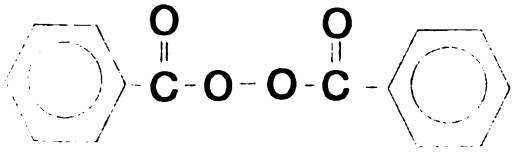
STYRENE: 40 to 50% by weight.



ACCELERATOR: Dimethyl aniline. 0.1% by weight.



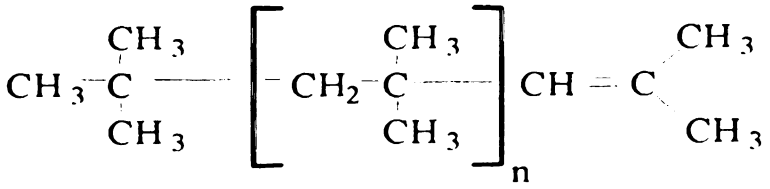
Catalyst: Benzoyl peroxide, 2.0% by weight. Used as 40% emulsion in reactive diluent, Diisobutyl phthalate.
Specific Gravity 1.152. (emulsion)



OTHER CHEMICALS

Dye: Oil Red biological dye, from Aldrich Chemical Co.

Polybutene: Amoco Chemical Co., INDOPOL L-50
Density: 0.845-0.860 g/cm^3
Number avg. M.w.: 420
Viscosity at 20° C: 300 cSt



n (average) = 5.5

Reference: Amoco Chemical Company / Bulletin 12-M.

Mold Release Sprays:
Frekote 700 (silicone)
Miller-Stephenson MS-136/CO_2 (teflon)

Nylon Mold Release Film:
International Plastic Products, Inc.
Wrightcast 7500 Nylon 6-6 cast film, Pin-Hole Free
Thickness: 2 - 3 mils
Specific Gravity: 1.14

GLASS MATS
Hexcel Glass Fabric: #7532
E-glass
Plain weave: warp, 16 ends per inch;
fill, 14 ends per inch (16 × 14 count).
Thickness: 11.0 mils
Weight: 7.30 oz/yd^2
Yarn Type: 75 1/3 warp
75 1/3 fill
Breaking Strength: 300 #/in warp
300 #/in fill

Vetrotex Certainteed Fiberglass Reinforcements,
Unifilo U816, #K55U816500
Weight: 1.5 oz/yd^2
Low solubility binder.

APPARATUS

Equipment used at Michigan State Univ. Composite Materials and Structures Center:

Tensile, flex and short beam shear tests using:
UTS test frame, model SFM-20
United Calibration Corp.
5802 Engineering Drive
Huntington Beach, CA

Dynamic viscosity measurements:
Rheometrics Mechanical Spectrometer, model RMS 8000

Michigan Molecular Institute laboratory:
Differential Scanning Calorimeter
Horizontal-vertical Cathetometer M-912
Gaertner Scientific Corp.

Meier's Camera Shop, Midland MI.
Photometric Densitometer, Model 810
Noritsu Corp.

APPENDIX B

DERIVATIONS

METHOD OF CALCULATING PERMEABILITY COEFFICIENTS

This section will show the derivation of the relations used in Chapter 3 to determine the permeability of various preforms. The flow situation is depicted in Figure B.1 as flow between two flat plates, spreading radially from a source of radius R_0. Rectangular coordinates will be employed, despite the cylindrical nature of the flow because the possibility exists that the flow will not be radially symmetrical. For the purposes of this derivation, it will be assumed that the principle axes of the flow will coincide with the laboratory axes. Chan and Hwang (1991) treat the more general situation of flow which is neither isotropic nor orthotropic, but it is not necessary to treat that case here.

Given the flow as shown in Figure B.1, we will use the equation of continuity and Darcy's law in rectangular coordinates, along with the following boundary conditions on pressure and time, to find the radius of the flow front as a function of time, pressure drop, viscosity, and permeability.

Continuity: $\nabla \cdot \underline{v} = 0$

Darcy's law: $\bar{v} = -\frac{\underline{\underline{\kappa}}}{\mu} \cdot \nabla P$ (B.1)

$\underline{v}$ = velocity vector

$\bar{v}$ = average or bulk velocity

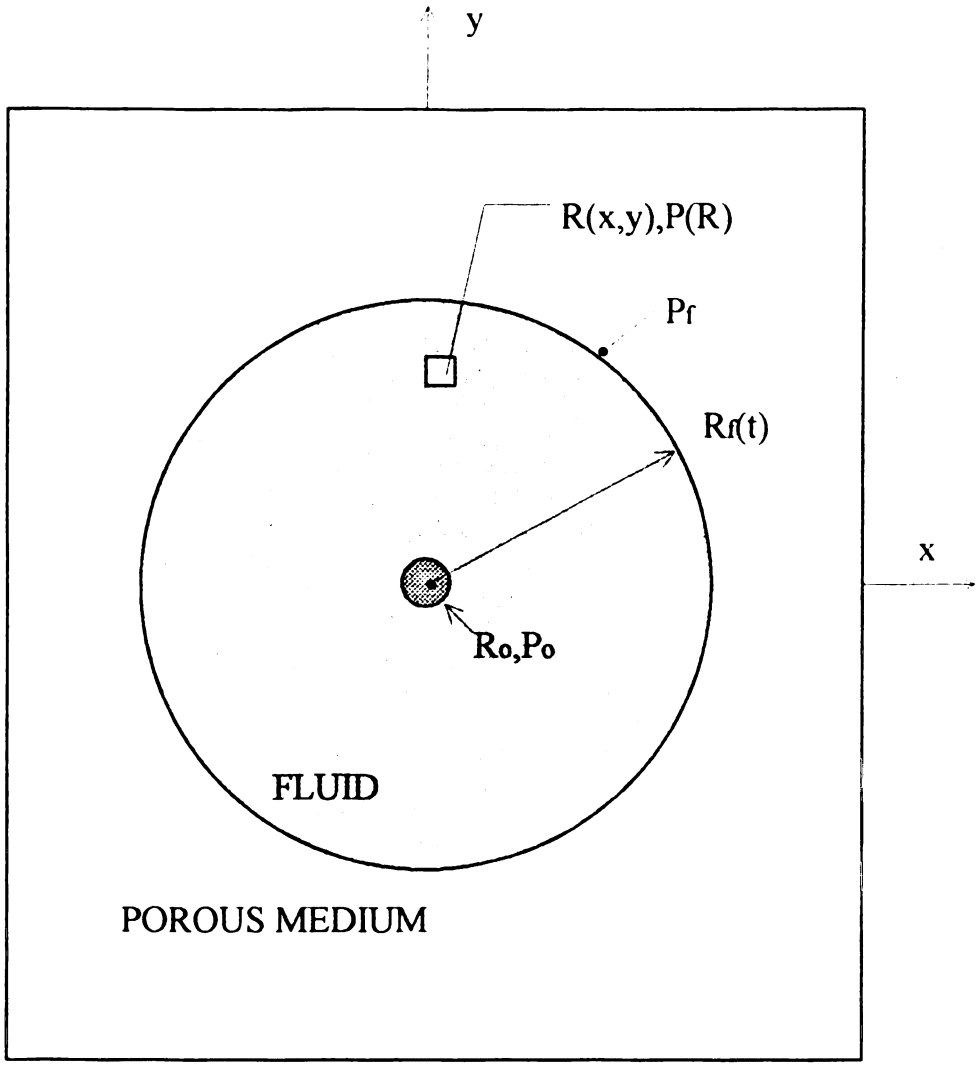
$\underline{\underline{\kappa}}$ = permeability tensor

μ = viscosity

P = pressure

R = radius of circle , convertible to rectangular coordinates

Boundary conditions:



FLOW CELL: TWO FLAT PLATES, GAP<<LENGTH

Figure B.1: Flow between two flat plates with coordinates for calculating permeability of preforms from data.

$$P = P_o \text{ at } R = R_o$$

$$P = P_f \text{ at } R = R_f \tag{B.2}$$

$$R_o = R_f \text{ at } t = 0$$

Using cylindrical coordinates, it can be shown that the pressure drop across an expanding circular (i.e. radially symmetrical) flow front is:

$$\frac{P - P_f}{P_o - P_f} = 1 - ln\frac{R}{R_o} \tag{B.3}$$

Now, using Darcy's law and the fact that the interstitial velocity is related to the bulk velocity by the porosity, ε, we can show that the velocity of the flow at the front is, at any time:

$$v_f\big|_{R_f} = -\frac{\underline{\underline{\kappa}} \cdot \nabla P}{\varepsilon\mu}\bigg|_{R_f} = -\frac{\underline{\underline{\kappa}}}{\varepsilon\mu}\frac{\partial P}{\partial R}\bigg|_{R_f}$$

$$v_f = \frac{dR_f}{dt} = -\frac{\underline{\underline{\kappa}}}{\varepsilon\mu}\frac{P_f - P_o}{R_f\, ln(R_f/R_o)} \tag{B.4}$$

If it is assumed that the permeability, porosity, pressure drop, and viscosity are constant in time, then separation of variables and integration yields:

$$\frac{dR_f}{dt} = -\frac{\underline{\underline{\kappa}}\Delta P}{\varepsilon\mu}\frac{1}{R_f\, ln(R_f/R_o)}$$

$$\int R_f\, ln(R_f/R_o)dR_f = -\frac{\underline{\underline{\kappa}}\Delta P}{\varepsilon\mu}\int dt$$

$$R_o^2\int \frac{R_f}{R_o} ln(R_f/R_o)d(R_f/R_o) = -\frac{\underline{\underline{\kappa}}\Delta P}{\varepsilon\mu}t + C_1$$

$$R_o^2\left[\frac{1}{2}\left(\frac{R_f}{R_o}\right)^2 ln\left(\frac{R_f}{R_o}\right) - \frac{1}{4}\left(\frac{R_f}{R_o}\right)^2\right] + C_2 = \frac{\underline{\underline{\kappa}}\Delta P}{\varepsilon\mu}t + C_1 \tag{B.5}$$

Applying the initial condition leads to:

$$4\frac{\underline{\underline{\kappa}}\Delta P}{\varepsilon\mu R_o^{\,2}}t = \left(\frac{R_f}{R_o}\right)^2\left[2ln\left(\frac{R_f}{R_o}\right)-1\right]+1 \qquad \text{(B.6)}$$

This is the exact result for Darcy's law flow in an isotropic system. That is, a circular flow front, and a permeability tensor that looks like this:

$$\underline{\underline{\kappa}} = \begin{bmatrix} \kappa_{xx} & 0 \\ 0 & \kappa_{yy} \end{bmatrix} \qquad \text{(B.7)}$$

For an isotropic system, the diagonal components are equal. For an anisotropic permeability, the diagonal terms are not equal, and the off-diagonal terms are zero only if the principal axes of the flow coincide with the coordinate axes.

If the flow is orthotropic, the flow front will be elliptical, with major and minor axes coincident with the x and y axes. Figure B.2 shows the flow front at successive times in both the isotropic and orthotropic permeability cases. It is argued here that the elliptical and circular flow fronts are equivalent, and that elliptical flow front can be mapped onto the circular flow front, if the proper values for $\underline{\underline{\kappa}}$ are found. Therefore, given the equation of continuity for the elliptical system in rectangular coordinates:

$$\kappa_{xx}\frac{\partial^2 P}{\partial x^2}+\kappa_{yy}\frac{\partial^2 P}{\partial y^2}=0$$

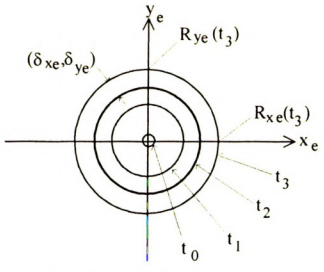
$$\text{isotropic: } \kappa_{xx}=\kappa_{yy},\ \kappa_{xy}=\kappa_{yx}=0 \qquad \text{(B.8)}$$

$$\text{orthotropic: } \kappa_{xx}\neq\kappa_{yy},\ \kappa_{xy}=\kappa_{yx}=0$$

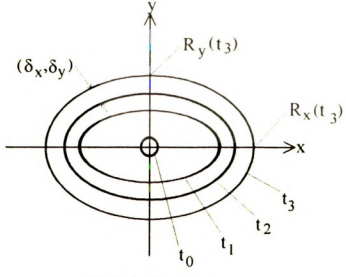
Let there be a set of equivalent coordinates (subscripted e) for which:

$$\kappa_{x_e x_e}\frac{\partial^2 P_e}{\partial x_e^{\,2}}+\kappa_{y_e y_e}\frac{\partial^2 P_e}{\partial y_e^{\,2}}=0 \qquad \text{(B.9)}$$

$$\kappa_{x_e x_e}=\kappa_{y_e y_e},\ \kappa_{x_e y_e}=\kappa_{y_e x_e}=0$$



Equivalent circular system



Elliptical system

Figure B.2: Comparison of elliptical and circular flow fronts.

For convenience, let the permeability notation be:

$$\kappa_{x_e x_e} = \kappa_{x_e}$$

$$\kappa_{y_e y_e} = \kappa_{ye} \tag{B.10}$$

Figure B.2 shows a series of flow fronts at incremental time ticks. For any given time tick, the flow front advances an incremental distance in each coordinate, as shown. Taking the ratios of dimensions in the elliptical (no subscript) and circular (subscript e) systems yields the following dimensionless quantities:

$$\mathbf{X} = \frac{\delta x_e}{\delta x}$$

$$\mathbf{Y} = \frac{\delta y_e}{\delta y}$$

$$\mathbf{P} = \frac{\delta P_e}{\delta P}$$

$$K_x = \frac{\kappa_{xe}}{\kappa_{xx}}$$

$$K_y = \frac{\kappa_{ye}}{\kappa_{yy}} \tag{B.11}$$

The equation of continuity:

$$\kappa_{xx}\frac{\partial^2 P}{\partial x^2} + \kappa_{yy}\frac{\partial^2 P}{\partial y^2} = 0 \tag{B.12}$$

can be restated:

$$\frac{\kappa_{xx}\mathbf{X}^2}{\mathbf{P}^2}\frac{\partial^2 P_e}{\partial x_e^{\,2}} + \frac{\kappa_{yy}\mathbf{Y}^2}{\mathbf{P}^2}\frac{\partial^2 P_e}{\partial y_e^{\,2}} = 0 \tag{B.13}$$

If $$\frac{\partial^2 P_e}{\partial x_e^{\,2}} + \frac{\partial^2 P_e}{\partial y_e^{\,2}} = 0 \tag{B.14}$$

then: $$\frac{\kappa_{yy}\mathbf{Y}^2}{\kappa_{xx}\mathbf{X}^2} = 1 \tag{B.15}$$

or: $$\mathbf{Y} = \left(\frac{\kappa_{xx}}{\kappa_{yy}}\right)^{1/2} \mathbf{X} \qquad \text{(B.16)}$$

in the equivalent system, $\delta x_e / \delta y_e = 1$, so that the relationship between the x and y coordinates in the elliptical system can be defined as:

$$\delta y = \left(\frac{\kappa_{xx}}{\kappa_{yy}}\right)^{1/2} \delta x \qquad \text{(B.17)}$$

or macroscopically:

$$y = \left(\frac{\kappa_{xx}}{\kappa_{yy}}\right)^{1/2} x \qquad \text{(B.18)}$$

The equivalent permeability can be taken as the geometric mean:

$$\kappa_e = \left(\kappa_{xx}\kappa_{yy}\right)^{1/2} \qquad \text{(B.19)}$$

and the x and y coordinates can be related between systems as:

$$x_e = \left(\frac{\kappa_{yy}}{\kappa_{xx}}\right)^{1/4} x$$

$$y_e = \left(\frac{\kappa_{xx}}{\kappa_{yy}}\right)^{1/4} y$$

$$R|_{x_e} = \left(\frac{\kappa_{yy}}{\kappa_{xx}}\right)^{1/4} R|_x \qquad \text{(B.20)}$$

The radius of the flow front in the equivalent system is $R(x_e)$. When substituted into Eq. (B.6), a linear relationship between time and a function (F) of $R(x_e)$ becomes

clear:

$$4\frac{\kappa_e \Delta P}{\varepsilon \mu R_o^{\,2}} t = \left(\frac{R|_{x_c}}{R_o}\right)^2 \left[2 ln\left(\frac{R|_{x_c}}{R_o}\right) - 1\right] + 1 \qquad (B.21)$$

$$F\left(R|_{x_c}\right) = m_2 t - 1$$

These relations can now be used to determine the components of the permeability tensor, given data from a flow experiment such as that depicted in Figure B.1. The experiment must be conducted so that the pressure drop is constant and known, and the porosity, viscosity, and inlet radius are known. The data should consist of the front location of the spreading ellipse in the x and y direction, at several times, t. A plot of R_x versus R_y should yield a straight line, passing through (R_o, R_o) and having a slope, m_1, given by Eq. (B.18). A plot of F(Rxe) versus t should yield a straight line with an intercept of -1, and a slope of m_2. Figure B.3 depicts the necessary plots.

When the values of the two slopes are known, they can be used along with known experimental conditions and the equations above to solve for the values of κ_{xx} and κ_{yy}, which are the components of the permeability of the porous medium in the two principal directions, which coincide with the laboratory coordinates. For a treatment of a porous medium whose permeability is not orthotropic, see Chan and Hwang.

DERIVATION OF THE LONGITUDINAL DISPERSION COEFFICIENT

Figure (B.4) shows a coordinate system for flow between two flat plates. The fluid velocity is u_x, and there is an interface with the coordinate x_I, which moves with the fluid. The interface divides the fluid into two regions of different concentration of some component which is soluble in both regions of fluid. Far ahead of the interface, the concentration is taken as zero, and far behind the interface the concentration is unity. The concentration at the interface will change with time, as depicted in Figure (B.4). The

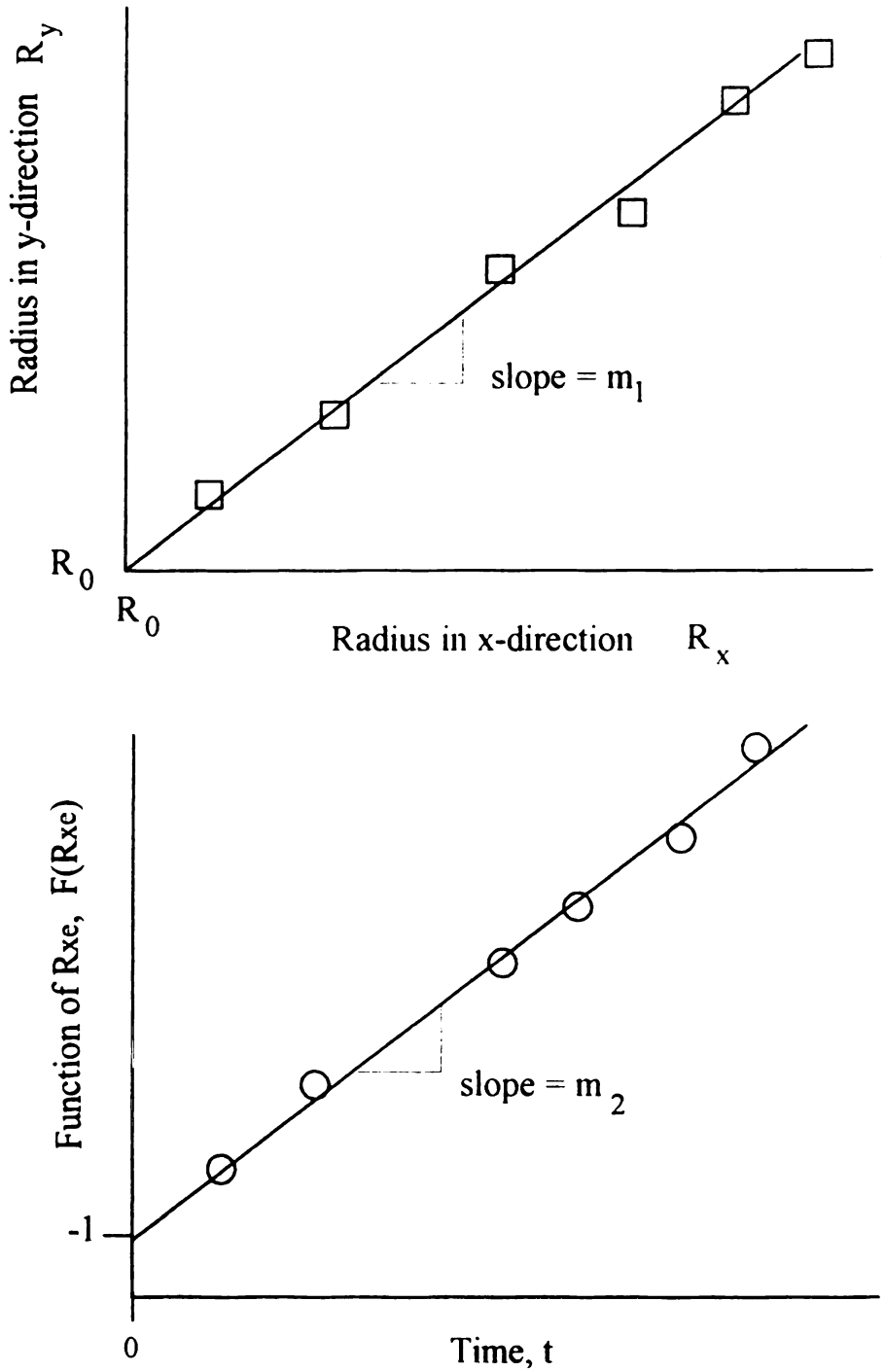


Figure B.3: Example plots of data from permeability experiments.

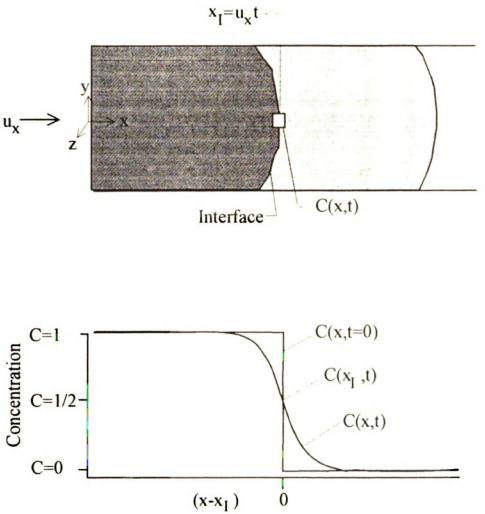


Figure B.4: Coordinates and definitions for derivation of longitudinal dispersion coefficient.

derivation below will use Fick's law to find an expression of the concentration of the component near the interface as a function of time.

Fick's law for the concentration in the differential element of Figure (B.4) is:

$$\frac{DC}{Dt} = D_L \nabla^2 C \tag{B.22}$$

given that there are no velocity components in the y or z directions, this reduces to:

$$\frac{\partial C}{\partial t} + u_x \frac{\partial C}{\partial x} = D_L \frac{\partial^2 C}{\partial x^2} \tag{B.23}$$

with boundary conditions:

$$C(+\infty, t) = 0$$

$$C(-\infty, t) = 1 \tag{B.24}$$

$$C(x_I, t > 0) = \frac{1}{2}$$

This equation is written in the laboratory coordinate system, but it will be convenient to define a coordinate system that has its origin at the interface, and which moves with the interface. Thus, Eq.(B.24) and boundary conditions become:

$$\xi = x - x_I = x - u_x t$$

$$\frac{\partial C}{\partial t} = D_L \frac{\partial^2 C}{\partial \xi^2}$$

$$C(+\infty, t) = 0$$

$$C(-\infty, t) = 1$$

$$C(0, t > 0) = \frac{1}{2} \tag{B.25}$$

To integrate the above expression, a similarity transformation is introduced, which transforms the expression and boundary conditions to:

$$\beta = \frac{\xi}{\sqrt{4D_L t}}$$

$$\frac{\partial^2 C}{\partial \beta^2} + 2\beta \frac{\partial C}{\partial \beta} = 0$$

$$C(\beta = +\infty) = 0$$

$$C(\beta = -\infty) = 1$$

$$C(\beta = 0) = \frac{1}{2} \qquad \text{(B.26)}$$

Recognizing the definition of the error function as:

$$erf(\varphi) = \frac{2}{\sqrt{\pi}} \int_0^{\varphi} exp\left(-\zeta^2\right) d\zeta \qquad \text{(B.27)}$$

and integrating twice, with evaluation of constants of integration yields the expression for the concentration at any location and time in the system defined above.

$$C = \frac{1}{2}\left[1 - erf\left(\frac{\xi}{\sqrt{4D_L t}}\right)\right] \qquad \text{(B.28)}$$

By similar arguments, the concentration as a function of location and time of a component which is dispersing in the direction transverse to the main flow, as shown in Figure (B.5) can be shown to be:

$$C(y,t)\big|_x = \frac{1}{2}\left[1 - erf\left(\frac{(y - y_I)\big|_x}{\sqrt{4D_T t}}\right)\right] \qquad \text{(B.29)}$$

where C, y and t are evaluated at a constant value of x.

REGRESSION METHOD USED TO CALCULATE DISPERSION COEFFICIENTS

Given the expression for the concentration as a function of location and time, derived above, derive the value of the dispersion coefficient that best fits the data available in the form of C(x,y,t). Only the longitudinal case will be derived here, as the

transverse case is exactly similar, with the substitution of $(y-y_I)$ for $(x-x_I)$.

Given

$$C = \frac{1}{2}\left[1 \pm erf\left(\frac{x - x_I}{2\sqrt{Dt}}\right)\right] \tag{B.30}$$

Where: C is the concentration of interest, $0 \le C \le 1$.

x_I is the location of the interface, i.e. $C(x_I) = 0.5$, in cm.

x and t are the location and time where C was measured. Units are cm and sec, respectively.

D is the dispersion coefficient [cm^2/sec]

When the initial concentration steps up, i.e., $C(0^+) = 0$ and $C(0^-) = 1$, use the negative sign in the brackets.

The error function is:

$$erf(x) = \frac{2}{\sqrt{\pi}}\int_0^x e^{-\xi^2} d\xi \tag{B.31}$$

other properties of the error function worth noting:

$$\frac{d}{d\xi} erf(\xi) = \frac{2}{\sqrt{\pi}} e^{-\xi^2}$$

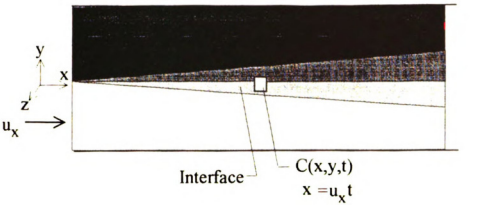
$$\frac{d}{d\xi} erf(f(\xi)) = \frac{2}{\sqrt{\pi}} e^{-f(\xi)^2} \frac{df(\xi)}{d\xi} \tag{B.32}$$

$$\frac{d}{d\xi}\left[erf(f(\xi))\right]^2 = 2\, erf(f(\xi)) \frac{d}{d\xi} erf(f(\xi))$$

Say there is a set of data, $C_i(x_i, t_i)$ where the subscript indicates the i'th point in a set of N points. Each point will individually satisfy Eq. (B.21). To find the parameters of the equation which allow the best fit of a number of points, first define the residual as the amount by which the equation with a given set of points is *not* satisfied.

$$R_i = C_i - \frac{1}{2}\left[1 - erf\left(\frac{A_i}{\sqrt{D}}\right)\right]$$

$$A_i = \left(\frac{x_i - x_{I_i}}{2\sqrt{t_i}}\right) \tag{B.33}$$



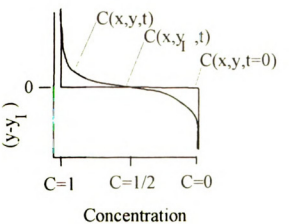


Figure B.5 Coordinates and definitions for derivation of transverse dispersion coefficient.

Since it is desired to minimize negative as well as positive values of R, take the square of R, and sum over all sets of data.

$$\sum_{i=1}^{N} R_i^2 = \sum_{i=1}^{N} C_i^2 - \sum_{i=1}^{N} C_i \, erf\left(\frac{A_i}{\sqrt{D}}\right) + \frac{N}{4} - \frac{1}{2}\sum_{i=1}^{N} erf\left(\frac{A_i}{\sqrt{D}}\right) + \frac{1}{4}\sum_{i=1}^{N}\left(erf\left(\frac{A_i}{\sqrt{D}}\right)\right)^2 \tag{B.34}$$

Now, to minimize the residual with respect to $\sqrt{D}$, take the derivative, and set it equal to zero. Making use of the derivative properties of the error function listed above, this yields:

$$\frac{d}{d\sqrt{D}}\sum_{i=1}^{N} R_i^2 = 0 = \sum_{i=1}^{N} -\frac{C_i A_i}{D} exp\left(-\frac{A_i^2}{D}\right) - \frac{1}{2}\sum_{i=1}^{N} -\frac{A_i}{D} exp\left(-\frac{A_i^2}{D}\right) + \frac{1}{2}\sum_{i=1}^{N} -\frac{A_i}{D} exp\left(-\frac{A_i^2}{D}\right) erf\left(\frac{A_i}{\sqrt{D}}\right) \tag{B.35}$$

This equation was solved in a spreadsheet, by using a look-up table for the error function, and varying D until the sum of R^2 was less than 0.005. In order to check the quality of the fit, a fitting coefficient was also computed:

$$\text{Fit coefficient} = 1 - \frac{\sum_{i=1}^{N}(C_i - C_c)^2}{\sum_{i=1}^{N}(C_i - \bar{C})^2}$$

$$\bar{C} = \frac{1}{N}\sum_{i=1}^{N} C_i$$

$$C_c = \frac{1}{2}\left[1 - erf\left(\frac{A_i}{\sqrt{D}}\right)\right] \tag{B.36}$$

A value of 1 for the fit coefficient indicates that the fit is perfect, or that the data are

scattered perfectly symmetrically around the model curve. It is generally best to plot the data and model curve to distinguish between these two possibilities.

APPENDIX C

DATA AND CALCULATIONS

This appendix contains the experimental data and calculations in tabular form. Some data is in pictorial form, and these are also included. The data and calculations are arranged in the order in which they are treated in the text. Nearly all calculations were performed on QuattroPro 3.0, a spreadsheet program, so no source code is listed here, but sample calculations are shown where appropriate.

Table C.1: Viscosity by time data for DGEBA/TETA epoxy resin system. Data were taken on Brookfield viscometer. Isothermal at 323 °K.

TIME (min)	VISCOSITY (Pa·sec)
0.0	0.135
1.0	0.130
3.0	0.130
8.0	0.175
9.0	0.193
10.0	0.215
11.0	0.240
12.0	0.275
13.0	0.317
14.0	0.373
15.0	0.442
16.0	0.550
17.0	0.645
18.0	0.810
19.0	1.02
20.0	1.30
21.0	1.71
22.0	2.28
23.0	3.12
24.0	4.30
25.0	6.20

Table C.2: Data from Rheometrics viscometer. Includes G' and G" data as well as viscosity data. Lowest reliable torque reading is 2.0 g·cm.

TIME (min)	TORQUE (g·cm)	VISCOSITY (Pa·sec)	G' (Pa)	G" (Pa)	TEMP (°C)
29.5	1.517 E+00	6.054 E+00	0.000 E+00	6.054 E+01	50.7
30.0	1.731 E+00	6.907 E+00	0.000 E+00	6.907 E+01	50.7
30.5	1.950 E+00	7.779 E+00	0.000 E+00	7.779 E+01	50.7
31.0	2.193 E+00	8.754 E+00	0.000 E+00	8.754 E+01	50.7
31.5	2.490 E+00	9.939 E+00	0.000 E+00	9.939 E+01	50.7
32.0	2.807 E+00	1.120 E+01	0.000 E+00	1.120 E+02	50.7
32.5	3.210 E+00	1.281 E+01	0.000 E+00	1.281 E+02	50.7
33.0	3.650 E+00	1.457 E+01	0.000 E+00	1.457 E+02	50.7
33.5	4.170 E+00	1.665 E+01	0.000 E+00	1.665 E+02	50.7
34.0	4.789 E+00	1.911 E+01	0.000 E+00	1.911 E+02	50.7
34.5	5.509 E+00	2.199 E+01	0.000 E+00	2.199 E+02	50.7
35.0	6.333 E+00	2.528 E+01	0.000 E+00	2.528 E+02	50.7
35.5	7.329 E+00	2.925 E+01	0.000 E+00	2.925 E+02	50.7
36.0	8.478 E+00	3.383 E+01	0.000 E+00	3.383 E+02	50.7
36.5	9.816 E+00	3.918 E+01	0.000 E+00	3.918 E+02	50.7
37.0	1.140 E+01	4.551 E+01	0.000 E+00	4.551 E+02	50.7
37.5	1.328 E+01	5.296 E+01	0.000 E+00	5.296 E+02	50.7
38.0	1.553 E+01	6.195 E+01	0.000 E+00	6.195 E+02	50.7
38.5	1.817 E+01	7.250 E+01	0.000 E+00	7.250 E+02	50.7
39.0	2.131 E+01	8.502 E+01	0.000 E+00	8.502 E+02	50.7
39.5	2.508 E+01	1.001 E+02	0.000 E+00	1.001 E+03	50.7
40.0	2.957 E+01	1.180 E+02	0.000 E+00	1.180 E+03	50.7
40.5	3.498 E+01	1.395 E+02	0.000 E+00	1.395 E+03	50.7
41.0	4.148 E+01	1.655 E+02	0.000 E+00	1.655 E+03	50.7
41.5	4.939 E+01	1.970 E+02	0.000 E+00	1.970 E+03	50.7
42.0	5.917 E+01	2.361 E+02	0.000 E+00	2.361 E+03	50.7
42.5	7.067 E+01	2.819 E+02	0.000 E+00	2.819 E+03	50.7
43.0	8.466 E+01	3.375 E+02	0.000 E+00	3.375 E+03	50.7
43.5	1.018 E+02	4.060 E+02	0.000 E+00	4.060 E+03	50.7
44.0	1.230 E+02	4.909 E+02	0.000 E+00	4.909 E+03	50.7
44.5	1.485 E+02	5.929 E+02	0.000 E+00	5.929 E+03	50.7
45.0	1.799 E+02	7.191 E+02	0.000 E+00	7.191 E+03	50.7
45.5	2.183 E+02	8.744 E+02	0.000 E+00	8.744 E+03	50.7
46.0	2.645 E+02	1.063 E+03	0.000 E+00	1.063 E+04	50.7
46.5	3.208 E+02	1.296 E+03	0.000 E+00	1.296 E+04	50.7
47.0	3.883 E+02	1.580 E+03	0.000 E+00	1.580 E+04	50.7
47.5	4.685 E+02	1.929 E+03	0.000 E+00	1.929 E+04	50.6

Table C.2: Continued.

TIME (min)	TORQUE (g·cm)	VISCOSITY (Pa·sec)	G' (Pa)	G" (Pa)	TEMP (°C)
48.0	5.623 E+02	2.350 E+03	0.000 E+00	2.350 E+04	50.7
48.5	6.695 E+02	2.860 E+03	0.000 E+00	2.860 E+04	50.6
49.0	7.881 E+02	3.458 E+03	0.000 E+00	3.458 E+04	50.7
49.5	9.201 E+02	4.174 E+03	0.000 E+00	4.174 E+04	50.7
50.0	1.061 E+03	5.008 E+03	0.000 E+00	5.008 E+04	50.7
50.5	1.061 E+03	5.964 E+03	0.000 E+00	5.964 E+04	50.7
51.0	1.061 E+03	7.030 E+03	0.000 E+00	7.030 E+04	50.7
51.5	1.061 E+03	8.153 E+03	0.000 E+00	8.153 E+04	50.7
52.0	1.061 E+03	9.222 E+03	0.000 E+00	9.222 E+04	50.7
52.5	1.061 E+03	1.013 E+04	0.000 E+00	1.013 E+05	50.6
53.0	1.061 E+03	1.072 E+04	0.000 E+00	1.072 E+05	50.7

Table C.3: Time by viscosity data for Derakane® 411 resin. Data taken on Brookfield viscometer, isothermal at 22 °C.

TIME (min)	VISCOSITY (Pa·sec)
0.0	0.476
1.0	0.476
3.0	0.468
5.0	0.462
7.0	0.456
9.0	0.452
11.0	0.462
13.0	0.512
13.5	0.536
14.0	0.554
14.5	0.586
15.0	0.622
15.5	0.674
16.0	0.734
16.5	0.820
16.75	0.870
17.0	0.920
17.25	1.01
17.5	1.07
17.75	1.19
18.0	1.27
18.5	1.62
18.75	1.98

Table C.4: DSC data for DGEBA/TETA epoxy system. Scan rate is 1 °C/min.

TEMP (°C)	HEAT FLOW (W/g)	Integral (J/g)	α
26	-0.0286		
28	-0.0291	0.057	0.000
30	-0.0260	0.435	0.001
32	-0.0219	1.29	0.003
34	-0.0134	2.75	0.006
36	-0.0108	4.85	0.011
38	-0.0030	7.69	0.018
40	0.0050	11.38	0.026
42	0.0157	16.26	0.037
44	0.0279	22.42	0.051
46	0.0402	29.98	0.068
48	0.0575	39.32	0.090
50	0.0758	50.75	0.116
52	0.0960	64.17	0.146
54	0.1196	80.22	0.183
56	0.1419	98.93	0.226
58	0.1675	120.8	0.275
60	0.1879	145.3	0.331
62	0.2035	171.9	0.392
64	0.2129	200.2	0.456
66	0.2123	229.6	0.523
68	0.2027	258.0	0.588
70	0.1856	285.0	0.650
72	0.1629	309.9	0.706
74	0.1386	331.9	0.757
76	0.1144	351.0	0.800
78	0.0915	367.2	0.837
80	0.0711	380.6	0.868
82	0.0527	391.9	0.893
84	0.0365	401.0	0.914
86	0.0246	408.4	0.931
88	0.0132	414.5	0.945
90	0.0044	419.4	0.956
92	-0.0009	423.4	0.965
94	-0.0066	426.7	0.973

Table C.4: Continued.

TEMP (°C)	HEAT FLOW (W/g)	Integral (J/g)	α
96	-0.0107	429.5	0.979
98	-0.0138	431.8	0.984
100	-0.0179	433.8	0.989
102	-0.0195	435.4	0.992
104	-0.0214	436.8	0.996
106	-0.0243	437.9	0.998
108	-0.0259	438.7	1.000

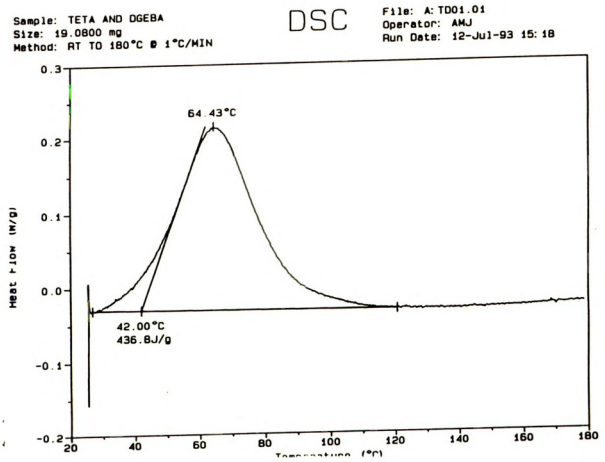


Figure C.1: Graph of DSC data, DGEBA/TETA epoxy resin. Scan rate is 1 °C/min.

Table C.5: DSC data for DGEBA/TETA epoxy system. Scan rate is 2 °C/min.

TEMP (°C)	HEAT FLOW (W/g)	Integral (J/g)	α
26	-0.0615	0.009	0.000
28	-0.0583	0.136	0.000
30	-0.0558	0.430	0.001
32	-0.0514	0.948	0.002
34	-0.0471	1.70	0.004
36	-0.0425	2.71	0.006
38	-0.0343	4.10	0.010
40	-0.0239	6.09	0.014
42	-0.0144	8.61	0.020
44	-0.0025	11.77	0.028
46	0.0113	15.64	0.037
48	0.0282	20.41	0.048
50	0.0449	26.14	0.062
52	0.0675	32.95	0.078
54	0.0923	41.18	0.098
56	0.1193	50.82	0.120
58	0.1499	62.09	0.147
60	0.1830	75.62	0.179
62	0.2174	90.61	0.215
64	0.2527	107.8	0.255
66	0.2856	126.8	0.300
68	0.3136	147.7	0.350
70	0.3348	170.1	0.403
72	0.3449	193.4	0.458
74	0.3464	217.9	0.516
76	0.3308	242.1	0.573
78	0.3074	265.1	0.628
80	0.2783	286.6	0.679
82	0.2419	306.2	0.725
84	0.2078	323.7	0.767
86	0.1742	339.1	0.803
88	0.1416	352.7	0.835
90	0.1148	364.3	0.863

Table C.5: Continued.

TEMP (°C)	HEAT FLOW (W/g)	Integral (J/g)	α
92	0.0890	374.2	0.886
94	0.0657	382.7	0.906
96	0.0467	389.8	0.923
98	0.0296	395.8	0.937
100	0.0146	400.8	0.949
102	0.0036	405.2	0.960
104	-0.0087	408.8	0.968
106	-0.0174	411.8	0.975
108	-0.0255	414.3	0.981
110	-0.0332	416.2	0.986
112	-0.0411	417.8	0.990
114	-0.0449	419.0	0.992
116	-0.0492	419.9	0.995
118	-0.0535	420.6	0.996
120	-0.0561	421.1	0.997
122	-0.0580	421.5	0.998
124	-0.0590	421.8	0.999
126	-0.0599	422.0	1.000
128	-0.0613	422.1	1.000
130	-0.0622	422.2	1.000

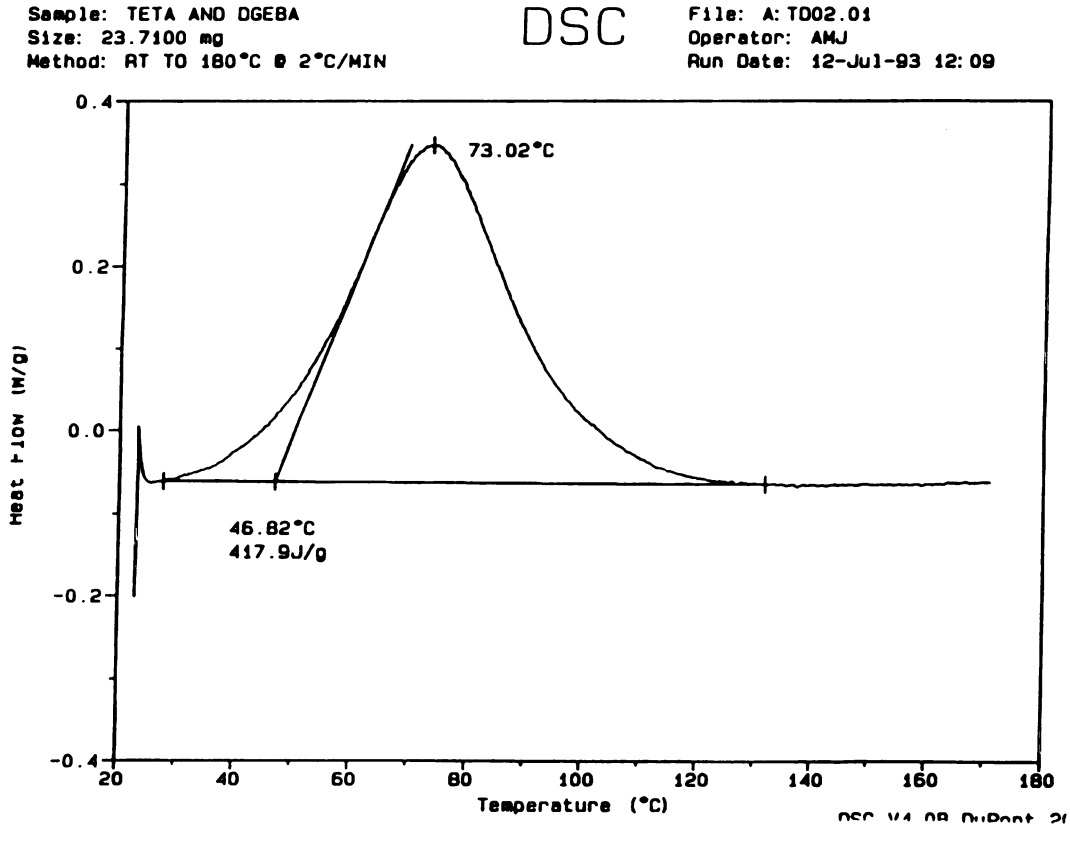


Figure C.2: Graph of DSC data, DGEBA/TETA epoxy resin. Scan rate is 2°C/min.

Table C.6: DSC data for DGEBA/TETA epoxy system. Scan rate is 5°C/min.

TEMP (°C)	HEAT FLOW (W/g)	Integral (J/g)	α
28	-0.1585	0.558	0.001
30	-0.1580	0.163	0.000
32	-0.1544	0.318	0.001
34	-0.1514	0.559	0.001
36	-0.1489	0.864	0.002
38	-0.1439	1.270	0.003
40	-0.1381	1.804	0.004
42	-0.1309	2.513	0.006
44	-0.1242	3.360	0.007
46	-0.1168	4.378	0.010
48	-0.1074	5.604	0.012
50	-0.0963	7.075	0.016
52	-0.0857	8.731	0.019
54	-0.0696	10.75	0.024
56	-0.0516	13.16	0.029
58	-0.0301	16.06	0.035
60	-0.0052	19.47	0.043
62	0.0217	23.47	0.052
64	0.0543	28.15	0.062
66	0.0927	33.63	0.074
68	0.1324	39.90	0.088
70	0.1833	47.21	0.104
72	0.2404	55.70	0.123
74	0.3051	65.60	0.144
76	0.3763	76.91	0.169
78	0.4521	89.75	0.198
80	0.5329	104.2	0.229
82	0.6184	120.6	0.265
84	0.6968	138.8	0.306
86	0.7690	158.6	0.349
88	0.8286	180.5	0.397
90	0.8635	204.1	0.449
92	0.8678	228.6	0.503

Table C.6: Continued.

TEMP (°C)	HEAT FLOW (W/g)	Integral (J/g)	α
94	0.8408	253.5	0.558
96	0.7861	277.6	0.611
98	0.7119	300.6	0.662
100	0.6271	321.7	0.708
102	0.5404	340.8	0.750
104	0.4581	357.7	0.787
106	0.3807	372.3	0.820
108	0.3121	385.1	0.848
110	0.2506	396.3	0.872
112	0.1960	406.0	0.894
114	0.1463	414.5	0.912
116	0.1013	421.6	0.928
118	0.0623	427.7	0.941
120	0.0260	432.9	0.953
122	-0.0048	437.2	0.962
124	-0.0316	440.9	0.971
126	-0.0571	444.0	0.977
128	-0.0782	446.4	0.983
130	-0.0960	448.4	0.987
132	-0.1117	450.0	0.991
134	-0.1253	451.3	0.993
136	-0.1369	452.2	0.995
138	-0.1476	452.9	0.997
140	-0.1535	453.4	0.998
142	-0.1596	453.8	0.999
144	-0.1641	454.0	0.999
146	-0.1675	454.2	1.000
148	-0.1710	454.3	1.000
150	-0.1722	454.3	1.000

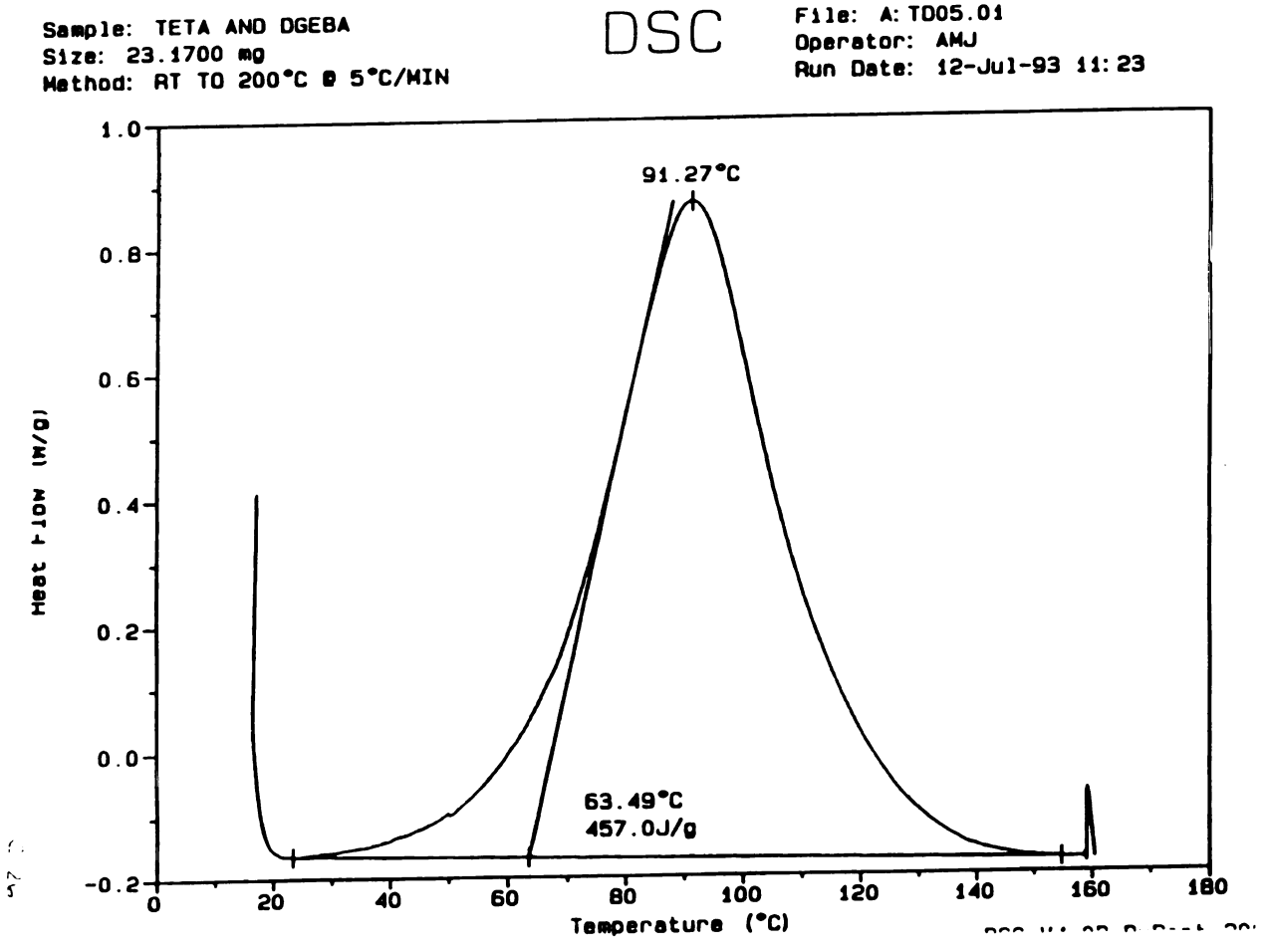


Figure C.3: Graph of DSC data, DGEBA/TETA epoxy resin. Scan rate is 5°C/min.

Table C.7: DSC data for DGEBA/TETA epoxy system. Scan rate is 10°C/min.

TEMP (°C)	HEAT FLOW (W/g)	Integral (J/g)	α
48	-0.3237	0.046	0.000
50	-0.2945	0.432	0.001
52	-0.2748	1.095	0.003
54	-0.2580	1.966	0.004
56	-0.2408	3.034	0.007
58	-0.2219	4.320	0.010
60	-0.2012	5.833	0.013
62	-0.1789	7.591	0.017
64	-0.1531	9.616	0.022
66	-0.1226	11.97	0.027
68	-0.0891	14.67	0.033
70	-0.0505	17.77	0.041
72	-0.0048	21.34	0.049
74	0.0474	25.47	0.058
76	0.1062	30.18	0.069
78	0.1719	35.50	0.081
80	0.2471	41.58	0.095
82	0.3335	48.51	0.111
84	0.4300	56.38	0.129
86	0.5367	65.24	0.149
88	0.6545	75.23	0.172
90	0.7823	86.50	0.197
92	0.9169	99.08	0.226
94	1.0560	113.1	0.258
96	1.1900	128.4	0.293
98	1.3160	145.2	0.332
100	1.4220	163.6	0.374
102	1.4970	183.4	0.419
104	1.5300	204.7	0.467
106	1.5130	227.2	0.519
108	1.4930	249.9	0.571
110	1.3200	272.2	0.621

Table C.7: Continued.

TEMP (°C)	HEAT FLOW (W/g)	Integral (J/g)	α
112	1.1730	293.4	0.670
114	1.0150	312.6	0.714
116	0.8625	329.6	0.753
118	0.7217	344.5	0.787
120	0.5944	357.6	0.816
122	0.4811	368.9	0.842
124	0.3825	378.8	0.865
126	0.2962	387.4	0.884
128	0.2190	394.9	0.902
130	0.1501	401.5	0.917
132	0.0881	407.3	0.930
134	0.0317	412.3	0.941
136	-0.0193	416.6	0.951
138	-0.0658	420.3	0.960
140	-0.1066	423.4	0.967
142	-0.1432	426.1	0.973
144	-0.1745	428.4	0.978
146	-0.2030	430.3	0.982
148	-0.2282	431.8	0.986
150	-0.2483	433.1	0.989

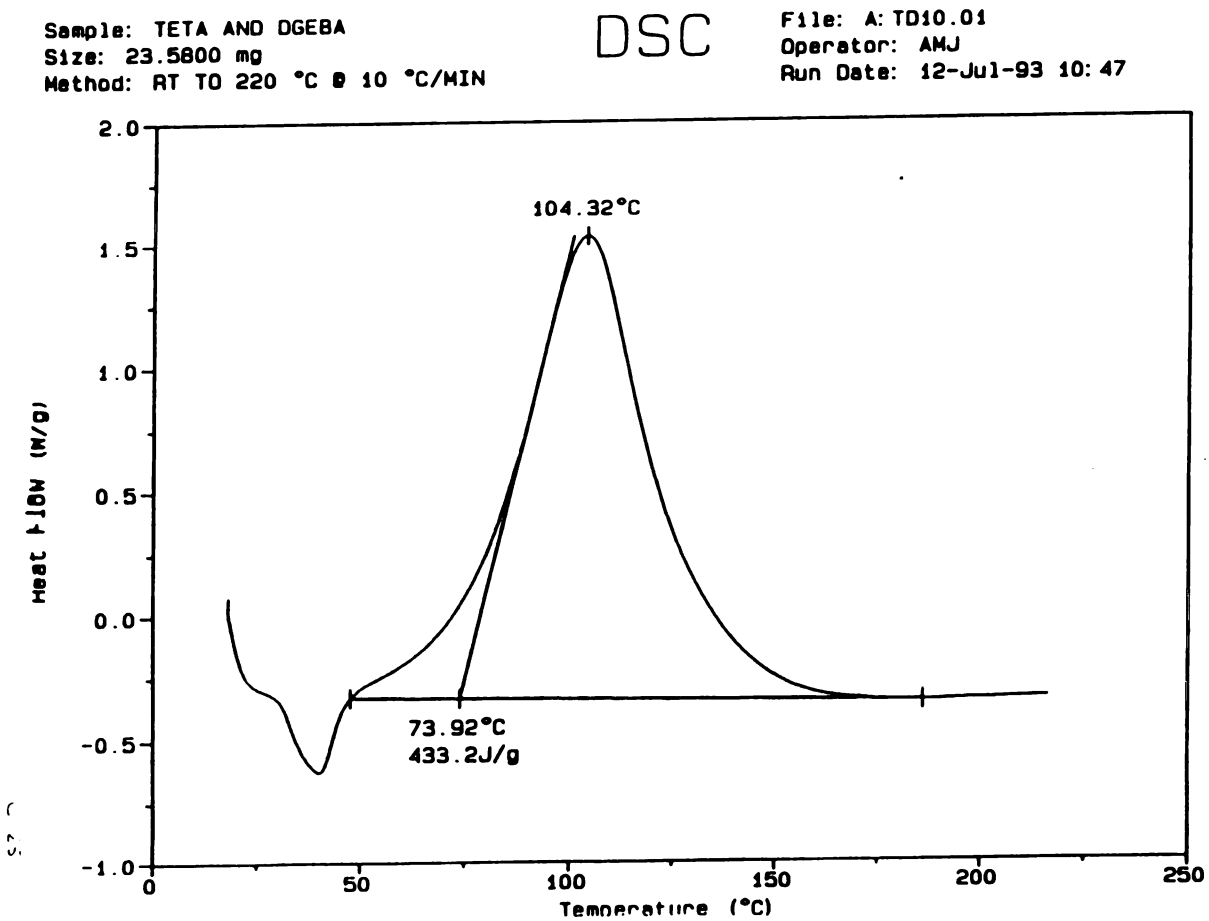


Figure C.4: Graph of DSC data, DGEBA/TETA epoxy resin. Scan rate is 10°C/min.

Table C.8: DSC data for DGEBA/TETA epoxy system. Scan rate is 20°C/min.

TEMP (°C)	HEAT FLOW (W/g)	Integral (J/g)	α
50	-0.7393		
52	-0.7118	0.069	0.000
54	-0.6896	0.280	0.001
56	-0.6699	0.612	0.001
58	-0.651	1.061	0.002
60	-0.6328	1.621	0.004
62	-0.614	2.288	0.005
64	-0.5932	3.070	0.007
66	-0.5702	3.981	0.009
68	-0.5518	5.019	0.011
70	-0.5215	6.178	0.013
72	-0.4818	7.547	0.016
74	-0.4395	9.148	0.020
76	-0.3936	11.00	0.024
78	-0.3431	13.11	0.029
80	-0.2865	15.52	0.034
82	-0.2223	18.26	0.040
84	-0.1496	21.37	0.047
86	-0.06731	24.89	0.054
88	0.02603	28.89	0.063
90	0.1321	33.43	0.073
92	0.2516	38.54	0.084
94	0.3857	44.28	0.097
96	0.5347	50.68	0.111
98	0.7009	57.85	0.126
100	0.8838	65.83	0.144
102	1.086	74.73	0.163
104	1.304	84.61	0.185
106	1.536	95.52	0.209
108	1.779	107.5	0.235
110	2.027	120.8	0.264
112	2.272	135.3	0.296
114	2.5	151.0	0.330
116	2.699	168.1	0.367
118	2.851	186.8	0.408

Table C.8: Continued.

TEMP (°C)	HEAT FLOW (W/g)	Integral (J/g)	α
120	2.934	207.0	0.452
122	2.929	228.6	0.499
124	2.824	251.2	0.549
126	2.625	273.9	0.598
128	2.356	296.0	0.647
130	2.05	316.6	0.692
132	1.742	335.1	0.732
134	1.455	351.5	0.768
136	1.196	365.7	0.799
138	0.9674	378.1	0.826
140	0.7683	388.8	0.849
142	0.5939	398.2	0.870
144	0.441	406.4	0.888
146	0.3052	413.6	0.903
148	0.1832	420.0	0.917
150	0.07358	425.5	0.929
152	-0.02427	430.4	0.940
154	-0.1135	434.7	0.950
156	-0.1942	438.5	0.958
158	-0.2671	441.7	0.965
160	-0.3332	444.6	0.971
162	-0.3932	447.0	0.976
164	-0.4469	449.0	0.981
166	-0.4947	450.8	0.985
168	-0.5368	452.3	0.988
170	-0.5737	453.5	0.991
172	-0.6063	454.5	0.993
174	-0.6346	455.3	0.995
176	-0.6593	456.0	0.996
178	-0.6809	456.5	0.997
180	-0.6987	456.9	0.998
182	-0.713	457.2	0.999
184	-0.7245	457.4	0.999
186	-0.7336	457.5	0.999
188	-0.7409	457.7	1.000
190	-0.7467	457.7	1.000
192	-0.7514	457.8	1.000

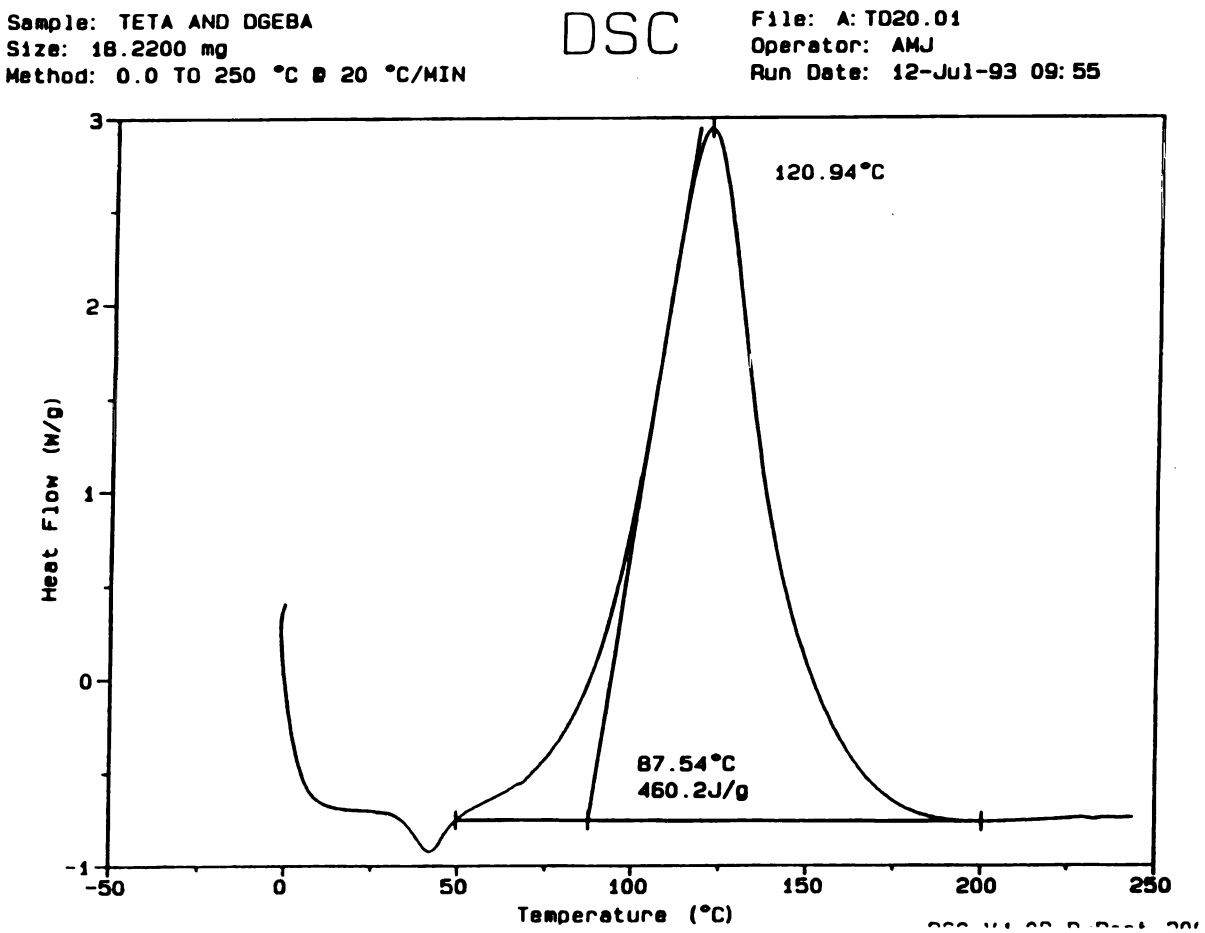


Figure C.5: Graph of DSC data, DGEBA/TETA epoxy resin. Scan rate is 20°C/min.

Table C.9: DSC data for DGEBA/TETA epoxy system. Scan rate is 30°C/min.

TEMP (°C)	HEAT FLOW (W/g)	Integral (J/g)	α
42	-1.025		
44	-1.042	-0.013	-0.000
46	-1.046	-0.062	-0.000
48	-1.033	-0.095	-0.000
50	-1.01	-0.587	-0.001
52	-0.988	0.064	0.000
54	-0.9695	0.264	0.001
56	-0.9535	0.528	0.001
58	-0.9389	0.850	0.002
60	-0.9247	1.227	0.003
62	-0.9103	1.657	0.004
64	-0.8956	2.141	0.005
66	-0.8796	2.679	0.006
68	-0.8616	3.282	0.008
70	-0.8417	3.955	0.009
72	-0.8191	4.708	0.011
74	-0.7936	5.548	0.013
76	-0.7646	6.489	0.015
78	-0.7319	7.540	0.018
80	-0.6945	8.723	0.021
82	-0.6517	10.05	0.024
84	-0.603	11.54	0.027
86	-0.5477	13.23	0.031
88	-0.485	15.12	0.036
90	-0.4137	17.26	0.041
92	-0.3339	19.66	0.046
94	-0.2438	22.35	0.053
96	-0.1426	25.36	0.060
98	-0.02809	28.74	0.068
100	0.101	32.52	0.076
102	0.2465	36.72	0.086
104	0.4094	41.39	0.097
106	0.5931	46.64	0.110
108	0.797	52.44	0.123

Table C.9: Continued.

TEMP (°C)	HEAT FLOW (W/g)	Integral (J/g)	α
110	1.023	58.84	0.138
112	1.272	65.97	0.155
114	1.543	73.76	0.173
116	1.832	82.27	0.193
118	2.142	91.67	0.215
120	2.464	101.9	0.240
122	2.793	113.1	0.266
124	3.119	125.4	0.295
126	3.424	138.7	0.326
128	3.694	153.3	0.360
130	3.906	169.2	0.398
132	4.029	186.8	0.439
134	4.04	206.1	0.484
136	3.913	226.9	0.533
138	3.645	248.7	0.585
140	3.261	270.3	0.635
142	2.817	290.7	0.683
144	2.372	308.9	0.726
146	1.958	324.8	0.764
148	1.594	338.4	0.795
150	1.278	350.1	0.823
152	1.004	360.2	0.847
154	0.7695	368.9	0.867
156	0.5656	376.5	0.885
158	0.3878	383.1	0.901
160	0.231	388.9	0.914
162	0.09208	394.0	0.926
164	-0.03104	398.5	0.937
166	-0.1422	402.4	0.946
168	-0.2422	405.9	0.954
170	-0.333	408.9	0.961
172	-0.4155	411.6	0.968
174	-0.4897	413.9	0.973
176	-0.5566	415.8	0.977
178	-0.617	417.5	0.981

Table C.9: Continued.

TEMP (°C)	HEAT FLOW (W/g)	Integral (J/g)	α
180	-0.6712	419.0	0.985
182	-0.7195	420.2	0.988
184	-0.7623	421.3	0.990
186	-0.7998	422.2	0.992
188	-0.8329	422.9	0.994
190	-0.8619	423.5	0.996
192	-0.8871	424.0	0.997
194	-0.9086	424.4	0.998
196	-0.9268	424.7	0.998
198	-0.942	424.9	0.999
200	-0.9544	425.1	0.999
202	-0.9651	425.3	1.000
204	-0.974	425.4	1.000

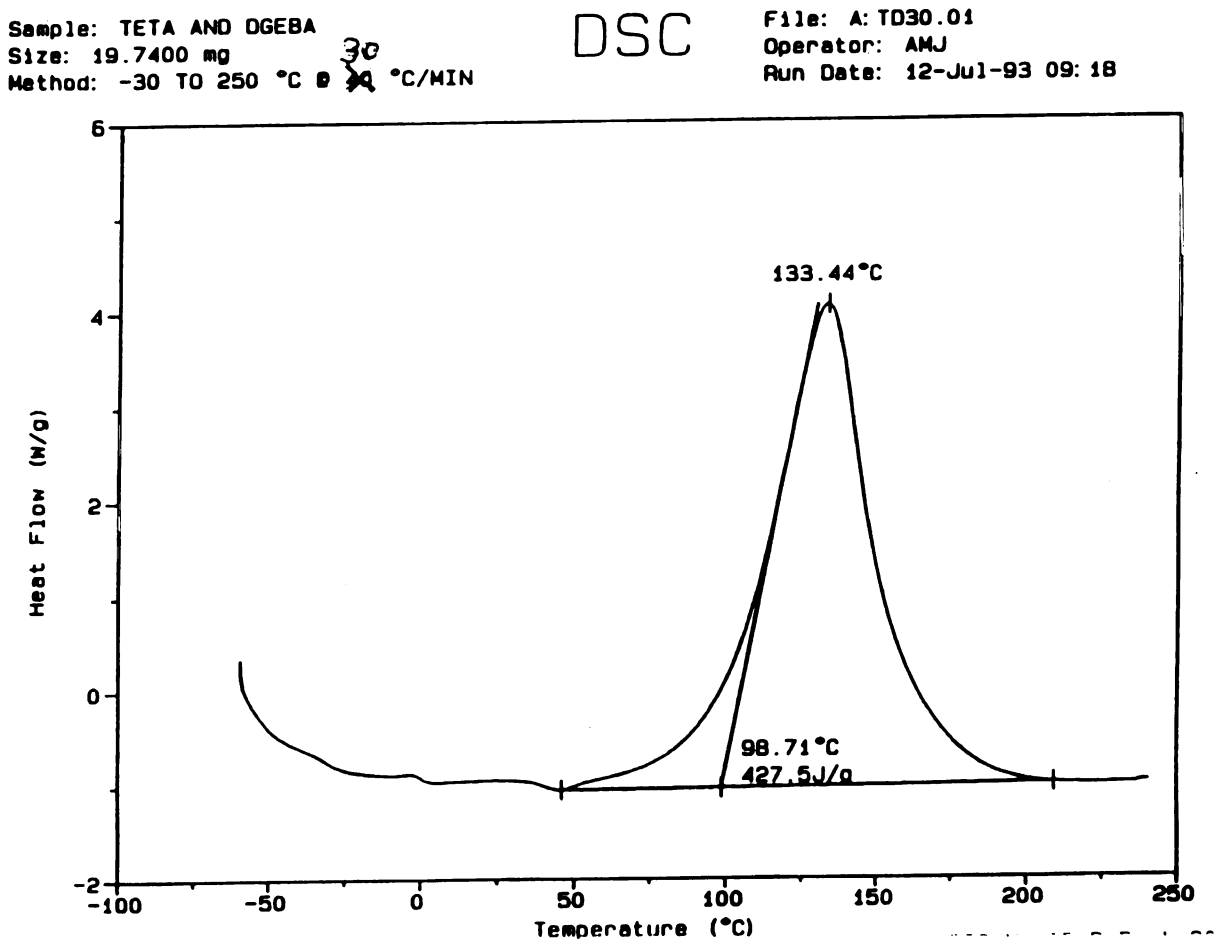


Figure C.6: Graph of DSC data, DGEBA/TETA epoxy resin. Scan rate is 30°C/min.

Table C.10: DSC data for DGEBA/TETA epoxy system. Scan rate is 40°C/min.

TEMP (°C)	HEAT FLOW (W/g)	Integral (J/g)	α
48	-1.471		
50	-1.467	0.005	0.000
52	-1.455	0.033	0.000
54	-1.439	0.101	0.000
56	-1.422	0.218	0.000
58	-1.405	0.379	0.001
60	-1.39	0.591	0.001
62	-1.375	0.843	0.002
64	-1.359	1.141	0.003
66	-1.343	1.482	0.003
68	-1.327	1.869	0.004
70	-1.309	2.306	0.005
72	-1.289	2.793	0.006
74	-1.267	3.344	0.007
76	-1.242	3.954	0.009
78	-1.215	4.639	0.010
80	-1.184	5.399	0.012
82	-1.15	6.250	0.014
84	-1.109	7.206	0.016
86	-1.065	8.266	0.018
88	-1.013	9.471	0.021
90	-0.9542	10.82	0.024
92	-0.8878	12.33	0.028
94	-0.8125	14.02	0.031
96	-0.7282	15.90	0.036
98	-0.6322	18.01	0.040
100	-0.5243	20.36	0.046
102	-0.4035	22.97	0.051
104	-0.2671	25.88	0.058
106	-0.113	29.13	0.065
108	0.05866	32.73	0.073
110	0.2502	36.68	0.082
112	0.4647	41.05	0.092
114	0.7038	45.85	0.102
116	0.9674	51.08	0.114
118	1.257	56.79	0.127

Table C.10: Continued.

TEMP (°C)	HEAT FLOW (W/g)	Integral (J/g)	α
120	1.576	63.00	0.141
122	1.923	69.74	0.156
124	2.297	77.02	0.172
126	2.694	84.82	0.190
128	3.111	93.16	0.208
130	3.546	102.1	0.228
132	3.994	111.8	0.250
134	4.442	122.2	0.273
136	4.85	133.5	0.298
138	5.127	145.7	0.326
140	5.226	158.9	0.355
142	5.235	173.3	0.387
144	5.205	189.3	0.423
146	5.151	207.6	0.464
148	5.078	229.9	0.514
150	4.994	257.2	0.575
152	4.401	288.3	0.644
154	3.446	316.6	0.708
156	2.62	339.2	0.758
158	1.965	356.7	0.797
160	1.447	370.4	0.828
162	1.033	381.4	0.852
164	0.6971	390.5	0.873
166	0.4203	398.0	0.890
168	0.1883	404.4	0.904
170	-0.00862	409.9	0.916
172	-0.1777	414.6	0.927
174	-0.3233	418.7	0.936
176	-0.4518	422.2	0.944
178	-0.5647	425.4	0.951
180	-0.6638	428.1	0.957
182	-0.7528	430.5	0.962
184	-0.8319	432.6	0.967

Table C.10: Continued.

TEMP (°C)	HEAT FLOW (W/g)	Integral (J/g)	α
186	-0.9027	434.5	0.971
188	-0.9661	436.1	0.975
190	-1.023	437.6	0.978
192	-1.075	438.9	0.981
194	-1.12	440.0	0.983
196	-1.161	441.0	0.986
198	-1.197	441.8	0.987
200	-1.228	442.6	0.989
202	-1.256	443.3	0.991
204	-1.28	443.8	0.992
206	-1.302	444.4	0.993
208	-1.32	444.8	0.994
210	-1.336	445.2	0.995
212	-1.349	445.5	0.996
214	-1.361	445.8	0.996
216	-1.37	446.1	0.997
218	-1.379	446.4	0.998
220	-1.386	446.6	0.998
222	-1.391	446.8	0.999
224	-1.395	447.0	0.999
226	-1.409	447.2	1.000
228	-1.423	447.3	1.000
230	-1.436	447.4	1.000

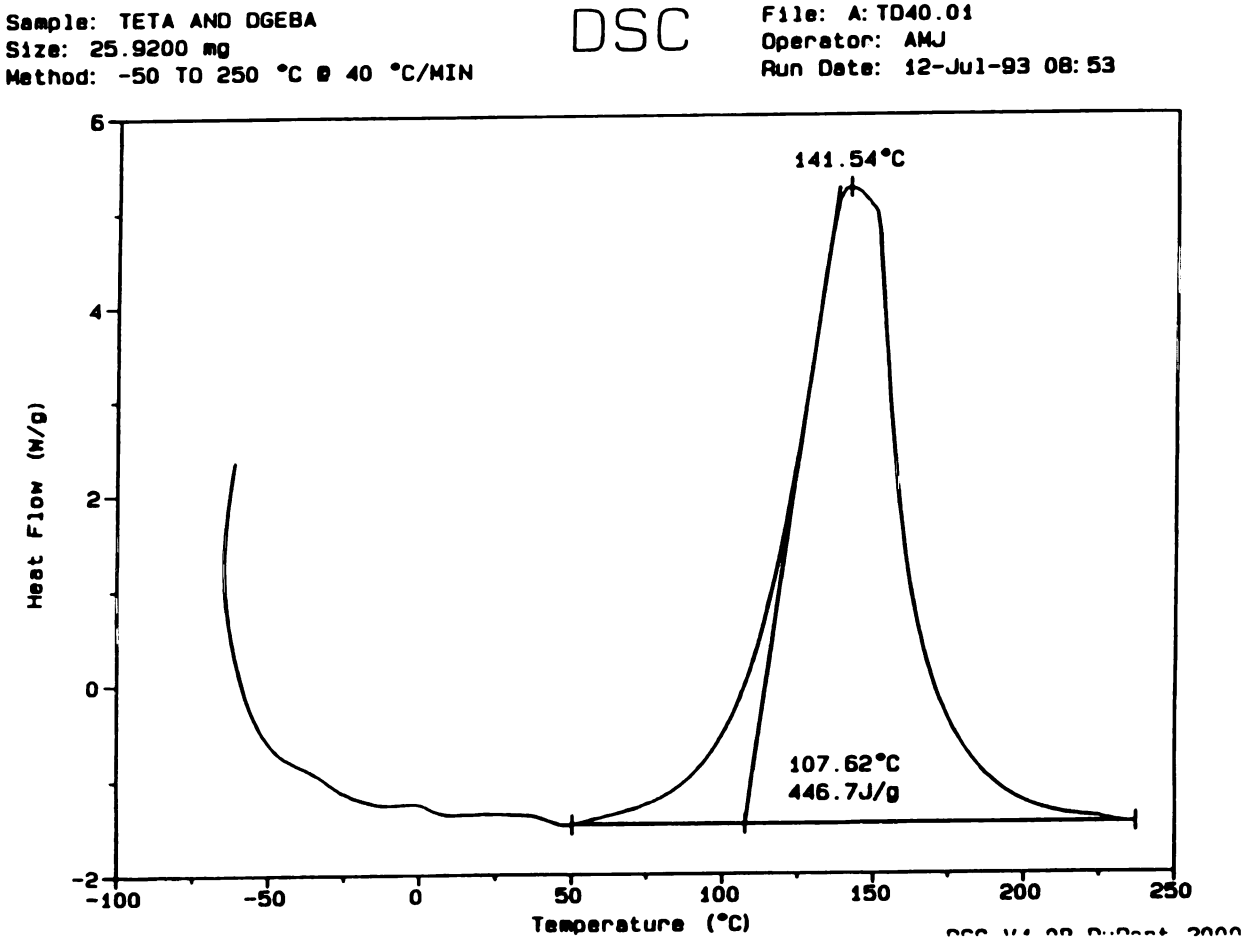


Figure C.7: Graph of DSC data, DGEBA/TETA epoxy resin. Scan rate is 40°C/min.

Table C.11: DSC data for DGEBA/TETA epoxy system. Scan rate is 50°C/min.

TEMP (°C)	HEAT FLOW (W/g)	Integral (J/g)	α
50	-1.747		
52	-1.744	0.004	0.000
54	-1.738	0.181	0.000
56	-1.732	0.048	0.000
58	-1.724	0.093	0.000
60	-1.717	0.157	0.000
62	-1.708	0.240	0.001
64	-1.698	0.346	0.001
66	-1.688	0.474	0.001
68	-1.677	0.628	0.002
70	-1.663	0.810	0.002
72	-1.648	1.024	0.002
74	-1.632	1.275	0.003
76	-1.612	1.568	0.004
78	-1.59	1.908	0.005
80	-1.565	2.301	0.006
82	-1.536	2.754	0.007
84	-1.503	3.275	0.008
86	-1.466	3.872	0.009
88	-1.423	4.557	0.011
90	-1.375	5.342	0.013
92	-1.319	6.248	0.015
94	-1.256	7.278	0.018
96	-1.185	8.442	0.020
98	-1.104	9.761	0.024
100	-1.014	11.26	0.027
102	-0.9117	12.94	0.031
104	-0.7975	14.83	0.036
106	-0.6692	16.95	0.041
108	-0.5255	19.32	0.047
110	-0.3645	21.97	0.053
112	-0.1849	24.92	0.060
114	0.01466	28.17	0.068
116	0.2364	31.75	0.077
118	0.4834	35.70	0.086

Table C.11: Continued.

TEMP (°C)	HEAT FLOW (W/g)	Integral (J/g)	α
120	0.7576	40.02	0.096
122	1.06	44.75	0.108
124	1.393	49.87	0.120
126	1.753	55.37	0.133
128	2.15	61.38	0.148
130	2.578	67.80	0.163
132	3.033	74.65	0.180
134	3.512	81.90	0.197
136	4.021	89.81	0.216
138	4.531	98.20	0.237
140	5.005	107.0	0.258
142	5.316	116.4	0.281
144	5.474	126.2	0.304
146	5.546	136.3	0.329
148	5.556	147.1	0.355
150	5.523	159.0	0.383
152	5.461	172.3	0.415
154	5.369	187.9	0.453
156	5.255	207.2	0.499
158	5.137	232.0	0.559
160	5.03	262.3	0.632
162	4.124	292.4	0.705
164	3.071	315.9	0.761
166	2.253	333.6	0.804
168	1.621	347.1	0.837
170	1.121	357.8	0.862
172	0.7193	366.4	0.883
174	0.3899	373.5	0.900
176	0.1126	379.4	0.914
178	-0.1205	384.4	0.926
180	-0.3212	388.7	0.937
182	-0.4968	392.4	0.946
184	-0.6477	395.6	0.953
186	-0.7812	398.4	0.960

Table C.11: Continued.

TEMP (°C)	HEAT FLOW (W/g)	Integral (J/g)	α
188	-0.8997	400.8	0.966
190	-1.004	402.9	0.971
192	-1.097	404.7	0.975
194	-1.181	406.3	0.979
196	-1.255	407.7	0.983
198	-1.321	408.9	0.986
200	-1.38	409.9	0.988
202	-1.433	410.8	0.990
204	-1.48	411.6	0.992
206	-1.522	412.2	0.993
208	-1.56	412.8	0.995
210	-1.593	413.2	0.996
212	-1.622	413.6	0.997
214	-1.648	413.9	0.998
216	-1.671	414.2	0.998
218	-1.691	414.4	0.999
220	-1.708	414.6	0.999
222	-1.723	414.7	1.000
224	-1.735	414.8	1.000
226	-1.746	414.9	1.000

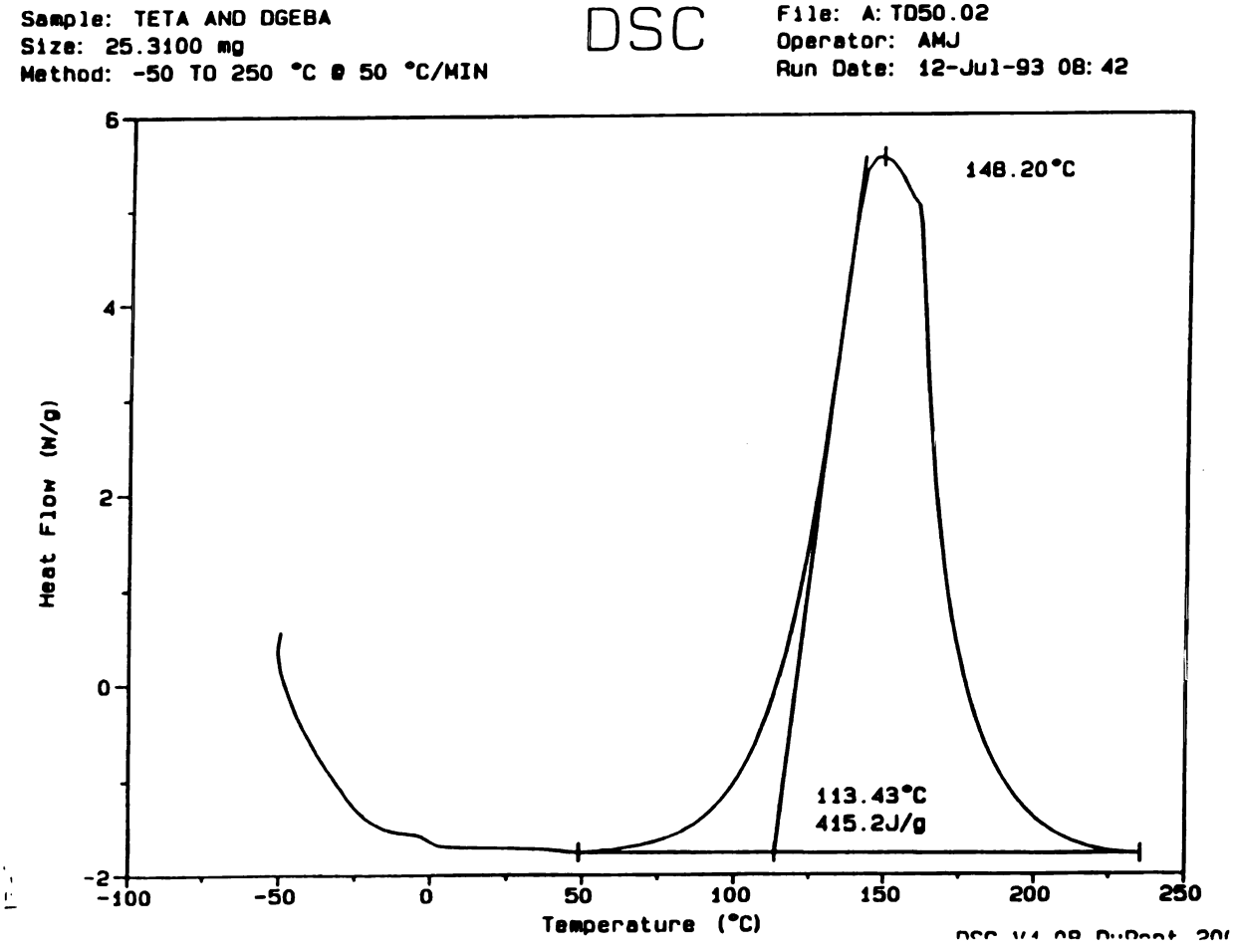


Figure C.8: Graph of DSC data, DGEBA/TETA epoxy resin. Scan rate is 50°C/min.

Table C.12: Exotherm data for DGEBA/TETA epoxy resin and Derakane® 411 resin.

EPOXY		DERAKANE	
TIME (min)	TEMP (°C)	TIME (min)	TEMP (°C)
0.00	27	3.13	28
5.00	28	6.37	29
6.00	28	7.57	30
7.00	28	9.47	31
8.00	28	10.80	32
10.00	29	12.10	33
12.00	29	13.20	34
14.00	30	13.92	35
15.00	30	14.65	36
16.00	31	15.32	37
17.00	31	15.92	38
18.00	31	16.47	39
20.00	32	16.93	40
22.00	32	17.38	41
23.00	33	17.75	42
24.00	33	18.08	43
26.13	34	18.37	44
28.75	35	18.67	45
31.67	36	18.87	46
34.25	37	19.50	49
36.77	38	20.00	52
39.12	39	20.25	55
41.23	40	20.50	58
43.15	41	20.75	62
44.78	42	21.00	67
46.40	43	21.25	77
47.92	44	21.50	95
49.38	45	21.75	131
50.73	46	22.00	155
51.83	47	22.17	159
52.68	48	22.33	162
53.68	49	22.50	164
54.57	50	22.67	167
55.33	51	22.83	169
56.03	52	23.00	169

Table C.12: Continued.

EPOXY		DERAKANE	
TIME (min)	TEMP (°C)	TIME (min)	TEMP (°C)
56.62	53	23.50	170
57.22	54	24.00	170
57.80	55	25.00	169
58.28	56	25.18	168
58.77	57	25.65	167
59.22	58	25.98	166
59.65	59	26.42	165
60.05	60	26.73	164
60.42	61	27.15	163
61.00	62	27.50	162
62.00	65	27.88	161
63.00	70	28.23	160
64.00	77	28.90	158
65.00	91	29.63	156
66.00	146	30.33	154
67.00	215	31.07	152
67.50	215	31.68	150
68.00	215	32.33	148
69.00	212	33.05	146
70.00	209	33.78	144
71.00	205	35.22	140
72.00	201	37.00	135
73.00	197	38.97	130
74.00	193	40.98	125
75.00	189	43.10	120
76.00	184	45.17	115
77.00	180	47.42	110
79.00	172	52.20	100
81.00	165	57.77	90
83.00	158	64.37	80
87.00	146	71.53	70
90.00	138	82.00	60
100.00	113	91.02	50
		107.15	40
		143.67	31

Table C.13: Data from residual cure runs on DGEBA/TETA epoxy resin.

CURE CYCLE	MELT PEAK TEMP (°C)	MELT PEAK AREA (J/g)	REACTION PEAK MAX TEMP (°C)	REACTION PEAK AREA (jJ/g)	EXTENT OF REACTION BEFORE DSC (α)
2 Hrs @	67.44	6.05	113.06	36.06	0.917
50 °C	67.14	6.68	112.06	34.92	0.920
+ 2 days @	66.64	7.74	112.31	32.16	0.926
rm temp	68.00	7.22	113.02	38.38	0.912
AVG	67.37	6.92	112.61	35.38	0.919
STD DEV	0.56	0.72	0.50	2.58	0.006
2 days @	48.03	10.25	107.92	99.94	0.771
rm temp	47.77	11.45	108.06	96.52	0.779
	48.10	11.10	109.07	93.58	0.786
	48.02	11.09	107.69	100.10	0.771
AVG	47.98	10.97	108.19	97.54	0.777
ATD DEV	0.14	0.51	0.61	3.11	0.007

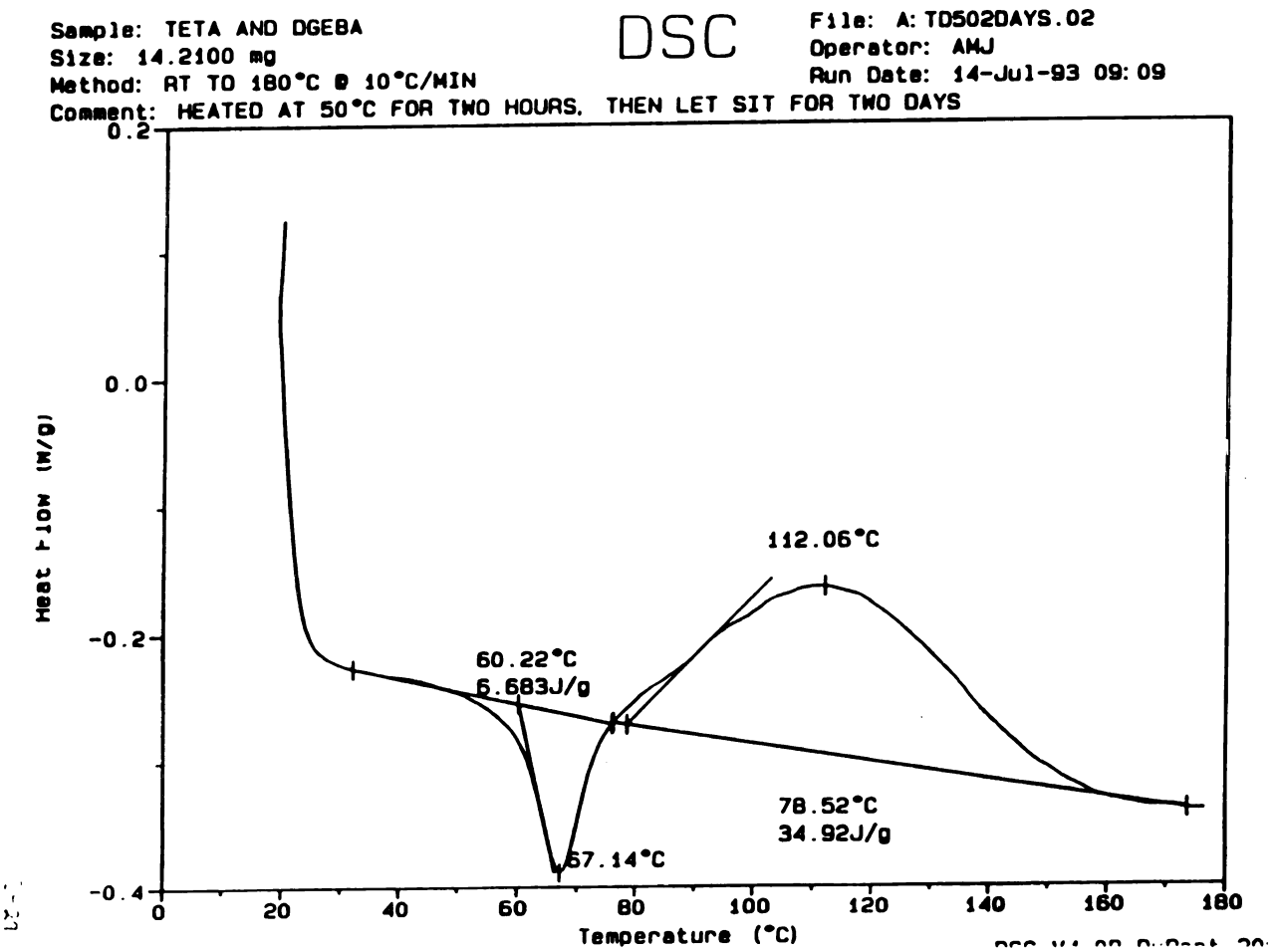


Figure C.9: Sample Residual cure run, of DGEBA/TETA epoxy resin on DSC. Resin was cured at 50 °C for two hours, then at room temp. for 2 days before DSC run.

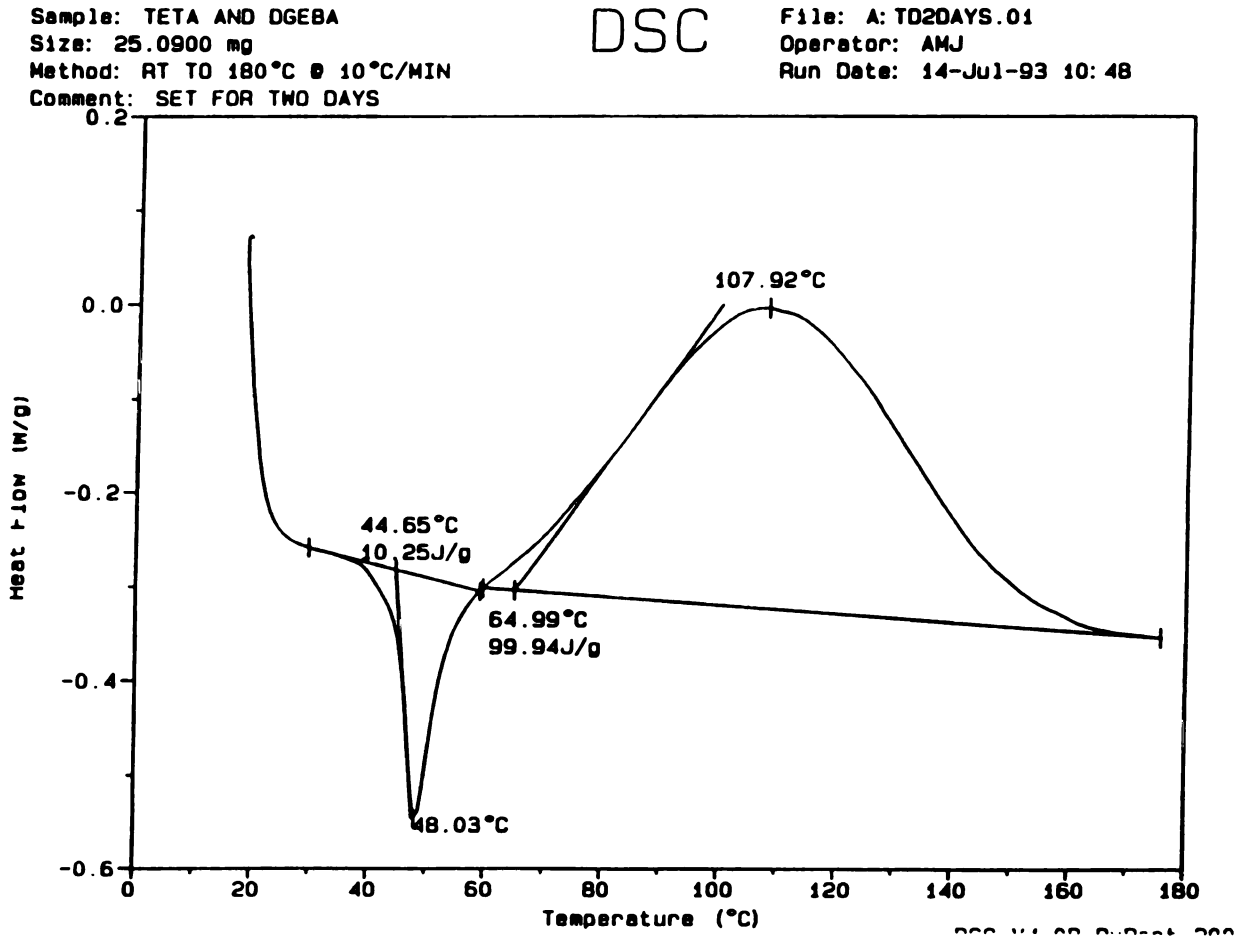


Figure C.10: Sample Residual cure run, of DGEBA/TETA epoxy resin on DSC. Resin was cured at room temp. for 2 days before DSC run.

Table C.14: Shrinkage data for DGEBA/TETA epoxy resin.

		TUBE B	TUBE C	TUBE D	TUBE E
MASS RESIN (g)		2.3596	3.2606	3.2960	0.0000
VOL RESIN (cm^3)		2.5638	3.5427	3.5812	0.0000
MASS WATER (g)		27.9818	26.7081	26.8479	30.6347
VOL WATER (cm^3)		28.3197	27.0306	27.1721	31.0046
ΔH for $\Delta Vol = 1\ cm^3$ (cm)		5.350	5.200	5.300	5.200
TIME HH.MM.SS	TEMP (° C)	HEIGHT (cm)	HEIGHT (cm)	HEIGHT (cm)	HEIGHT (cm)
00.00.00	24.7	7.665	7.735	7.975	8.177
00.22.00	50.0	12.370	12.665	13.160	12.157
00.27.00	50.0	12.680	12.960	13.491	12.365
00.29.15	50.0	12.874	13.100	13.595	12.478
00.35.00	50.0	12.993	13.206	13.710	12.735
00.40.00	50.0	12.980	13.115	13.620	12.910
00.45.00	50.0	12.965	13.036	13.550	12.975
00.50.00	50.0	12.930	12.920	13.380	13.180
00.55.00	50.0	12.749	12.850	13.240	13.198
01.00.00	50.0	12.785	12.685	13.195	13.300
01.05.00	50.0	12.700	12.565	13.025	13.425
01.10.00	50.0	12.650	12.480	12.950	13.490
01.15.00	50.0	12.670	12.430	12.900	13.560
01.20.00	50.0	12.565	12.345	12.840	13.680
01.25.00	50.0	12.519	12.292	12.785	13.600
01.30.00	50.0	12.530	12.275	12.760	13.732
01.35.00	50.0	12.500	12.254	12.755	13.781
01.40.00	50.0	12.460	12.200	12.745	13.730
01.45.00	50.0	12.449	12.207	12.726	13.860
01.50.00	50.0	12.455	12.200	12.698	13.915
01.55.00	50.0	12.465	12.200	12.695	13.905
02.00.00	50.0	12.434	12.175	12.698	13.970
02.15.00	50.0	12.350	12.095	12.655	14.020

Table C.14: Continued.

		TUBE B	TUBE C	TUBE D	TUBE E
TIME HH.MM.SS	TEMP (° C)	HEIGHT (cm)	HEIGHT (cm)	HEIGHT (cm)	HEIGHT (cm)
02.30.00	50.0	12.325	12.018	12.595	14.017
02.45.00	50.0	12.290	12.042	12.565	14.110
03.00.00	50.0	12.280	11.995	12.505	14.125
03.15.00	50.0	12.235	11.940	12.535	14.135
03.30.00	50.0	12.205	11.940	12.505	14.145
03.45.00	50.0	12.150	11.880	12.480	14.148
04.00.00	43.5	10.925	10.726	11.335	13.160
04.15.00	37.0	9.610	9.395	9.895	11.805
04.30.00	30.5	8.520	8.325	8.780	10.606
04.45.00	27.5	7.810	7.635	8.050	9.965

Table C.15: Shrinkage data for Derakane® 411 resin.

		TUBE 1	TUBE 2	TUBE 4
MASS RESIN (g)		3.7592	4.8551	0.0000
VOL RESIN (cm^3)		3.9171	5.0590	0.0000
MASS WATER (g)		19.4246	17.9829	23.0598
VOL WATER (cm^3)		19.4817	18.0357	23.1276
ΔH for $\Delta Vol = 1\ cm^3$ (cm)		10.500	10.100	10.400
TIME (min)	TEMP (° C)	HEIGHT (cm)	HEIGHT (cm)	HEIGHT (cm)
0.00	25.0	14.050	13.070	13.580
16.00	25.0	13.420	12.870	13.570
17.35	25.0	13.355	12.790	13.565
20.00	25.0	13.305	12.700	13.565
23.00	25.0	13.205	12.570	13.560
25.60	25.0	13.130	12.480	13.560
28.50	25.0	13.035	12.310	13.555
30.50	25.0	13.005	12.235	13.575
34.27	25.0	12.855	12.035	13.570
35.83	25.0	12.740	11.910	13.570
37.33	25.0	12.735	11.800	

Table C.15: Continued.

		TUBE 1	TUBE 2	TUBE 4
TIME (min)	TEMP (° C)	HEIGHT (cm)	HEIGHT (cm)	HEIGHT (cm)
38.75	25.0	12.645	11.715	13.575
40.33	25.0	12.615	11.560	13.575
42.83	25.0	12.440	11.345	13.550
44.42	25.0	12.350	11.175	
45.88	25.0	12.245	11.010	13.595
48.47	25.0	12.060	10.850	
49.50	25.0	12.010	10.805	13.600
51.50	25.0	11.935	10.740	
52.67	25.0	11.890	10.675	13.600
54.67	25.0	11.825	10.640	
56.65	25.0	11.795	10.575	
59.50	25.0	11.745	10.530	13.604
61.33	25.0	11.705	10.505	
64.50	25.0	11.660	10.460	
67.42	25.0	11.550	10.410	13.595
71.15	25.0	11.565	10.390	
74.38	25.0	11.590	10.385	13.605
79.08	25.0	11.575	10.355	
83.67	25.0	11.530	10.310	13.615
88.57	25.0	11.535	10.300	13.610
94.12	25.0	11.500	10.255	
98.57	25.0	11.475	10.245	13.605
103.95	25.0	11.465	10.215	
108.33	25.0	11.440	10.190	13.605
115.83	25.0	11.435	10.180	13.610
122.13	25.0	11.410	10.150	13.620
1155.98	25.0	10.810	9.300	13.135
1168.75	25.0	10.830	9.285	13.160

Table C.16: Summary of calculatione for permeability rune. Viscosity = 290 mPa·sec, R_o = 0.952 cm.

RUN	Δ P (psig)	ε	M1	M2 (1/sec)	Ke (m^2)	Kxx (m^2)	Kyy (m^2)
5.7.B	0.5	1.000	0.98	42.2	1.98E-08	2.01E-08	1.94E-08
5.7.C	0.5	1.000	0.99	39.5	1.86E-08	1.88E-08	1.84E-08
5.7.D	0.3	0.813	1.06	13.5	9.26E-09	8.72E-09	9.82E-09
5.7.E	0.3	0.822	1.11	10.7	7.75E-09	6.96E-09	8.64E-09
5.7.F	0.5	0.620	0.89	2.8	7.26E-10	8.18E-10	6.45E-10
5.7.G	3.5	0.629	0.83	21.4	7.56E-10	9.14E-10	6.25E-10

Table C.17: Results of permeability calculations.

FABRIC	Vf	Ke (m^2)	Kxx (m^2)	Kyy (m^2)	Kxx/Kyy
NO PREFORM	0.00	1.912E-08 ±8.01E-10	1.947E-08 ±9.21E-10	1.892E-08 ±6.84E-10	1.03
SWIRL GLASS	0.18	8.50E-09 ±1.06E-09	7.84E-09 ±1.25E-09	9.23E-09 ±8.36E-10	0.85
WOVEN GLASS	0.38	7.41E-10 ±2.13E-11	8.66E-10 ±6.85E-11	6.35E-10 ±1.37E-11	1.36

Table C.18: Data from permeability runs.

RUN #	TIME (sec)	Dx (cm)	Dy (cm)
5.7.B	0.00	0.000	0.000
	23.70	2.070	2.04
	25.70	4.590	4.67
	29.80	7.410	7.29
	33.90	9.480	9.33
	39.70	12.300	11.67
	42.40	12.740	12.83
5.7.C	0.00	0.00	
	15.50	2.96	2.94
	18.10	5.33	5.29
	21.40	7.56	7.35
	25.60	9.48	9.41
	29.30	10.96	10.88
	34.30	12.74	12.65
5.7.D	0.00	0.00	
	2.70	2.37	2.33
	10.30	5.33	5.69
	15.50	6.52	7.00
	21.00	7.70	8.17
	25.80	8.59	9.04
	33.40	9.48	10.21
	40.50	10.67	11.23
	50.10	11.85	12.54
	60.80	12.89	13.71
5.7.E	0.00	0.00	
	7.2	2.07	2.33
	10.4	3.56	3.94
	20.3	6.22	6.71
	30.4	7.85	8.60
	40.4	9.19	10.21
	51	10.37	11.67
	60.2	11.41	12.83

Table C.18: Continued.

RUN #	TIME (sec)	Dx (cm)	Dy (cm)
5.7.F	0.00	0.00	
	5.00	1.19	1.17
	10.60	2.52	2.63
	20.50	3.85	3.50
	40.40	5.33	4.67
	60.50	6.22	5.69
	80.90	7.11	6.42
	100.80	8.00	7.00
	140.50	9.19	8.17
	180.40	10.37	9.04
	220.90	11.41	9.92
	269.90	12.44	10.97
	360.40	14.22	12.83
5.7.G	0.00	0.00	
	5.6	2.67	2.63
	10.3	6.22	5.25
	15.4	8	6.71
	20.3	9.19	7.88
	25.6	10.07	8.45
	30.8	10.96	9.33
	35.8	11.85	9.92
	41.4	13.04	10.5
	45.8	13.63	10.79

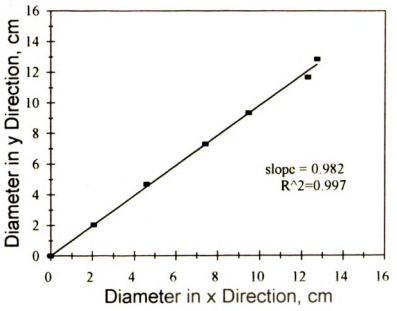


Figure C.11: Graph of D_x by D_y for permeability run 5.7.B.

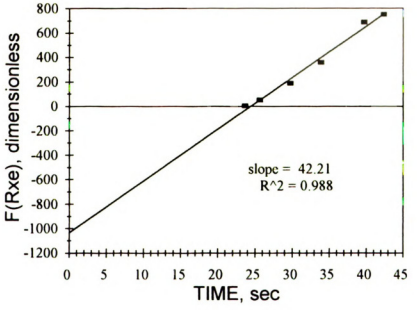


Figure C.12: Graph of $F(R_{xe})$ versus time for permeability run 5.7.B.

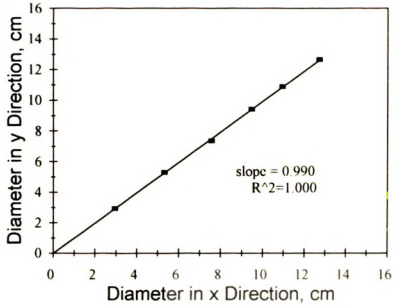


Figure C.13: Graph of D_x by D_y for permeability run 5.7.C.

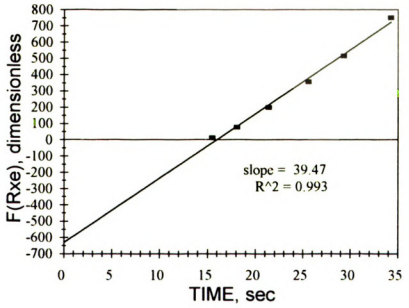


Figure C.14: Graph of $F(R_{xe})$ versus time for permeability run 5.7.C.

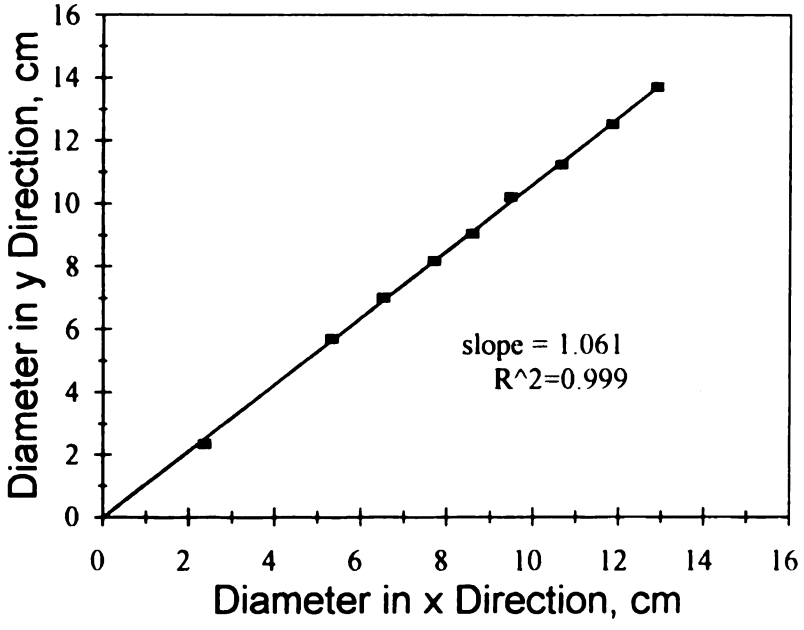


Figure C.15: Graph of D_x by D_y for permeability run 5.7.D.

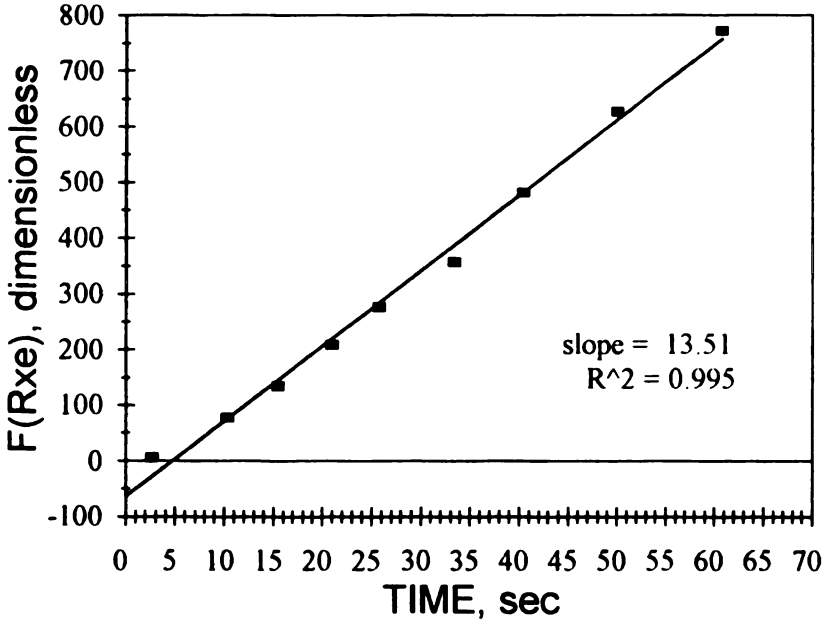


Figure C.16: Graph of $F(R_{xe})$ versus time for permeability run 5.7.D.

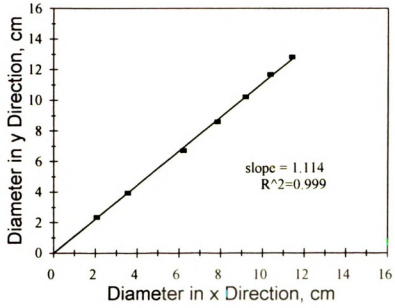


Figure C.17: Graph of D_x by D_y for permeability run 5.7.E.

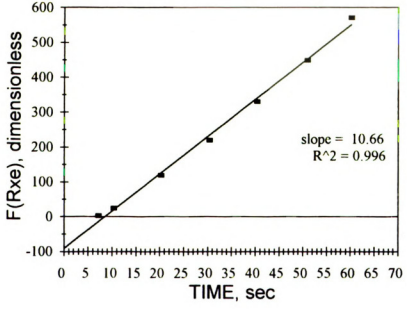


Figure C.18: Graph of $F(R_{xe})$ versus time for permeability run 5.7.E.

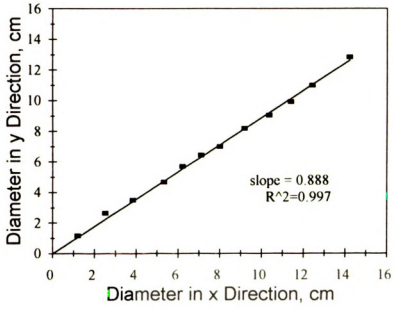


Figure C.19: Graph of D_x by D_y for permeability run 5.7.F.

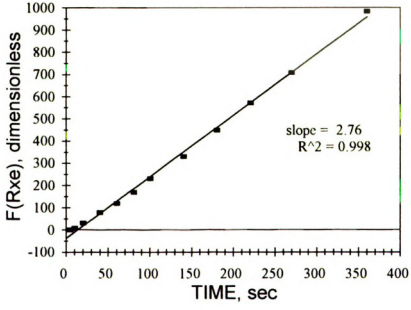


Figure C.20: Graph of $F(R_{xe})$ versus time for permeability run 5.7.F.

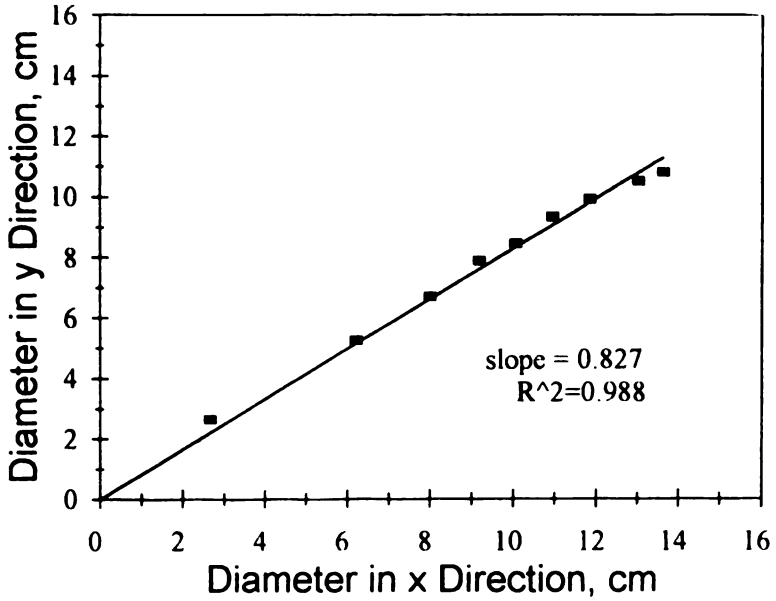


Figure C.21: Graph of D_x by D_y for permeability run 5.7.G.

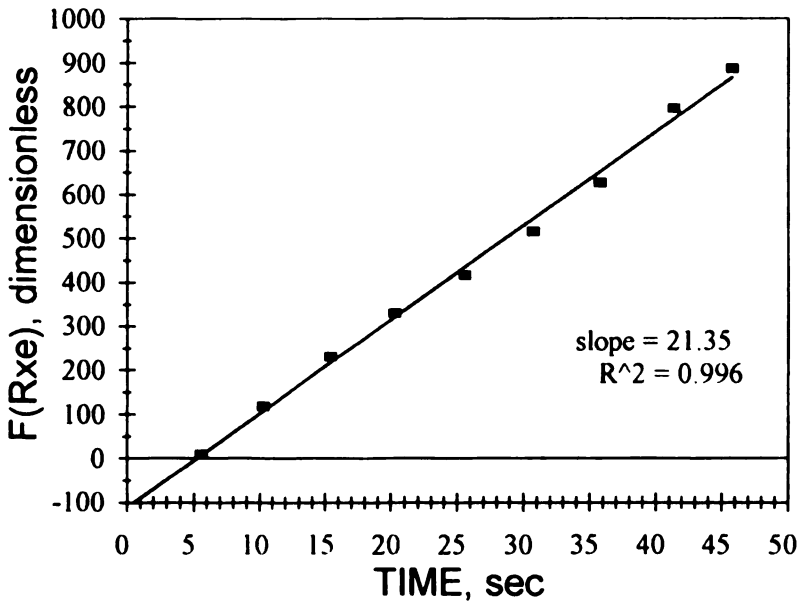


Figure C.22: Graph of $F(R_{xe})$ versus time for permeability run 5.7.G.

Table C.19: Longitudinal dispersion coefficient summary.

RUN	PREFORM	XI (cm)	tI (sec)	DL (cm^2/sec)	R^2
5.14.AB	none	14.64	32	0.01465	0.992
5.20.AA	swirl mat	17.24	157	0.01776	0.983
5.20.AB	swirl mat	22.74	186	0.01337	0.987
5.18.AA	swirl mat	17.27	117	0.01043	0.982
5.21.AA	woven mat	15.38	181	0.01167	0.988
5.21.AB	woven mat	13.94	216	0.00670	0.990

Table C.20: Location of resin/air interface by time for longitudinal dispersion runs.

RUN	TIME (min)	X-COORD (cm)
5.14.AB	8.62	4.50
	8.83	10.50
	9.05	16.30
	9.17	19.80
5.20.AA	5.62	0.50
	5.95	4.50
	6.72	10.50
5.20.AB	5.62	1.50
	5.95	4.00
	6.72	9.50
5.21.AA	10.54	0.00
	11.57	5.23
	12.25	8.73
	12.85	11.80
	13.15	13.31
	13.52	15.24

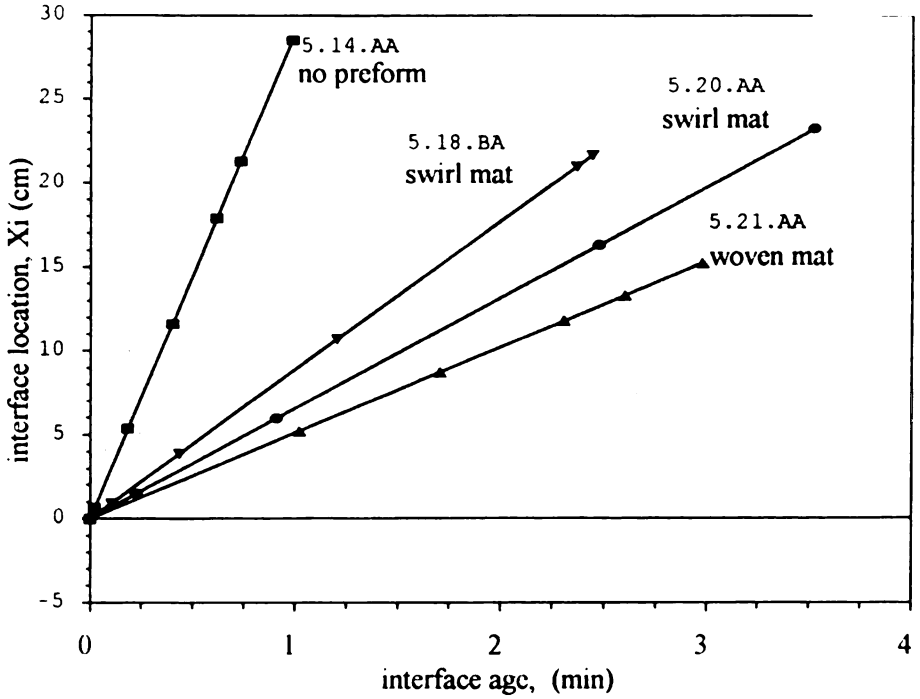


Figure C.23: Location of resin/air interface by time for longitudinal dispersion runs.

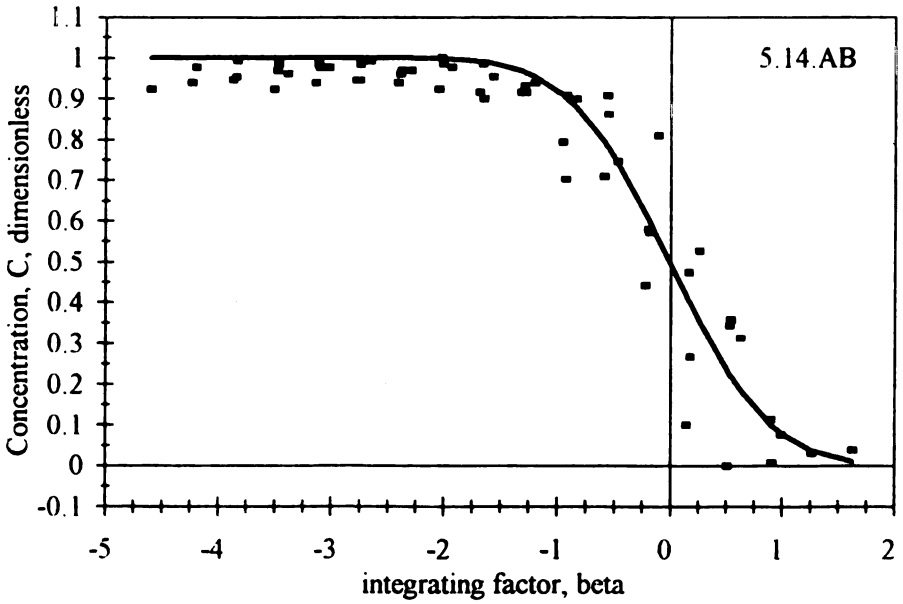


Figure C.24: Similarity plot of longitudinal dispersion data and model for 5.14.AB: no preform.

Table C.21: Absorbance versus location for longitudinal dispersion run, 5.14.AB, no preform. Origin at (x,y) = (8.9,-2.5).

x (cm)	absorbance	conc. calculated from absorbance	corrected x (cm)
9.15	1.960	0.924	8.744
9.65	1.980	0.939	9.244
10.15	1.990	0.947	9.744
10.65	1.960	0.924	10.244
11.15	1.980	0.939	10.744
11.65	1.990	0.947	11.244
12.15	1.980	0.939	11.744
12.65	1.960	0.924	12.244
13.15	1.950	0.916	12.744
13.65	1.950	0.916	13.244
14.15	1.790	0.794	13.744
14.65	1.680	0.710	14.244
15.15	1.330	0.443	14.744
15.65	0.880	0.099	15.244
16.15	0.750	0.000	15.744
9.15	2.000	0.954	9.262
9.65	2.020	0.969	9.762
10.15	2.040	0.985	10.262
10.65	1.990	0.947	10.762
11.15	2.010	0.962	11.262
11.65	2.060	1.000	11.762
12.15	2.040	0.985	12.262
12.65	1.970	0.931	12.762
13.15	1.670	0.702	13.262
13.65	1.940	0.908	13.762
14.15	1.510	0.580	14.262
14.65	1.370	0.473	14.762
15.15	1.200	0.344	15.262
15.65	0.900	0.115	15.762
16.15	0.790	0.031	16.262
16.65	0.800	0.038	16.762
9.15	2.030	0.977	9.019
9.65	2.050	0.992	9.519
10.15	2.040	0.985	10.019

Table C.21: Continued.

x (cm)	absorbance	conc. calculated from absorbance	corrected x (cm)
10.65	2.030	0.977	10.519
11.15	2.040	0.985	11.019
11.65	2.020	0.969	11.519
12.15	2.040	0.985	12.019
12.65	1.930	0.901	12.519
13.15	1.950	0.916	13.019
13.65	1.940	0.908	13.519
14.15	1.880	0.863	14.019
14.65	1.500	0.573	14.519
15.15	1.100	0.267	15.019
15.65	1.220	0.359	15.519
16.15	0.760	0.008	16.019
9.15	2.010	0.962	9.575
9.65	2.030	0.977	10.075
10.15	2.050	0.992	10.575
10.65	2.020	0.969	11.075
11.15	2.030	0.977	11.575
11.65	2.000	0.954	12.075
12.15	1.980	0.939	12.575
12.65	1.930	0.901	13.075
13.15	1.730	0.748	13.575
13.65	1.810	0.809	14.075
14.15	1.440	0.527	14.575
14.65	1.160	0.313	15.075
15.15	0.850	0.076	15.575

Table C.22: Absorbance versus location for longitudinal dispersion run, 5.20.AA., random swirl mat preform. Origin at (x,y) = (11.0,-2.5)

x (cm)	absorbance	conc. calculated from absorbance	corrected x (cm)
11.25	1.86	0.947	13.56
11.75	1.83	0.908	14.06
12.25	1.82	0.895	14.56
12.75	1.79	0.855	15.06
13.25	1.69	0.724	15.56
13.75	1.71	0.750	16.06
14.25	1.63	0.645	16.56
14.75	1.55	0.539	17.06
15.25	1.48	0.447	17.56
15.75	1.35	0.276	18.06
16.25	1.22	0.105	18.56
16.75	1.22	0.105	19.06
17.25	1.21	0.092	19.56
17.75	1.14	0.000	20.06
18.25	1.16	0.026	20.56
11.25	1.97	1.092	11.36
11.75	1.83	0.908	11.86
12.25	1.82	0.895	12.36
12.75	1.89	0.987	12.86
13.25	1.8	0.868	13.36
13.75	1.75	0.803	13.86
14.25	1.78	0.842	14.36
14.75	1.79	0.855	14.86
15.25	1.7	0.737	15.36
15.75	1.61	0.618	15.86
16.25	1.57	0.566	16.36
16.75	1.61	0.618	16.86
17.25	1.5	0.474	17.36
17.75	1.4	0.342	17.86
18.25	1.29	0.197	18.36
18.75	1.24	0.132	18.86
19.25	1.2	0.079	19.36
19.75	1.18	0.053	19.86

Table C.22: Continued.

x (cm)	absorbance	conc. calculated from absorbance	corrected x (cm)
11.25	1.9	1.000	10.47
11.75	1.88	0.974	10.97
12.25	1.9	1.000	11.47
12.75	1.8	0.868	11.97
13.25	1.83	0.908	12.47
13.75	1.87	0.961	12.97
14.25	1.71	0.750	13.47
14.75	1.71	0.750	13.97
15.25	1.78	0.842	14.47
15.75	1.79	0.855	14.97
16.25	1.74	0.789	15.47
16.75	1.695	0.730	15.97
17.25	1.65	0.671	16.47
17.75	1.61	0.618	16.97
18.25	1.46	0.421	17.47
18.75	1.38	0.316	17.97
19.25	1.32	0.237	18.47
19.75	1.29	0.197	18.97
20.25	1.2	0.079	19.47
11.25	1.85	0.934	9.61
11.75	1.9	1.000	10.11
12.25	1.89	0.987	10.61
12.75	1.88	0.974	11.11
13.25	1.92	1.026	11.61
13.75	1.9	1.000	12.11
14.25	1.87	0.961	12.61
14.75	1.86	0.947	13.11
15.25	1.64	0.658	13.61
15.75	1.86	0.947	14.11
16.25	1.85	0.934	14.61
16.75	1.88	0.974	15.11
17.25	1.78	0.842	15.61
17.75	1.64	0.658	16.11
18.25	1.55	0.539	16.61

Table C.22: Continued.

x (cm)	absorbance	conc. calculated from absorbance	corrected x (cm)
18.75	1.57	0.566	17.11
19.25	1.41	0.355	17.61
19.75	1.23	0.118	18.11
20.25	1.22	0.105	18.61
20.75	1.21	0.092	19.11

Table C.23: Absorbance versus location for longitudinal dispersion run, 5.20.AB., random swirl mat preform. origin at (x,y) = (11.0,-2.5)

x (cm)	absorbance	conc. calculated from absorbance	Corrected x (cm)
11.25	1.940	0.966	10.272
11.75	1.970	1.000	10.772
12.25	1.950	0.977	11.272
12.75	1.920	0.943	11.772
13.25	1.890	0.909	12.272
13.75	1.920	0.943	12.772
14.25	1.830	0.841	13.272
14.75	1.910	0.932	13.772
15.25	1.830	0.841	14.272
15.75	1.710	0.705	14.772
16.25	1.880	0.898	15.272
16.75	1.750	0.750	15.772
17.25	1.710	0.705	16.272
17.75	1.520	0.489	16.772
18.25	1.340	0.284	17.272
18.75	1.230	0.159	17.772
19.25	1.160	0.080	18.272
19.75	1.190	0.114	18.772
20.25	1.110	0.023	19.272
20.75	1.090	0.000	19.772
11.25	1.920	0.943	10.454
11.75	1.960	0.989	10.954
12.25	1.930	0.955	11.454

Table C.23: Continued.

x (cm)	absorbance	conc. calculated from absorbance	corrected x (cm)
12.75	1.940	0.966	11.954
13.25	1.910	0.932	12.454
13.75	1.750	0.750	12.954
14.25	1.860	0.875	13.454
14.75	1.810	0.818	13.954
15.25	1.840	0.852	14.454
15.75	1.790	0.795	14.954
16.25	1.730	0.727	15.454
16.75	1.680	0.670	15.954
17.25	1.600	0.580	16.454
17.75	1.480	0.443	16.954
18.25	1.380	0.330	17.454
18.75	1.280	0.216	17.954
19.25	1.190	0.114	18.454
19.75	1.150	0.068	18.954
20.25	1.140	0.057	19.454
20.75	1.130	0.045	19.954
11.25	1.940	0.966	11.559
11.75	1.990	1.023	12.059
12.25	1.890	0.909	12.559
12.75	1.900	0.920	13.059
13.25	1.920	0.943	13.559
13.75	1.800	0.807	14.059
14.25	1.840	0.852	14.559
14.75	1.810	0.818	15.059
15.25	1.670	0.659	15.559
15.75	1.690	0.682	16.059
16.25	1.590	0.568	16.559
16.75	1.430	0.386	17.059
17.25	1.390	0.341	17.559
17.75	1.260	0.193	18.059
18.25	1.210	0.136	18.559
18.75	1.110	0.023	19.059
19.25	1.160	0.080	19.559

Table C.23: Continued.

x (cm)	absorbance	conc. calculated from absorbance	corrected x (cm)
11.25	1.870	0.886	12.715
11.75	1.910	0.932	13.215
12.25	1.84	0.852	13.715
12.75	1.75	0.750	14.215
13.25	1.81	0.818	14.715
13.75	1.85	0.864	15.215
14.25	1.78	0.784	15.715
14.75	1.62	0.602	16.215
15.25	1.54	0.511	16.715
15.75	1.38	0.330	17.215
16.25	1.35	0.295	17.715
16.75	1.26	0.193	18.215
17.25	1.24	0.170	18.715
17.75	1.17	0.091	19.215
18.25	1.12	0.034	19.715
18.75	1.18	0.102	20.215

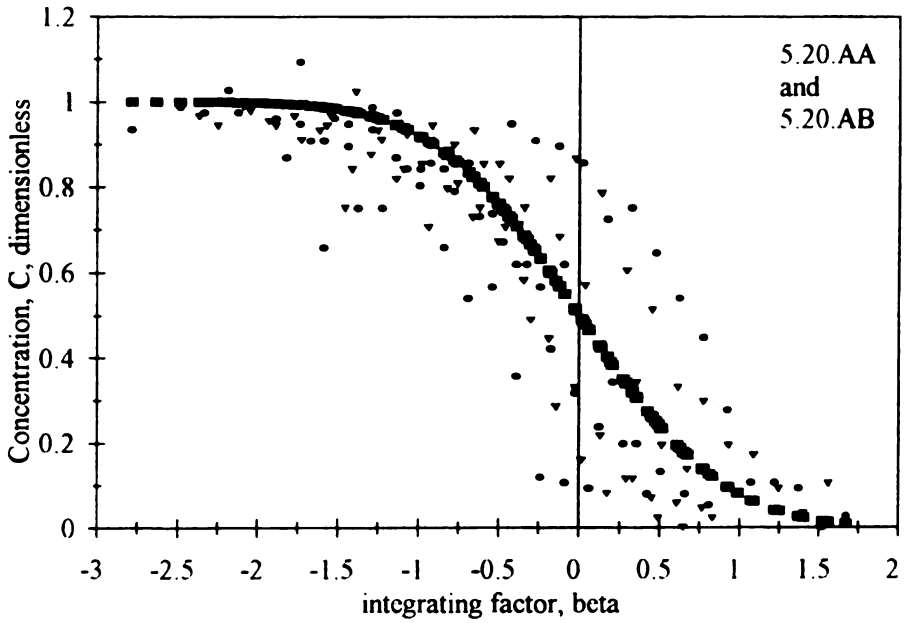


Figure C.25: Similarity plot of longitudinal dispersion data and model for 5.20.AA and 5.20.AB: swirl mat preform.

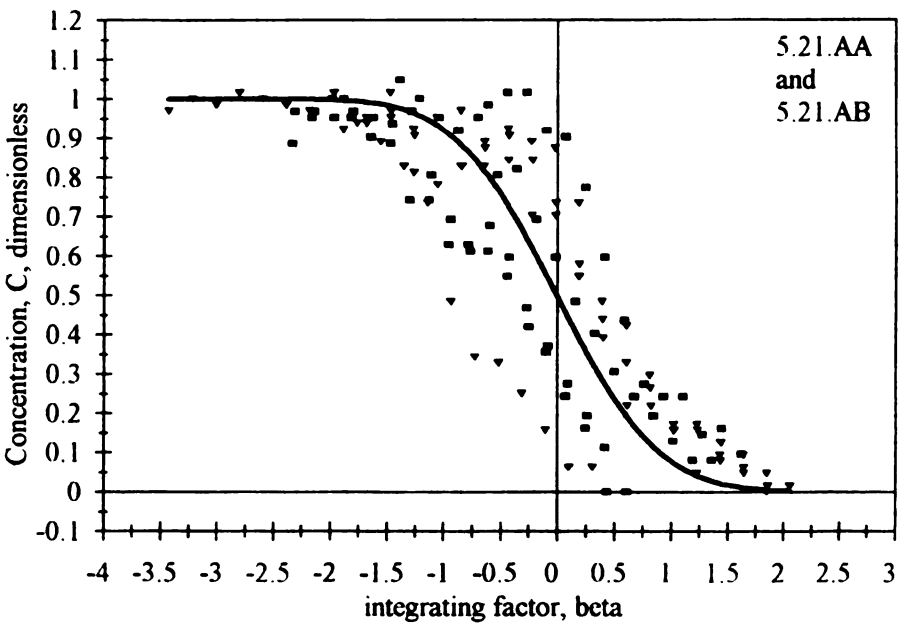


Figure C.26: Similarity plot of longitudinal dispersion data and model for 5.21.AA, and 5.21.AB, woven fabric preform.

Table C.24: Absorbance versus location for longitudinal dispersion run, 5.21.AA., woven fabric preform. Origin at (x,y) = (10.0,-2.5)

x (cm)	absorbance	conc. calculated from absorbance	corrected x (cm)
10.55	1.940	0.984	12.075
11.05	1.960	1.016	12.575
11.55	1.960	1.016	13.075
12.05	1.900	0.919	13.575
12.55	1.890	0.903	14.075
13.05	1.810	0.774	14.575
13.55	1.700	0.597	15.075
14.05	1.600	0.435	15.575
14.55	1.500	0.274	16.075
15.05	1.480	0.242	16.575
15.55	1.480	0.242	17.075
16.05	1.420	0.145	17.575
16.55	1.430	0.161	18.075
17.05	1.390	0.097	18.575
10.55	1.930	0.968	9.603
11.05	1.930	0.968	10.103
11.55	1.920	0.952	10.603
12.05	1.930	0.968	11.103
12.55	1.920	0.952	11.603
13.05	1.910	0.935	12.103
13.55	1.930	0.968	12.603
14.05	1.830	0.806	13.103
14.55	1.760	0.694	13.603
15.05	1.710	0.613	14.103
15.55	1.750	0.677	14.603
16.05	1.700	0.597	15.103
16.55	1.590	0.419	15.603
17.05	1.560	0.371	16.103
17.55	1.500	0.274	16.603
18.05	1.450	0.194	17.103
18.55	1.330	0.000	17.603
19.05	1.330	0.000	18.103
10.55	1.880	0.887	9.575
11.05	1.920	0.952	10.075

Table C.24: Continued.

x (cm)	absorbance	conc. calculated from absorbance	corrected x (cm)
11.55	1.950	1.000	10.575
12.05	1.920	0.952	11.075
12.55	1.890	0.903	11.575
13.05	1.880	0.887	12.075
13.55	1.790	0.742	12.575
14.05	1.790	0.742	13.075
14.55	1.720	0.629	13.575
15.05	1.720	0.629	14.075
15.55	1.710	0.613	14.575
16.05	1.670	0.548	15.075
16.55	1.620	0.468	15.575
17.05	1.550	0.355	16.075
17.55	1.480	0.242	16.575
18.05	1.430	0.161	17.075
18.55	1.400	0.113	17.575
10.55	1.980	1.048	10.947
11.05	1.950	1.000	11.447
11.55	1.920	0.952	11.947
12.05	1.900	0.919	12.447
12.55	1.920	0.952	12.947
13.05	1.830	0.806	13.447
13.55	1.840	0.823	13.947
14.05	1.760	0.694	14.447
14.55	1.700	0.597	14.947
15.05	1.630	0.484	15.447
15.55	1.58	0.403	15.947
16.05	1.52	0.306	16.447
16.55	1.48	0.242	16.947
17.05	1.45	0.194	17.447
17.55	1.41	0.129	17.947
18.05	1.38	0.081	18.447
18.55	1.38	0.081	18.947

Table C.25: Absorbance versus location for longitudinal dispersion run, 5.21.AB, woven fabric preform. Origin at (x,y) = (10.0,-2.5)

x (cm)	absorbance	conc. calculated from absorbance	corrected x (cm)
10.25	1.96	0.969	7.97
10.75	1.98	1.000	8.47
11.25	1.97	0.984	8.97
11.75	1.99	1.016	9.47
12.25	1.98	1.000	9.97
12.75	1.97	0.984	10.47
13.25	1.96	0.969	10.97
13.75	1.99	1.016	11.47
14.25	1.94	0.937	11.97
14.75	1.91	0.891	12.47
15.25	1.87	0.828	12.97
15.75	1.81	0.734	13.47
16.25	1.65	0.484	13.97
16.75	1.56	0.344	14.47
17.25	1.55	0.328	14.97
17.75	1.5	0.250	15.47
18.25	1.44	0.156	15.97
18.75	1.38	0.062	16.47
19.25	1.38	0.062	16.97
8.05	1.95	0.953	8.97
8.55	1.99	1.016	9.47
9.05	1.93	0.922	9.97
9.55	1.95	0.953	10.47
10.05	1.96	0.969	10.97
10.55	1.87	0.828	11.47
11.05	1.93	0.922	11.97
11.55	1.91	0.891	12.47
12.05	1.9	0.875	12.97
12.55	1.81	0.734	13.47
13.05	1.65	0.484	13.97
13.55	1.61	0.422	14.47
14.05	1.53	0.297	14.97
14.55	1.44	0.156	15.47
15.05	1.37	0.047	15.97

Table C.25: Continued.

x (cm)	absorbance	conc. calculated from absorbance	corrected x (cm)
15.55	1.4	0.094	16.47
16.05	1.4	0.094	16.97
16.55	1.34	0.000	17.47
17.05	1.35	0.016	17.97
8.05	1.98	1.000	8.73
8.55	1.95	0.953	9.23
9.05	1.96	0.969	9.73
9.55	1.92	0.906	10.23
10.05	1.95	0.953	10.73
10.55	1.87	0.828	11.23
11.05	1.9	0.875	11.73
11.55	1.92	0.906	12.23
12.05	1.88	0.844	12.73
12.55	1.81	0.734	13.23
13.05	1.71	0.578	13.73
13.55	1.59	0.391	14.23
14.05	1.48	0.219	14.73
14.55	1.48	0.219	15.23
15.05	1.44	0.156	15.73
15.55	1.44	0.156	16.23
16.05	1.42	0.125	16.73
16.55	1.37	0.047	17.23
17.05	1.35	0.016	17.73
8.05	1.93	0.922	8.73
8.55	1.94	0.937	9.23
9.05	1.95	0.953	9.73
9.55	1.86	0.813	10.23
10.05	1.84	0.781	10.73
10.55	1.87	0.828	11.23
11.05	1.91	0.891	11.73
11.55	1.88	0.844	12.23
12.05	1.79	0.703	12.73
12.55	1.79	0.703	13.23
13.05	1.69	0.547	13.73
13.55	1.62	0.438	14.23

Table C.25: Continued.

x (cm)	absorbance	conc. calculated from absorbance	corrected x (cm)
14.05	1.55	0.328	14.73
14.55	1.51	0.266	15.23
15.05	1.45	0.172	15.73
15.55	1.45	0.172	16.23
16.05	1.39	0.078	16.73
16.55	1.38	0.062	17.23
17.05	1.37	0.047	17.73

Table C.26: Location of resin/air interface by time for transverse dispersion runs.

RUN #	TIME (min)	LOCATION (cm)
5.25.A no preform	2.55	1.00
	2.82	6.00
	2.98	9.00
	3.17	13.50
	3.40	18.50
5.26.A swirl glass mat	0.25	1.70
	0.38	3.90
	0.73	9.20
	1.17	14.20
	1.67	18.70
	2.15	23.40
	2.53	24.90
	3.13	28.60
	3.62	31.20
	4.02	32.00
5.27.A woven glass mat	0.35	2.50
	0.90	6.50
	1.47	9.50
	2.60	14.00
	3.43	16.00
	4.47	19.50
	7.17	33.00
	7.22	33.00

Table C.27: Absorbance by location data for transverse dispersion, 5.25.A.

PLAQUE 5.25.A : no preform, transverse dispersion.					
x -coordinate (cm)	calculated time (min)	y-coordinate (cm)	absorbance	Conc. calculated from absorbance	corrected y (cm)
0.50	0.02	0.50	2.04	1.000	-1.144
0.50	0.02	1.00	1.76	0.772	-0.644
3.00	0.14	0.50	2.02	0.984	-1.261
3.00	0.14	1.00	1.99	0.959	-0.761
3.00	0.14	1.50	2.03	0.992	-0.261
3.00	0.14	2.00	0.87	0.049	0.239
5.50	0.27	1.00	2.01	0.976	-0.321
5.50	0.27	1.50	1.10	0.236	0.179
5.50	0.27	2.00	0.87	0.049	0.679
8.00	0.39	1.00	2.00	0.967	-0.819
8.00	0.39	1.50	1.98	0.951	-0.319
8.00	0.39	2.00	1.11	0.244	0.181
8.00	0.39	2.50	0.91	0.081	0.681
10.50	0.51	1.50	2.02	0.984	-0.714
10.50	0.51	2.00	1.81	0.813	-0.214
10.50	0.51	2.50	0.91	0.081	0.286
10.50	0.51	3.00	0.88	0.057	0.786
13.00	0.63	1.00	1.97	0.943	-1.424
13.00	0.63	1.50	1.96	0.935	-0.924
13.00	0.63	2.00	1.79	0.797	-0.424
13.00	0.63	2.50	1.36	0.447	0.076
13.00	0.63	3.00	1.23	0.341	0.576
13.00	0.63	3.50	0.75	-0.049	1.076
13.00	0.63	4.00	0.78	-0.024	1.576
15.50	0.75	2.00	2.06	1.016	-0.782
15.50	0.75	2.50	1.91	0.894	-0.282
15.50	0.75	3.00	1.05	0.195	0.218
15.50	0.75	3.50	0.95	0.114	0.718
15.50	0.75	4.00	0.83	0.016	1.218
18.00	0.87	1.50	2.00	0.967	-1.168
18.00	0.87	2.00	1.92	0.902	-0.668
18.00	0.87	2.50	1.68	0.707	-0.168
18.00	0.87	3.00	0.92	0.089	0.332

Table C.27: Continued.

x-coordinate (cm)	calculated time (min)	y-coordinate (cm)	absorbance	Conc. calculated from absorbance	corrected y (cm)
18.00	0.87	3.50	0.87	0.049	0.832
20.50	0.99	1.50	1.99	0.959	-1.401
20.50	0.99	2.00	1.92	0.902	-0.901
20.50	0.99	2.50	1.81	0.813	-0.401
20.50	0.99	3.00	1.33	0.423	0.099
20.50	0.99	3.50	0.87	0.049	0.599
20.50	0.99	4.00	0.78	-0.024	1.099
23.00	1.11	2.00	1.95	0.927	-0.784
23.00	1.11	2.50	1.88	0.870	-0.284
23.00	1.11	3.00	1.08	0.220	0.216
23.00	1.11	3.50	0.81	0.000	0.716
25.50	1.23	2.00	1.84	0.837	-0.984
25.50	1.23	2.50	1.87	0.862	-0.484
25.50	1.23	3.00	1.41	0.488	0.016
25.50	1.23	3.50	0.82	0.008	0.516
28.00	1.35	1.50	2.00	0.967	-1.643
28.00	1.35	2.00	1.95	0.927	-1.143
28.00	1.35	2.50	2.01	0.976	-0.643
28.00	1.35	3.00	1.68	0.707	-0.143
28.00	1.35	3.50	0.79	-0.016	0.357
30.50	1.47	2.00	2.01	0.976	-1.065
30.50	1.47	2.50	1.99	0.959	-0.565
30.50	1.47	3.00	1.52	0.577	-0.065
30.50	1.47	3.50	0.79	-0.016	0.435
33.00	1.59	2.00	2.02	0.984	-1.083
33.00	1.59	2.50	2.00	0.967	-0.583
33.00	1.59	3.00	1.54	0.593	-0.083
33.00	1.59	3.50	0.85	0.033	0.417
35.50	1.72	2.50	2.03	0.992	-1.121
35.50	1.72	3.00	1.96	0.935	-0.621
35.50	1.72	3.50	1.57	0.618	-0.121
35.50	1.72	4.00	0.97	0.130	0.379
35.50	1.72	4.50	0.77	-0.033	0.879
38.00	1.84	1.50	2.08	1.033	-2.358
38.00	1.84	2.00	2.03	0.992	-1.858

Table C.27: Continued.

x-coordinate (cm)	calculated time (min)	y-coordinate (cm)	absorbance	Conc. calculated from absorbance	corrected y (cm)
38.00	1.84	2.50	2.01	0.976	-1.358
38.00	1.84	3.00	1.75	0.764	-0.858
38.00	1.84	3.50	1.64	0.675	-0.358
38.00	1.84	4.00	1.34	0.431	0.142
38.00	1.84	4.50	0.91	0.081	0.642
38.00	1.84	5.00	0.80	-0.008	1.142

Table C.28: Absorbance by location data for transverse dispersion, 5.26A.

PLAQUE 5.26.A : Swirl glass mat, transverse dispersion.					
x-coordinate (cm)	calculated time (min)	y-coordinate (cm)	absorbance	Conc. calculated from absorbance	corrected y (cm)
0.50	0.03	0.00	1.69	0.887	-1.511
0.50	0.03	0.50	1.72	0.943	-1.011
0.50	0.03	1.00	1.71	0.925	-0.511
0.50	0.03	1.50	1.49	0.509	-0.011
0.50	0.03	2.00	1.26	0.075	0.489
0.50	0.03	2.50	1.26	0.075	0.989
3.00	0.17	0.00	1.74	0.981	-1.063
3.00	0.17	0.50	1.69	0.887	-0.563
3.00	0.17	1.00	1.52	0.566	-0.063
3.00	0.17	1.50	1.24	0.038	0.438
3.00	0.17	2.00	1.18	-0.075	0.938
3.00	0.17	2.50	1.23	0.019	1.438
5.50	0.33	0.00	1.79	1.075	-1.036
5.50	0.33	0.50	1.81	1.113	-0.536
5.50	0.33	1.00	1.50	0.528	-0.036
5.50	0.33	1.50	1.29	0.132	0.464
5.50	0.33	2.00	1.17	-0.094	0.964
5.50	0.33	2.50	1.21	-0.019	1.464
8.00	0.51	0.00	1.75	1.000	-1.130

Table C.28: Continued.

x-coordinate (cm)	calculated time (min)	y-coordinate (cm)	absorbance	Conc. calculated from absorbance	corrected y (cm)
8.00	0.51	0.50	1.68	0.868	-0.630
8.00	0.51	1.00	1.55	0.623	-0.130
8.00	0.51	1.50	1.30	0.151	0.370
8.00	0.51	2.00	1.27	0.094	0.870
8.00	0.51	2.50	1.20	-0.038	1.370
10.50	0.70	0.00	1.77	1.038	-1.298
10.50	0.70	0.50	1.75	1.000	-0.798
10.50	0.70	1.00	1.64	0.792	-0.298
10.50	0.70	1.50	1.38	0.302	0.202
10.50	0.70	2.00	1.24	0.038	0.702
10.50	0.70	2.50	1.17	-0.094	1.202
13.00	0.93	0.00	1.77	1.038	-1.303
13.00	0.93	0.50	1.68	0.868	-0.803
13.00	0.93	1.00	1.60	0.717	-0.303
13.00	0.93	1.50	1.41	0.358	0.197
13.00	0.93	2.00	1.31	0.170	0.697
13.00	0.93	2.50	1.26	0.075	1.197
15.50	1.19	0.00	1.72	0.943	-1.088
15.50	1.19	0.50	1.69	0.887	-0.588
15.50	1.19	1.00	1.52	0.566	-0.088
15.50	1.19	1.50	1.32	0.189	0.412
15.50	1.19	2.00	1.23	0.019	0.912
15.50	1.19	2.50	1.25	0.057	1.413
18.00	1.48	0.50	1.74	0.981	-0.780
18.00	1.48	1.00	1.67	0.849	-0.280
18.00	1.48	1.50	1.34	0.226	0.220
18.00	1.48	2.00	1.22	0.000	0.720
18.00	1.48	2.50	1.28	0.113	1.220
20.50	1.80	0.00	1.73	0.962	-1.469
20.50	1.80	0.50	1.66	0.830	-0.969
20.50	1.80	1.00	1.56	0.642	-0.469
20.50	1.80	1.50	1.48	0.491	0.031
20.50	1.80	2.00	1.30	0.151	0.531
20.50	1.80	2.50	1.21	-0.019	1.031
23.00	2.17	0.00	1.73	0.962	-1.369

Table C.28: Continued.

x-coordinate (cm)	calculated time (min)	y-coordinate (cm)	absorbance	Conc. calculated from absorbance	corrected y (cm)
23.00	2.17	0.50	1.72	0.943	-0.869
23.00	2.17	1.00	1.64	0.792	-0.369
23.00	2.17	1.50	1.43	0.396	0.131
23.00	2.17	2.00	1.28	0.113	0.631
23.00	2.17	2.50	1.20	-0.038	1.131
25.50	2.57	0.00	1.80	1.094	-1.446
25.50	2.57	0.50	1.70	0.906	-0.946
25.50	2.57	1.00	1.69	0.887	-0.446
25.50	2.57	1.50	1.46	0.453	0.054
25.50	2.57	2.00	1.34	0.226	0.554
25.50	2.57	2.50	1.18	-0.075	1.054
25.50	2.57	3.00	1.14	-0.151	1.554
28.00	3.00	0.00	1.76	1.019	-1.313
28.00	3.00	0.50	1.72	0.943	-0.813
28.00	3.00	1.00	1.61	0.736	-0.313
28.00	3.00	1.50	1.41	0.358	0.188
28.00	3.00	2.00	1.31	0.170	0.688
28.00	3.00	2.50	1.22	0.000	1.188
28.00	3.00	3.00	1.27	0.094	1.688
30.50	3.45	0.00	1.68	0.868	-1.228
30.50	3.45	0.50	1.70	0.906	-0.728
30.50	3.45	1.00	1.59	0.698	-0.228
30.50	3.45	1.50	1.36	0.264	0.272
30.50	3.45	2.00	1.26	0.075	0.772
30.50	3.45	2.50	1.28	0.113	1.272
33.00	3.92	0.00	1.72	0.943	-1.393
33.00	3.92	0.50	1.64	0.792	-0.893
33.00	3.92	1.00	1.54	0.604	-0.393
33.00	3.92	1.50	1.47	0.472	0.107
33.00	3.92	2.00	1.32	0.189	0.607
33.00	3.92	2.50	1.28	0.113	1.107
35.50	4.41	0.00	1.67	0.849	-1.083
35.50	4.41	0.50	1.54	0.604	-0.583
35.50	4.41	1.00	1.51	0.547	-0.083
35.50	4.41	1.50	1.36	0.264	0.417

Table C.28: Continued.

x-coordinate (cm)	calculated time (min)	y-coordinate (cm)	absorbance	Conc. calculated from absorbance	corrected y (cm)
35.50	4.41	2.00	1.27	0.094	0.917
35.50	4.41	2.50	1.28	0.113	1.417
37.50	4.80	0.00	1.65	0.811	-0.528
37.50	4.80	0.50	1.49	0.509	-0.028
37.50	4.80	1.00	1.40	0.340	0.472
37.50	4.80	1.50	1.25	0.057	0.972
37.50	4.80	2.00	1.23	0.019	1.472

Table C.29: Absorbance by location data for transverse dispersion, 5.27.A.

PLAQUE 5.27.A : Woven glass mat, transverse dispersion.					
x-coordinate (cm)	calculated time (min)	y-coordinate (cm)	absorbance	Conc. calculated from absorbance	corrected y (cm)
3.00	0.31	0.50	1.81	1.00	-3.059
3.00	0.31	1.00	1.83	1.04	-2.559
3.00	0.31	1.50	1.81	1.00	-2.059
3.00	0.31	2.00	1.77	0.91	-1.559
3.00	0.31	2.50	1.70	0.76	-1.059
3.00	0.31	3.00	1.71	0.78	-0.559
3.00	0.31	3.50	1.60	0.54	-0.059
3.00	0.31	4.00	1.43	0.17	0.441
3.00	0.31	4.50	1.37	0.04	0.941
3.00	0.31	5.00	1.35	0.00	1.441
5.50	0.64	0.50	1.81	1.00	-3.550
5.50	0.64	1.00	1.78	0.93	-3.050
5.50	0.64	1.50	1.82	1.02	-2.550
5.50	0.64	2.00	1.82	1.02	-2.050
5.50	0.64	2.50	1.74	0.85	-1.550
5.50	0.64	3.00	1.74	0.85	-1.050
5.50	0.64	3.50	1.68	0.72	-0.550
5.50	0.64	4.00	1.60	0.54	-0.050
5.50	0.64	4.50	1.40	0.11	0.450
5.50	0.64	5.00	1.32	-0.07	0.950

Table C.29: Continued.

x-coordinate (cm)	calculated time (min)	y-coordinate (cm)	absorbance	Conc. calculated from absorbance	corrected y (cm)
8.00	1.04	2.00	1.82	1.02	-2.143
8.00	1.04	2.50	1.78	0.93	-1.643
8.00	1.04	3.00	1.73	0.83	-1.143
8.00	1.04	3.50	1.67	0.70	-0.643
8.00	1.04	4.00	1.62	0.59	-0.143
8.00	1.04	4.50	1.48	0.28	0.357
8.00	1.04	5.00	1.37	0.04	0.857
10.50	1.56	2.00	1.80	0.98	-2.045
10.50	1.56	2.50	1.73	0.83	-1.545
10.50	1.56	3.50	1.54	0.41	-0.545
10.50	1.56	4.00	1.59	0.52	-0.045
10.50	1.56	4.50	1.48	0.28	0.455
10.50	1.56	5.00	1.36	0.02	0.955
13.00	2.21	2.00	1.78	0.93	-1.000
13.00	2.21	2.50	1.74	0.85	-0.500
13.00	2.21	3.00	1.58	0.50	0.000
13.00	2.21	3.50	1.52	0.37	0.500
13.00	2.21	4.00	1.52	0.37	1.000
13.00	2.21	4.50	1.41	0.13	1.500
13.00	2.21	5.00	1.33	-0.04	2.000
15.50	3.00	0.50	1.75	0.87	-2.462
15.50	3.00	2.00	1.70	0.76	-0.962
15.50	3.00	2.50	1.70	0.76	-0.462
15.50	3.00	3.00	1.57	0.48	0.038
15.50	3.00	3.50	1.48	0.28	0.538
15.50	3.00	4.00	1.46	0.24	1.038
15.50	3.00	4.50	1.42	0.15	1.538
15.50	3.00	5.00	1.35	0.00	2.038
18.00	3.88	1.50	1.85	1.09	-1.538
18.00	3.88	2.00	1.78	0.93	-1.038
18.00	3.88	2.50	1.72	0.80	-0.538
18.00	3.88	3.00	1.59	0.52	-0.038
18.00	3.88	3.50	1.46	0.24	0.462
18.00	3.88	4.00	1.38	0.07	0.962
18.00	3.88	4.50	1.40	0.11	1.462

Table C.29: Continued.

x-coordinate (cm)	calculated time (min)	y-coordinate (cm)	absorbance	Conc. calculated from absorbance	corrected y (cm)
18.00	3.88	5.00	1.36	0.02	1.962
20.50	4.81	1.50	1.72	0.80	-1.286
20.50	4.81	2.00	1.70	0.76	-0.786
20.50	4.81	2.50	1.62	0.59	-0.286
20.50	4.81	3.00	1.55	0.43	0.214
20.50	4.81	3.50	1.44	0.20	0.714
20.50	4.81	4.00	1.38	0.07	1.214
20.50	4.81	4.50	1.37	0.04	1.714
20.50	4.81	5.00	1.43	0.17	2.214
23.00	5.77	1.50	1.72	0.80	-1.100
23.00	5.77	2.00	1.68	0.72	-0.600
23.00	5.77	2.50	1.59	0.52	-0.100
23.00	5.77	3.00	1.54	0.41	0.400
23.00	5.77	3.50	1.51	0.35	0.900
23.00	5.77	4.00	1.45	0.22	1.400
23.00	5.77	4.50	1.37	0.04	1.900
23.00	5.77	5.00	1.34	-0.02	2.400
25.50	6.73	1.50	1.72	0.80	-0.893
25.50	6.73	2.00	1.69	0.74	-0.393
25.50	6.73	2.50	1.55	0.43	0.107
25.50	6.73	3.00	1.53	0.39	0.607
25.50	6.73	3.50	1.47	0.26	1.107
25.50	6.73	4.00	1.36	0.02	1.607
25.50	6.73	4.50	1.33	-0.04	2.107
25.50	6.73	5.00	1.28	-0.15	2.607
28.00	7.70	1.00	1.68	0.72	-0.778
28.00	7.70	1.50	1.63	0.61	-0.278
28.00	7.70	2.00	1.54	0.41	0.222
28.00	7.70	2.50	1.52	0.37	0.722
28.00	7.70	3.00	1.42	0.15	1.222
28.00	7.70	3.50	1.34	-0.02	1.722
28.00	7.70	4.00	1.29	-0.13	2.222
28.00	7.70	4.50	1.30	-0.11	2.722
28.00	7.70	5.00	1.30	-0.11	3.222
30.50	8.68	1.50	1.72	0.80	-0.667

Table C.29: Continued.

x-coordinate (cm)	calculated time (min)	y-coordinate (cm)	absorbance	Conc. calculated from absorbance	corrected y (cm)
30.50	8.68	2.00	1.60	0.54	-0.167
30.50	8.68	2.50	1.54	0.41	0.333
30.50	8.68	3.00	1.49	0.30	0.833
30.50	8.68	3.50	1.43	0.17	1.333
30.50	8.68	4.00	1.31	-0.09	1.833
30.50	8.68	4.50	1.29	-0.13	2.333
32.50	9.45	0.50	1.57	0.48	-1.000
32.50	9.45	1.00	1.65	0.65	-0.500
32.50	9.45	1.50	1.58	0.50	0.000
32.50	9.45	2.00	1.53	0.39	0.500
32.50	9.45	2.50	1.46	0.24	1.000
32.50	9.45	3.00	1.41	0.13	1.500
32.50	9.45	3.50	1.29	-0.13	2.000
32.50	9.45	4.00	1.27	-0.17	2.500
32.50	9.45	4.50	1.32	-0.07	3.000
32.50	9.45	5.00	1.27	-0.17	3.500
35.50	10.62	1.00	1.71	0.78	-0.650
35.50	10.62	2.00	1.51	0.35	0.350
35.50	10.62	2.50	1.47	0.26	0.850
35.50	10.62	3.00	1.39	0.09	1.350
35.50	10.62	3.50	1.33	-0.04	1.850
35.50	10.62	4.00	1.32	-0.07	2.350
35.50	10.62	4.50	1.39	0.09	2.850
35.50	10.62	5.00	1.32	-0.07	3.350
38.00	11.59	0.50	1.71	0.78	-0.750
38.00	11.59	2.00	1.45	0.22	0.750
38.00	11.59	2.50	1.41	0.13	1.250
38.00	11.59	3.00	1.34	-0.02	1.750
38.00	11.59	3.50	1.40	0.11	2.250
38.00	11.59	4.00	1.34	-0.02	2.750
38.00	11.59	4.50	1.31	-0.09	3.250
38.00	11.59	5.00	1.30	-0.11	3.750

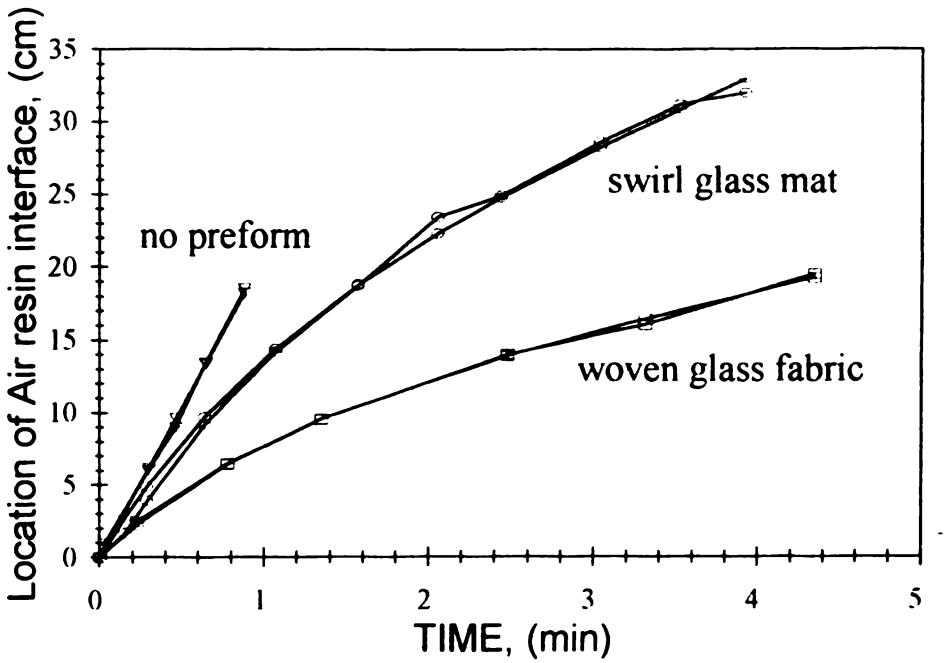


Figure C.23: Position of flow front by time for transverse dispersion runs.

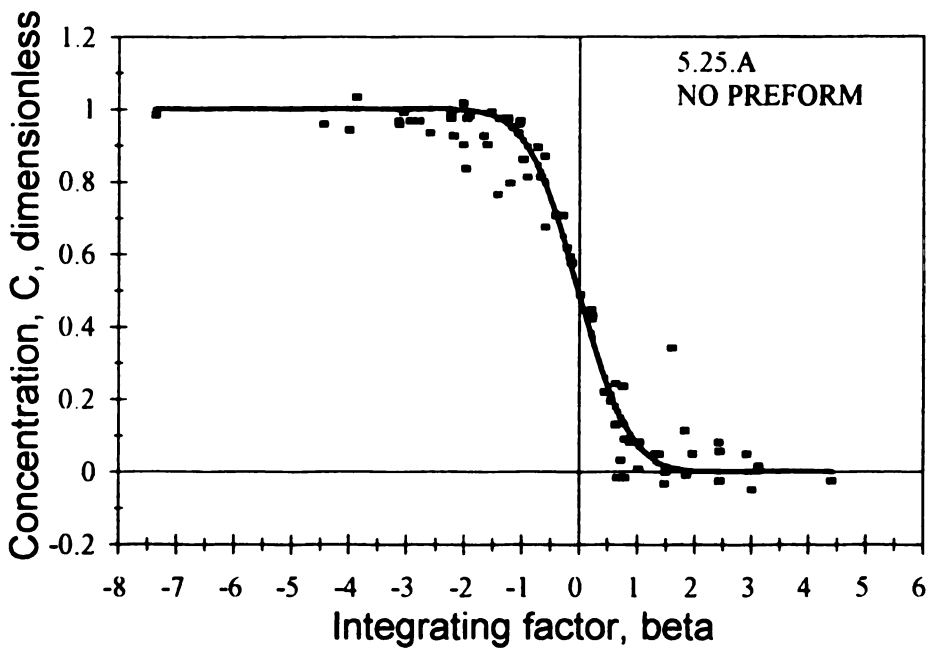


Figure C.24: Similarity plot of transverse dispersion data and model for 5.25.A, no preform.

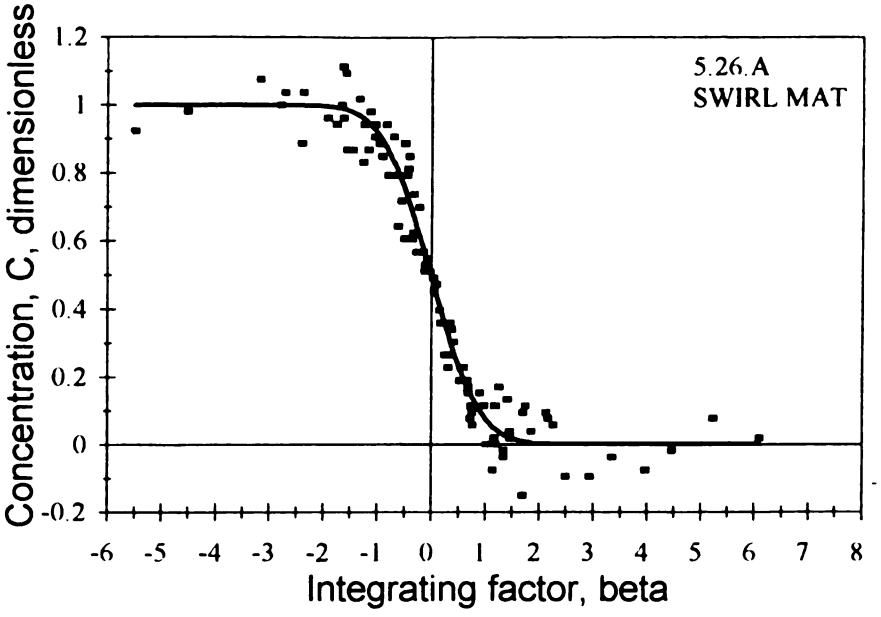


Figure C.25: Similarity plot of transverse dispersion data and model for 5.26.A, swirl mat preform.

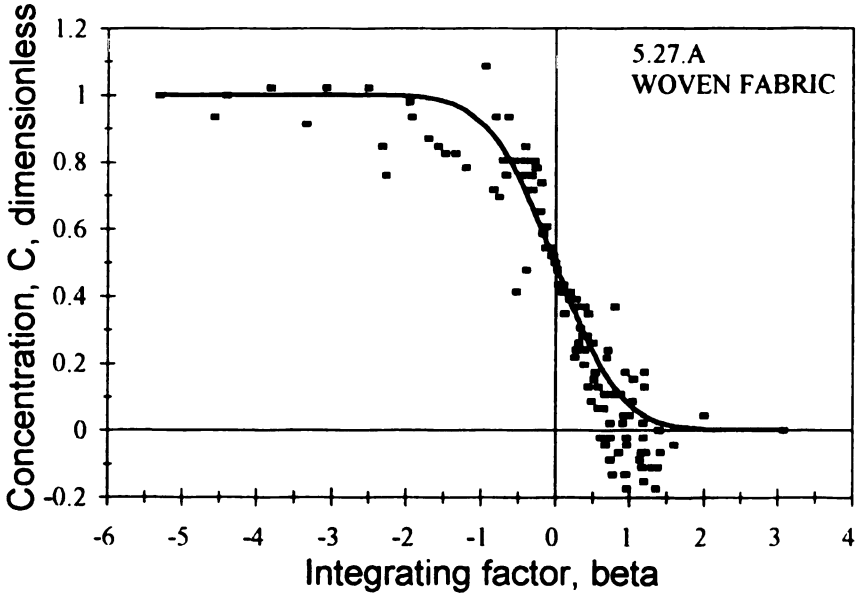


Figure C.26: Similarity plot of transverse dispersion data and model for 5.27.A, woven fabric preform.

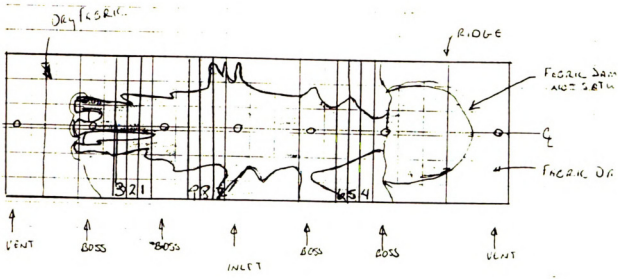


Figure C.27: Cut-up diagram of Plaque 9.11.A. Derakane resin; woven fabric preform.

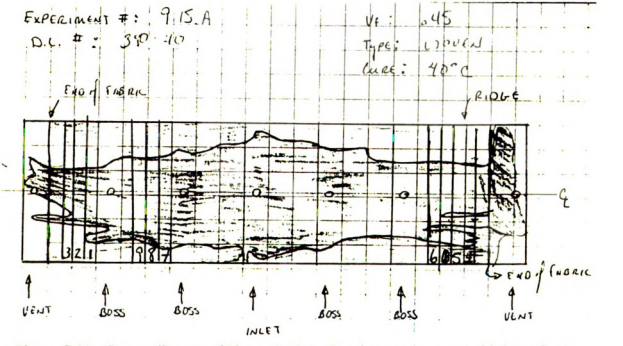


Figure C.28: Cut-up diagram of Plaque 9.15.A. Derakane resin; woven fabric preform.

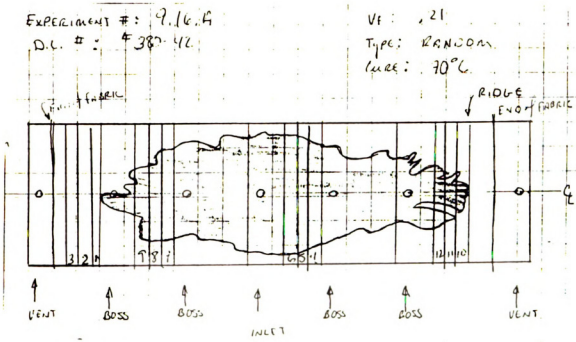


Figure C.29: Cut-up diagram of Plaque 9.16.A. Derakane resin, swirl mat preform.

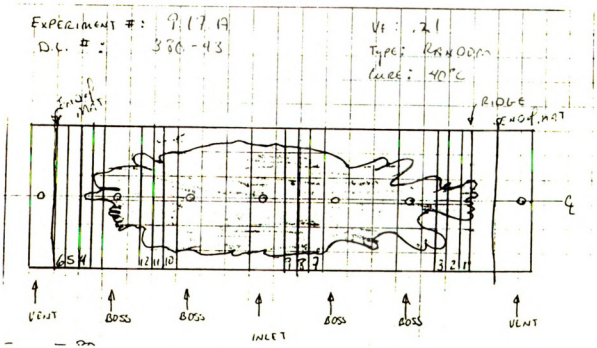


Figure C.30: Cut-up diagram of Plaque 9.17.A. Derakane resin, swirl mat preform.

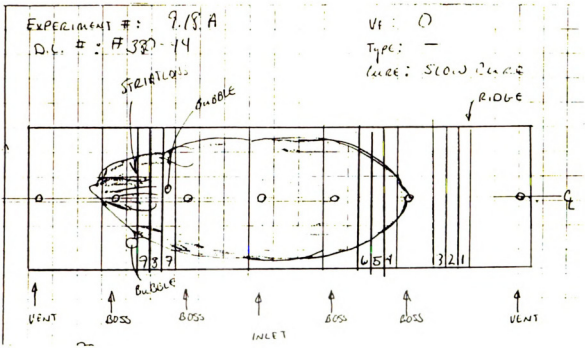


Figure C.31: Cut-up diagram of Plaque 9.18.A. Derakane resin, no preform.

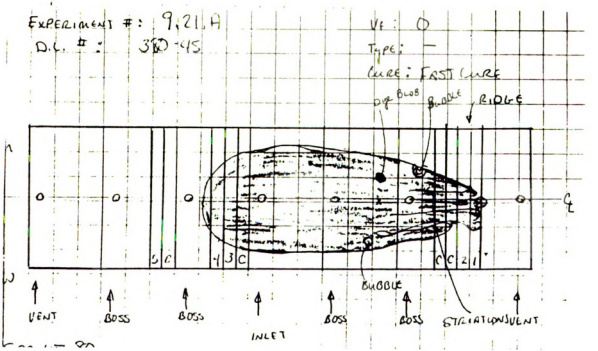


Figure C.32: Cut-up diagram of Plaque 9.21.A. Derakane resin; no preform.

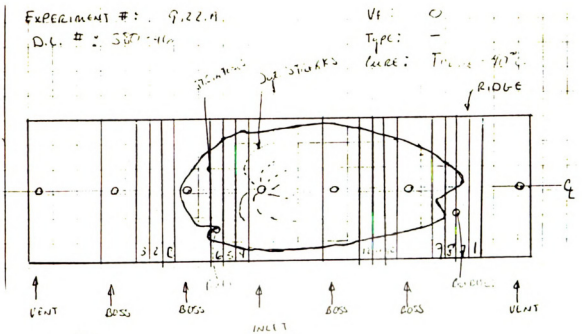


Figure C.33: Cut-up diagram of Plaque 9.22.A. Derakane resin; no preform.

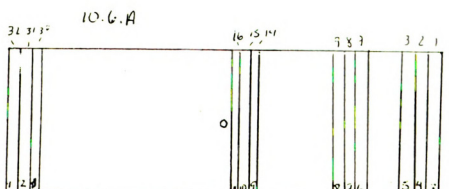


Figure C.34: Cut-up diagram of Plaque 10.6.A Derakane resin; swirl mat preform, no age difference between batches.

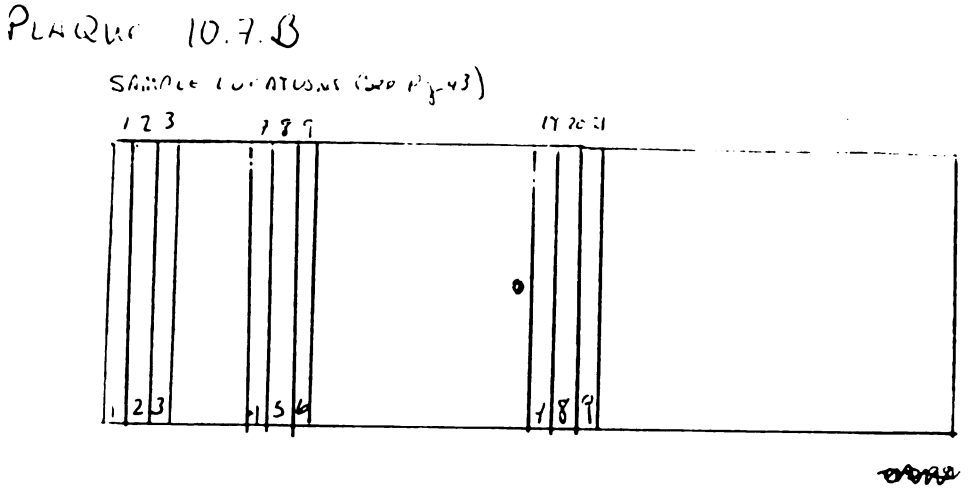


Figure C.35: Cut-up diagram of Plaque 10.07.B. Derakane resin; no preform. No age difference between batches.

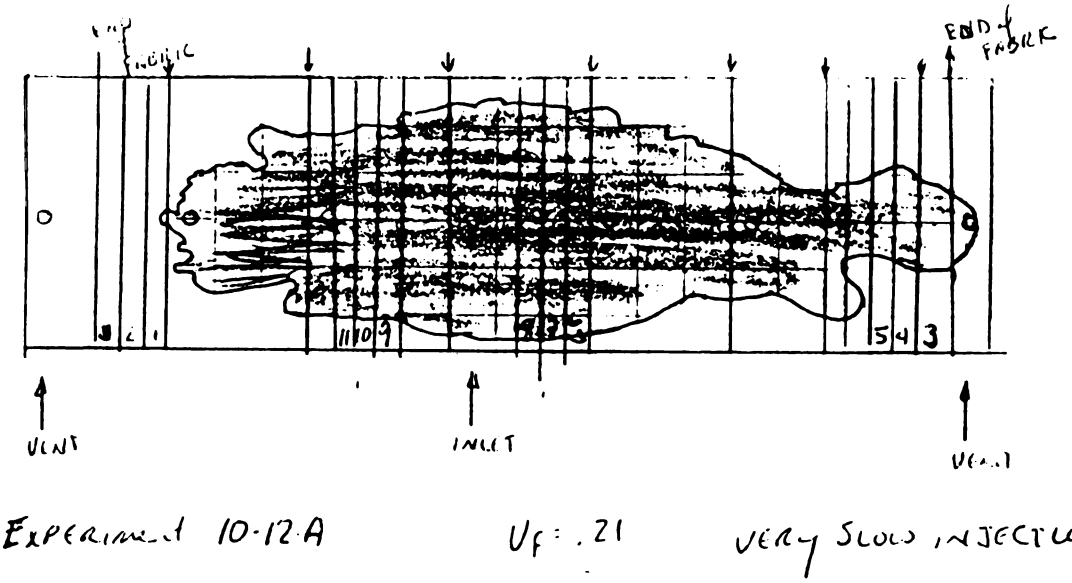


Figure C.36: Cut-up diagram of Plaque 10.12.A Derakane resin; swirl mat preform, very long injection.

Table C.30: Fingered structures of sample bars

PLAQUE 9.11. A NO PREFORM	
SAMPLE NO.	FEATURE TYPE
1	SHAFTS-4
2	SHAFTS-4
3	SHAFTS-4
4	SHAFTS-2
5	SHAFTS-2
6	SHAFTS-2
6X	SHAFTS-2
7	SHAFTS-2
7X	SHAFTS-1
8	SHAFTS-2
8X	SHAFTS-1
9	SHAFTS-2
9X	SHAFTS-1

PLAQUE 9.16.A SWIRL MAT PREFORM	
SAMPLE NO.	FEATURE TYPE
1	ALL BATCH 1
2	ALL BATCH 1
3	ALL BATCH 1
4	SHAFT-0
4X	SHAFT-1
5	SHAFT-0
5X	SHAFT-1
6	ALL BATCH 2
7	SHAFT-2
7X	SHAFT-1
8	SHAFT-2
8X	SHAFT-1
9	SHAFTS
9X	SHAFTS
10	MULTI-TIPS
10X	MULTI-TIPS
11	SHAFT-4
11X	SHAFT-4
12	SHAFT-4
12X	SHAFT-4

PLAQUE 9.18.A NO PREFORM	
SAMPLE NO.	FEATURE TYPE
1	ALL BATCH 1
2	ALL BATCH 1
3	ALL BATCH 1
4	SHAFT-2
4X	SHAFT-1
5	SHAFT-2
5X	SHAFT-1
6	SHAFT-2
6X	SHAFT-1
9	STRIATIONS

PLAQUE 9.22.A NO PREFORM	
SAMPLE NO.	FEATURE TYPE
1	ALL BATCH 1
2	ALL BATCH 1
3	ALL BATCH 1
4	ALL BATCH 2
5	STRIATIONS
6	STRIATIONS
8	SHAFT-2
9	SHAFT-4
9X	SHAFT-3
10	ALL BATCH 2
11	ALL BATCH 2
12	ALL BATCH 2

Table C.30: Continued.

PLAQUE 10.07.B NO PREFORM	
SAMPLE NO.	FEATURE TYPE
1	ALL BATCH 1
2	ALL BATCH 1
3	ALL BATCH 1
4	ALL BATCH 1
5	ALL BATCH 1
6	ALL BATCH 1
7	ALL BATCH 1
8	ALL BATCH 1

PLAQUE 9.15.A NO PREFORM	
SAMPLE NO.	FEATURE TYPE
1	ROUND TIP
1X	ROUND TIP
2	SHAFTS-2
2X	SHAFTS-1
3	SHAFTS-4
3X	SHAFTS-4
4	MULTI-TIPS
4X	MULTI-TIPS
5	SHAFTS-6
5R	SHAFTS-5
6	SHAFTS-4
6X	SHAFTS-3
7	SHAFTS-2
7X	SHAFTS-1
8	ALL BATCH 2
8X	ALL BATCH 2
9	ALL BATCH 2
9X	ALL BATCH 2

PLAQUE 9.17.A SWIRL MAT PREFORM	
SAMPLE NO.	FEATURE TYPE
1	MULTI-TIPS
1R	MULTI-TIPS
2	SHAFT-2
3	SHAFT-4
4	ROUND TIP
5	ALL BATCH 1
6	ALL BATCH 1
7	ALL BATCH 2
8	ALL BATCH 2
9	ALL BATCH 2
10	SHAFT-0
10X	SHAFT-1
11	SHAFT-0
11X	SHAFT-1
12	SHAFT-0
12X	SHAFT-1

PLAQUE 9.21.A NO PREFORM	
SAMPLE NO.	FEATURE TYPE
1	ROUND TIPS
2	STRIATIONS
3	SHAFT-2
3X	SHAFT-1
4	SHAFT-2
4X	SHAFT-1
5	ALL BATCH 1
5X	ALL BATCH 1

Table C.30: Continued.

PLAQUE 10.06.A SWIRL MAT PREFORM	
SAMPLE NO.	FEATURE TYPE
1	ALL BATCH 1
2	ALL BATCH 1
4	ALL BATCH 1
5	ALL BATCH 1
6	ALL BATCH 1
7	ALL BATCH 1
8	ALL BATCH 1
9	ALL BATCH 1
10	ALL BATCH 1
11	ALL BATCH 1

PLAQUE 10.12.A SWIRL MAT PREFORM	
SAMPLE NO.	FEATURE TYPE
1	ROUND TIP
2	ALL BATCH 1
3	SHAFT-2
4	SHAFT-2
5	SHAFT-2
6	ALL BATCH 2
7	ALL BATCH 2
8	ALL BATCH 2
9	ALL BATCH 2
10	ALL BATCH 2
11	ALL BATCH 2

Table C.31: Physical propeties testing for Derakane plaques with fingered structures. Plaque 9.11.A; Woven fabric preform. All spans 80 mm.

SAMPLE NO.	WIDTH (mm)	THICKNESS (mm)	FLEX MODULUS (GPa)	TENSILE MODULUS (GPa)	TENSILE STRENGTH (MPa)	STRAIN TO FAILURE (%)
911A1	13.54	3.50	19.50	3.48	193.00	6.59
911A2	13.38	3.49	19.50	3.48	169.50	7.21
911A2R			18.60			
911A3	13.52	3.45	19.00	3.50	188.90	7.35
911A4	13.55	3.51	18.10	3.44	193.00	8.08
911A5	13.09	3.49	18.10	3.31	186.90	7.46
911A6	13.52	3.47	18.80	3.43	189.60	7.52
911A6X			18.30			
911A7	13.53	3.58	18.40	3.33	184.20	9.13
911A7X			18.10			
911A8	13.70	3.57	18.00	3.31	169.10	6.77
911A8X			17.70			
911A9	13.74	3.56	18.60	3.34	190.10	7.63
911A9X			18.00			
AVE	13.51	3.51	18.48	3.40	184.92	7.53
ST DEV	0.18	0.04	0.54	0.07	8.74	0.71

Table C.32: Physical propeties testing for Derakane plaques with fingered structures. Plaque 9.15.A; woven fabric preform. All spans 80 mm.

SAMPLE NO.	WIDTH (mm)	THICKNESS (mm)	FLEX MODULUS (GPa)	TENSILE MODULUS (GPa)	TENSILE STRENGTH (MPa)	STRAIN TO FAILURE (%)
915A1	13.77	3.44	19.00	3.25	176.00	6.40
915A1X			19.10			
915A2	13.48	3.37	19.10	3.44	186.50	6.88
915A2X			19.00			
915A3	13.62	3.23	19.50	3.56	195.70	7.82
915A3X			19.50			
915A4	13.71	3.28	16.60	3.51	152.20	6.22
915A4X			15.50			
915A5	13.60	3.16	19.50	3.48	173.40	7.22
915A5R			19.60			
915A6	13.49	3.23	19.30	3.67	205.00	8.33
915A6X			19.40			
915A7	13.80	3.43	18.30	3.44	186.40	6.99
915A7X			18.30			
915A8	13.76	3.41	18.90	3.06	166.40	8.08
915A8X			18.80			
915A9	13.68	3.40	19.60	3.56	205.80	7.00
915A9X			18.70			
915A9R			19.90			
AVE	13.66	3.33	18.82	3.44	183.04	7.22
ST DEV	3.05	0.75	3.43	0.78	43.04	1.70

Table C.33: Physical propeties testing for Derakane plaques with fingered structures. Plaque 9.16.A; swirl mat preform. All spans 80 mm.

SAMPLE NO.	WIDTH (mm)	THICKNESS (mm)	FLEX MODULUS (GPa)	TENSILE MODULUS (GPa)	TENSILE STRENGTH (MPa)	STRAIN TO FAILURE (%)
916A1	13.71	3.33	9.07	1.77	77.93	4.54
916A1R			9.62			
916A1RR			9.57			
916A2	13.77	3.28	10.60	1.71	86.89	5.63
916A2R			10.90			
916A3	13.88	3.17	9.29	1.83	80.71	5.06
916A3R			9.27			
916A4	13.72	3.48	10.70	1.76	98.06	5.98
916A4X			10.30			
916A5	13.73	3.45	9.27	2.01	98.15	6.12
916A5X			9.26			
916A6	13.69	3.39	10.80	2.09	105.10	6.51
916A7	13.71	3.42	9.53	2.04	104.10	5.97
916A7X			9.45			
916A8	13.83	3.45	8.88	1.75	96.93	6.30
916A8X			9.00			
916A9	13.82	3.40	10.00	1.94	100.10	6.82
916A9X			9.05			
916A10	13.69	3.20	9.35	1.78	87.32	6.60
916A10X			9.79			
916A11	13.68	3.26	9.02	1.84	100.50	6.59
916A11X			9.28			
916A12	13.73	3.30	9.36			
916A12X			9.42			
AVE	13.75	3.34	9.62	1.87	94.16	6.01
ST DEV	0.06	0.10	0.60	0.13	8.93	0.67

Table C.34: Physical propeties testing for Derakane plaques with fingered structures. Plaque 9.17.A; swirl mat preform. All spans 80 mm.

SAMPLE NO.	WIDTH (mm)	THICKNESS (mm)	FLEX MODULUS (GPa)	TENSILE MODULUS (GPa)	TENSILE STRENGTH (MPa)	STRAIN TO FAILURE (%)
917A1	13.55	3.49	6.00	1.88	86.92	5.15
917A1X			6.40			
917A2	13.58	3.20	9.89	2.95	102.10	5.11
917A3	13.70	3.25	9.49	2.15	96.59	5.52
917A4	14.00	3.40	8.84	2.04	96.13	5.43
917A5	13.80	3.34	8.78	2.26	88.67	5.08
917A6	13.76	3.30	9.95	2.21	102.50	5.74
917A7	13.50	3.67	7.73	1.73	80.77	4.86
917A8	13.58	3.43	9.58	2.13	106.40	5.21
917A9	13.54	3.46	9.63	2.14	93.25	4.93
917A10	13.65	3.47	9.71			
917A10X			9.17	2.05	105.10	6.63
917A11	13.46	3.52	8.03			
917A11X			8.59	1.83	92.13	5.14
917A12	13.61	3.35	10.60			
917A12X			10.30	2.06	96.11	6.34
AVR	13.64	3.41	8.92	2.12	95.56	5.43
ST DEV	0.14	0.12	1.27	0.29	7.41	0.53

Table C.35: Physical propeties testing for Derakane plaques with fingered structures. Plaque 9.18.A; no preform. All spans 80 mm.

SAMPLE NO.	WIDTH (mm)	THICKNESS (mm)	FLEX MODULUS (GPa)	TENSILE MODULUS (GPa)	TENSILE STRENGTH (MPa)	STRAIN TO FAILURE (%)
918A1	13.66	2.93	3.81	0.94	29.98	3.45
918A1U			3.78			
918A2	13.69	2.97	3.82	1.01	45.97	4.52
918A2R			3.81			
918A3	13.79	2.99	4.02	0.70	12.94	1.06
918A4	13.19	3.12	3.79	1.03	67.75	7.83
918A4X			3.79			
918A5	13.54	3.11	3.83	1.03	56.48	5.64
918A5X			3.67			
918A6	13.52	3.05	4.12	0.96	28.30	3.79
918A6X			4.12			
918A7	12.96	3.08	3.02			
918A7R			3.59			
918A9	13.19	3.02	3.24			
AVE	13.44	3.03	3.74	0.95	40.24	4.38
ST DEV	0.28	0.06	0.29	0.11	18.47	2.07

Table C.36: Physical propeties testing for Derakane plaques with fingered structures. Plaque 9.21.A; no preform. All spans 80 mm.

SAMPLE NO.	WIDTH (mm)	THICKNESS (mm)	FLEX MODULUS (GPa)	TENSILE MODULUS (GPa)	TENSILE STRENGTH (MPa)	STRAIN TO FAILURE (%)
921A1	13.20	3.01	3.98	1.06	36.08	4.18
921A2	13.46	3.02	3.56	0.97	25.01	3.00
921A2R			3.48			
921A3	13.21	3.16	4.02	0.97	29.82	3.42
921A3X			3.83			
921A4	13.17	3.16	3.96	1.00	46.87	4.92
921A4X			3.84			
921A5	13.73	3.10	3.76	0.88	24.97	2.81
921A5R			3.64			
AVE	13.35	3.09	3.79	0.98	32.55	3.67
ST DEV	0.21	0.07	0.18	0.06	8.24	0.78

Table C.37: Physical propeties testing for Derakane plaques with fingered structures. Plaque 9.22.A; no preform. All spans 80 mm.

SAMPLE NO.	WIDTH (mm)	THICKNESS (mm)	FLEX MODULUS (GPa)	TENSILE MODULUS (GPa)	TENSILE STRENGTH (MPa)	STRAIN TO FAILURE (%)
922A1	12.73	2.97	3.46	1.06	45.70	5.53
922A1U			3.64			
922A2	12.40	2.85	4.02	1.08	70.56	8.38
922A3	13.00	2.83	4.03	0.97	62.50	6.77
922A4	12.75	2.95	3.62	1.00	33.71	3.38
922A4R			3.67			
922A5	13.00	2.90	4.04	1.10	52.32	5.38
922A5R			4.05			
922A6B	13.00	2.94	3.79	1.02	41.70	4.34
922A6N			3.78			
922A7B	12.59	2.83	3.88			
922A7N			3.84			
922A8B	12.70	2.82	4.10	1.04	64.43	7.36
922A8N			4.07			
922A9	13.00	2.79	4.01			
922A9X			4.13	1.11	42.44	3.76
922A10	12.83	2.87	3.98	1.01	26.06	2.58
922A11	12.90	2.87	4.22	1.06	69.26	8.12
922A12	13.00	2.84	4.10			
AVE	12.83	2.87	3.92	1.05	50.87	5.56
ST DEV	0.19	0.05	0.20	0.04	14.63	1.94

Table C.38: Physical propeties testing for Derakane plaques with fingered structures. Plaque 10.06.A; swirl mat preform, no age difference. All spans 80 mm.

SAMPLE NO.	WIDTH (mm)	THICKNESS (mm)	FLEX MODULUS (GPa)	TENSILE MODULUS (GPa)	TENSILE STRENGTH (MPa)	STRAIN TO FAILURE (%)
1006A1	13.66	3.39	9.35	2.10	95.62	5.06
1006A2	13.63	3.48	9.34	1.95	79.94	4.84
1006A3	13.68	3.97	6.12	1.80	84.97	5.72
1006A4	13.71	3.51	8.63	1.92	84.15	5.38
1006A5	13.61	3.86	8.81	1.79	84.38	5.54
1006A6	13.43	3.63	8.40	1.80	78.47	5.28
1006A7	13.67	3.86	9.30	1.74	88.17	5.71
1006A8	13.64	3.85	8.67	1.70	74.04	5.11
1006A9	13.67	3.84	8.51	1.72	69.61	4.79
1006A10	13.68	3.87	8.44	1.66	78.45	5.74
1006A11	13.73	3.87	8.13	1.47	71.26	6.03
AVE	13.65	3.74	8.52	1.79	80.82	5.38
STDEV	0.08	0.19	0.85	0.16	7.32	0.38

Table C.39: Physical propeties testing for Derakane plaques with fingered structures. Plaque 10.07.B no preform, no age difference between batches. All spans 80 mm.

SAMPLE NO.	WIDTH (mm)	THICKNESS (mm)	FLEX MODULUS (GPa)	TENSILE MODULUS (GPa)	TENSILE STRENGTH (MPa)	STRAIN TO FAILURE (%)
1007B1	13.63	3.62	3.96	1.10	65.22	6.94
1007B2	13.62	3.62	3.84	1.12	53.22	4.83
1007B2R			3.93			
1007B3	13.63	3.67	3.98	0.96		
1007B4	13.69	3.83	4.08	1.05	43.99	4.37
1007B5	13.63	3.77	4.24	1.01	31.05	3.10
1007B6	13.73	3.80	3.99	0.99	44.14	4.35
1007B7	13.74	3.99	4.14	1.02	52.10	5.44
1007B8	13.74	3.95	4.16	0.97	52.50	5.77
1007B9	13.75	3.94	4.12	0.93	42.01	4.85
AVE	13.68	3.80	4.04	1.02	48.03	4.96
ST DEV	0.05	0.13	0.11	0.06	8.91	1.00

Table C.40: Physical propeties testing for Derakane plaques with fingered structures. Plaque 10.12.A swirl mat preform, very long injection. All spans 80 mm.

SAMPLE NO.	WIDTH (mm)	THICKNESS (mm)	FLEX MODULUS (GPa)	TENSILE MODULUS (GPa)	TENSILE STRENGTH (MPa)	STRAIN TO FAILURE (%)
1012A1	13.71	4.10	8.56	1.91	91.24	5.04
1012A2	13.71	3.84	7.33	1.99	86.65	4.41
1012A3	13.72	3.88	8.15	1.81	83.02	4.79
1012A4	13.69	3.87	9.77	2.06	100.90	5.63
1012A5	13.71	3.91	9.30	1.77	92.96	5.56
1012A6	13.72	4.28	8.71	1.57	90.12	5.75
1012A7	13.69	4.30	8.30	1.69	88.22	5.82
1012A8	13.68	4.37	7.82	1.76	81.85	5.14
1012A9	13.70	4.27	8.08	1.59	96.79	6.20
1012A10	13.60	4.29	8.25	1.67	75.28	4.75
1012A11	13.54	4.26	8.68	1.95	97.50	6.06
AVE	13.68	4.12	8.45	1.80	89.50	5.38
ST DEV	0.05	0.20	0.64	0.16	7.23	0.56

Table C.41: Short beam shear testing of two-ply bars. Epoxy resin, $\Delta t = 0$ min, Batch 1 tested in tension.

SAMPLE NO.	WIDTH (mm)	THICKNESS (mm)	BREAKING LOAD (N)	MAXIMUM TENSILE STRESS (MPa)	MAXIMUM SHEAR STRESS (MPa)
7.15.A1	13.67	3.36	489.00	150.90	7.98
2	12.49	3.37	436.00	146.39	7.77
3	12.44	3.40	425.00	140.75	7.54
4	12.31	3.52	400.00	124.90	6.92
5	11.42	3.45	417.00	146.11	7.94
2.15.A1	12.40	8.20	2769.32	158.18	20.43
2	12.21	8.71	3062.58	157.46	21.60
3	12.30	8.90	2532.56	123.80	17.35
4	12.12	8.80	3086.03	156.59	21.70
5	12.18	8.90	2016.78	99.56	13.95
3.01.A1	11.57	8.07	2378.50	151.52	19.11
2	11.87	8.07	2032.50	126.20	15.91
3	13.68	8.13	2221.00	117.90	14.98
4	13.74	8.06	2231.5	120.00	15.11
AVG				137.16	14.16
ST DEV				18.26	5.58

Table C.42: Short beam shear testing of two-ply bars. Epoxy resin, Δt = 15 min, Batch 1 tested in tension.

SAMPLE NO.	WIDTH (mm)	THICKNESS (mm)	BREAKING LOAD (N)	MAXIMUM TENSILE STRESS (MPa)	MAXIMUM SHEAR STRESS (MPa)
7.16.B1	12.14	7.09	2134.00	166.54	18.59
2	12.11	7.17	2012.00	153.91	17.38
3	11.40	7.36	1758.00	135.58	15.71
4	12.05	7.45	2192.00	156.09	18.31
5	12.13	7.50	2279.00	159.07	18.79
2.15.B1	12.34	8.60	3007.63	156.95	21.26
2	12.30	8.35	2258.80	125.44	16.49
3	12.32	8.30	2918.56	163.77	21.41
4	12.37	8.37	3012.80	165.57	21.82
5	12.32	8.27	2889.40	163.31	21.27
AVG	12.15	7.85	2446.22	154.62	19.10
STDEV	0.29	0.58	464.65	13.59	2.22

Table C.43: Short beam shear testing of two-ply bars. Epoxy resin, Δt = 45 min, Batch 1 tested in tension.

SAMPLE NO.	WIDTH (mm)	THICKNESS (mm)	BREAKING LOAD (N)	MAXIMUM TENSILE STRESS (MPa)	MAXIMUM SHEAR STRESS (MPa)
7.15.B1	12.41	7.16	1966.00	147.17	16.59
2	12.51	7.27	2388.00	172.01	19.69
3	12.44	7.43	2420.00	167.82	19.64
4	12.45	7.53	2304.00	155.44	18.43
5	12.39	7.58	2509.00	167.85	20.04
2.18.B1	12.36	7.10	2291.50	175.15	19.58
2	12.39	7.27	2343.01	170.40	19.51
3	12.35	7.33	2431.62	174.52	20.15
4	12.35	7.52	2067.14	140.96	16.69
5	12.34	7.59	2574.85	172.50	20.62
AVG	12.40	7.38	2329.51	164.38	19.09
ST DEV	0.05	0.18	187.88	12.15	1.41

Table C.44: Short beam shear testing of two-ply bars. Epoxy resin, Δt = 60 min, Batch 1 tested in tension.

SAMPLE NO.	WIDTH (mm)	THICKNESS (mm)	BREAKING LOAD (N)	MAXIMUM TENSILE STRESS (MPa)	MAXIMUM SHEAR STRESS (MPa)
7.20.B1	12.02	6.72	1792.00	157.23	16.64
2	11.74	6.71	1739.00	156.68	16.56
3	12.15	6.90	1792.00	147.54	16.03
4	12.17	7.04	2062.00	162.81	18.05
5	12.21	7.17	2051.00	155.61	17.57
2.19.B1	11.28	7.39	2014.53	155.74	18.13
2	11.16	7.56	2050.50	153.10	18.23
3	11.24	7.67	2144.86	154.48	18.66
5	11.30	7.99	2205.86	145.63	18.32
AVG	11.70	7.24	1983.53	154.31	17.58
ST DEV	0.45	0.44	167.62	5.16	0.93

Table C.45: Short beam shear testing of two-ply bars. Epoxy resin, Δt = 75 min, Batch 1 tested in tension.

SAMPLE NO.	WIDTH (mm)	THICKNESS (mm)	BREAKING LOAD (N)	MAXIMUM TENSILE STRESS (MPa)	MAXIMUM SHEAR STRESS (MPa)
7.16.A1	12.25	7.16	2165.00	164.18	18.51
2	12.36	7.23	2237.00	164.89	18.77
3	12.33	7.28	2078.00	151.44	17.36
4	12.19	7.37	2175.00	156.44	18.16
5	12.41	7.44	2245.00	155.64	18.24
2.12.A1	13.55	7.47	2381.41	150.00	17.65
2	12.34	7.54	2025.07	137.47	16.32
3	12.43	7.61	2571.96	170.16	20.39
4	12.43	7.60	2408.96	159.80	19.13
5	12.40	7.70	2138.27	138.51	16.80
7	12.76	7.84	2554.66	155.13	19.15
AVG	12.50	7.48	2270.94	154.88	18.23
ST DEV	0.38	0.21	184.36	10.27	1.16

Table C.46: Short beam shear testing of two-ply bars. Epoxy resin, Δt = 90 min, Batch 1 tested in tension.

SAMPLE NO.	WIDTH (mm)	THICKNESS (mm)	BREAKING LOAD (N)	MAXIMUM TENSILE STRESS (MPa)	MAXIMUM SHEAR STRESS (MPa)
7.20.A1	12.40	7.40	1697.00	119.02	13.87
2	12.10	7.49	1847.00	129.58	15.28
3	12.17	7.53	1505.00	103.87	12.32
4	12.35	7.50	1471.00	100.85	11.91
2.25.A1	11.38	7.75	2265.91	157.88	19.27
2	11.32	7.69	2219.82	157.93	19.13
3	11.36	7.68	2169.78	154.22	18.65
4	11.32	7.70	2303.11	163.43	19.82
5	11.37	7.78	1846.10	127.75	15.65
AVG	11.75	7.61	1924.97	134.95	16.21
ST DEV	0.49	0.13	326.50	24.24	3.10

Table C.47: Short beam shear testing of two-ply bars. Epoxy resin, Δt = 120 min, Batch 1 tested in tension.

SAMPLE NO.	WIDTH (mm)	THICKNESS (mm)	BREAKING LOAD (N)	MAXIMUM TENSILE STRESS (MPa)	MAXIMUM SHEAR STRESS (MPa)
7.19.A1	12.46	7.01	1812.00	140.94	15.56
2	12.22	7.24	1968.00	146.32	16.68
3	12.45	7.15	1853.00	138.65	15.61
4	12.37	7.29	2265.91	164.15	18.85
5	11.88	7.29	2219.82	167.45	19.22
2.18.A1	12.34	7.25	1088.40	79.92	9.12
2	12.37	7.25	1674.24	122.63	14.00
3	12.40	7.45	2237.59	154.84	18.17
4	12.35	7.57	1661.63	111.82	13.33
5	12.37	7.59	1525.52	101.95	12.19
AVG	12.32	7.31	1830.61	132.87	15.27
ST DEV	0.17	0.18	368.68	28.37	3.19

Table C.48: Short beam shear testing of two-ply bars. Epoxy resin, Δt = 75 min, and interface treated with Teflon spray. Batch 1 tested in tension.

SAMPLE NO.	WIDTH (mm)	THICKNESS (mm)	BREAKING LOAD (N)	MAXIMUM TENSILE STRESS (MPa)	MAXIMUM SHEAR STRESS (MPa)
7.19.B1	11.04	7.33	1446.00	116.10	13.40
2	11.82	7.53	1894.00	134.59	15.96
3	12.57	7.38	2118.00	147.34	17.12
4	12.08	7.81	2172.00	140.39	17.27
5	12.21	8.04	1881.00	113.50	14.37
AVG	11.94	7.62	1902.20	130.38	15.62
ST DEV	0.57	0.30	286.36	14.95	1.70
2.19.A1	12.33	7.31	1635.71	118.23	13.61
2	12.35	7.28	1779.45	129.48	14.84
3	12.36	7.49	1916.82	131.65	15.53
AVG	12.35	7.36	1777.33	126.46	14.66
ST DEV	0.02	0.11	140.56	7.20	0.97

Table C.49: Short beam shear testing of two-ply bars. Epoxy resin, $\Delta t = 0$ min, Batch 2 tested in tension.

SAMPLE NO.	WIDTH (mm)	THICKNESS (mm)	BREAKING LOAD (N)	MAXIMUM TENSILE STRESS (MPa)	MAXIMUM SHEAR STRESS (MPa)
7.15.A6	12.43	3.59	509.00	151.32	8.55
7	12.39	3.63	443.00	129.23	7.39
8	12.33	3.68	509.00	145.18	8.41
10	12.44	3.74	563.00	154.09	9.08
2.15.A6	12.83	8.10	2705.12	153.05	19.52
7	12.83	7.72	2555.59	159.17	19.35
8	12.77	7.81	2612.46	159.73	19.65
9	12.72	8.10	2758.15	157.40	20.08
10	12.80	8.18	2810.56	156.28	20.13
3.01.A6	13.8	8.08	2834	150.99	19.06
7	13.8	8.02	3173.5	171.61	21.51
8	13.69	8.17	2798	146.97	18.76
9	13.75	7.98	2687.5	147.33	18.37
10	13.63	8.2	2582	135.23	17.33
AVG			2110.06	151.72	14.68
ST DEV			1063.35	9.55	6.02

Table C.50: Short beam shear testing of two-ply bars. Epoxy resin, Δt = 15 min, Batch 2 tested in tension.

SAMPLE NO.	WIDTH (mm)	THICKNESS (mm)	BREAKING LOAD (N)	MAXIMUM TENSILE STRESS (MPa)	MAXIMUM SHEAR STRESS (MPa)
7.16.B6	12.11	7.62	2456.00	166.34	19.96
7	12.31	7.74	2491.00	160.87	19.61
8	12.38	7.87	2153.00	133.72	16.57
9	12.36	7.90	2680.00	165.46	20.58
10	12.38	7.94	2712.00	165.49	20.69
2.15.B6	12.52	8.35	2937.97	160.29	21.08
7	12.56	8.21	2759.50	155.23	20.07
8	12.70	8.17	2858.16	160.57	20.66
9	12.74	8.16	2695.59	151.34	19.45
10	12.75	8.26	2954.89	161.77	21.04
AVG	12.48	8.02	2669.81	158.11	19.97
ST DEV	0.21	0.24	245.86	9.76	1.32

Table C.51: Short beam shear testing of two-ply bars. Epoxy resin, Δt = 45 min, Batch 2 tested in tension.

SAMPLE NO.	WIDTH (mm)	THICKNESS (mm)	BREAKING LOAD (N)	MAXIMUM TENSILE STRESS (MPa)	MAXIMUM SHEAR STRESS (MPa)
7.15.B6	12.42	7.65	2669.00	174.88	21.07
7	12.44	7.71	2732.00	175.95	21.36
8	12.52	7.76	2465.00	155.71	19.03
9	12.45	7.81	2815.00	176.54	21.71
10	12.54	7.83	2799.00	173.39	21.38
2.18.B7	12.74	7.71	2291.26	144.09	17.49
8	12.77	7.79	2568.52	157.85	19.36
9	12.71	7.85	2745.64	166.95	20.64
10	12.77	7.93	2730.30	161.92	20.22
AVG	12.60	7.78	2646.19	165.25	20.25
ST DEV	0.15	0.09	173.76	11.23	1.38

Table C.52: Short beam shear testing of two-ply bars. Epoxy resin, Δt = 60 min, Batch 2 tested in tension.

SAMPLE NO.	WIDTH (mm)	THICKNESS (mm)	BREAKING LOAD (N)	MAXIMUM TENSILE STRESS (MPa)	MAXIMUM SHEAR STRESS (MPa)
7.20.B6	12.27	7.48	2492.00	172.88	20.36
7	12.07	7.50	2157.00	151.31	17.87
8	12.30	7.67	2671.00	175.80	21.23
9	12.20	7.79	2572.00	165.45	20.30
10	12.43	7.77	2617.00	166.08	20.32
2.19.B6	12.62	7.65	2679.67	172.80	20.82
7	12.79	7.86	2903.25	174.99	21.66
8	12.67	7.84	2895.91	177.10	21.87
9	12.75	7.88	2977.70	179.12	22.23
10	12.76	7.92	3006.23	178.88	22.31
AVG	12.49	7.74	2697.18	171.44	20.90
ST DEV	0.26	0.16	261.01	8.51	1.31

Table C.53: Short beam shear testing of two-ply bars. Epoxy resin, Δt = 75 min, Batch 2 tested in tension.

SAMPLE NO.	WIDTH (mm)	THICKNESS (mm)	BREAKING LOAD (N)	MAXIMUM TENSILE STRESS (MPa)	MAXIMUM SHEAR STRESS (MPa)
7.16.A6	12.38	7.52	2553.00	173.67	20.57
7	12.43	7.55	2580.00	173.42	20.62
9	12.28	7.68	2606.00	171.35	20.72
10	12.39	7.71	2661.00	172.07	20.89
2.12.A6	12.65	7.75	2688.91	168.55	20.57
8	12.68	7.93	2873.61	171.63	21.43
9	12.66	7.99	2924.04	172.30	21.68
10	12.71	8.07	2945.31	169.46	21.54
AVG	12.52	7.78	2728.98	171.56	21.00
ST DEV	0.17	0.20	160.48	1.78	0.47

Table C.54: Short beam shear testing of two-ply bars. Epoxy resin, Δt = 90 min, Batch 2 tested in tension.

SAMPLE NO.	WIDTH (mm)	THICKNESS (mm)	BREAKING LOAD (N)	MAXIMUM TENSILE STRESS (MPa)	MAXIMUM SHEAR STRESS (MPa)
7.20.A6	12.13	7.80	2595.00	167.46	20.57
7	11.70	7.84	2466.00	163.31	20.16
8	12.08	7.79	2487.00	161.57	19.82
9	12.30	7.97	2735.00	166.71	20.92
10	12.52	7.99	2746.00	163.62	20.59
2.25.A6	12.64	7.76	2657.11	166.25	20.32
7	12.55	7.70	2596.61	166.19	20.15
8	12.56	7.76	2616.26	164.74	20.13
9	12.64	7.83	2697.35	165.77	20.44
10	12.77	7.84	2692.91	163.39	20.17
AVE	12.39	7.83	2628.92	164.90	20.33
STDEV	0.33	0.09	96.36	1.88	0.31

Table C.55: Short beam shear testing of two-ply bars. Epoxy resin, Δt = 120 min, Batch 2 tested in tension.

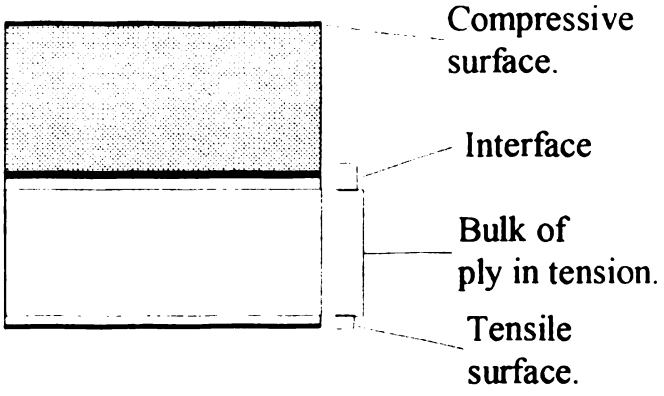
SAMPLE NO.	WIDTH (mm)	THICKNESS (mm)	BREAKING LOAD (N)	MAXIMUM TENSILE STRESS (MPa)	MAXIMUM SHEAR STRESS (MPa)
7.19.A6	12.41	7.51	2465.00	167.73	19.84
7	12.30	7.45	2407.00	167.92	19.70
8	12.39	7.47	2327.00	160.29	18.86
9	12.44	7.56	2484.00	166.39	19.81
10	12.38	7.68	2542.00	165.79	20.05
2.18.A6	12.79	7.67	2452.28	155.22	18.75
7	12.77	7.74	2561.06	159.43	19.43
8	12.78	7.80	2628.46	161.00	19.78
9	12.80	7.89	2650.04	158.39	19.68
10	12.84	7.92	2651.71	156.80	19.56
AVG	12.59	7.67	2516.85	161.90	19.54
ST DEV	0.22	0.17	109.04	4.69	0.43

Table C.56: Short beam shear testing of two-ply bars. Epoxy resin, Δt = 75 min, and interface treated with Teflon spray. Batch 2 tested in tension.

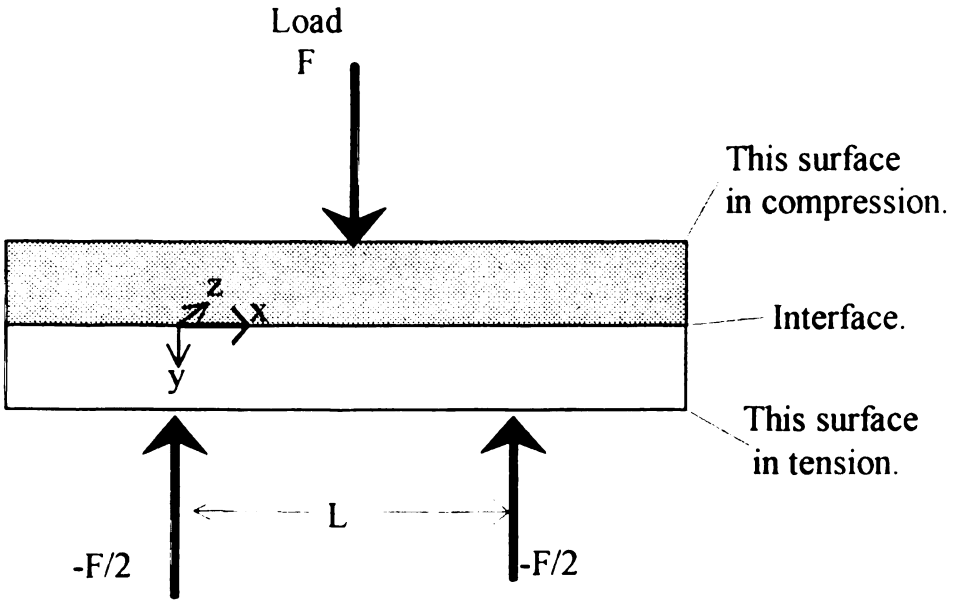
SAMPLE NO.	WIDTH (mm)	THICKNESS (mm)	BREAKING LOAD (N)	MAXIMUM TENSILE STRESS (MPa)	MAXIMUM SHEAR STRESS (MPa)
7.19.B6	11.68	7.76	560.60	33.77	3.87
7	12.27	8.26	552.50	31.43	4.09
8	12.02	8.23	562.00	32.88	4.26
9	12.43	7.82	659.70	41.33	5.09
10	12.03	7.83	601.30	38.83	4.79
AVG	12.09	7.98	587.22	35.65	4.42
ST DEV	0.28	0.24	44.73	4.23	0.51
2.19.A6	12.57	8.14	1939.13	110.88	14.21
7	12.78	8.13	1952.02	110.05	14.09
8	12.76	8.16	1821.12	102.08	13.12
9	12.84	8.10	1467.60	82.97	10.58
10	12.72	8.31	1210.64	65.64	8.59
AVG	12.73	8.17	1678.10	94.32	12.12
ST DEV	0.10	0.08	326.52	19.58	2.45

Table C.57: Summary of failure modes for two-ply bars in short beam shear. See Figure C.37.

PLAQUE	Δt (min)	TENSILE SURFACE	TENSILE BULK	INTERFACE	COMPRES. FAILURE
2.15.A	0	8	0	0	0
7.15.A	0	7	2	0	0
3.01.A	0	10	0	0	0
2.15.B	15	6	3	0	0
7.16.B	15	9	1	0	0
2.18.B	45	4	5	1	0
7.15.B	45	9	1	0	0
2.19.B	60	3	7	0	0
7.20.B	60	8	2	0	0
2.12.A	75	8	1	0	0
7.16.A	75	8	1	0	0
2.25.A	90	4	5	0	0
7.20.A	90	9	0	0	0
2.18.A	120	4	1	3	0
7.19.A	120	9	1	0	0
2.19.A	75 TEFLON	3	0	6	0
7.19.B	75 TEFLON	2	0	8	0



Cross-section of 2-ply bar.



Short-beam shear test configuration.

Figure C.37: Explanation of terms used in Table C.57.

Table C.58: Summary of fingering flow run conditions.

RUN NO.	Vol. Flow Rate, Q (cm^3/sec)	Piston Speed, S (cm/sec)	Velocity V_x (cm/sec)	Pre-form V_f	$t_{residence}$ (sec)	t_{delav} (sec)	Fingers (Y/N)
8.19.A	0.450	0.5	0.0170	0	388	134	N @ t = 916
8.19.B	0.450	0.5	0.071	0	292	63	N @ t = 861
8.20.A	0.450	0.5	0.077	0	396	83	N @ t = 936 Y @ t = 975
8.20.B	0.180	0.2	0.044	0	462	87	N @ t = 2031 Y @ t = 2139
8.24.A	0.180	0.2	0.039	0	787	62	N @ t = 2102
8.24.B	0.180	0.2	0.036	0.17	818	52	Y @ t = 1871
9.9.A	0.450	0.5	0.100	0.16	442	120	Y @ t = 1135
9.9.B	0.450	0.5	0.100	0.15	347	240	Y @ t = 1292
9.17.A	0.09	0.1	0.015	0.15	1888	120	Y @ t = 3604
9.20.A	0.09	1.0	0.148	0.15	494	151	Y @ t = 1167
9.21.A	0.09	1.0	0.194	0.16	252	240	N @ t = 687
9.22.A	1.80	2.0	0.300	0.15	84	50	N @ t = 347

Table C.59: Data and calculations for fingering flow run # 8.20.A. $\mathcal{V}$ = 862.8.

FINGER ID	TIME OF PHOTO (min)	TIP LOCATION (cm)	TIP VELOCITY dL/dt (cm/sec)	FINGER WIDTH Wf (mm)	AGE OF INTER-FACE t_I	VISCOSITY $\mu_I(I)$ (Pa·sec)	TIP GROWTH RATE λ	REACTION EXTENT $\alpha(I)$	MOBILITY RATIO $\mathcal{M}$
1	16.98	23.5	0.1512	3.0	13.07	0.250	0.964	0.197	14.139
	17.70	30.0	0.1512	1.5	14.48	0.317	0.964	0.214	16.298
2	16.48	20.7	0.1273	2.3	12.46	0.228	0.653	0.189	13.214
	16.98	24.6	0.1273	2.3	13.31	0.260	0.653	0.200	14.504
	17.70	30.0	0.1273	3.0	14.48	0.317	0.653	0.214	16.298
3	16.48	21.0	0.1291	2.3	12.53	0.230	0.677	0.190	13.313
	16.98	24.7	0.1291	2.7	13.33	0.261	0.677	0.200	14.537
	17.70	30.4	0.1291	3.0	14.56	0.322	0.677	0.215	16.431
4	16.25	19.0	0.1328		12.10	0.216	0.725	0.184	12.653
	16.48	21.0	0.1328	3.0	12.53	0.230	0.725	0.190	13.313
	16.98	25.0	0.1328	2.3	13.39	0.263	0.725	0.201	14.636
	17.70	30.6	0.1328	3.0	14.61	0.325	0.725	0.216	16.498
5	16.25	19.3	0.1352	2.3	12.16	0.218	0.756	0.185	12.752
	16.48	21.0	0.1352	3.0	12.53	0.230	0.756	0.190	13.313
	16.98	25.0	0.1352	3.0	13.39	0.263	0.756	0.201	14.636
	17.70	31.0	0.1352	3.0	14.69	0.330	0.756	0.217	16.631
6	16.25	19.3	0.1343	2.3	12.16	0.218	0.744	0.185	12.752
	16.48	21.2	0.1343	3.0	12.57	0.232	0.744	0.190	13.379
	16.68	22.6	0.1343	2.3	12.88	0.243	0.744	0.194	13.841
	16.98	25.0	0.1343	3.0	13.39	0.263	0.744	0.201	14.636
	17.70	31.0	0.1343	3.0	14.69	0.330	0.744	0.217	16.631

Table C.59: Continued.

FINGER ID	TIME OF PHOTO (min)	TIP LOCATION (cm)	TIP VELOCITY dL/dt (cm/sec)	FINGER WIDTH Wf (mm)	AGE OF INTER-FACE t_I	VISCOSITY $\mu_1(I)$ (Pa·sec)	TIP GROWTH RATE λ	REACTION EXTENT $\alpha(I)$	MOBILITY RATIO $\mathcal{M}$
7	16.25	19.7	0.1178	3.0	12.25	0.221	0.530	0.186	12.884
	16.48	21.6	0.1178	2.3	12.66	0.235	0.530	0.191	13.511
	16.68	23.0	0.1178	2.3	12.96	0.246	0.530	0.195	13.974
	16.98	25.3	0.1178	2.3	13.46	0.266	0.530	0.201	14.736
	17.70	31.4	0.1178	2.3	14.78	0.335	0.530	0.218	16.764
8	16.25	19.9	0.1368	2.3	12.29	0.222	0.777	0.187	12.950
	16.48	21.8	0.1368	1.5	12.70	0.236	0.777	0.192	13.577
	16.68	23.2	0.1368	2.7	13.00	0.248	0.777	0.196	14.040
	16.98	25.7	0.1368	1.5	13.55	0.270	0.777	0.203	14.868
	17.70	31.8	0.1368	1.5	14.87	0.340	0.777	0.219	16.898
9	16.25	20.0	0.1372	3.0	12.31	0.223	0.782	0.187	12.983
	16.48	22.0	0.1372	3.0	12.75	0.238	0.782	0.192	13.643
	16.68	23.5	0.1372	3.0	13.07	0.250	0.782	0.197	14.139
	16.98	25.8	0.1372	3.0	13.57	0.271	0.782	0.203	14.902
	17.70	32.0	0.1372	2.3	14.91	0.343	0.782	0.219	16.964
11	16.48	21.4	0.1459	1.5	12.62	0.233	0.895	0.191	13.445
	16.68	23.0	0.1459	1.5	12.96	0.246	0.895	0.195	13.974
	16.98	25.6	0.1459	1.5	13.52	0.269	0.895	0.202	14.835
	17.70	32.0	0.1459	1.5	14.91	0.343	0.895	0.219	16.964

Table C.60: Data and calculations for fingering flow run # 8.20.B. $\mathcal{Q}$ = 493.0.

FINGER ID	TIME OF PHOTO (min)	TIP LOCATION (cm)	TIP VELOCITY dL/dt (cm/sec)	FINGER WIDTH Wf (mm)	AGE OF INTER-FACE t_I	VISCOSITY $\mu_1(I)$ (Pa·sec)	TIP GROWTH RATE λ	REACTION EXTENT $\alpha(I)$	MOBILITY RATIO $\mathcal{M}$
2	35.65	18.5	0.0588	2.0	15.06	0.463	0.336	0.221	17.192
	36.58	22.0	0.0588	2.0	16.38	0.617	0.336	0.237	19.238
	37.63	25.5	0.0588	1.1	17.71	0.840	0.336	0.252	21.286
3	35.65	20.0	0.0504	1.3	15.63	0.522	0.145	0.228	18.068
	36.58	23.0	0.0504	1.3	16.76	0.672	0.145	0.241	19.823
	37.63	26.0	0.0504	2.2	17.90	0.879	0.145	0.254	21.578
4	35.65	20.0	0.0587	1.3	15.63	0.522	0.334	0.228	18.068
	36.58	23.6	0.0587	1.3	16.99	0.708	0.334	0.244	20.174
	37.63	27.0	0.0587	1.1	18.28	0.964	0.334	0.258	22.163
5	35.65	21.0	0.0504	1.3	16.00	0.567	0.145	0.232	18.653
	36.58	24.0	0.0504	1.3	17.14	0.734	0.145	0.245	20.408
	37.63	27.0	0.0504	1.1	18.28	0.964	0.145	0.258	22.163
6	35.65	21.0	0.0504	1.3	16.00	0.567	0.145	0.232	18.653
	36.58	24.0	0.0504	1.3	17.14	0.734	0.145	0.245	20.408
	37.63	27.0	0.0504	2.2	18.28	0.964	0.145	0.258	22.163
7	35.65	21.0	0.0546	1.3	16.00	0.567	0.241	0.232	18.653
	36.58	24.2	0.0546	2.0	17.22	0.747	0.241	0.246	20.525
	37.63	27.5	0.0546	2.2	18.47	1.011	0.241	0.260	22.455
13	35.65	21.0	0.0545	2.0	16.00	0.567	0.239	0.232	18.653
	36.58	24.5	0.0545	2.6	17.33	0.767	0.239	0.248	20.701
	37.63	27.5	0.0545	1.7	18.47	1.011	0.239	0.260	22.455

Table C.60: Continued.

FINGER ID	TIME OF PHOTO (min)	TIP LOCATION (cm)	TIP VELOCITY dL/dt (cm/sec)	FINGER WIDTH Wf (mm)	AGE OF INTER-FACE t_I	VISCOSITY $\mu_1(I)$ (Pa·sec)	TIP GROWTH RATE λ	REACTION EXTENT $\alpha(I)$	MOBILITY RATIO $\mathcal{M}$
14	35.65	20.5	0.0546	1.3	15.82	0.544	0.241	0.230	18.361
	36.58	23.5	0.0546	1.3	16.95	0.702	0.241	0.243	20.116
	37.63	27.0	0.0546	1.7	18.28	0.964	0.241	0.258	22.163
15	35.65	20.0	0.0545	5.3	15.63	0.522	0.239	0.228	18.068
	36.58	23.5	0.0545	2.6	16.95	0.702	0.239	0.243	20.116
	37.63	26.5	0.0545	3.3	18.09	0.920	0.239	0.256	21.871
16	35.65	19.5	0.0505	2.6	15.44	0.502	0.148	0.226	17.776
	36.58	22.0	0.0505	2.6	16.38	0.617	0.148	0.237	19.238
	37.63	25.2	0.0505	3.3	17.60	0.817	0.148	0.251	21.110

Table C.61: Data and calculations for fingering flow run # 8.24.B. $\mathcal{V}$ = 403.4.

FINGER ID	TIME OF PHOTO (min)	TIP LOCATION (cm)	TIP VELOCITY dL/dt (cm/sec)	FINGER WIDTH Wf (mm)	AGE OF INTER-FACE t_I	VISCOSITY $\mu_I(I)$ (Pa·sec)	TIP GROWTH RATE λ	REACTION EXTENT $\alpha(I)$	MOBILITY RATIO $\mathcal{M}$
2	31.18	3.7	0.0323	3.7	9.35	0.181	-0.103	0.147	8.513
	31.60	4.0	0.0323	4.0	9.49	0.184	-0.103	0.149	8.720
	31.92	4.8	0.0323	4.8	9.86	0.193	-0.103	0.154	9.273
	32.27	5.6	0.0323	5.6	10.23	0.202	-0.103	0.159	9.827
	32.97	7.0	0.0323	7.0	10.87	0.221	-0.103	0.168	10.802
	33.63	8.3	0.0323	8.3	11.48	0.242	-0.103	0.176	11.712
	33.92	8.7	0.0323	8.7	11.66	0.249	-0.103	0.178	11.993

Table C.61: Continued.

FINGER ID	TIME OF PHOTO (min)	TIP LOCATION (cm)	TIP VELOCITY dL/dt (cm/sec)	FINGER WIDTH Wf (mm)	AGE OF INTER-FACE t_I	VISCOSITY $\mu_I(I)$ (Pa·sec)	TIP GROWTH RATE λ	REACTION EXTENT $\alpha(I)$	MOBILITY RATIO $\mathcal{M}$
2A	31.18	4.0	0.0309	4.0	9.49	0.184	-0.142	0.149	8.720
	31.60	4.0	0.0309	4.0	9.49	0.184	-0.142	0.149	8.720
	31.92	4.8	0.0309	4.8	9.86	0.193	-0.142	0.154	9.273
	32.27	5.6	0.0309	5.6	10.23	0.202	-0.142	0.159	9.827
	33.92	8.7	0.0309	8.7	11.66	0.249	-0.142	0.178	11.993
3	31.18	4.5	0.0344	7.7	9.72	0.189	-0.044	0.152	9.065
	31.60	4.7	0.0344	7.1	9.81	0.192	-0.044	0.154	9.203
	31.92	5.2	0.0344	8.2	10.04	0.197	-0.044	0.157	9.550
	32.27	6.0	0.0344	7.7	10.41	0.207	-0.044	0.162	10.105
	32.97	7.9	0.0344	7.1	11.29	0.235	-0.044	0.174	11.432
	33.63	9.0	0.0344	8.2	11.80	0.255	-0.044	0.180	12.204
	33.92	9.8	0.0344	6.6	12.17	0.270	-0.044	0.185	12.767
3A	31.18	4.5	0.0331	5.9	9.72	0.189	-0.081	0.152	9.065
	31.60	4.7	0.0331	5.9	9.81	0.192	-0.081	0.154	9.203
	31.92	5.2	0.0331	7.7	10.04	0.197	-0.081	0.157	9.550
	32.27	7.2	0.0331	7.7	10.97	0.224	-0.081	0.169	10.942
	32.97	7.9	0.0331	7.7	11.29	0.235	-0.081	0.174	11.432
	33.63	8.8	0.0331	7.7	11.71	0.251	-0.081	0.179	12.063
	33.92	9.8	0.0331	7.1	12.17	0.270	-0.081	0.185	12.767

Table C.61: Continued.

FINGER ID	TIME OF PHOTO (min)	TIP LOCATION (cm)	TIP VELOCITY dL/dt (cm/sec)	FINGER WIDTH Wf (mm)	AGE OF INTER-FACE t_I	VISCOSITY $\mu_1(I)$ (Pa·sec)	TIP GROWTH RATE λ	REACTION EXTENT $\alpha(I)$	MOBILITY RATIO $\mathcal{M}$
4	31.18	4.5	0.0339	5.9	9.72	0.189	-0.058	0.152	9.065
	31.60	4.7	0.0339	4.7	9.81	0.192	-0.058	0.154	9.203
	31.92	5.2	0.0339	6.5	10.04	0.197	-0.058	0.157	9.550
	32.27	7.2	0.0339	4.7	10.97	0.224	-0.058	0.169	10.942
	32.97	7.9	0.0339	7.1	11.29	0.235	-0.058	0.174	11.432
	33.63	9.1	0.0339	4.7	11.85	0.257	-0.058	0.181	12.274
	33.92	9.8	0.0339	5.9	12.17	0.270	-0.058	0.185	12.767
5	31.18	4.2	0.0343	7.1	9.58	0.186	-0.047	0.150	8.858
	31.60	4.7	0.0343	3.5	9.81	0.192	-0.047	0.154	9.203
	31.92	5.2	0.0343	4.7	10.04	0.197	-0.047	0.157	9.550
	32.27	7.2	0.0343	3.5	10.97	0.224	-0.047	0.169	10.942
	32.97	7.8	0.0343	4.1	11.24	0.234	-0.047	0.173	11.362
	33.63	8.9	0.0343	8.2	11.75	0.253	-0.047	0.180	12.133
	33.92	9.8	0.0343	9.4	12.17	0.270	-0.047	0.185	12.767
6	31.18	4.0	0.0347	5.9	9.49	0.184	-0.036	0.149	8.720
	31.60	4.6	0.0347	7.7	9.76	0.190	-0.036	0.153	9.134
	31.92	5.2	0.0347	9.4	10.04	0.197	-0.036	0.157	9.550
	32.27	6.9	0.0347	4.7	10.83	0.220	-0.036	0.167	10.733
	32.97	7.9	0.0347	4.7	11.29	0.235	-0.036	0.174	11.432
	33.63	9.0	0.0347	4.7	11.80	0.255	-0.036	0.180	12.204
	33.92	9.5	0.0347	4.7	12.03	0.264	-0.036	0.183	12.555

Table C.62: Data and calculations for fingering flow run # 9.9.A Q = 1120.5.

FINGER ID	TIME OF PHOTO (min)	TIP LOCATION (cm)	TIP VELOCITY dL/dt (cm/sec)	FINGER WIDTH Wf (mm)	AGE OF INTER-FACE t_I	VISCOSITY $\mu_1(I)$ (Pa·sec)	TIP GROWTH RATE λ	REACTION EXTENT $\alpha(I)$	MOBILITY RATIO M
4	18.92	3.5	0.0758	4.8	9.18	0.178	-0.242	0.145	8.270
	19.33	5.3	0.0758	6.4	9.48	0.184	-0.242	0.149	8.717
	19.67	7.0	0.0758	6.4	9.77	0.191	-0.242	0.153	9.140
	19.98	7.3	0.0758	6.4	9.82	0.192	-0.242	0.154	9.214
	20.32	9.7	0.0758	8.0	10.22	0.202	-0.242	0.159	9.813
	20.48	11.0	0.0758	8.0	10.43	0.208	-0.242	0.162	10.139
5	18.92	3.5	0.0771	6.4	9.18	0.178	-0.229	0.145	8.270
	19.33	5.3	0.0771	8.0	9.48	0.184	-0.229	0.149	8.717
	19.67	7.0	0.0771	6.4	9.77	0.191	-0.229	0.153	9.140
	19.98	8.0	0.0771	6.4	9.93	0.195	-0.229	0.155	9.389
	20.32	9.7	0.0771	6.4	10.22	0.202	-0.229	0.159	9.813
	20.48	10.0	0.0771	11.2	10.27	0.203	-0.229	0.160	9.888
6	19.33	4.0	0.0509	9.6	9.27	0.179	-0.491	0.146	8.394
	19.67	5.0	0.0509	8.0	9.43	0.183	-0.491	0.148	8.642
	19.98	6.0	0.0509	8.0	9.60	0.187	-0.491	0.151	8.891
	20.32	7.0	0.0509	9.6	9.77	0.191	-0.491	0.153	9.140
	20.48	7.5	0.0509	8.0	9.85	0.193	-0.491	0.154	9.264

Table C.63: Data and calculations for fingering flow run # 9.9.B. $\mathcal{N}$ = 1120.5.

FINGER ID	TIME OF PHOTO (min)	TIP LOCATION (cm)	TIP VELOCITY dL/dt (cm/sec)	FINGER WIDTH Wf (mm)	AGE OF INTER-FACE t_I	VISCOSITY $\mu_1(I)$ (Pa·sec)	TIP GROWTH RATE λ	REACTION EXTENT $\alpha(I)$	MOBILITY RATIO $\mathcal{M}$
1	21.53	4.5	0.0759	5.9	11.35	0.237	-0.241	0.174	11.521
	21.80	6.0	0.0759	5.9	11.60	0.247	-0.241	0.178	11.900
	22.02	6.8	0.0759	6.5	11.73	0.252	-0.241	0.179	12.102
	22.15	7.2	0.0759	6.7	11.80	0.255	-0.241	0.180	12.204
	22.40	9.0	0.0759	6.5	12.10	0.267	-0.241	0.184	12.660
	22.70	9.7	0.0759	6.5	12.22	0.273	-0.241	0.186	12.837
2	21.53	4.8	0.0726	8.9	11.40	0.239	-0.274	0.175	11.597
	21.80	6.0	0.0726	8.9	11.60	0.247	-0.274	0.178	11.900
	22.02	7.0	0.0726	11.7	11.77	0.253	-0.274	0.180	12.153
	22.15	7.5	0.0726	11.7	11.85	0.257	-0.274	0.181	12.280
	22.40	9.0	0.0726	10.4	12.10	0.267	-0.274	0.184	12.660
	22.70	9.7	0.0726	10.4	12.22	0.273	-0.274	0.186	12.837
4	21.53	5.0	0.1001	14.8	11.43	0.240	0.001	0.175	11.648
	21.80	6.5	0.1001	18.0	11.68	0.250	0.001	0.179	12.027
	22.02	8.0	0.1001	19.5	11.93	0.260	0.001	0.182	12.406
	22.15	9.0	0.1001	19.5	12.10	0.267	0.001	0.184	12.660
	22.40	10.5	0.1001	19.5	12.35	0.279	0.001	0.187	13.040
	22.70	11.8	0.1001	18.3	12.57	0.289	0.001	0.190	13.371

Table C.64: Data and calculations for fingering flow run # 9.17.A $\mathcal{N}$ = 168.1.

FINGER ID	TIME OF PHOTO (min)	TIP LOCATION (cm)	TIP VELOCITY dL/dt (cm/sec)	FINGER WIDTH Wf (mm)	AGE OF INTER-FACE t_I	VISCOSITY $\mu_1(I)$ (Pa·sec)	TIP GROWTH RATE λ	REACTION EXTENT $\alpha(I)$	MOBILITY RATIO $\mathcal{M}$
2	60.37	2.5	0.0385	6.9	11.38	0.238	1.567	0.175	11.563
	60.63	3.2	0.0385	7.5	12.16	0.270	1.567	0.185	12.744
	60.97	4.0	0.0385	9.3	13.04	0.314	1.567	0.196	14.100
	61.57	5.4	0.0385	9.5	14.60	0.422	1.567	0.215	16.488
	62.18	6.7	0.0385	10.8	16.04	0.572	1.567	0.233	18.715
3	60.37	2.5	0.0261	6.9	11.38	0.238	0.740	0.175	11.563
	60.63	2.8	0.0261	11.2	11.71	0.251	0.740	0.179	12.069
	60.97	3.8	0.0261	13.3	12.82	0.302	0.740	0.193	13.761
	61.57	4.5	0.0261	9.5	13.60	0.348	0.740	0.203	14.951
	62.18	5.3	0.0261	6.8	14.49	0.413	0.740	0.214	16.317
4	60.37	3.0	0.0293	6.9	11.93	0.260	0.953	0.182	12.406
	60.63	3.0	0.0293	4.5	11.93	0.260	0.953	0.182	12.406
	60.97	4.0	0.0293	6.0	13.04	0.314	0.953	0.196	14.100
	61.57	5.0	0.0293	8.1	14.16	0.387	0.953	0.210	15.804
	62.18	6.0	0.0293	5.4	15.27	0.484	0.953	0.224	17.515
5	60.37	2.3	0.0315	3.4	11.16	0.231	1.100	0.172	11.227
	60.63	3.0	0.0315	7.5	11.93	0.260	1.100	0.182	12.406
	60.97	3.7	0.0315	5.3	12.71	0.296	1.100	0.192	13.591
	61.57	4.5	0.0315	9.5	13.60	0.348	1.100	0.203	14.951
	62.18	5.9	0.0315	8.1	15.16	0.473	1.100	0.222	17.343

Table C.64: Continued.

FINGER ID	TIME OF PHOTO (min)	TIP LOCATION (cm)	TIP VELOCITY dL/dt (cm/sec)	FINGER WIDTH Wf (mm)	AGE OF INTER-FACE t_I	VISCOSITY $\mu_1(I)$ (Pa·sec)	TIP GROWTH RATE λ	REACTION EXTENT $\alpha(I)$	MOBILITY RATIO $\mathcal{M}$
6	60.37	2.2	0.0345	6.9	11.04	0.227	1.300	0.170	11.059
	60.63	3.0	0.0345	6.0	11.93	0.260	1.300	0.182	12.406
	60.97	3.7	0.0345	10.0	12.71	0.296	1.300	0.192	13.591
	61.57	5.0	0.0345	12.2	14.16	0.387	1.300	0.210	15.804
	62.18	6.0	0.0345	14.9	15.27	0.484	1.300	0.224	17.515

Table C.65: Data and calculations for fingering flow run # 9.20.A. $\mathcal{V}$ = 1658.

FINGER ID	TIME OF PHOTO (min)	TIP LOCATION (cm)	TIP VELOCITY dL/dt (cm/sec)	FINGER WIDTH Wf (mm)	AGE OF INTER-FACE t_I	VISCOSITY $\mu_1(I)$ (Pa·sec)	TIP GROWTH RATE λ	REACTION EXTENT $\alpha(I)$	MOBILITY RATIO $\mathcal{M}$
1	19.45	3.0	0.1951	7.1	11.09	0.228	0.318	0.171	11.125
	19.68	6.0	0.1951	8.9	11.43	0.240	0.318	0.175	11.636
	20.38	14.0	0.1951	14.2	12.33	0.278	0.318	0.187	13.005
2	19.45	3.0	0.1951	26.7	11.09	0.228	0.318	0.171	11.125
	19.68	6.0	0.1951	26.7	11.43	0.240	0.318	0.175	11.636
	20.38	14.0	0.1951	34.7	12.33	0.278	0.318	0.187	13.005

Table C.66: Data and calculations for fingering flow runs which had no fingers. Calculations are for the interface.

RUN NO.	$\mathcal{V}$	TIME OF PHOTO (min)	INTERFACE LOCATION (cm)	AGE OF INTER-FACE t_I	VISCOSITY $\mu_1(I)$ (Pa·sec)	REACTION EXTENT $\alpha(I)$	MOBILITY RATIO $\mathcal{M}$
8.19.A	1905	13.55	2	8.90	0.172	0.141	7.844
		15.27	18.7	10.53	0.211	0.163	10.289
8.19.B	403.4	12.73	1.0	7.75	0.153	0.125	6.159
		14.35	17.8	11.70	0.250	0.179	12.044
8.24.A	403.4	29.93	2.0	8.43	0.164	0.134	7.149
		35.03	19.0	16.30	0.605	0.236	19.104
9.22.A	3361	5.15	5.0	2.51	0.127	0.043	-1.232
		5.78	15.0	4.38	0.127	0.074	1.340
9.21.A	2174	13.17	8.0	8.89	0.172	0.141	7.831
		13.45	9.0	9.25	0.179	0.146	8.370
8.20.A		14.17	2.0	8.42	0.163	0.134	7.135
		15.60	14.0	11.01	0.226	0.170	11.013
8.20.B	493.0	29.75	1.0	8.43	0.164	0.134	7.154
		33.85	16.0	14.11	0.383	0.210	15.735

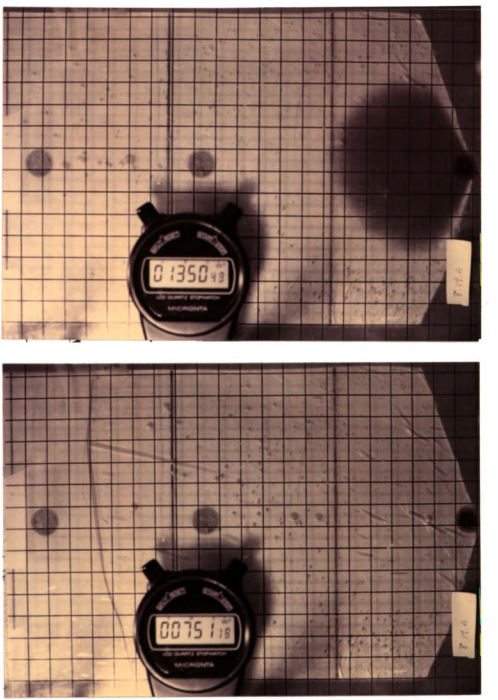


Figure C.38: Photographs for fingering flow run 8.19.A. Photos 1 and 2.

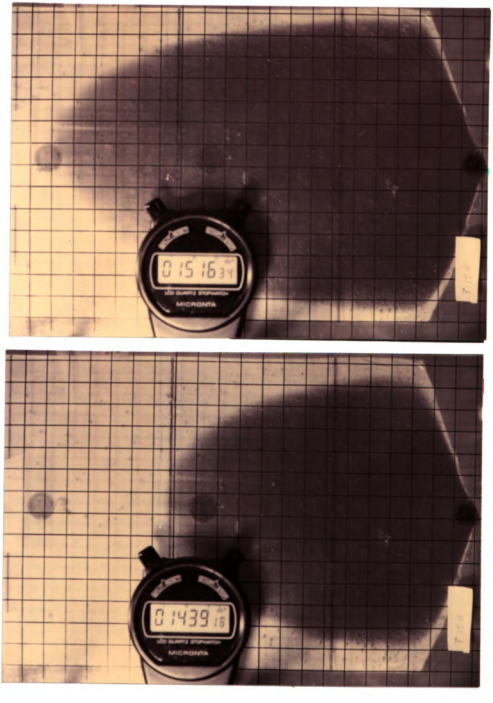


Figure C.38: Continued. Photos 3 and 4.

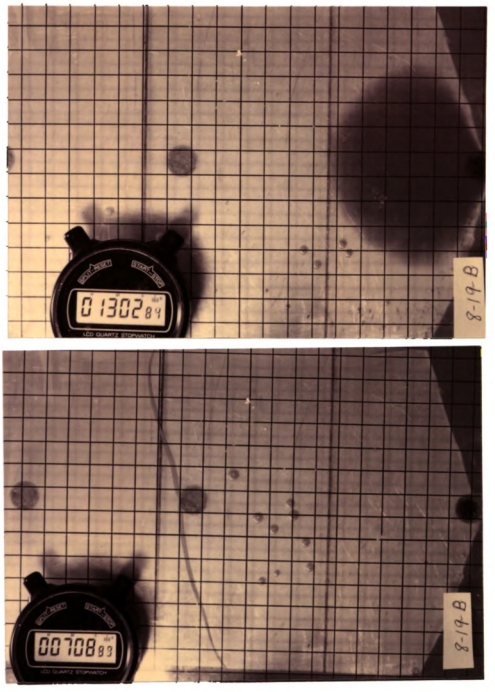


Figure C.39: Photographs for fingering flow run 8.19.B. Photos 1 and 2.

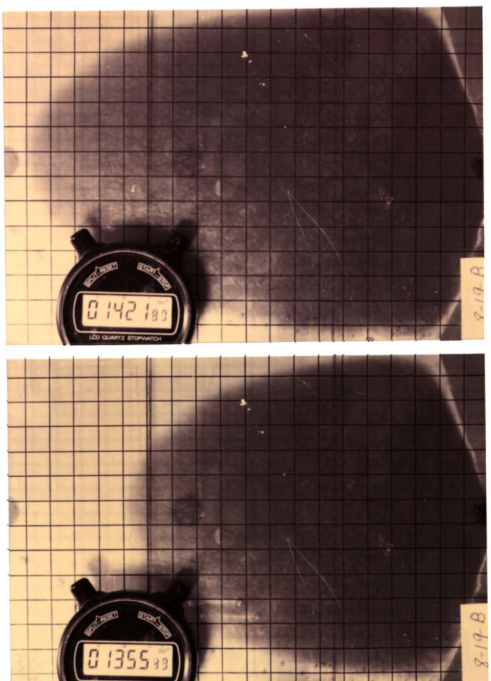


Figure C.39: Continued. Photos 3 and 4.

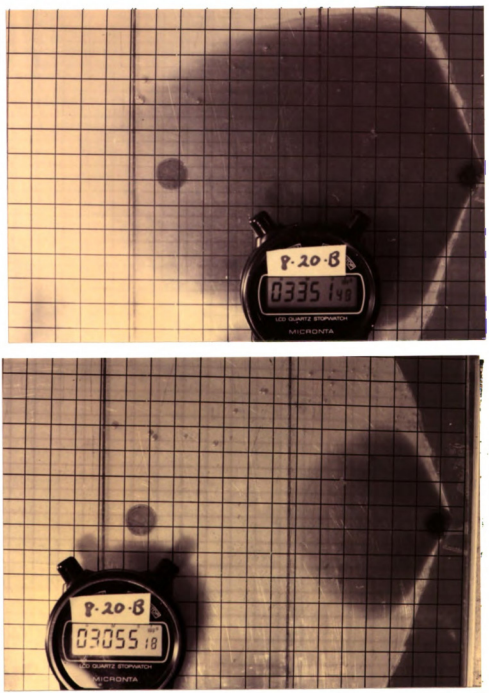


Figure C.40: Photographs for fingering flow run 8.20.B. Photos 1 and 2.

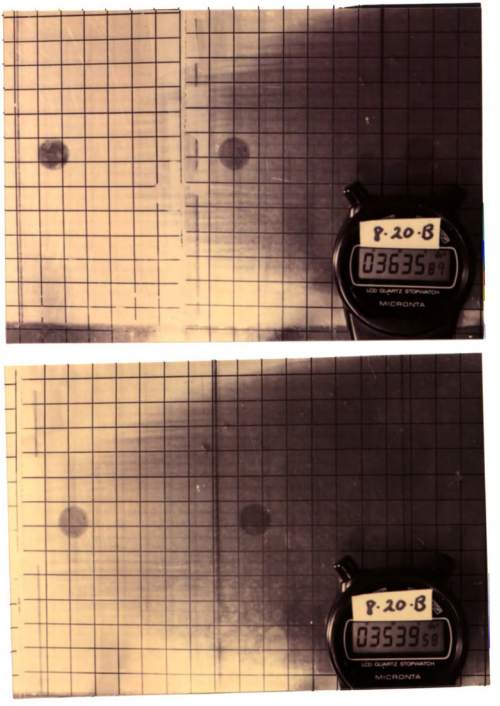


Figure C.40: Continued. Photos 3 and 4.

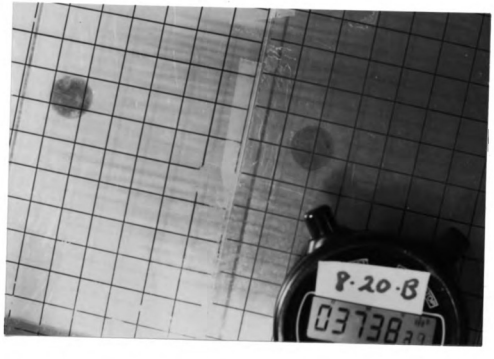


Figure C.40: Continued. Photo 5.

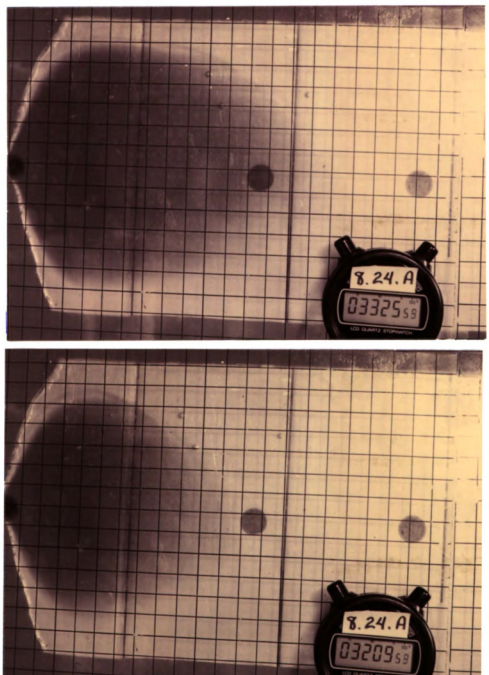


Figure C.41: Photographs for fingering flow run 8.24.A. Photos 1 and 2.

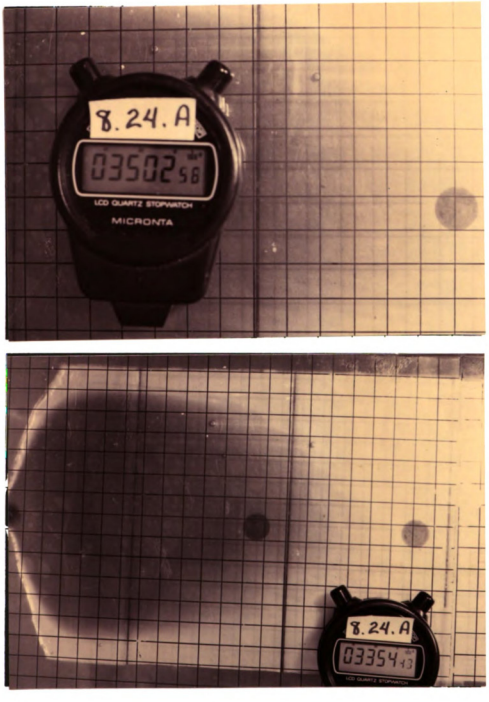


Figure C.41: Continued. Photos 3 and 4.

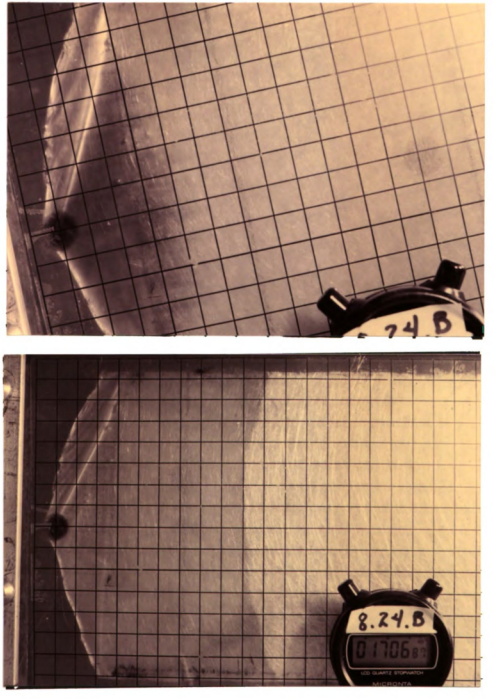


Figure C.42: Photographs for fingering flow run 8.24.B. Photos 1 and 2.



Figure C 42: continued. Photos 3 and 4.

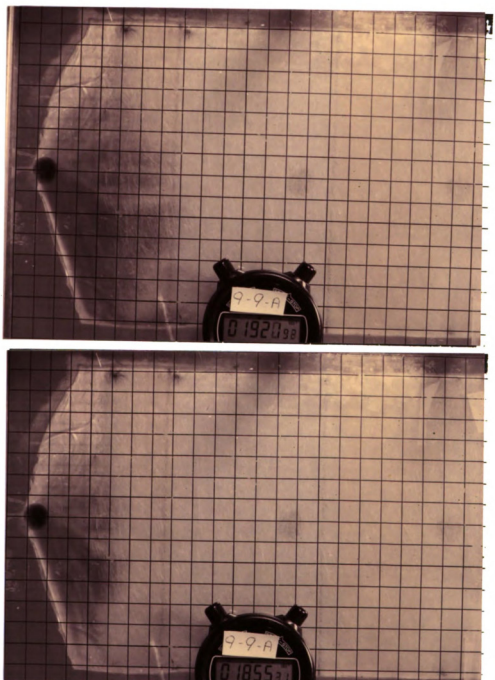


Figure C.43: Photographs for fingering flow run 9.9.A. Photos 1 and 2.

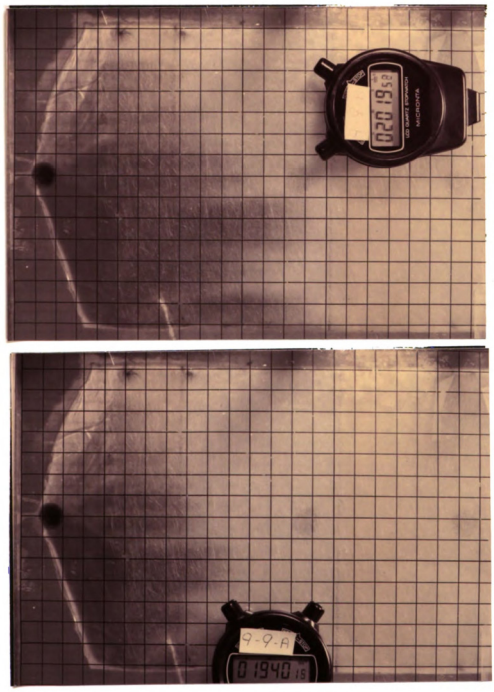


Figure C.43: Continued. Photos 3 and 4.

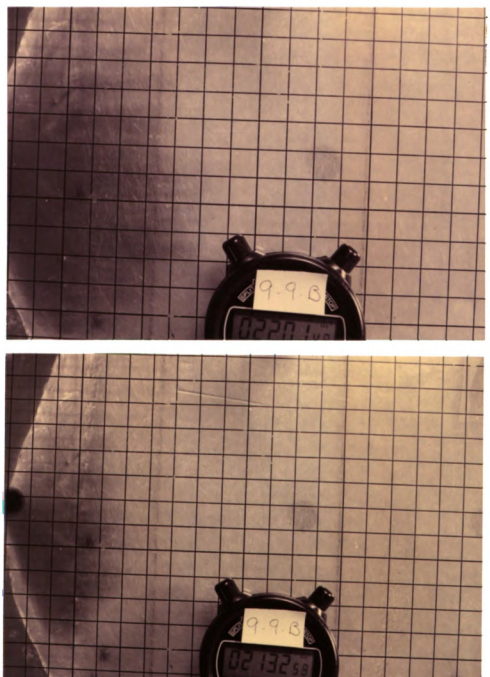


Figure C.44: Photographs for fingering flow run 9.9.B. Photos 1 and 2.

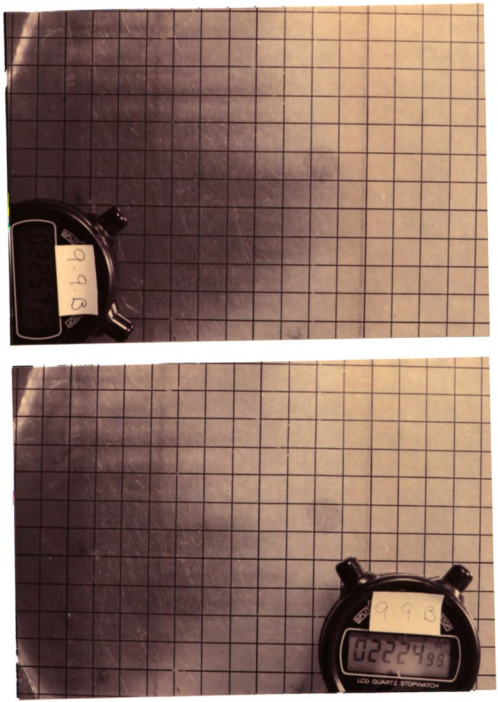


Figure C.44: Continued. Photos 3 and 4.

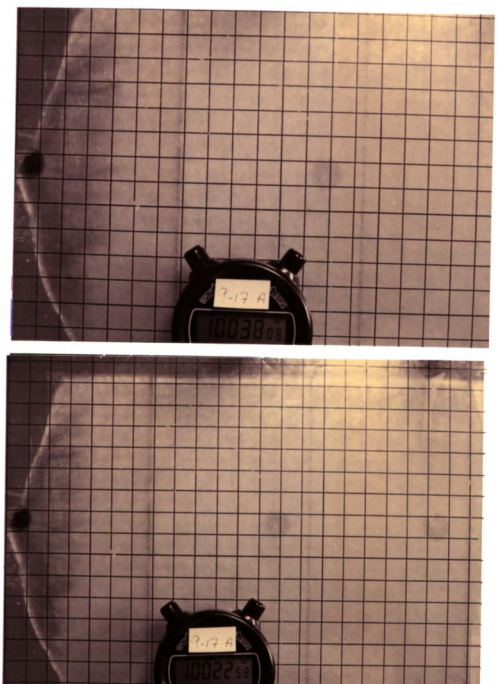


Figure C.45: Photographs for fingering flow run 9.17.A. Photos 1 and 2.

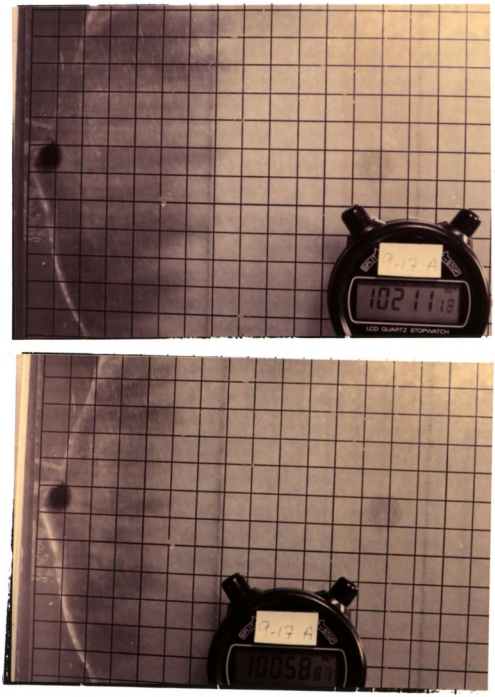


Figure C.45: Continued. Photos 3 and 4.

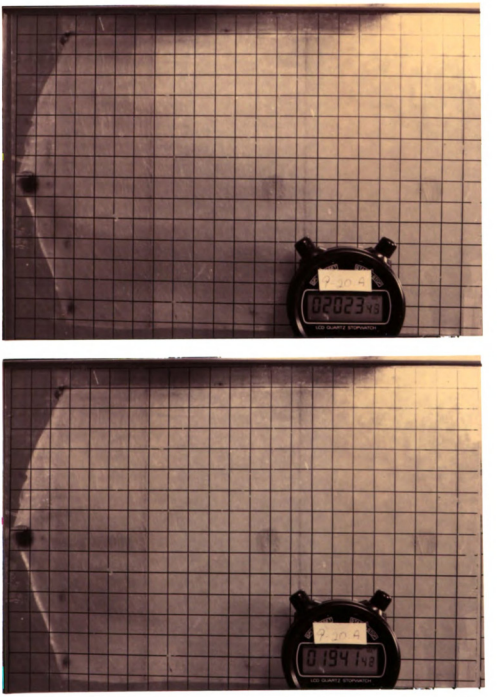


Figure C.46: Photographs for fingering flow run 9.20.A. Photos 1 and 2.

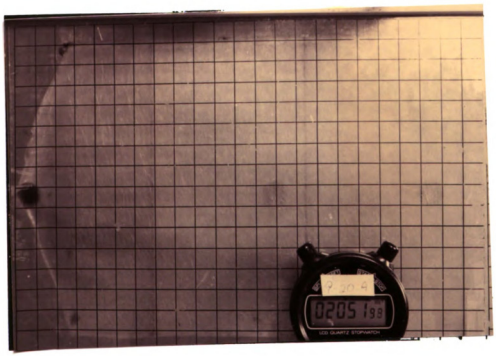


Figure C.46: Continued. Photo 3.



Figure C.47: Photograph for fingering flow run 9.21.A. Photo 1.



Figure C.48: Photograph for fingering flow run 9.22.A. Photo 1.

REFERENCES

Abolafia, O.R., 1969, "Application of Differential Scanning Calorimetry to Epoxy Curing Studies", SPE ANTEC Tech. Papers, Vol. 15, pp. 610-616.

Adams, K.L.; W.B. Russel and L. Rebenfeld; 1988, "Radial Penetration of a Viscous Liquid into a Planar Anisotropic Porous Medium", *Int. J. Multiphase Flow*, vol. 14, no. 2, pp. 203-215.

ASTM Standard, D2471-71. "Standard Test Method for Gel Time and Peak Exothermic Temperature of Reacting Thermosetting Resins", 1979.

Bakkes, Douglas, 1993, Master's thesis, Michigan State University.

Bird, R.B.; W.E. Stewart, and E.N. Lightfoot; 1960 Transport Phenomena, John Wiley & Sons.

Brown, Michael E.; 1988, Introduction to Thermal Analysis: Techniques and Applications, Chapman and Hall, London, pg. 136.

Chan, A.W.; and S-T Hwang, 1991, "Anisotropic In-Plane Permeability of Fabric Media", *Polymer Engineering and Science*, vol. 31, no. 16, pp. 1233-1239.

Fava, R.A.; 1968, "Differential Scanning Calorimetry of Epoxy Resins", *Polymer*, Vol. 9, pp. 137-151.

Fisa, B.; and M. Rahmani, 1991, "Weldline Strength in Injection Molded Flass Fiber-Reinforced Polypropylene", *Polymer Engineering and Science*, vol. 31, no. 18, pp. 1330-1336.

Gere, J.M., and S.R. Timoshenko, 1984, Mechanics of Materials, 2nd. ed., PWS Pub., Boston.

Gonzales-Romero, V.M.; and C.W. Macosko, 1990, "Process Parameters Estimation for Structural Reaction Injection Molding and Resin Transfer Molding", *Polymer Engineering and Science*, vol. 30, no. 3, pp. 142-146.

Gorell, S.B.; and G.M. Homsy, 1985, "A Theory for the Most Stable Variable Viscosity Profile in Graded Mobility Displacement Processes", *AIChE Journal*, vol. 31, no. 9, pp. 1498-1503.

Hill, S., 1952, "Channelling in packed columns", *Chemical Engineering Science*, vol. 1, no. 6, pp. 247-253.

Holmberg, J.A., 1992,"On Flexural and Tensile Strength for Composites Manufactures by RTM", *J. Reinforced Plastics and Composites*, vol. 11, pp. 1302-1320.

Homsy, G.M., 1987, "Viscous Fingering in Porous Media", *Annual Review of Fluid Mechanics*, vol. 19, pp. 271-311.

Horie, K.; H. Hiura, M. Sawada, I. Mita, and H. Kambe, 1970, "Calorimetric Investigation of Polymerization Reactions. III. Curing Reaction of Epoxides with Amines", *J. Polymer Science, Part A-1*. Vol. 8, pp. 1357-1372.

Hull, D., 1987, An introduction to composite materials, Cambridge Univ. Press,

Kim, D.H., and S.C. Kim, 1987, "Engineering Analysis of Reaction Injection Molding Process of Epoxy Resin", *Polymer Composites*, Vol. 8, No. 3, pp. 208-217.

Koch and Brady, 1986, "The Effective Diffusivity of Fibrous Media", *AIChE Journal*, vol. 32, no. 4, pp. 575-591.

Larson, Brent K., 1993, PhD. Dissertation, Michigan State University.

Lee, H.; and K. Neville, 1967, Handbook of Epoxy Resins, McGraw-Hill Book Co., New York.

Macosko, C.W.; 1989, RIM: Fundamentals of Reaction Injection Molding, Hanser Pub., NY.

Mijovic, J.; J. Kim, and J. Slaby, 1984, "Cure Kinetics of Epoxy Formulations of the type Used in Advanced Composites", *J. Applied Polymer Science*, Vol. 29, pp. 1449-1462.

Morgan, R.J.; E.T. Mones and W.J.Steele, 1982, "Tensile deformation and failure processed of amine-cured epoxies", *POLYMER*, vol. 23, pp. 295-304.

Park, C.W.; and G.M. Homsy, 1985, "The instability of long fingers in Hele-Shaw flows", *Physics of Fluids*, vol. 28, no. 6, pp. 1583-1585.

Patankar, Suhas V., 1990, Numerical Heat Transfer and Fluid Flow, Hemisphere Pub. Co., New York.

Paterson, L., 1985, "Fingering with miscible fluids in a Hele-Shaw cell", *Physics of Fluids*, vol. 28, no. 1, pp. 26-30.

Perkins, T.K.; and O.C. Johnston, 1963, "A Review of Diffusion and Dispersion in Porous Media", *Soc. of Petroleum Engineers J.*, March 1963, pp. 70-84.

Perkins, T.K.; and O.C. Johnston, 1965, "Mechanics of Viscous Fingering in Miscible Systems", *Soc. of Petroleum Engineers J.*, Dec. 1965, pp. 301-317.

Peyser, P.; and W.D. Bascom, 1977, "Kinetics of Epoxy Resin Polymerization Using Differential Scanning Calorimetry", *J. Applied Polymer Science*, Vol. 21, pp. 2359-2373.

Prime, R.B.; 1973, "Differential Scanning Calorimetry of The Epoxy Cure Reaction", *Polymer Engineering and Science*, Vol. 13, No. 5, pp. 365-371.

Raghave, R.S., 1988, "Development and Characterization of Thermosetting-Thermoplastic Polymer Blends for Applications in Damage-tolerant Composites", *J. Polymer Science: Part B: Ploymer Physics*, vol. 26, pp. 65-81.

SACMA, Suppliers of Advanced Composite Materials Association, "Recommended Test Method for Apparent Interlaminar Shear Strength of Oriented Fiber-Resin Composites by the Short-Beam Method. SRM 8.88.

Saffman, P.G.; and G. Taylor, 1958, "The penetration of a fluid into a porous medium or Hele-Shaw cell containing a more viscous fluid", *Proc. R. Soc. London Series*, A245, pp. 312-329.

Slobod, R.L.; and R.A. Thomas, 1963, "Effect of Transverse Diffusion on Fingering In Miscible-Phase Displacement", *Soc. of Petroleum Engineers J.*, March 1963, pp. 9-13.

Tan, C.T.; and G.M. Homsy, 1986, "Stability of miscible displacements in porous media: Rectilinear flow", *Physics of Fluids*, vol 29, no. 11, pp. 3549-3556.

Tanner, R.I., 1985, Engineering Rheology, Clarendon Press, Oxford.

Voyutskii, S.S., 1963, Autohesion and Adhesion of high polymers Interscience Pub.

Winter, H.H., 1987, "Can the Gel Point of a Cross-linking Polymer Be Detected by the G' - G" Crossover?", *Polymer Engineering and Science*, Vol. 27, No. 22, pp. 1698-1702.

Wisanrakkit, G.; and J.K. Gillham, 1990, "The Glass Transition Temperature (T_g) As an Index of Chemical Conversion For a High-T_g Amine/Epoxy System: Chemical And Diffusion Controlled Reaction Kinetics", *J. Coatings Technology*, Vol. 62, No. 783, pp. 35-50.

Wooding, R.A.; and H.J. Morel-Seytoux, 1976, "Multiphase Fluid Flow Through Porous Media", *Annual Review of Fluid Mechanics*, vol. 8, pp. 233-274.

Wool, R.P., 1984, "Molecular Aspects of Tack", *Rubber Chemistry and Technology*, vol. 57, pp. 307-319.

Wool, R.P., B.-L. Yuan, and O.J. McGarel, 1989, "Welding of Polymer Interfaces", *Polymer Engineering and Science*, vol. 29, no. 19, pp. 1340-1367.

MICHIGAN STATE UNIV. LIBRARIES
31293010281834